



## 저작자표시-비영리-변경금지 2.0 대한민국

이용자는 아래의 조건을 따르는 경우에 한하여 자유롭게

- 이 저작물을 복제, 배포, 전송, 전시, 공연 및 방송할 수 있습니다.

다음과 같은 조건을 따라야 합니다:



저작자표시. 귀하는 원저작자를 표시하여야 합니다.



비영리. 귀하는 이 저작물을 영리 목적으로 이용할 수 없습니다.



변경금지. 귀하는 이 저작물을 개작, 변형 또는 가공할 수 없습니다.

- 귀하는, 이 저작물의 재이용이나 배포의 경우, 이 저작물에 적용된 이용허락조건을 명확하게 나타내어야 합니다.
- 저작권자로부터 별도의 허가를 받으면 이러한 조건들은 적용되지 않습니다.

저작권법에 따른 이용자의 권리는 위의 내용에 의하여 영향을 받지 않습니다.

이것은 [이용허락규약\(Legal Code\)](#)을 이해하기 쉽게 요약한 것입니다.

[Disclaimer](#)

공학박사학위논문

Instability in Crystalline Phase of  
Chalcogenide Materials under  
Electric Current for  
Phase Change Memory

결정상 상변화 물질의 전류 인가에 따른  
불안정성 연구

2016년 2월

서울대학교 대학원

재료공학부

박 용 진

결정상 상변화 물질의 전류 인가에 따른  
불안정성 연구

INSTABILITY IN CRYSTALLINE PHASE OF  
CHALCOGENIDE MATERIALS UNDER ELECTRIC CURRENT FOR  
PHASE CHANGE MEMORY

지도교수: 주 영 창

이 논문을 공학박사 학위논문으로 제출함

2016년 1월

서울대학교 대학원

재료공학부

박 용 진

박 용 진의 박사학위 논문을 인준함

2016년 1월

위 원 장	김 기 범	(인)
-------	-------	-----

부 위 원 장	주 영 창	(인)
---------	-------	-----

위 원	한 승 우	(인)
-----	-------	-----

위 원	양 철 웅	(인)
-----	-------	-----

위 원	안 동 호	(인)
-----	-------	-----

## **ABSTRACT**

### **Instability in crystalline phase of chalcogenide materials under electric current for phase change memory**

Yong-Jin Park

Department of Materials Science and Engineering

The Graduate School

Seoul National University

Reliability problems such as void formation have been reported in phase change random access memory (PcRAM), which originates from harsh operating conditions and high temperatures and current density. Previous research has examined the migration behavior of phase-change materials when induced by electric currents, while most studies of failure mechanisms have only focused on liquid states. Crystalline phase have been considered a stable state for electric currents because the diffusivity of atoms in a liquid phase is much faster than that in a crystalline phase.

Here, we observe the mechanism behaviors in crystalline chalcogenide materials, which noticeably degrade or upgrade the conductivity. A simple structure with a line shape is used for a model study to avoid the side effects



from the structure and environment of the actual device.

Three different behaviors with respect to the electric current are observed in crystalline  $\text{Ge}_2\text{Sb}_2\text{Te}_5$ . The criteria for mechanism divergence include the resistivity behavior and evolution of voids. Continuous increase in the resistivity over tens of hours and nano-scaled voids are generated at a current density that ranges from 1 to  $1.5 \text{ MA/cm}^2$ ; this behavior is completely different from previous results regarding molten phase failure. This phenomenon develops from electromigration, because alternating (AC) bias cannot trigger this behavior. Localized melting that occurs at the defect site is induced by electromigration, and the molten phase becomes the void area; this phenomenon is called defect-induced melting. The homogeneous nano-voids explains the gradual increase in quantitative resistivity.

Decrease in resistance below a current density of  $1 \text{ MA/cm}^2$  originate from the rearrangement of vacancies. The nature of the material changes from an insulator to a metal, i.e., metal-insulator transition, which is affected by the electric current and temperature. However, the metallic cubic phase of  $\text{Ge}_2\text{Sb}_2\text{Te}_5$  is first demonstrated by using an electric current of  $1 \text{ MA/cm}^2$ , which differs significantly from the thermal annealing accompanying phase transition to a hexagonal phase. The final resistivity of  $\text{Ge}_2\text{Sb}_2\text{Te}_5$  varies according to the peak current density, regardless of the initial resistivity and temperature, which implies that the conductivity can be modulated by an

electric current. Furthermore, a current-induced metal transition is more effective in  $\text{GeSb}_4\text{Te}_7$  than  $\text{Ge}_2\text{Sb}_2\text{Te}_5$ , which depends on the intrinsic vacancy of the materials.

This work represents a possible side effect of device shrinkage, which increases the current density within the crystalline phase. Because only the active region, which is the limited zone near the heater, can be transformed into a liquid phase, the effect of atomic migration in non-active region is cumulative without recovery by melting. Resistivity changes in crystalline phases affect the reliability of the *SET* state of PcRAM devices, which becomes more significant in multi-level cell (MLC) devices. We believe that this work provides new insight regarding electrical reliability in the crystalline phase of chalcogenide, which offers the design rules and applications for reliable PcRAM devices. Scientifically, this work adds to the fundamental knowledge of the influence of electric currents on the crystalline phase of chalcogenide materials.

---

**Keywords:** phase change random access memory (PcRAM), electromigration, crystalline chalcogenide, categorization of mechanism, current-induced metal insulator transition (MIT)

***Student Number:*** 2010-20602



# Table of Contents

---

<b>Abstract.....</b>	<b>i</b>
<b>Table of contents.....</b>	<b>iv</b>
<b>List of Tables.....</b>	<b>viii</b>
<b>List of Figures.....</b>	<b>ix</b>

## **Chapter 1. Introduction**

---

1.1. Phase change random access memory (PcRAM) .....	1
1.2. Reliability issues in PcRAM .....	5
1.2.1. Endurance problem .....	5
1.2.2. Migration behavior in PcRAM .....	6
1.3. Objective of the thesis .....	10
1.4. Organization of the thesis .....	13

## **Chapter 2. Theoretical Background**

---

2.1. Physical properties of phase-change materials .....	14
2.1.1. Ge-Sb-Te alloys .....	15
2.1.2. Crystalline structure of Ge-Sb-Te compounds .....	17
2.1.3. Temperature dependence of resistivity .....	22

2.1.4. Metal-insulator transition in Ge-Sb-Te alloys .....	25
2.2. Theory of electromigration .....	30
2.2.1. Electromigration .....	30
2.2.2. Driving forces for electromigration .....	31
2.3. Mass transport in phase-change materials .....	34
2.3.1. Electromigration behaviors in molten phase $\text{Ge}_2\text{Sb}_2\text{Te}_5$ .....	35
2.3.2. Electromigration behaviors in crystalline phase $\text{Ge}_2\text{Sb}_2\text{Te}_5$ ..	41

### **Chapter 3. Experimental Procedures**

---

3.1. Sample preparation .....	44
3.2. Electrical stressing method .....	49
3.2.1. Wafer-level test .....	49
3.2.2. Package-level test .....	52
3.3. Compositional analysis .....	55

### **Chapter 4. Gradual degradation in the crystalline $\text{Ge}_2\text{Sb}_2\text{Te}_5$ under electric current**

---

4.1. Introduction .....	57
4.2. Experiments .....	59
4.3. Electrical stressing in crystalline $\text{Ge}_2\text{Sb}_2\text{Te}_5$ .....	59
4.3.1. High current .....	60
4.3.2. Low current .....	60

4.3.2. Mid current .....	61
4.4. Frequency dependence in gradual failure .....	64
4.5. Microstructural analysis .....	66
4.5.1. Quantification of voids .....	66
4.5.2. Resistivity according to void fraction .....	71
4.5.3. Composition at the defect site .....	74
4.6. Mechanism for the void generation .....	77
4.7. Summary .....	78

## **Chapter 5. Formation of metallic cubic-phase Ge-Sb-Te compounds when induced by an electric current**

---

5.1. Introduction .....	80
5.2. Experiments .....	82
5.3. Current-driven electrical sweep in $\text{Ge}_2\text{Sb}_2\text{Te}_5$ .....	83
5.3.1. I-V characteristics of $\text{Ge}_2\text{Sb}_2\text{Te}_5$ .....	83
5.3.2. TCR measurement of current-stressed $\text{Ge}_2\text{Sb}_2\text{Te}_5$ .....	87
5.3.3. Complex effect of current and temperature in $\text{Ge}_2\text{Sb}_2\text{Te}_5$ ...	91
5.4. Time-dependent behavior of $\text{Ge}_2\text{Sb}_2\text{Te}_5$ .....	93
5.5. Microstructural analysis of $\text{Ge}_2\text{Sb}_2\text{Te}_5$ .....	96
5.5.1. Phase of current- and temperature-stressed $\text{Ge}_2\text{Sb}_2\text{Te}_5$ .....	96
5.5.2. Gradual decrease in resistivity during thermal annealing ...	102
5.6. Comparison between $\text{Ge}_2\text{Sb}_2\text{Te}_5$ and $\text{GeSb}_4\text{Te}_7$ .....	104
5.7. Role of electric current in vacancy rearrangement .....	110

5.8. Summary .....	114
--------------------	-----

## **Chapter 6. Divergence of failure mechanisms with current and temperature in crystalline chalcogenide**

---

6.1. Introduction .....	115
6.2. Experiments .....	116
6.3. Limitations of the mechanism map for $\text{Ge}_2\text{Sb}_2\text{Te}_5$ .....	116
6.4. Mechanism map for chalcogenide materials .....	122
6.4.1. Resistivity behavior in ternary and binary chalcogenide .....	122
6.4.2. Mechanism behavior in crystalline $\text{Bi}_2\text{Te}_3$ .....	124
6.4.3. Failure criteria with respect to the stoichiometric effect .....	129
6.5. Summary .....	130

## **Chapter 7. Conclusions**

---

7.1. Summary of results .....	134
7.2. Future works and suggested research .....	139

<b>References</b> .....	141
-------------------------	-----

<b>Abstract (In Korean)</b> .....	149
-----------------------------------	-----

<b>Curriculum Vitae</b> .....	151
-------------------------------	-----





## LIST OF TABLES

- Table 3.1** Detailed sputtering conditions for deposition of chalcogenide materials.
- Table 5.1** Comparison between the calculated distance in **Figure 5.9(b)** and crystallographic distance in cubic phase of  $\text{Ge}_2\text{Sb}_2\text{Te}_5$ .
- Table 5.2** Fraction of vacancies in the pseudo-binary compound of  $(\text{GeTe})_x(\text{Sb}_2\text{Te}_3)_{1-x}$  according to  $x$ .

## LIST OF FIGURES

- Figure 1.1** A graphical representation of material phases and principle of operation in PcRAM device. The crystalline phase is denoted as *SET* state, and the amorphous phase is denoted as *RESET* state. The phase transformation is caused by Joule heating with modulating the power and time of pulse.
- Figure 1.2** Schematic image for a PcRAM cell of the *SET* state (left) and the *RESET* state (right), where the phase change material (PCM) is in a crystalline or amorphous phase. PcRAM storage element is conceptually a tunable resistor, usually realized by connecting the PCM layer with a metallic electrode, called a heater, that forces high current density; a Joule heating-induced phase change then occurs in the phase change volume.

**Figure 1.3** (a) STEM image of PcRAM cell and EDS line profiles show the non-stoichiometric composition on vertical line 1. Sb accumulated in the phase change volume. [9] (b) An EDS mapping shows Sb accumulated in the phase change volume and Ge diffused out of the phase change volume after cycling.

**Figure 1.4** (a) Void generated at the interface between the phase change volume (blue dotted line) and bottom electrode after cyclic operation in PcRAM. [14] (b) Void generation in the inside of phase change material with *RESET-stuck* failure. [8]

**Figure 1.5** Reported results of current-induced change in phase change materials with respect to current density level. The behavior of applying current density ranged approximately  $10^6$  A/cm<sup>2</sup> has not been reported yet.

**Figure 2.1** Equilibrium phase diagram for alloys along the pseudo-binary tie-line GeTe-Sb<sub>2</sub>Te<sub>3</sub> (adapted from references [20, 21]. In the lower section of the figure, the existence of metastable phases is also shown. Reprinted with permission from [22].

**Figure 2.2** (a) Atomic arrangement for metastable rock-salt  $\text{Ge}_2\text{Sb}_2\text{Te}_5$  structure built based on (111) planes along the [111] direction. (b) Atomic arrangement for stable hexagonal  $\text{Ge}_2\text{Sb}_2\text{Te}_5$  structure built based on (0001) planes along the [0001] direction. [32]

**Figure 2.3** (a) Pressure-induced changes of the XRD pattern of  $\text{Ge}_2\text{Sb}_2\text{Te}_5$  upon compression. The peaks marked by \* are the corresponding peaks of the NaCl marker. (b) Volume of unit cell according to pressure (solid point) and fitting using Birch-Murnaghan EOS (solid line). [35]

**Figure 2.4** (a) Sheet resistance of 80 nm thin  $\text{Ge}_2\text{Sb}_2\text{Te}_5$  film measured with increasing temperature. Sharp drops accompany the amorphous-FCC transformation at  $T_1$  and the FCC-HCP transformation at  $T_2$ . (b) Sheet resistance upon subsequent cooling. The resistance of the FCC phase (Curve 1) increases with cooling, whereas that of the HCP phase (Curve 2) decreases. [27]

**Figure 2.5** (a) Temperature dependence of the sheet resistance on GeTe. (b) Temperature dependence of the sheet resistance on  $\text{GeSb}_2\text{Te}_4$ . [45]

**Figure 2.6** Total energy per atoms,  $E_{\text{diff}}$ , of the metastable cubic  $\text{GeSb}_2\text{Te}_4$  and stable hexagonal  $\text{GeSb}_2\text{Te}_4$  with respect to vacancy layer formation. [48]

**Figure 2.7** (a) Compositional profiles in  $\text{Ge}_2\text{Sb}_2\text{Te}_5$  line from WDS analysis shown as atomic concentration and their SEM image. [13] (b) Image of the capped pattern of  $\text{Ge}_2\text{Sb}_2\text{Te}_5$  after voltage sweeping. Mass depleted regions were blackened out in the individual element mapping. [11]

**Figure 2.8** (a) Cell structure of the real device (mushroom-structure). (b) Current density and (c) temperature profile in  $\text{Ge}_2\text{Sb}_2\text{Te}_5$  layer of structure (a). (d) Compositional profiles after pulse stressing with various duration time for Ge, Sb, and Te calculated from the finite differential method (FDM). [55]

**Figure 2.9** (a) atomic concentration and (b) relative intensity showing the atomic diffusion from the anode to the cathode in crystalline  $\text{Ge}_2\text{Sb}_2\text{Te}_5$  line after the DC stressing.

**Figure 3.1** (a) SEM Images and (b) schematic of cross-section image of the line-shaped structure of chalcogenide material for electromigration test, which dimension is 20  $\mu\text{m}$  in length, 2  $\mu\text{m}$  in width and 300 nm in thickness. The chalcogenide materials were isolated by Mo contact pads and passivated with a silicon nitride film 100 nm in thickness.

**Figure 3.2** Schematic diagram of the system for electromigration test using electrical pulse stressing in the wafer-level.

**Figure 3.3** The electromigration tester for package-level test (Qualitau MIRA EM tester). Two EM modules are housed in one MIRA mainframe, with each module providing a capability of running experiments on up to 60 devices under test (DUTs), each at different stress conditions. This equipment was automatically controlled by a commercial program (Qualitau Co.)

**Figure 4.1** (a) Relative resistance-time curves during constant DC current stress on  $\text{Ge}_2\text{Sb}_2\text{Te}_5$  line samples. The stress current ranged from 0.17 to 1.83  $\text{MA}/\text{cm}^2$  at 200 °C. (b) Based on the current density, different microstructures developed in the  $\text{Ge}_2\text{Sb}_2\text{Te}_5$  line samples, as shown by the SEM images. Current densities below 0.83  $\text{MA}/\text{cm}^2$ , ranging from 1 to 1.5  $\text{MA}/\text{cm}^2$  and above 1.67  $\text{MA}/\text{cm}^2$  are denoted as “low current”, “mid current” and “high current”, respectively.

**Figure 4.2** Compositional changes of the sample after the EM stressing at a current density of 1.83  $\text{MA}/\text{cm}^2$  (high current) and 1.17  $\text{MA}/\text{cm}^2$  (mid current).

**Figure 4.3** Resistance-time curves illustrating DC and AC (frequency of 10 MHz) current stressing of  $1.17 \text{ MA/cm}^2$  at  $200^\circ\text{C}$ . The SEM image for each result is also displayed.

**Figure 4.4** (a) High-contrast image of the  $\text{Ge}_2\text{Sb}_2\text{Te}_5$  line sample after testing at  $1.17 \text{ MA/cm}^2$  at  $200^\circ\text{C}$ , as observed by TEM. The gray region denotes  $\text{Ge}_2\text{Sb}_2\text{Te}_5$ , and the dark areas denote defects. (b) The area analysis of the defects as measured by the image analyzer.

**Figure 4.5** Schematic image of homogenous particle model on the (a) rectangular type and (b) top view. (c) Calculation of area sectioned from sphere according to the y-axis distance.

**Figure 4.6** Simulation of relative resistance according to volume fraction of voids, which is calculated using the dispersed particle model. (eq. 4.7) The expansion graph for volume fraction ranged from 0 to 0.5 is displayed in the inset image.

**Figure 4.7** Compositional analysis from SEM and TEM, which contain different interaction volumes. Three different quantitative results are included: the total composition of the sample by SEM, the composition of the non-voided area by TEM, and the composition of the void by TEM.

**Figure 4.8** Pseudo-binary phase diagram of  $\text{Sb}_2\text{Te}_3$  and  $\text{GeTe}$ . Molten state of  $\text{Ge}_2\text{Sb}_2\text{Te}_5$  is separated into two phase during solidification process, which are Sb-rich liquid phase and Ge-rich solid phase.

**Figure 4.9** Schematic diagram of the defect-induced melting and phase separation behavior during solidification.

**Figure 5.1** Resistivity of  $\text{Ge}_2\text{Sb}_2\text{Te}_5$  for a current sweep using the double directional mode, with a sweep from zero to peak current and a return to zero, at room temperature for the 0.33 and 0.5  $\text{MA/cm}^2$  conditions. (b) Resistivity change for peak current densities ranging from 0.33 to 1.67  $\text{MA/cm}^2$  in increments of 0.17  $\text{MA/cm}^2$ .

**Figure 5.2** Cyclic test for current sweep from 0 to 1.67  $\text{MA/cm}^2$  with a fixed peak-current-density of 1.67  $\text{MA/cm}^2$  at room temperature for  $\text{Ge}_2\text{Sb}_2\text{Te}_5$ . The inset of **Figure 5.2** shows a resistivity during cyclic current sweep ranging from 0.0018 to 0.0035  $\Omega\text{cm}$ . An irreversible change in resistivity was completed during the first cycle of applied current.



**Figure 5.3** (a) The resistivity of current-stressed  $\text{Ge}_2\text{Sb}_2\text{Te}_5$  from **Figure 5.1(b)** for temperatures ranging from 30 to 90 °C. The dotted lines are extrapolations whose slopes correspond to the temperature coefficient of resistance (TCR). (b) Resistivity of current-stressed  $\text{Ge}_2\text{Sb}_2\text{Te}_5$  for temperature ranging from 150 to 373 K. Conditions of current density were 0.67 MA/cm<sup>2</sup> (black square), 1 MA/cm<sup>2</sup> (red diamond), and 1.5 MA/cm<sup>2</sup> (blue triangle).

**Figure 5.4** Resistivity slope for current density and temperature according to the stress peak current density results from **Figure 5.1(b)** and **5.3(a)**, respectively. The behavior of the TCR in  $\text{Ge}_2\text{Sb}_2\text{Te}_5$  was similar to the resistivity slope for the current density, which changed from negative to positive at the peak current density of 1 MA/cm<sup>2</sup>.

**Figure 5.5** (a)-(c) Resistivity of  $\text{Ge}_2\text{Sb}_2\text{Te}_5$  for peak-current densities ranging from 0.17 to 2 MA/cm<sup>2</sup> in increments of 0.08 MA/cm<sup>2</sup> at different temperatures which are (a) room temperature, (b) 100 °C, and (c) 200 °C, respectively. (d) Final resistivity and (e) slope of resistivity of  $\text{Ge}_2\text{Sb}_2\text{Te}_5$  according to peak current density at various temperature based on the results from (a)-(c).

**Figure 5.6** (a) Resistivity change of  $\text{Ge}_2\text{Sb}_2\text{Te}_5$  according to the duration of applied current density, ranging from 0.17 to 1.33  $\text{MA}/\text{cm}^2$ , for 30 hours and its expansion (dotted box) from 0 to 1 hour. (b) Initial and final resistivities of  $\text{Ge}_2\text{Sb}_2\text{Te}_5$  according to the current density for the current-stressed condition result from (a).

**Figure 5.7** (a) Resistivity change of  $\text{Ge}_2\text{Sb}_2\text{Te}_5$  according to the duration of applied temperature, ranging from 200 to 350  $^{\circ}\text{C}$ , for 30 hours and its expansion (dotted box) from 0 to 1 hour. (d) Initial and final resistivities of  $\text{Ge}_2\text{Sb}_2\text{Te}_5$  according to the ambient temperature for the isothermal annealing condition result from (c). The electric current has a kinetically fast effect on resistivity compared with thermal stress, which involves a thermally activated change.

**Figure 5.8** (a) TEM image and (b) diffraction pattern of the initial  $\text{Ge}_2\text{Sb}_2\text{Te}_5$  sample, which was not applied by thermal and electrical stress. The microstructure of the current sample was in a polycrystalline cubic phase and the average grain size was approximately 20 nm.

**Figure 5.9** (a) TEM image and (b) diffraction pattern of the current-stressed  $\text{Ge}_2\text{Sb}_2\text{Te}_5$  sample (Current sample:  $1 \text{ MA/cm}^2$  condition). The yellow dotted lines indicate the grain boundary. The microstructure of the current sample was in a polycrystalline cubic phase and the average grain size was approximately 20 nm. (c) TEM image and (d) diffraction pattern of the temperature-stressed  $\text{Ge}_2\text{Sb}_2\text{Te}_5$  sample (temperature sample:  $250^\circ\text{C}$  condition). An HRTEM image of a single grain is displayed in the inset of (c). Large grains of more than 100 nm in a hexagonal phase were observed in the temperature sample.

**Figure 5.10** JCPDS database of (a) face-centered cubic phase and (b) hexagonal close-packed phase of  $\text{Ge}_2\text{Sb}_2\text{Te}_5$ .

**Figure 5.11** XRD result of  $\text{Ge}_2\text{Sb}_2\text{Te}_5$  for different annealing temperatures: Si substrate (blue), pre-annealed  $\text{Ge}_2\text{Sb}_2\text{Te}_5$  (red),  $\text{Ge}_2\text{Sb}_2\text{Te}_5$  annealed at  $250^\circ\text{C}$  for 30 hours (black), and  $\text{Ge}_2\text{Sb}_2\text{Te}_5$  annealed at  $350^\circ\text{C}$  for 1 hour (green).

**Figure 5.12** (a) Resistivity change of GeSb<sub>4</sub>Te<sub>7</sub> with current densities for peak current densities ranging from 0.17 to 1.67 MA/cm<sup>2</sup> in increments of 0.17 MA/cm<sup>2</sup> at room temperature. (b) Final resistivity of Ge<sub>2</sub>Sb<sub>2</sub>Te<sub>5</sub> and GeSb<sub>4</sub>Te<sub>7</sub> according to peak current density at room temperature (results from **Figure 5.1(b)** and **Figure 5.12(a)**, respectively).

**Figure 5.13** (a) The resistivity of current-stressed GeSb<sub>4</sub>Te<sub>7</sub> for temperatures ranging from 30 to 90 °C. The dotted lines are extrapolations whose slopes correspond to the TCR. (b) Resistivity slope of Ge<sub>2</sub>Sb<sub>2</sub>Te<sub>5</sub> and GeSb<sub>4</sub>Te<sub>7</sub> for current density and temperature according to the stressed-peak-current-density results for Ge<sub>2</sub>Sb<sub>2</sub>Te<sub>5</sub> (**Figure 5.1(b)** and **Figure 5.3(a)**) and GeSb<sub>4</sub>Te<sub>7</sub> (**Figure 5.12(a)** and **Figure 5.13(a)**).

**Figure 5.13** (a)-(c) Resistivity change of GeSb<sub>4</sub>Te<sub>7</sub> for peak-current-densities ranging from 0.17 to 2 MA/cm<sup>2</sup> in increments of 0.08 MA/cm<sup>2</sup> at different temperatures: (a) room temperature, (b) 100 °C, and (c) 200 °C. (d) Final resistivity of GeSb<sub>4</sub>Te<sub>7</sub> according to the peak-current-density at various temperatures, based on the results from (a)-(c).

**Figure 5.14** Resistivity of  $\text{Ge}_2\text{Sb}_2\text{Te}_5$  affected by alternating current (AC) and direct current (DC). (a) Resistivity of  $\text{Ge}_2\text{Sb}_2\text{Te}_5$  according to AC frequency from  $10^2$  to  $10^7$  Hz with 1 sec of duration time and 10 V of voltage. (b) Resistivity of  $\text{Ge}_2\text{Sb}_2\text{Te}_5$  according to AC voltage from 1 to 10 V with 1 sec of duration time and 100 Hz of frequency. (c) Resistivity of  $\text{Ge}_2\text{Sb}_2\text{Te}_5$  according to AC time from 0 to 3 hours with voltage of 10 V and frequency of 100 Hz. (d) Resistivity of  $\text{Ge}_2\text{Sb}_2\text{Te}_5$  according to DC and 100 Hz of AC from 1 to 10 V with 1 sec of duration time.

**Figure 5.15** The schematic diagram of the energy states according to the vacancy rearrangement in the cubic and hexagonal phases of Ge-Sb-Te compound. The energy state decreases with vacancy ordering, which is a stable state. The energy barrier for the phase transition from the cubic to the hexagonal phase is much higher than the energy barrier for the rearrangement of vacancies.

**Figure 6.1** Resistivity change of  $\text{Ge}_2\text{Sb}_2\text{Te}_5$  according to the duration of applied current density, ranging from 0.17 to  $1.33 \text{ MA/cm}^2$ , for 30 hours at the different ambient temperature: (a) room temperature, (b)  $100^\circ\text{C}$ , and (c)  $200^\circ\text{C}$

**Figure 6.2** SEM image of  $\text{Ge}_2\text{Sb}_2\text{Te}_5$  line after current stressing test for 30 hours at room temperature, which are shown in **Figure 6.1(a)**. Background color means the group of failure behavior based on the morphological image. Current density below  $1.17 \text{ MA/cm}^2$  is determined to “no fail” (gray), current density ranged from  $1.17$  to  $1.67 \text{ MA/cm}^2$  is determined to “gradual fail” (red), and current density over  $1.83 \text{ MA/cm}^2$  is determined to “abrupt fail” (blue).

**Figure 6.3** Mechanism map of  $\text{Ge}_2\text{Sb}_2\text{Te}_5$  according to current density and temperature based only on the morphological behavior. All solid point are experiment results and failure mechanisms are expressed by background color. Black square shows “no fail”, red circle shows “gradual fail”, and blue triangle shows “abrupt fail”.

**Figure 6.4** Resistivity change with applying current density of  $0.33 \text{ MA/cm}^2$  for 30 hours at  $100^\circ\text{C}$  according to different Te-based chalcogenide materials, which are  $\text{Bi}_2\text{Te}_3$ ,  $\text{Sb}_2\text{Te}_3$ ,  $\text{GeTe}$ , and  $\text{Ge}_2\text{Sb}_2\text{Te}_5$ . The relative resistance means that value of resistance is divided by the initial resistance of each material.

**Figure 6.5** Phase diagram of bismuth and tellurium according to atomic percent of tellurium.

**Figure 6.6** Relative resistance of  $\text{Bi}_2\text{Te}_3$  according to current density ranged from 0.33 to 1.33  $\text{MA}/\text{cm}^2$  for 30 hours at 100 °C, and their SEM image. Current densities below 0.83  $\text{MA}/\text{cm}^2$ , ranging from 0.83 to 1.17  $\text{MA}/\text{cm}^2$  and above 1.17  $\text{MA}/\text{cm}^2$  are denoted as “no fail”, “gradual fail” and “abrupt fail”, respectively.

**Figure 6.7** Relative resistance of  $\text{Bi}_2\text{Te}_3$  according to current density ranged from 0.33 to 1.5  $\text{MA}/\text{cm}^2$  for 30 hours at (a) room temperature, (b) 100 °C, and (c) 200 °C. (d) The mechanism map according to current density and temperature, which is the merging of the results from (a)-(c).

**Figure 6.8** Relative resistance of  $\text{Bi}_{35}\text{Te}_{65}$  according to current density ranged from 0.33 to 1.5  $\text{MA}/\text{cm}^2$  for 30 hours at (a) room temperature, (b) 100 °C, (c) 150, and 200 °C. (d) The mechanism map according to current density and temperature, which is the merging of the results from (a)-(c).

**Figure 6.9** The failure time according to current density and temperature in the  $\text{Bi}_{35}\text{Te}_{65}$  and  $\text{Bi}_2\text{Te}_3$ . Failure time is displayed in the log-scale.

**Figure 6.10** Expanded phase diagram of Bi and Te with atomic percent of Te ranged from 60 to 90 at. %, and mechanism map of stoichiometric  $\text{Bi}_2\text{Te}_3$  (Te : 60 at. %) and non-stoichiometric  $\text{Bi}_{35}\text{Te}_{65}$  (Te : 65 at. %).

**Figure 7.1** Summary of behavior in phase change materials according to current density.

# CHAPTER 1

## Introduction

### 1.1. Phase change random access memory (PcRAM)

Phase change random access memory (PcRAM) is a promising device for non-volatile memory that uses a reversible transition between a material's phases.<sup>1,2,3</sup> PcRAM uses two types of phases to store information: amorphous and crystalline phases. **Figure 1.1** shows a graphical representation of the material phases in PcRAM devices. The crystal structure exhibits regularity over long distances in the crystal lattice, which is called long-range ordering. In this phase, the material has high electrical conductivity and high reflectivity. In contrast, the crystal structure of amorphous phases is disordered and randomly distributed with atomic-scale regularity, which is called short-range ordering. In this phase, the material has low electrical conductivity and low reflectivity compared to the crystalline phase. The difference in resistivity between crystalline and amorphous phases is approximately three orders of magnitude.<sup>2</sup> Thus, these phases can be easily recognized by an electrical signal, such as a current or voltage, in the device system, which enables a PcRAM device to store information.<sup>4</sup>



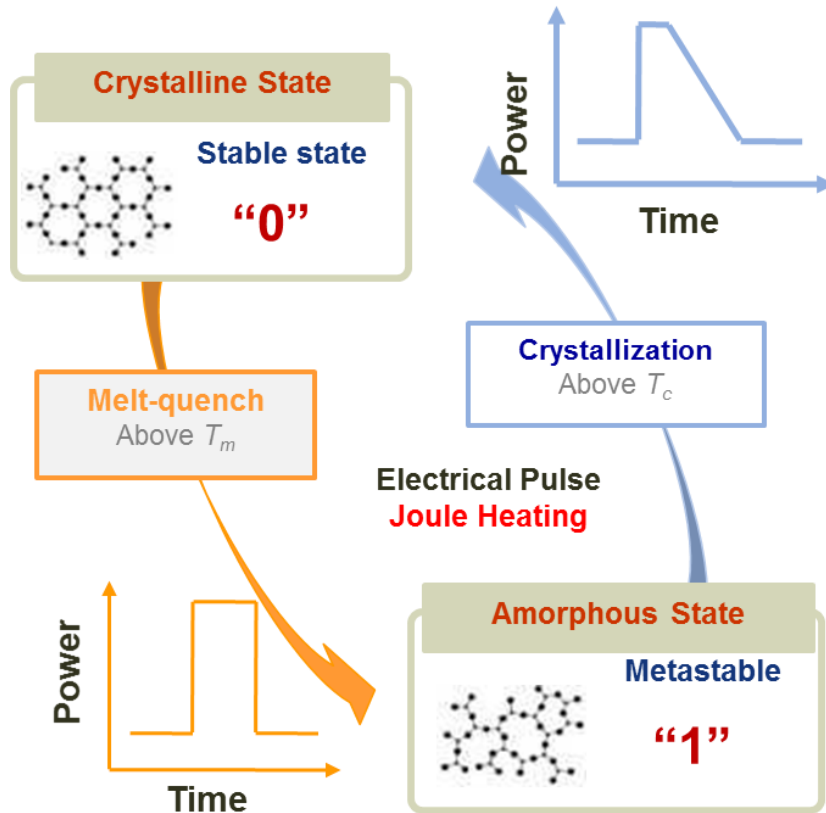


**Figure 1.1** A graphical representation of material phases and principle of operation in PcRAM device. The crystalline phase is denoted as *SET* state, and the amorphous phase is denoted as *RESET* state. The phase transformation is caused by Joule heating with modulating the power and time of pulse.

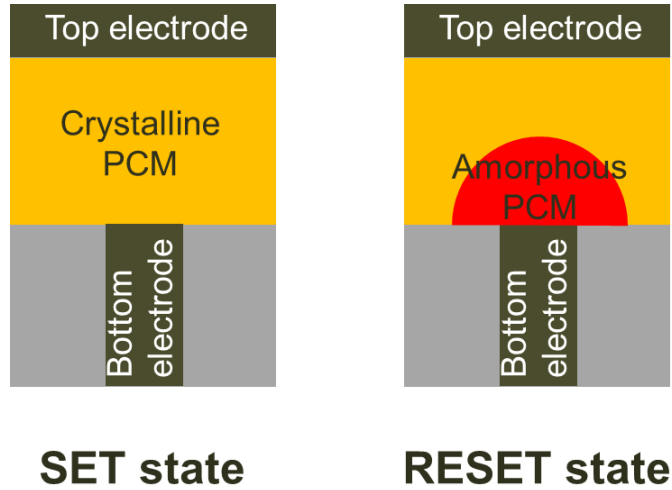


**Figure 1.2** Schematic image for a PcRAM cell of the *SET* state (left) and the *RESET* state (right), where the phase change material (PCM) is in a crystalline or amorphous phase. PcRAM storage element is conceptually a tunable resistor, usually realized by connecting the PCM layer with a metallic electrode, called a heater, that forces high current density; a Joule heating-induced phase change then occurs in the phase change volume.

The phases of phase-change materials can be altered by applying an electric pulse ( $\sim 10^8$  A/cm<sup>2</sup>). A high current density generates localized heat from Joule heating. The material states that form from Joule heating are influenced by the current density and duration of the electric pulse. A high-density electric pulse applies enough Joule heating to raise the temperature above the melting temperature ( $T_m$ ) to change the phase of a material, thus allowing a transformation to a liquid phase during the pulse. This liquid phase is an intermediate state. To transform an amorphous phase into a crystalline phase, the electric pulse is reduced for a sufficient amount of time to allow the crystallization of a liquid phase, which is referred to as the *SET* operation in PcRAM and ranges from 100 ns to 1  $\mu$ s.<sup>5</sup> To transform a crystalline phase into an amorphous phase, however, the electric pulse is reduced quickly enough to quench the liquid phase, which is referred to as the *RESET* operation in a PcRAM device. Strong confinement of the heat and electric current are required for efficient Joule heating in the cell. This condition is usually satisfied by a narrow bottom electrode, which is known as the heater. Therefore, only a portion of the volume of the phase-change material is melted and transformed into an amorphous phase. The amorphous phase occupies a typical dome-shaped volume, which is called a mushroom cell structure.

PcRAM has various advantages for application in memory devices, including fast programming speed<sup>1</sup>, high endurance<sup>2</sup>, and high scalability<sup>3</sup>. Theoretically, phase change mechanisms occur at the nanometer scale.<sup>3</sup> In addition, PcRAM cells have a 1T1R (one transistor and one resistor) structure, which is a very simple structure.<sup>6</sup> Using this simple cell structure facilitates the integration of PcRAM cells into conventional CMOS process technology for conventional memory devices such as DRAM and FLASH, which is a huge advantage for device integration with respect to cost.

However, PcRAM should overcome reliability problems that originate from extrinsically harsh operating conditions. To employ PcRAM as the main memory device, its endurance characteristic should achieve  $10^{16}$  cycles. However, recently developed PcRAM devices typically exhibit only  $10^8 \sim 10^9$  cycles. The reliability issues in PcRAM will be considered in the next section.

## 1.2. Reliability issues in PcRAM

### 1.2.1. Endurance problem

After many *SET-RESET* cycles, PcRAM cells end up with one of two types of failure: *SET*-stuck failure and *RESET*-stuck failure.<sup>7</sup> This practical problem in PcRAM devices originates from high current density. In a *SET*-stuck problem, the resistance of the phase-change material is degraded and fixed at a low resistance value. Switching from a crystalline to amorphous phase is prohibited despite any *RESET* operation. *SET*-stuck problems originate from compositional changes in the phase-change material in the phase change region. Recent studies have shown that  $\text{Ge}_2\text{Sb}_2\text{Te}_5$  (GST) materials-based PcRAM cells tend to show depletion in germanium (Ge) and enrichment in antimony (Sb) inside the active volume of the  $\text{Ge}_2\text{Sb}_2\text{Te}_5$ .<sup>7,8</sup> Park et al. reported that enrichment in Sb and depletion in tellurium (Te) were observed at the bottom electrode. The behavior of Ge was not observed in this study.<sup>9</sup> Although the directions of elements are controversial issues, compositional changes and atomic demixing are obvious results after cyclic switching, which is related to *SET*-stuck failure. Previous reports on the origin of compositional changes in  $\text{Ge}_2\text{Sb}_2\text{Te}_5$  suggested that incongruent melting<sup>10</sup>, thermal diffusion<sup>9</sup>, and mass flow

were enhanced by electric fields.<sup>11,12,13</sup>

In a *RESET*-stuck problem, the resistance of the phase-change material is fixed at a high resistance value, which is the amorphous phase. Switching from an amorphous to a crystalline phase is prohibited despite any *SET* operation. *RESET*-stuck problems originate from delamination at the bottom electrode, which is related to the formation of voids in the phase-change material.<sup>7, 8, 14</sup> These endurance problems originate from the migration of atoms.

### 1.2.2. Migration behavior in PcRAM

As the memory density increases, the phase-change material experiences harsher operating conditions, such as high current density and temperature, which cause reliability issues and failure. Compositional changes and void formation in phase-change materials are major reliability problems in PcRAM.<sup>8,9</sup> These durability problems are caused by the mass transport of compositional elements including electric and thermal stress. First, an electric stress results in the mass transport of constituent atoms, including the electric current of the field, which is known as electromigration (EM). Previous research has focused on the liquid phase, which is the intermediate state of transformation between crystalline and amorphous phases during PcRAM operation. For example, the separation of elements in  $\text{Ge}_2\text{Sb}_2\text{Te}_5$  has been observed during high current stressing in the liquid phase.<sup>12,13</sup> During current stressing, the ionized elements of liquid GST are affected by the electric field and their direction depends on the charge of the ion.

Thermal stress also influences the migration of atoms in PcRAM.  $\text{Ge}_2\text{Sb}_2\text{Te}_5$ , which is one of the most promising materials for PcRAM, should be separately phased to a liquid phase and a solid phase because Ge-Sb-Te compounds do not melt congruently.

<sup>10</sup> The temperature range from 630 to 650 °C is the region of incongruent melting,

which contains liquid and solid phases simultaneously. The problem is the composition difference between the liquid phase and solid phase in the incongruent region, namely, a Sb and Te-rich liquid phase and Ge-rich solid phase. This phase separation occurs with the formation of a Ge-rich solid phase at the heat sink during the solidification of the phase-change material. Phase transformation in phase-change materials generates mechanical stress because of density differences. Various phases exist in Ge-Sb-Te compounds, including amorphous, cubic crystalline, and hexagonal crystalline phases. The difference in density between the amorphous phase and hexagonal crystalline phase is theoretically approximately 10 %. <sup>14</sup> This difference in density causes volume shrinkage for the *SET* state, which generates large tensile stress at the active region in the phase-change material. Repeating these thermal operations during programming causes the coalescence of voids and eventually results in cell failure.

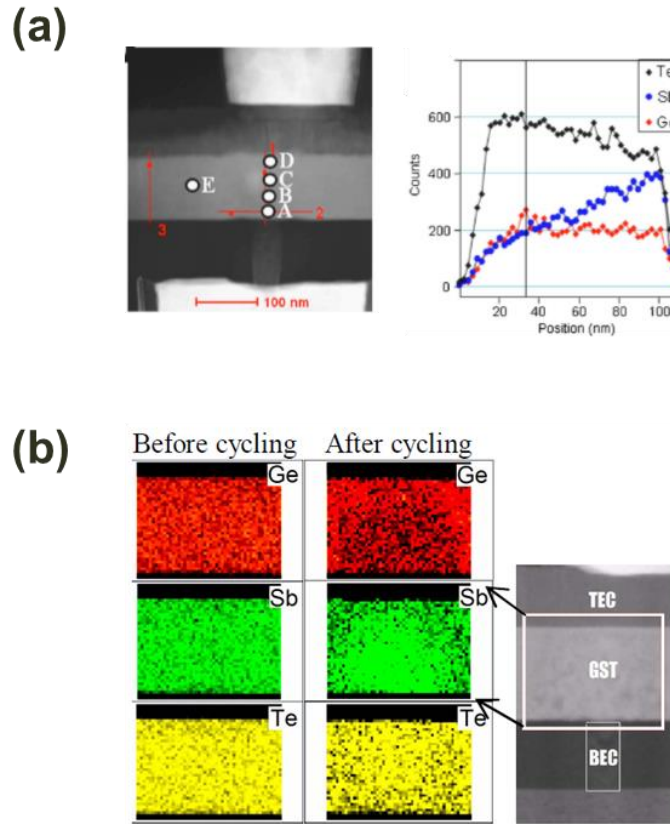


**Figure 1.3** (a) STEM image of PcRAM cell and EDS line profiles show the non-stoichiometric composition on vertical line 1. Sb accumulated in the phase change volume. [9] (b) An EDS mapping shows Sb accumulated in the phase change volume and Ge diffused out of the phase change volume after cycling.



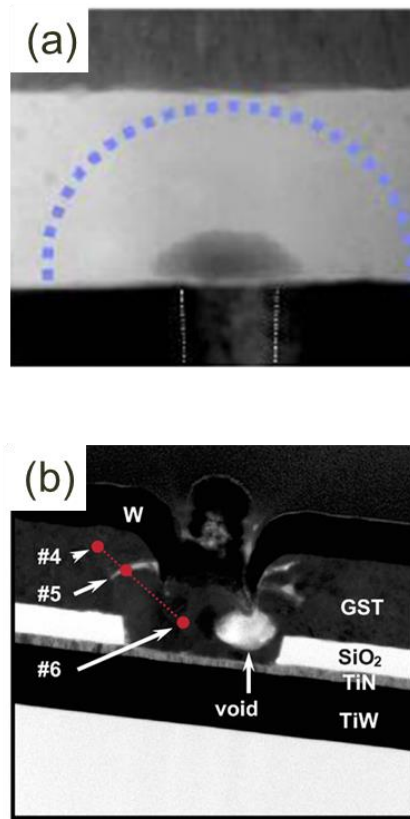


**Figure 1.4** (a) Void generated at the interface between the phase change volume (blue dotted line) and bottom electrode after cyclic operation in PcRAM. [14]  
(b) Void generation in the inside of phase change material with *RESET-stuck* failure. [8]

### **1.3 Objective of the thesis**

As mentioned above, previous research regarding PcRAM reliability predominantly focused on liquid phases. Because the atomic diffusivity of liquid phases is much faster than the atomic diffusivity in crystalline phases,<sup>13</sup> electric field-induced failures predominantly occur in the liquid phase. Therefore, the effect of a current density below  $10^7$  A/cm<sup>2</sup> on phase-change materials has not been reported and crystalline phases have been considered a stable state for electromigration.

However, not all regions of a phase-change material experience melting during PcRAM operation. Only the active region, which is the limited zone near the heater, can be transformed into a liquid phase. The alternate region remains a crystalline phase without melting, despite repeated PcRAM operation. The effect of atomic migration in the crystalline regions is cumulative, whereas the effect that evolves in the active region can be recovered through melting and solidification processes. This cumulative effect on the crystalline phase can affect the reliability of the *SET* state of the phase-change material, which becomes more significant in multi-level cell (MLC) devices. Therefore, investigating the migration behavior of the crystalline phase of Ge<sub>2</sub>Sb<sub>2</sub>Te<sub>5</sub> is important to gain a comprehensive understanding of the reliability of phase-change materials. The elements of crystalline GST are affected by an electric current, which is the momentum transfer between charge carriers and atoms.<sup>15</sup> EM in crystalline GST has been demonstrated to cause direct amorphization without melting, which signifies that EM in the crystalline phase has sufficient power to affect the solid-state structure.<sup>16</sup> As the dimensions of devices diminish, the current density is anticipated to increase,<sup>17</sup> and degradation in the crystalline state may become a significant reliability problem for a PcRAM cell.

The objective of this thesis is to clearly identify the effect of electric currents on the crystalline phase of phase-change materials and to provide the guidelines for improving their endurance. The atomic displacement from a low current, approximately  $10^6$  A/cm<sup>2</sup>, is negligible compared to that from a high current because the driving force is insufficient to generate a massive flux of atoms. Although no catastrophic failure is induced by an electric current in crystalline phase-change materials, various phenomena that have not been reported are observed in crystalline Ge<sub>2</sub>Sb<sub>2</sub>Te<sub>5</sub>. The resistance of phase-change materials, especially Ge-Sb-Te compounds, is very sensitive to external signals such as thermal stress and electric stress because phase-change materials have various phases, such as cubic and hexagonal structures.<sup>18</sup> Therefore, investigating the migration behavior of the crystalline phase of Ge<sub>2</sub>Sb<sub>2</sub>Te<sub>5</sub> is important to gain a comprehensive understanding of the reliability of phase-change materials. To achieve this objective, a simple structure with a line shape is used for a model study instead of a PcRAM cell structure. Because the factors that influence the material structure and environment are mixed in the actual device, we cannot distinguish the effect of electric currents from those of other factors. In addition, actual devices are too small to investigate the degradation behaviors in phase-change materials. By using a line structure for a model study, we can clearly identify the various mechanisms that are related to degradation or structural changes in phase-change materials, depending on the current density. We believe that this work provides new insight regarding electrical reliability in the crystalline phase of phase-change materials, which offers new design rules and applications for crystalline-based PcRAM devices. Scientifically, this work adds to the fundamental understanding of the influence of electric currents on the crystalline phase of chalcogenide materials.



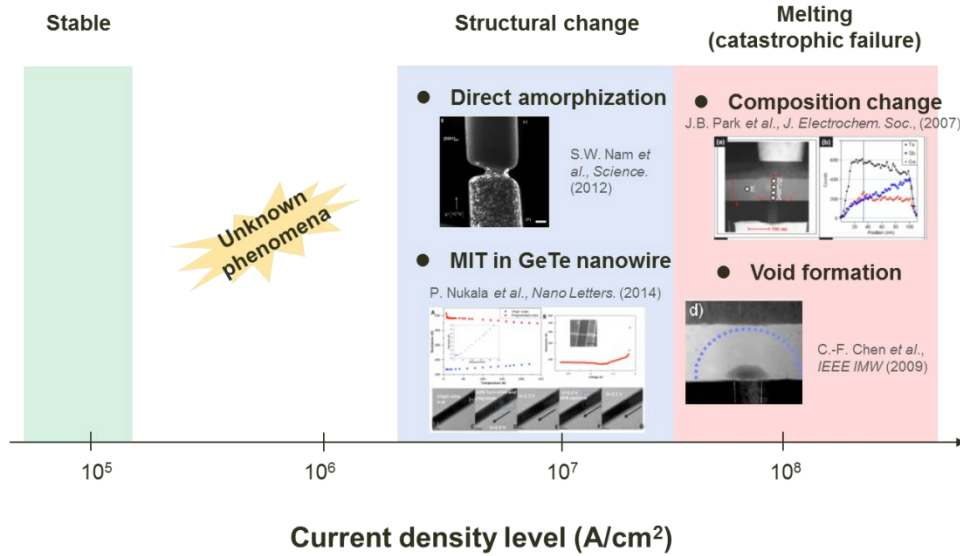


**Figure 1.5** Reported results of current-induced change in phase change materials with respect to current density level. The behavior of applying current density ranged approximately  $10^6 A/cm^2$  has not been reported yet.

## **1.4. Organization of the thesis**

This thesis consists of seven chapters. In **Chapter 2**, the physical properties of phase change material is reviewed. The previous research of current effect on GST is also explained in **Chapter 2**. The basic theory of mass transport induced by electric stress, electromigration is discussed in detail. **Chapter 3** describes the experimental procedure, including the fabrication of samples. In **Chapter 4**, gradual degradation in the crystalline  $\text{Ge}_2\text{Sb}_2\text{Te}_5$  under electric current is explained, which has never been reported. **Chapter 5** discusses the metal-insulator transition induced by electric current without phase transition. This phenomenon differs significantly from the thermal annealing accompanying phase transition. **Chapter 6** describes mechanism change with respect to the current density and temperature. **Chapter 7** summarizes the results of this study and suggests a method for the improvement of PcRAM reliability.

## CHAPTER 2

### Theoretical background

#### 2.1. Physical properties of phase-change materials

Over the past forty years, many materials have been investigated for their suitability as phase change materials.  $\text{Te}_{48}\text{As}_{30}\text{Si}_{12}\text{Ge}_{10}$  and  $\text{Te}_{81}\text{Ge}_{15}\text{Sb}_2\text{S}_2$  are the materials that Ovshinsky used for his first electrical and optical switching experiments, respectively.

<sup>19</sup> Variations of  $\text{Ge}_2\text{Sb}_2\text{Te}_5$ , Ag or In doped  $\text{Sb}_{69}\text{Te}_{31}$  and Ge-In-Sn-Sb are currently used in various optical recording formats. Phase-change materials should be able to form glasses, which are characterized by a sufficiently low melting point, for the successful application of electrical devices. Furthermore, these materials should have a stable amorphous phase that is characterized by high activation energy toward crystallization and should be able to crystallize rapidly. A high contrast between the amorphous and crystalline states is also important for electrical devices. Chalcogenide alloys, which contain various chalcogen atoms (e.g., sulfur, selenium, and tellurium), show a large contrast in electrical conductivity and optical reflectivity between their crystalline and amorphous phases. In particular, materials that are composed of antimony, tellurium and germanium in various ratios fulfill all these requirements and

are major materials that are used in PcRAM devices. Compositions are usually determined by means of a “composition triangle”, as depicted in **Figure 2.1**. In this chapter, we review the physical properties of phase-change materials with a focus on Ge-Sb-Te compounds.

### 2.1.1. Ge-Sb-Te alloys

Some of the most promising materials for optical devices and phase change memory include phase-change material alloys from the Ge-Sb-Te phase diagram. These materials are mainly focused along the pseudo-binary tie line between GeTe and Sb<sub>2</sub>Te<sub>3</sub>, although other parts of the phase diagram are being investigated as well. **Figure 2.1** shows the pseudo-binary phase diagram along the tie line between GeTe and Sb<sub>2</sub>Te<sub>3</sub> with respect to equilibrium alloys.<sup>20,21</sup> The properties of Ge-Sb-Te alloys were first researched in the former Soviet Union at the end of the 1960s.<sup>19</sup>

At the beginning of the 1990s, Yamada *et al.* recognized that GeSb<sub>2</sub>Te<sub>4</sub> and Ge<sub>2</sub>Sb<sub>2</sub>Te<sub>5</sub> alloys show long-term stability at ambient temperatures and a low crystallization time (approximately 50 ns) under the influence of fast laser irradiation. These properties were advantageous for optical recording. Under the influence of laser irradiation, these alloys transformed into a simple and high-symmetry phase such as a face-centered cubic (FCC) shape, and not into an equilibrium hexagonal close-packed (HCP) crystalline phase.<sup>22</sup> Longer crystalline times would be required to obtain a nine-layer hexagonal structure.

Although the three intermetallic phases GeSb<sub>4</sub>Te<sub>7</sub>, GeSb<sub>2</sub>Te<sub>4</sub>, and Ge<sub>2</sub>Sb<sub>2</sub>Te<sub>5</sub> were possible candidates for phase change material alloys in PcRAM devices, the Ge<sub>2</sub>Sb<sub>2</sub>Te<sub>5</sub> composition exhibited the greatest stability in the amorphous to crystalline



transition with an activation energy of approximately 2.2 eV, as determined by a Kissinger analysis of differential scanning calorimetry (DSC) data.<sup>23</sup>

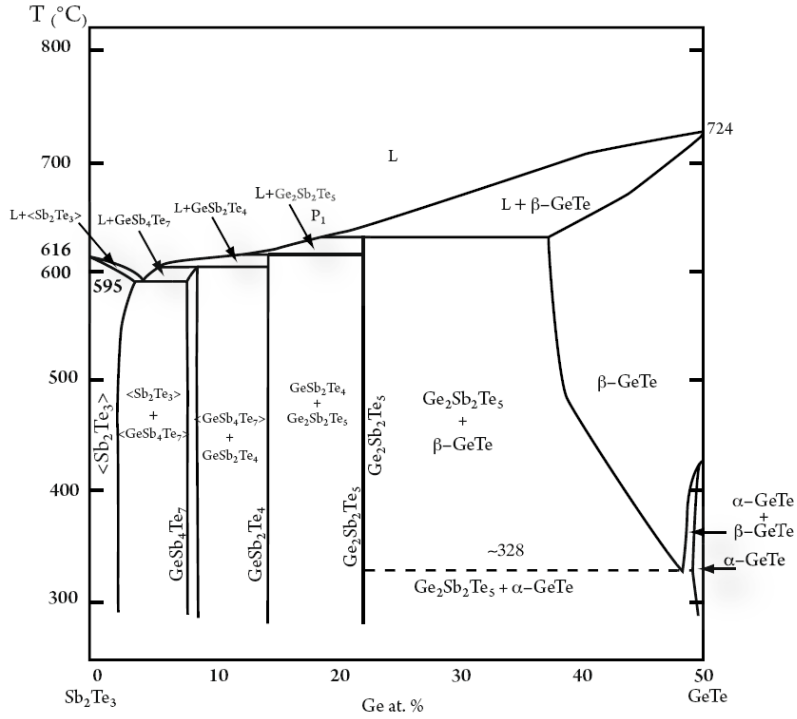


**Figure 2.1** Equilibrium phase diagram for alloys along the pseudo-binary tie-line GeTe-Sb<sub>2</sub>Te<sub>3</sub> (adapted from references [20, 21]). In the lower section of the figure, the existence of metastable phases is also shown. Reprinted with permission from [22].

### 2.1.2 Crystalline structure of Ge-Sb-Te compounds

The equilibrium structure of GeTe-Sb<sub>2</sub>Te<sub>3</sub> pseudo-binary alloys has been examined since the 1980s. The number of layers is listed in the unit cell by the expression (GeTe)<sub>n</sub>(Sb<sub>2</sub>Te<sub>3</sub>)<sub>m</sub> for homologous compounds. For example, the space groups of GeSb<sub>4</sub>Te<sub>7</sub> (n=1, m=2), GeSb<sub>2</sub>Te<sub>4</sub> (n=1, m=1), and Ge<sub>2</sub>Sb<sub>2</sub>Te<sub>5</sub> (n=2, m=1) are *P3m1*, *R3m*, *P3m1*, respectively.<sup>24, 25, 26</sup> The existence of these series has been confirmed for a wide range of compositions with  $n \leq 4$  and  $m \leq 4$ . However, extremely long unit cells such as GeSb<sub>8</sub>Te<sub>13</sub> (n=1, m=4) are difficult to form because they require long thermal annealing to allow for sufficient diffusion time.

The crystalline structures of Ge-Sb-Te alloys show two different crystalline phases. Ge-Sb-Te alloys first crystallize into a metastable rock-salt structure at low temperature and then into a stable hexagonal structure at higher temperature during heating.<sup>27</sup> **Figure 2.2(a)** shows a metastable rock-salt structure, which forms over 150 °C. The crystalline structures of GeSb<sub>4</sub>Te<sub>7</sub>, GeSb<sub>2</sub>Te<sub>4</sub>, and Ge<sub>2</sub>Sb<sub>2</sub>Te<sub>5</sub>, which were determined by diffraction-based investigation, formed in the rock-salt structure. The rock-salt structure consists of two interpenetrating FCC sub-lattices; one sub-lattice is located at the origin and the other is located at (0.25, 0.25, 0.25). Te atoms perfectly occupy one FCC sub-lattice, while Ge and Sb atoms randomly occupy the other FCC sub-lattice with an amount of vacancies that depends on the composition, which are 28.6 % for GeSb<sub>4</sub>Te<sub>7</sub>, 25 % for GeSb<sub>2</sub>Te<sub>4</sub>, and 20 % for Ge<sub>2</sub>Sb<sub>2</sub>Te<sub>5</sub>.<sup>18</sup> The presence of Peierls like distortion in the Ge-Sb-Te alloys was subsequently shown both theoretically and experimentally from x-ray diffraction.<sup>28, 29</sup>

**Figure 2.2(b)** shows the stable hexagonal phase of Ge<sub>2</sub>Sb<sub>2</sub>Te<sub>5</sub>, which forms a approximately 300 °C depending on the cooling rate.<sup>27</sup> Density functional theory (DFT) total energy calculations on Ge<sub>2</sub>Sb<sub>2</sub>Te<sub>5</sub> were performed to identify the

structural properties of hexagonal  $\text{Ge}_2\text{Sb}_2\text{Te}_5$  because the stacking order of atoms was hard to deduce from experimental results. *Ab-initio* simulations on  $\text{Ge}_2\text{Sb}_2\text{Te}_5$  alloys by Zhou *et al.* showed that stable hexagonal phases contain intrinsic vacancies within the Te-Te layers.<sup>30</sup> The stable hexagonal  $\text{Ge}_2\text{Sb}_2\text{Te}_5$  alloys consist of nine layers of atoms following the ABC stacking sequence Te-Ge-Te-Sb-Te-Te-Sb-Te-Ge along the [0001] direction in the unit cell.<sup>31, 32</sup> The DFT total energy calculations show that the most stable configuration is the model that was proposed by Kooi and De Hosson, which is Te-Ge-Te-Sb-Te-v-Te-Sb-Te-Ge.<sup>33</sup> This model added a vacancy layer, which is labeled 'v'. The vacancy layers are highly ordered and lie along the [0001] direction between the weak Te-Te layers. Hexagonal phases can exist in PcRAM devices because of the temperature of the fabrication process but are not observed in optical discs.

The concentration of vacancies and their role in the metastable structures of  $\text{GeSb}_4\text{Te}_7$ ,  $\text{GeSb}_2\text{Te}_4$ , and  $\text{Ge}_2\text{Sb}_2\text{Te}$  have been shown to be a necessity based on extended X-ray absorption fine structure (EXAFS) determination of local structures.<sup>34</sup> Vacancies are an intrinsic part of structures. In rock-salt structures, six saturated covalent bonds are populated by two electrons. For this phenomenon to occur, each atom must have six valence electrons, with the number of required electrons differing among elements: Sb needs one additional electron, while Ge needs two additional electrons. These missing electrons are donated to Ge and Sb from Te orbitals that point into vacancies to saturate all octahedral bonds. Therefore, vacancies are a significant factor in the formation of crystalline structures. Pressure has also been suggested to affect the formation of amorphous phases in phase-change materials. Actually, the phase-change materials in PcRAM devices generate 5-6 GPa of pressure because of the volume mismatch between amorphous and crystalline phases.

Diamond-anvil diffraction experiments showed that the hydrostatic compression of  $\text{Ge}_2\text{Sb}_2\text{Te}_5$  results in amorphization, which is a pressure-induced transformation.<sup>35</sup>

**Figure 2.3** shows a series of x-ray diffraction patterns of the metastable crystalline phase of  $\text{Ge}_2\text{Sb}_2\text{Te}_5$  as a function of applied pressure. The crystalline peaks vanished at a pressure over 22 GPa. EXAFS results showed that amorphization initiated at approximately 10 GPa when the Sb atoms in the distorted rock-salt structure reached the center of the cell, leaving vacancies to be compressed.<sup>36</sup> Furthermore, the  $\text{GeSb}_2\text{Te}_4$  phase was amorphized under a lower pressure than the  $\text{Ge}_2\text{Sb}_2\text{Te}_5$  phase. This result means that the concentration of vacancies affects pressure-induced amorphization. Near-edge x-ray absorption measurements also suggested that the local order in the laser-quenched and pressure amorphized phases were similar.<sup>37</sup>

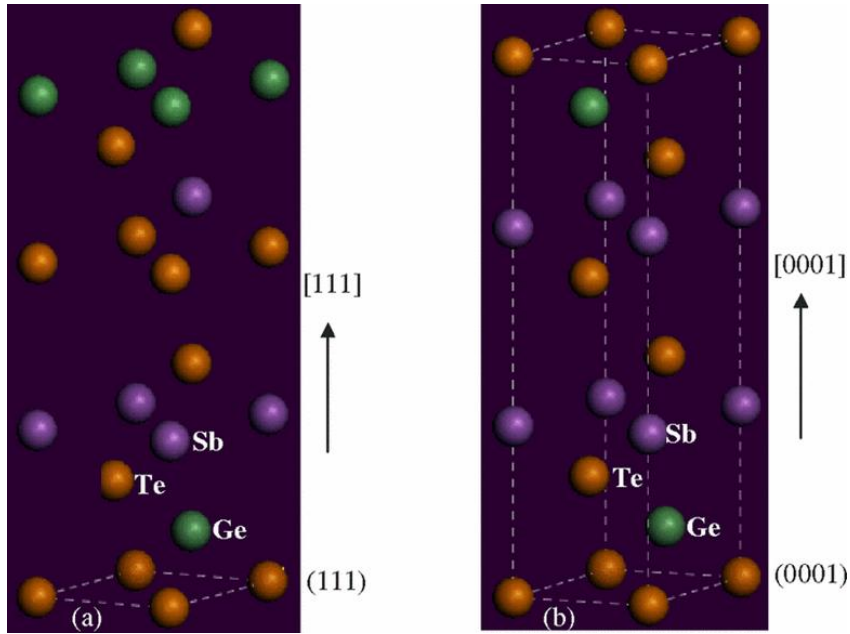


**Figure 2.2** (a) Atomic arrangement for metastable rock-salt  $\text{Ge}_2\text{Sb}_2\text{Te}_5$  structure built based on (111) planes along the [111] direction. (b) Atomic arrangement for stable hexagonal  $\text{Ge}_2\text{Sb}_2\text{Te}_5$  structure built based on (0001) planes along the [0001] direction. [32]

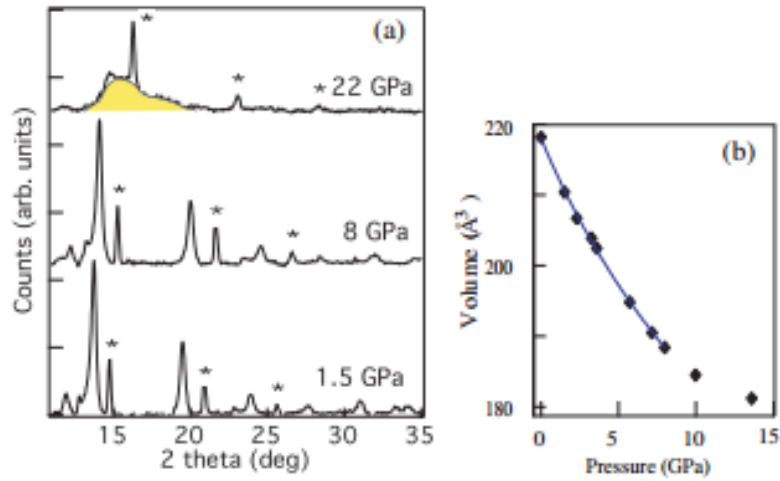


**Figure 2.3** (a) Pressure-induced changes of the XRD pattern of  $\text{Ge}_2\text{Sb}_2\text{Te}_5$  upon compression. The peaks marked by \* are the corresponding peaks of the NaCl marker. (b) Volume of unit cell according to pressure (solid point) and fitting using Birch-Murnaghan EOS (solid line). [35]

### 2.1.3. Temperature dependence of resistivity

The temperature dependence of the sheet resistance of a thin film of  $\text{Ge}_2\text{Sb}_2\text{Te}_5$  is shown in **Figure 2.4**. A 2-3 orders of magnitude drop in sheet resistance was observed at a  $T_1$  temperature near 150 °C, which marks the transformation from an amorphous to FCC crystalline phase.<sup>27</sup> This contrast in resistivity is the major feature of PcRAM devices. The transformation of a very small volume creates a sufficient resistance contrast, which enables the device to electrically read the digital signal. At a higher temperature  $T_2$ , which is approximately 300 °C depending on the sample's characteristics, the metastable FCC phase transformed into a stable hexagonal phase, as mentioned in **Section 2.1.2**. As shown in **Figure 2.4**, the resistances of both amorphous and crystalline phases continuously decrease with temperature, but the origins of these resistance changes are different for each phase. In amorphous  $\text{Ge}_2\text{Sb}_2\text{Te}_5$ , the number of excited carriers increases with temperature, which exponentially decreases the resistance. Because this process is reversible, the resistance returns to its original value when the temperature decreases. Decreases in the resistance of crystalline  $\text{Ge}_2\text{Sb}_2\text{Te}_5$ , however, mainly occur because of an increase in mobility rather than carrier concentration.<sup>38</sup> Declines in scattering at grain boundaries result from grain growth, which increases the mobility of carriers in crystalline  $\text{Ge}_2\text{Sb}_2\text{Te}_5$ . Because this process is irreversible, resistance is maintained at low values when the temperature decreases. During cooling, the FCC phase becomes slightly more resistive while the hexagonal phase becomes more conductive, which will be discussed in the next section.

The heat of crystallization is generated by electrical Joule heating in a PcRAM cell, which actually involves a very interesting electronic switching phenomenon. As the voltage that is applied across an amorphous region increases, the current also increases

but the magnitude is small because of the large resistivity. However, when the voltage exceeds a certain threshold, the material suddenly exhibits a negative differential resistance, which allows a high current. Consequently, the Joule heat from this high current can crystallize the amorphous region.



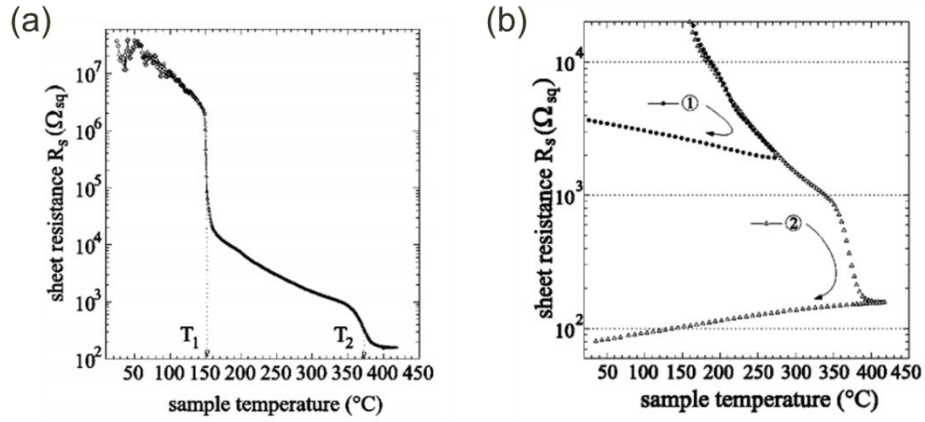


**Figure 2.4** (a) Sheet resistance of 80 nm thin  $\text{Ge}_2\text{Sb}_2\text{Te}_5$  film measured with increasing temperature. Sharp drops accompany the amorphous-FCC transformation at  $T_1$  and the FCC-HCP transformation at  $T_2$ . (b) Sheet resistance upon subsequent cooling. The resistance of the FCC phase (Curve 1) increases with cooling, whereas that of the HCP phase (Curve 2) decreases. [27]

### 2.1.4. Metal-insulator transition in Ge-Sb-Te alloys

Two different types of solids are distinguished by the relationship between temperature and conductivity. The temperature coefficient of resistivity (TCR) is used as the criterion of this relationship. Experimentally, materials with metallic behavior have positive TCR values and materials with insulating behavior have negative TCR values.<sup>39</sup> Theoretical studies have shown that the limit of resistivity at low temperature (approaching zero Kelvin) is a more accurate criterion for classifying material types. The resistivity of insulators diverges to infinity as the temperature approaches zero Kelvin, while metals maintain a finite resistivity.

Although many models of a metal-insulator transition (MIT) explain changes in the crystal structure and properties, Mott and Anderson's models are representative models for property transitions without a phase change. Mott argued that an MIT occurs when the electron interaction energy exceeds the Fermi energy.<sup>40</sup> On the other hands, Anderson showed that increasing disorder generates a localized state at the Fermi energy.<sup>41</sup> The properties of solids are strongly influenced by the interaction between electrons and the presence of disorder.<sup>42</sup> Both Coulomb correlations (electron) and randomness (disorder) are driving forces behind MITs and involve the localization and delocalization of particles. Although one might be a dominant driving force for MITs, this phenomenon is not always necessarily true. For example, weak disorder weakens the effect of correlation because it redistributes states into the Mott gap and may thus turn an insulator into a metal. Therefore, the interplay between disorder and interaction leads to many subtle body effects, which poses fundamental challenges for theories and experiments.<sup>43,44</sup>

The occurrence of MIT in crystalline Ge-Sb-Te alloys has been recently reported.<sup>39,</sup>

<sup>45</sup> **Figure 2.5** shows that resistivity measurements of as-deposited films of GeTe and

$\text{GeSb}_2\text{Te}_4$  depend on the ambient temperature. The resistivity of amorphous GeTe suddenly drops by several orders of magnitude at crystallization, while the resistivity of crystalline phases does not depend on temperature. The resistivity of  $\text{GeSb}_2\text{Te}_4$ , however, shows a pronounced temperature dependence. Furthermore, the value of TCR changes from negative to positive with increasing temperature, which means that the nature of  $\text{GeSb}_2\text{Te}_4$  changes from an insulator to a metal, as mentioned above. This result is also observed in other Ge-Sb-Te alloys.<sup>46,47</sup> Interestingly, the nature of  $\text{GeSb}_2\text{Te}_4$  changes from an insulator to a metal at 275 °C, while the phase transition from rock-salt to a hexagonal phase occurs at 225 °C. Thus, a transition in the crystallographic phase has no relationship with the transport mechanism. However, a hexagonal  $\text{GeSb}_2\text{Te}_4$  phase is a degenerate semiconductor, that is, the Fermi energy lies within the valence band, which results in metal-like behavior. Consequently, the hexagonal phase of  $\text{GeSb}_2\text{Te}_4$  shows positive TCR values.

Theoretical studies that used density functional theory (DFT) provided the microscopic origin of MIT in crystalline  $\text{GeSb}_2\text{Te}_4$ .<sup>48</sup> The transition from an insulator to a metal has been attributed to increasing order in the crystalline phase. This property is related to the resonance bonding of the p electrons in crystalline Ge-Sb-Te alloys. This unique bonding results in a high static dielectric constant and very weak effective electron interaction.<sup>49</sup> Furthermore, atomic displacements that are induced by Peierls distortions and the statistical distributions of vacancies and Ge and Sb atoms affect the electronic properties.<sup>29</sup> **Figure 2.6** shows the total energy per atom of the models of metastable cubic  $\text{GeSb}_2\text{Te}_4$  and stable hexagonal  $\text{GeSb}_2\text{Te}_4$  with respect to the ordering of vacancies and Ge/Sb atoms. Three factors play an important role in the MIT: the distribution of vacancies, the disordering of Ge/Sb, and the crystalline phase. The rearrangement of vacancies affects the degree of disorder and creates a

vacancy plane in both cubic and hexagonal planes. The hexagonal phase becomes lower in energy than the corresponding cubic structure with sufficiently high vacancy layer formation. Therefore, the phase transition from a cubic to hexagonal phase is a high priority before the rearrangements of vacancies can be completed. Consequently, the final product of Ge-Sb-Te alloys after MIT is a hexagonal phase, and the vacancy effect on the MIT is hard to prove experimentally. Although the substitutional disorder of Ge and Sb atoms also affects the total energy of the Ge-Sb-Te system, the energy differences are quite small compared to vacancy ordering.

More recently, the impact of stoichiometry was demonstrated by P. Jost et al. as a controllable parameter for the MIT of the most common compositions in the  $(\text{GeTe})_x\text{-(Sb}_2\text{Te}_3)_{1-x}$  system; i.e., disorder-induced localization results in MITs differ according to the average vacancy concentration of various compositions.<sup>50</sup> Therefore, the behaviors of MITs, which are controlled by the annealing temperature and the stoichiometry, are critical for tailoring the charge transport properties of cubic GST to increase the performance of PcRAM devices.

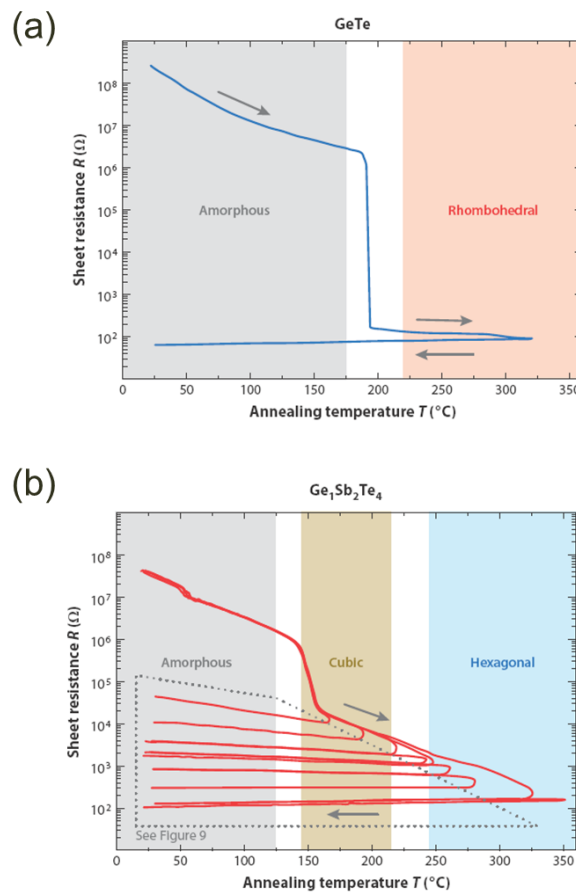


**Figure 2.5** (a) Temperature dependence of the sheet resistance on GeTe. (b) Temperature dependence of the sheet resistance on  $\text{GeSb}_2\text{Te}_4$ . [45]

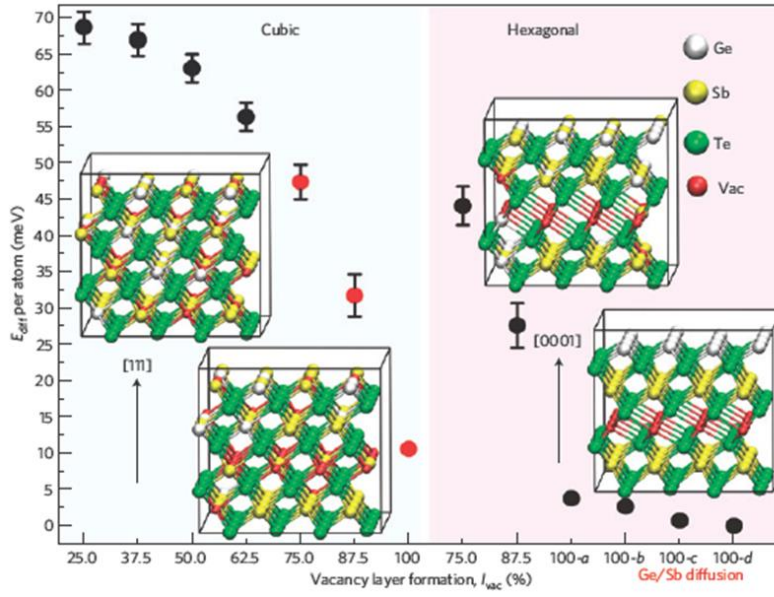


**Figure 2.6** Total energy per atoms,  $E_{\text{diff}}$ , of the metastable cubic  $\text{GeSb}_2\text{Te}_4$  and stable hexagonal  $\text{GeSb}_2\text{Te}_4$  with respect to vacancy layer formation. [48]

## **2.2. Theory of electromigration**

Endurance failures in PcRAM occur because of compositional changes and void formation in phase-change materials, as presented in **Section 1.2.1**. Both mechanisms of endurance failure are generated by mass transport in phase-change materials. When the atomic flux of constituent elements is different, the stoichiometry of multi-component alloys is broken. Voids are also generated by flux divergence because mass transport is dominant in one direction. Therefore, understanding mass transport in phase-change materials is essential to understand the failure mechanisms in PcRAM devices. This section will describe the theory of atomic migration phenomena and will discuss previous research on phase-change materials.

### **2.2.1. Electromigration**

Electromigration is the phenomenon of interconnecting metal self-diffusion along an interconnect when a high current density passes through the section. Voids form on some parts of the interconnect because of constituent atomic movement, and hillocks form on the other side because of the accumulation of atoms. The presence of voids increases the resistance of interconnects. The presence of hillocks causes short circuits between adjacent interconnects if these hillocks develop side-ways and between different levels of interconnects if these hillocks develop vertically and punch through the dielectric.

Electromigration has been a subject of scientific study for over 100 years, but the interest remained academic until it became a major failure mechanism for integrated circuits (IC) in 1959, when thin and narrow metal films began to be used as interconnects. Indeed, electromigration was the one of the first failure mechanisms

that were found in ICs. Unlike bulk conductors, which melt from Joule heating at high current density (above  $10^4$  A/cm<sup>2</sup>), the metallization in ICs can sustain current densities that are greater than  $10^7$  A/cm<sup>2</sup> because of the good thermal contact with the silicon substrate. This high current density significantly increases the effect of electromigration.

In addition, thin-film interconnects in ICs possess small grain sizes and high surface or interfacial area to volume ratios with many high mobility diffusion paths, which allows the mass transport of self-diffused metal atoms at low temperature. When these diffusion paths intersect with one another and when each path has different mobility, atoms accumulate or voids nucleate at the intersection. This combination of a high driving force for electromigration and the availability of inhomogeneous high-mobility diffusion paths makes thin-film conductors susceptible to electromigration damage.

### 2.2.2. Driving forces for electromigration

The driving force for electromigration has two major parts according to the direction of atomic migration. One is the direct action of an electrostatic field on the diffusing atoms, and the other is momentum exchange between charge carriers and diffusing atoms. For simplicity, the effective charge number ( $Z^*$ ) is introduced in the following manner:

$$F_{EM} = Z^* eE = (Z_{el}^* + Z_{wd}^*)eE, \quad (2.1)$$

where  $Z_{el}^*$  can be regarded as the nominal valence of the diffusion ion. Diffusing atoms are forced to migrate because of the direct electrostatic action of the electric



field, which is commonly called the electrostatic force.  $Z_{wd}^*$  is the charge number, which represents the momentum exchange effect and is commonly called the electron wind force.  $Z_{wd}^*$  has generally been shown to be approximately 10 in metallic systems, so the momentum exchange effect is much larger than the electrostatic field effect for electromigration in metals.

Although the physical meaning of  $Z_{el}^*$  is the valence charge of the diffusion ion, the evaluation of the quantity has been a prolific subject of controversy because of the shielding effect of conduction carriers. For metals,  $Z_{el}^*$  is usually much smaller than  $Z_{wd}^*$  because the valence charges of atoms in metal are blocked by free electrons.

The evaluation of  $Z_{wd}^*$  is more complex. The intuitive picture one forms from the classical model of momentum exchange in a continuous electronic fluid is too simple to illustrate the quantum mechanical phenomena between diffusing atoms and electrons. Several efforts in quantum mechanics have been made to estimate the electron wind force, yet no result has been widely accepted. The difficulty lies in conducting the proper and complete treatment of the scattering of electrons by a diffusing atom and its surrounding atoms. In the following, we discuss ballistic approaches to the scattering process, which were provided by Fiks<sup>51</sup> and by Huntington and Grone<sup>15</sup>.

The idea that was conceived by Fiks assumes that the diffusing atoms have an intrinsic cross-section  $\sigma_e$  for collision with electrons and that conduction electrons have an average velocity  $v$ , with  $n$  being the concentration of conduction electrons per unit volume.<sup>51</sup> The number of collisions per unit time between electrons and a moving atom is  $nv\sigma_e$ . For each collision, an electron conducts the average momentum it acquires during the relaxation time  $\tau_e$ ,  $F_x^1\tau_e = eE\tau_e$ , where the subscript  $x$  indicates that the electrical field and the force are acting along the  $x$ -direction. The total change

in momentum per unit time, i.e., the wind force, is the product of the number of collisions per unit time and the momentum exchange per collision,

$$F_x = -(nv\sigma_e)(eE_x\tau_e) = -eE_x n\lambda_e\sigma_e, \quad (2.2)$$

where  $\lambda_e = v\tau_e$  is the mean free path of scattering. This expression has been extended to cover the situation in which both electrons and holes are involved in the transport process:

$$Z_{wd}^* = -n_e\lambda_e\sigma_e + n_h\lambda_h\sigma_h. \quad (2.3)$$

The semi-classical model that was developed by Huntington and Grone postulates a transition probability per unit time from one free-electron state to another free-electron state because of scattering by diffusion atoms. A formal expression has been developed to describe the momentum transfer per unit time by treating electrons as free particles. Subsequently, this approach has been modified by considering the electron pseudo-momentum of electronic states. The force is calculated by summing over the initial and final states of the scattered electrons or by integrating a transition probability over the jumping path of the diffusing atoms. The force that acts on the diffusing atom is not constant along the jumping path, but the calculation is simplified by assuming that the electron reciprocal relaxation time that arises from collision with moving atoms is constant. The result shows that the effective charge number can be provided in terms of the specific resistivity,

$$Z_{wd}^* = -Z \frac{\rho_d / C_d}{\rho / C} \frac{m_0}{m^*}, \quad (2.4)$$

where  $Z$  is the electron-atom ratio;  $\rho = m_0 / ne^2\tau$  and  $\rho_d = m^* / ne^2\tau_d$  are the resistivity of the lattice atoms and the diffusing atoms, respectively, and  $m_0$  and  $m^*$  are the free electron mass and effective electron mass, respectively.

In an FCC lattice, 12 equivalent jump paths are present along the  $\langle 110 \rangle$  directions. For a given current, the average specific resistivity of a diffusing atom must be corrected by a factor of one-half. Therefore, if we consider both  $Z_{el}^*$  and  $Z_{wd}^*$ ,

$$Z^* = -Z \left[ \frac{1}{2} \frac{\rho_d / C_d}{\rho / C} \frac{m_0}{m^*} - 1 \right]. \quad (2.5)$$

The direction of the electron wind force, the first term in Eq. (2.5), appears to depend on the sign of the charge carriers. For electrons that interact with positive ions, the term is opposite to the electrostatic force; the direction of mass transport is determined by the relative magnitudes of these two forces. For holes that interact with positive ions, both forces are of the same sign; therefore, mass transport should always be toward the cathode.

### **2.3. Mass transport in phase-change materials**

Electromigration in multi-component alloys such as phase-change materials is quite different from that of metal interconnects. This difference is caused by the physical properties of materials and operating conditions of the device. For example, metals are good conductors with high concentrations of charge carriers, while phase-change

materials are poor conductors with relatively low concentrations of charge carriers. Furthermore, the mass transport behavior in phase-change materials changes with the current density because the material transforms into a molten state under severe Joule heating at a high current density (above  $10^7$  A/cm<sup>2</sup>). This operation condition is vulnerable to migration because the mobility of atoms in a molten state is some orders of magnitude faster than that in a solid state. Previous research regarding electromigration behavior in phase-change materials with respect to the phase is briefly introduced in this section.

### 2.3.1. Electromigration behaviors in molten-phase Ge<sub>2</sub>Sb<sub>2</sub>Te<sub>5</sub>

**Figure 2.7** shows the atomic concentration profile in the Ge<sub>2</sub>Sb<sub>2</sub>Te<sub>5</sub> line along the longitudinal direction after applying a single electric pulse with duration times on the scale of milliseconds.<sup>13</sup> The composition of Ge<sub>2</sub>Sb<sub>2</sub>Te<sub>5</sub> abruptly changed and the directions of the atoms differed among the elements. Ge and Sb atoms migrated to the anode, while Te atoms migrated to the cathode. This result was also shown in an EDS compositional map that was analyzed by TEM.<sup>11</sup> The driving force for the atomic migration is the electrostatic force that was exerted on the ionized atoms in the molten state. As mentioned in **Section 2.2**, electromigration has two driving force, namely, electron wind force and electrostatic force. Generally, the wind force is much higher than electrostatic force in solid-state electromigration. In a molten state, however, the electrostatic force becomes the dominant factor for electromigration because of the ionization of atoms. Each element has different ionicity when the materials are molten depending on the electronegativity. Therefore, atoms in a molten state donate or accept electrons and are ionized depending on their electronegativity. Because the

electronegativity of Te is much larger than that of Ge and Sb, Te becomes an anionic ion, and Ge and Sb become cationic ions.<sup>52</sup>

The atomic flux refers to the quantity of migrated atoms through a certain area over a unit time, which is the rate of electromigration. The atomic flux of electromigration can be written as

$$J^{EM} = \frac{CD}{RT} Z^* eE, \quad (2.6)$$

The electric field (E) and temperature (T) are determined by the operating conditions. If the dimensions of the sample and operating conditions are fixed, the atomic flux is determined by the effective charge number ( $Z^*$ ) and diffusion coefficient (D). The value of  $DZ^*$ , which is the product of the effective charge number and diffusion coefficient, can be used to quantify the electromigration rate. The  $DZ^*$  value of each element is calculated from the quantity of migrated atoms that can be measured by compositional analysis. The assumption is that the electric field and the number of atoms per volume are constant along the whole sample, and temperature is fixed to 900 K, which is the melting temperature. The  $DZ^*$  values of Ge, Sb, and Te were calculated to be 2.56, 3.02, and  $-2.13 \times 10^{-5} \text{ cm}^2\text{s}^{-1}$ , respectively.<sup>13</sup> A negative  $DZ^*$  value means that the mass flux of atoms is in the opposite direction compared to a positive value. These  $DZ^*$  values are a few orders of magnitudes larger than those of metal interconnects in semiconductors and are based on the large coefficient of diffusion in the molten state. Therefore, electrical stressing during *RESET* switching is critical to endurance failure in PcRAM devices.

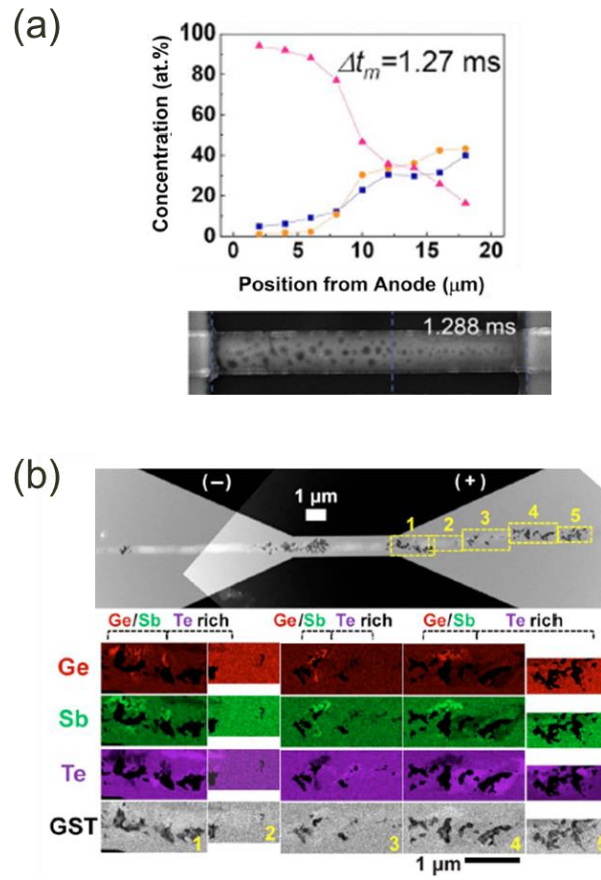


**Figure 2.7** (a) Compositional profiles in  $\text{Ge}_2\text{Sb}_2\text{Te}_5$  line from WDS analysis shown as atomic concentration and their SEM image. [13] (b) Image of the capped pattern of  $\text{Ge}_2\text{Sb}_2\text{Te}_5$  after voltage sweeping. Mass depleted regions were blackened out in the individual element mapping. [11]

After catastrophic atomic de-mixing in  $\text{Ge}_2\text{Sb}_2\text{Te}_5$ , voids are observed at the anode contact as shown in **Figure 2.7**. These voids are uniformly generated along the whole line during the as-melted state. As the duration time increase, however, voids that are near the cathode begin to disappear, and voids that are near the anode grow through agglomeration. These observations indicate that small voids are generated during the initial stage of electromigration and that voids migrate toward the anode upon coalescence. Void formation during electromigration has also been reported in metal interconnects, in which voids are generated at the point of flux divergence, such as material interfaces.<sup>53</sup> Atoms are depleted at this point because the incoming flux of atoms is different from the outgoing flux of atoms. The depletion of atoms leads to tensile stress in the cathode, which is the driving force for void nucleation. Although no point of flux divergence exists in molten  $\text{Ge}_2\text{Sb}_2\text{Te}_5$ , atomic fluxes are different among elements. Moreover, the crystalline structure of  $\text{Ge}_2\text{Sb}_2\text{Te}_5$  has many sites of intrinsic vacancies, as mentioned in **Section 2.1**, which results in the formation of free volume in the molten state. Free volume refers to a volume that was not occupied by constituent atoms in the liquid state. Under non-uniform atomic flux, vacancies migrate along the direction of lower atomic flux. Therefore, the flux of voids during electromigration is toward the anode because the total atomic flux is dominantly toward the cathode. This phenomenon is similar to the Kirkendall effect regarding inter-diffusion in complex metal systems.<sup>54</sup>

The electromigration behavior in line structures of  $\text{Ge}_2\text{Sb}_2\text{Te}_5$  cannot completely explain the failure behavior in actual PcRAM devices. The main difference in these devices because of the line structure is the distribution of the electric field and temperature, which leads to a divergence in the atomic flux. Furthermore, the temperature gradient is also a critical driving force for atomic migration in phase-

change materials, which is called thermomigration.<sup>55</sup> The driving forces for migration contain not only external factors, such as electric fields and temperature, but also internal factors that result from atomic migration. In a real system, a large amount of atomic accumulation generates compressive stress, which prevent high values of atomic density. An additional atomic flux is generated by the stress field from compressive to tensile regions to achieve equilibrium with electromigration. Atomic accumulation also generates a spontaneous diffusion flux to dissipate the concentration profile. According to the various driving forces for migration, mass fluxes in actual PcRAM devices can be explained by simulations and matched with experimental results.<sup>56</sup>



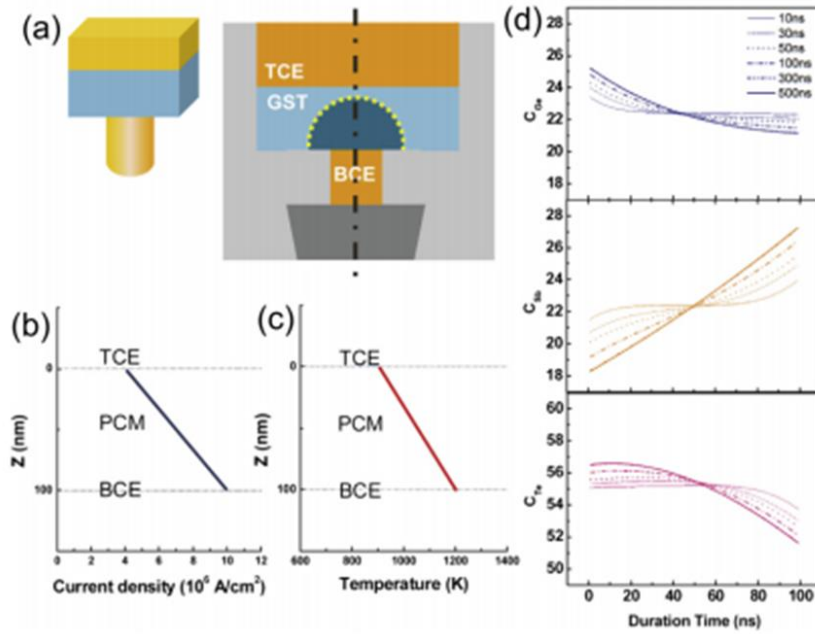


**Figure 2.8** (a) Cell structure of the real device (mushroom-structure). (b) Current density and (c) temperature profile in Ge<sub>2</sub>Sb<sub>2</sub>Te<sub>5</sub> layer of structure (a). (d) Compositional profiles after pulse stressing with various duration time for Ge, Sb, and Te calculated from the finite differential method (FDM). [55]

### 2.3.2. Electromigration behaviors in crystalline phase $\text{Ge}_2\text{Sb}_2\text{Te}_5$

As mentioned above, previous research has predominantly focused on the migration behavior in molten state of phase-change materials, because the mobility of atoms in molten states is some orders of magnitude faster than that in solid states. Obviously, the catastrophic failures in actual PcRAM devices have a close relationship with migration in molten states compared with that in solid states. However, except for kinetic differences, the mechanism of electromigration in solid states is different from that in liquid states.

**Figure 2.9** shows the atomic concentration profiles in crystalline  $\text{Ge}_2\text{Sb}_2\text{Te}_5$  line after electrical stressing.<sup>13</sup> Because the sum of the concentrations of constituent elements is fixed to 100 at. %, the concentration is expressed by relative values. The absolute mass according to the position is calculated from a comparison with the initial X-ray intensity of the atoms to verify the atomic flux. In the plot of the relative intensity, all the elements migrate from the anode to the cathode, which is different from the migration behavior in a molten state. The mass transport of all the elements to the cathode originates from the wind force of electromigration. This wind-force-induced electromigration results in the same directional migration regardless of the elements, while electrostatic-force-induced electromigration results in migration in various directions according to the ionicity of the elements.

The driving force for electromigration in crystalline structures is the wind force, which involves atomic migration by momentum transfer from conducting carriers. Because the wind force in metals is affected by electrons, which are the majority carrier, atoms migrate from the cathode to the anode, similar to the electron. However, the wind force in crystalline  $\text{Ge}_2\text{Sb}_2\text{Te}_5$  occurs in the opposite direction compared to that in metals. The sign of  $Z^*$  is determined by the sign of the effective mass of charge

carriers, as mentioned in **Section 2.2**. Crystalline  $\text{Ge}_2\text{Sb}_2\text{Te}_5$  is *p*-type semiconductor, i.e., the majority carriers are holes. The dependence of  $Z^*$  on the majority carriers has been observed in electromigration tests of doped Si.<sup>57</sup> After current stressing, catastrophic failure was observed in doped-Si, with differences in the behavior depending on their types. Voids were generated near the cathode in the *n*-type Si sample and near the anode in the *p*-type Si sample. No failure was observed in the AC pulse conditions even after 24 hours of stressing. These results are direct evidence that the sign of  $Z^*$  is determined by the majority carriers in materials.

Although crystalline  $\text{Ge}_2\text{Sb}_2\text{Te}_5$  is affected by the hole wind force, the quantity of migrated atoms is much smaller than that of molten  $\text{Ge}_2\text{Sb}_2\text{Te}_5$ , which is affected by the electrostatic force. Therefore, the compositional changes of phase-change materials in actual PcRAM devices are mainly affected by atomic migration in the molten state, and the effect of electromigration in the crystalline phase has been thought to be insignificant.

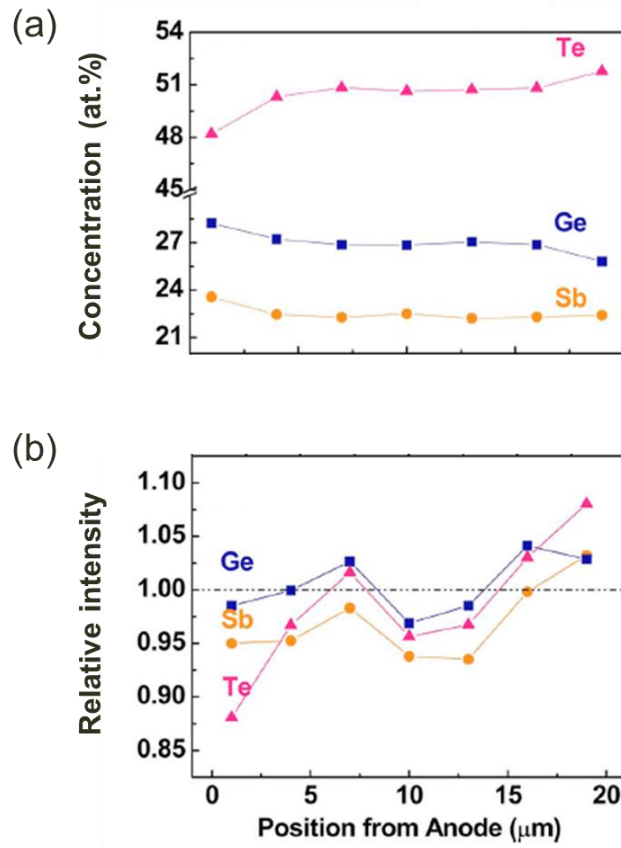


**Figure 2.9** (a) atomic concentration and (b) relative intensity showing the atomic diffusion from the anode to the cathode in crystalline  $\text{Ge}_2\text{Sb}_2\text{Te}_5$  line after the DC stressing.

## CHAPTER 3

### Experimental procedures

#### 3.1. Sample preparation

Line-patterned samples were used to apply an electric current. **Figure 3.1** shows the structure for the electromigration tests in this study. The dimensions of the line were 20  $\mu\text{m}$  in length, 2  $\mu\text{m}$  in width and 300 nm in thickness, which are much larger (micro scale) than those in actual devices (nano scale). The line structure in this study has many advantages for electromigration tests because microstructural and compositional changes from applying a current could be analyzed by SEM-level studies. PcRAM devices are too small to observe failure phenomena and analyze their mechanisms. In addition, failure mechanisms in PcRAM devices become confounded by the dispersion of the current density and temperature gradient because of a narrow bottom contact, which makes it difficult to concretely identify the failure mechanism. Various mechanisms are mixed into actual devices. The line structure in this study, however, was easy to analyze for failure phenomena

with a model study. The temperature and current density were more uniform in this structure compared to actual devices.

The chalcogenide materials that were used in this study are listed in **Table 3.1** with the deposition conditions.  $\text{Ge}_2\text{Sb}_2\text{Te}_5$  was the main materials that was used in this study, and Te-based chalcogenides were used for comparison. Thin films of chalcogenide were deposited by using a direct current (DC) magnetron sputtering on a 10-nm silicon oxide wafer. A single sputtering target with fixed composition was used to deposit thin films. The base pressure was approximately  $8 \times 10^{-8}$  torr and the working pressure was  $3 \times 10^{-3}$  torr with an argon ambient. The deposition conditions were fixed with 80 W of DC power and 20 sccm of  $\text{N}_2$  gas. Because a thick layer of oxide could interrupt thermal dispersion, 10-nm oxide was chosen as the maximum thickness for the dielectric layer. An AZ5214 photoresist was patterned by a photoaligner (Karl-Suss MA-6 II) and a lift-off method was performed to form line-shaped chalcogenide material. The as-deposited films were an amorphous phase.

Large molybdenum pads that were 500  $\mu\text{m}$  by 500  $\mu\text{m}$  were located on the end of the line-shaped chalcogenide materials for contact. Because the molybdenum pad was not affected by an electric current, these materials could act as boundaries for the atomic migration of chalcogenide materials. A highly accurate quantitative analysis can thus be conducted. To prevent the evaporation and oxidation of the chalcogenide materials, a 100 nm-thick film of silicon nitride ( $\text{Si}_3\text{N}_4$ ) was deposited on the chalcogenide line by using plasma-enhanced chemical vapor deposition (PECVD) at 200 °C. The chalcogenide materials crystallized during the passivation process because the process temperature was higher than the crystallization temperature of the chalcogenide materials.

### *Chapter 3: Experimental procedures*

---

The Pad opening process was conducted with a dry etcher (AMK P-5000 IV, Ar 10 sccm, CF<sub>4</sub> 10 sccm, CHF<sub>3</sub> 15 sccm, O<sub>2</sub> 8 sccm, 100 mtorr, radio frequency 600 W, and magnetic field 30 gauss for 25 sec). Silicon nitride films on the molybdenum pad were removed with a dry etcher for electrical contacts.

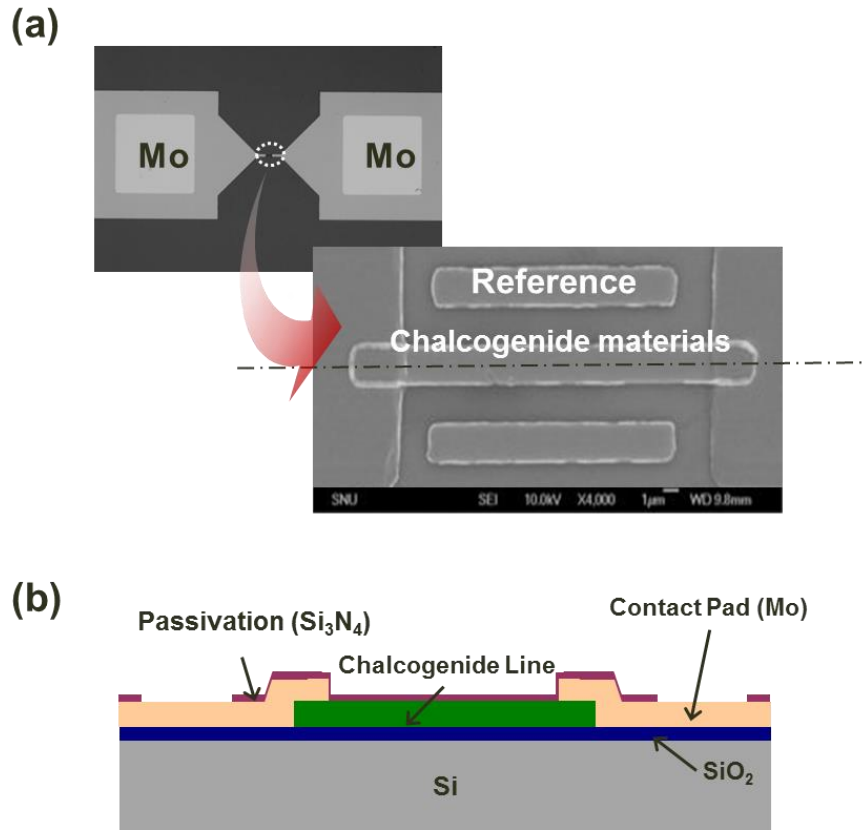




**Table 3.1** Detailed sputtering conditions for deposition of chalcogenide materials.

	Target	Power	Sputtering gas flow
<b>Ge<sub>2</sub>Sb<sub>2</sub>Te<sub>5</sub></b>	Ge <sub>2</sub> Sb <sub>2</sub> Te <sub>5</sub>	80 W	Ar: 20 sccm
<b>GeSb<sub>4</sub>Te<sub>7</sub></b>	GeSb <sub>4</sub> Te <sub>7</sub>	80 W	Ar: 20 sccm
<b>Bi<sub>2</sub>Te<sub>3</sub></b>	Bi <sub>2</sub> Te <sub>3</sub>	80 W	Ar: 20 sccm
<b>Bi<sub>35</sub>Te<sub>65</sub></b>	Bi <sub>2</sub> Te <sub>3</sub>	100 W	Ar: 20 sccm
	Te	10 W	

Base pressure:  $8.0 \times 10^{-8}$  Torr

Working pressure:  $3.0 \times 10^{-3}$  Torr

Temperature: room temperature

## **3.2. Electrical stressing method**

The methods that were used to characterize electromigration in chalcogenide materials were wafer-level electrical stressing on a hot-chuck-equipped probe station and package-level electrical stressing on an oven system. The former was a single-type test with various functional analysis, and the latter was a batch-type test with fixed conditions. In this section, the pulse dependency and IV sweep test were analyzed by using the wafer-level test, and the influences of temperature, current density, and time were analyzed by using the package-level test.

### **3.2.1. Wafer-level test**

IV sweep is the method for monitoring voltage by applying a current on the test sample. A DC current was applied to the test sample by a parameter analyzer (Agilent 4156C) under ambient air. A double-directional mode with a sweep from zero to the peak current and a return to zero was used, and the peak current density increased each cycle from 0.33 to 2 MA/cm<sup>2</sup> in 0.17 MA/cm<sup>2</sup> increments. A current density over 2 MA/cm<sup>2</sup> results in the melting of the chalcogenide materials because of severe Joule heating. Therefore, a current density under 2 MA/cm<sup>2</sup> was used in this study to maintain a crystalline phase. The ambient temperature could be changed by a hot chuck controller, which ranges from room temperature to 200 °C.

An alternating current (AC) was also applied to the chalcogenide sample by using a pulse generator (Agilent 81110A) under ambient air, which was equipped in the same probe station. The current pulse was identified from the voltage, which was measured by an oscilloscope (Agilent 54833D) with a 50 Ω input impedance. The resistance change in the sample during the test was monitored by a parameter tester (Keithley

2400). The pulse generator and the parameter tester were connected to the sample through a switching system (Keithley 7001) to switch between electrical stressing and resistance measurement. This equipment was automatically controlled by a program with LabVIEW (National Instruments). The maximum frequency that was applicable in this system was 10 MHz (minimum period of the pulse was 100 ns).

First, the parameter tester was connected to the sample through a switching system, and the resistance of the sample was measured by the parameter tester. Then, the switching system changed connection from the parameter tester to the pulse generator and oscilloscope. The pulse generator applied an electric current to the chalcogenide sample considering the resistance of the sample as measured by the parameter tester. The oscilloscope simultaneously measured the pulse shape and applied voltage. After applying a pulse current for 5 min, the connection of the sample was changed to the parameter tester by using the switching system, and the parameter tester measured and recorded the resistance of the sample again. This series of processes was repeated until the end of the experiment.

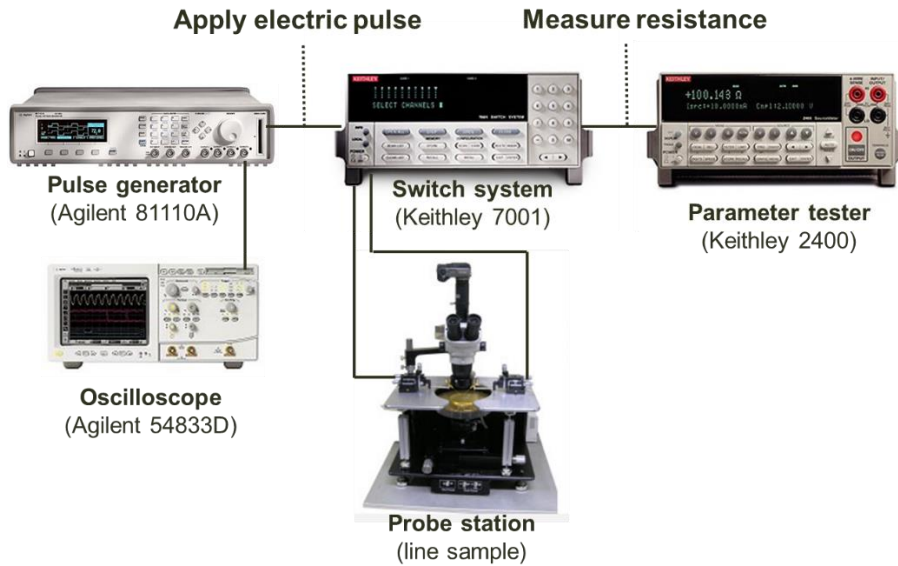


**Figure 3.2** Schematic diagram of the system for electromigration test using electrical pulse stressing in the wafer-level.

### **3.2.2. Package-level test**

Although wafer-level tests have the merits of precise and various functional analysis, only a single sample can be tested at one time. To determine the effect of various conditions, many experiments with various conditions must be conducted and compared. Wafer-level tests are limited in this case, and package-level tests are an alternative to experiments with various conditions. **Figure 3.3** shows the package-level tester (Qualitau MIRA EM test) that we used in this study.

The EM tester contains the MIRA mainframe with EM modules and controller, temperature chambers, an AC power distribution unit, and cooling fan trays. Several EM racks may be networked together and monitored by a workstation. The EM modules contain precision current sources and measurement circuits. Two EM modules are housed in one MIRA mainframe, with each module capable of running experiments on up to 60 devices under testing (DUTs), each at different stress conditions. The outputs of the current sources, which are controlled by the MIRA mainframe controller, are routed to the DUTs in the temperature chambers. The system measures the resulting current through and voltage across the DUTs by using separate sensor wires. For package-level testing, DUTs are housed in zero insertion force (ZIF) sockets, which are located on DUT boards in the temperature chambers. The devices must be packaged in a 28-pin (or less) dual in-line package (DIP). Each DUT package can contain one DUT line, one reference line and up to four independent extrusion monitors, which measure the leakage to adjacent lines. The equipment has three temperature chambers, which makes it possible to control the temperature with an individual temperature chamber. Each temperature chamber contains one DUT board, which includes 20 DUTs; therefore, the electric current can be stressed to 60 samples with different experimental conditions at the same time.

This equipment was automatically controlled by a commercial program (Qualitau Co.).

The sequence of this experiment involves two phases, which are the temperature coefficient of resistance (TCR) phase and stress phase. During the TCR phase, the resistance of each DUT is measured as a function of temperature. The purpose of the TCR phase is to generate a curve fit of these data so that the DUT line temperature can be determined. The line temperature is greater than the oven temperature during stress, because of the stress current and the effects of Joule heating. The first and lowest temperature the system can reach is 50 °C, which is the lowest temperature the oven can control without cooling from liquid nitrogen. The maximum temperature the oven can reach is the stress temperature as specified in the test conditions. The number of intermediate temperatures the oven can reach is generally three steps in this study. At the end of the TCR phase, the oven is at the stress temperature and the temperature has stabilized for one hour.

The system can also measure the actual stress current through each DUT for high-precision resistance measurements. For a standard EM module, this value amounts to approximately 10  $\mu$ A. At the stress phase, electrical tests are conducted for every sample by simultaneously monitoring their resistances.

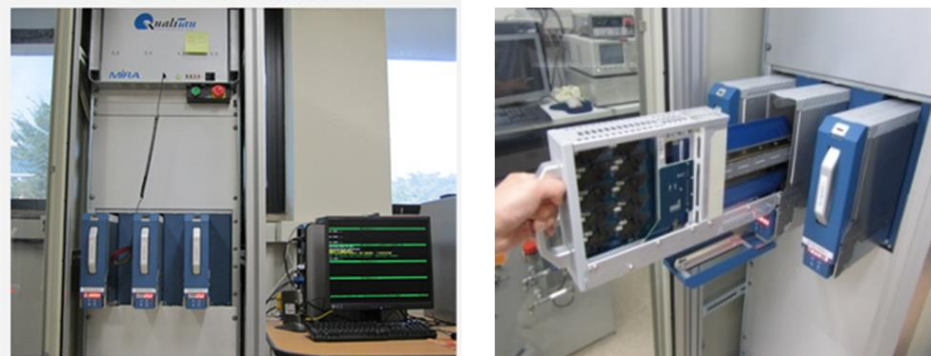


**Figure 3.3** The electromigration tester for package-level test (Qualitau MIRA EM tester). Two EM modules are housed in one MIRA mainframe, with each module providing a capability of running experiments on up to 60 devices under test (DUTs), each at different stress conditions. This equipment was automatically controlled by a commercial program (Qualitau Co.)

### **3.3. Compositional analysis**

Compositional changes that were induced by electromigration were analyzed by wavelength dispersive X-ray spectroscopy (WDS) under a scanning electron microscope (SEM) and by energy dispersive X-ray spectroscopy (EDS) under a transmission electron microscope (TEM). Because electromigration is mass transport that is induced by electric currents, the concentration of atoms can change depending on the position and element. Compositional analysis under SEMs and TEMs is similar, but the interaction volumes of each method are different.

The interaction volume of WDS electrons under the SEM was probably approximately 2  $\mu\text{m}$  with a hemispherical shape at the detection point. The dimensions of the chalcogenide line in this study were 20  $\mu\text{m}$  in length and 2  $\mu\text{m}$  in width. Therefore, 10 compositional analysis points were available in the direction of the line without overlap. We can quantify the composition of the chalcogenide materials, which depends on the line position. **Figure 3.1** shows the structure for the electromigration test in this study as mentioned above. Three independent chalcogenide lines were located between metal pads, but only one chalcogenide line was connected with the metal pad. The connected chalcogenide line was an actual test line, which was applied by an electric current. The rest of the lines without any connections, which were denoted by the reference line, experienced the same process and thermal history as the test line. Because the reference line did not experience electrical stress, the composition of reference line can be used as a standard to analyze the mass flux of chalcogenide materials after current stressing. The absolute quantity of each element was calculated from the results of pure elements. For example, 99.99 %



pure Ge, Sb, and Te samples were used to conduct a quantitative analysis of  $\text{Ge}_2\text{Sb}_2\text{Te}_5$ .

The interaction volume of EDS electrons under the TEM, however, was probably approximately 100 nm at the detection point because of the thickness of the sample. Compared to WDS under an SEM, EDS analysis under a TEM has low resolution and high precision with the location. The TEM samples were fabricated by using a focused ion beam (FIB).

## **CHAPTER 4**

# **Gradual degradation in the crystalline $\text{Ge}_2\text{Sb}_2\text{Te}_5$ under electric current**

### **4.1. Introduction**

Chalcogenides are used as phase-change materials in PcRAM.<sup>4,19</sup> As the memory density increases, PcRAM experiences harsher operating conditions, such as high current density and temperature, which can cause reliability issues and failure induced by compositional change and void formation.<sup>9, 58</sup> These durability problems are caused by the mass transport of compositional elements, including electric current or field-induced migration, also known as electromigration (EM). Previous research predominantly focused on the liquid phase, which is the intermediate state of transformation between the crystalline and amorphous phases during PcRAM operation. Because the atomic diffusivity of the liquid phase is much faster than the atomic diffusivity of the crystalline phase,<sup>13</sup> electric field-induced failures predominantly occur in the liquid phase; the crystalline phase has thus been considered the stable state for electromigration.

However, not all regions of the phase-change material experience the melting process during PcRAM operation. Only the active region, which is the limited zone near the heater, can be transformed into the liquid phase. The alternate region remains as a crystalline phase without melting, despite repeated device operation. The effect of atomic migration in the crystalline regions is cumulative, whereas the effect that evolves at the active region can be recovered through the melting and solidification process. This cumulative effect on the crystalline phase can affect the instability of the SET resistance. Therefore, it is important to investigate the migration behavior of the crystalline phase of  $\text{Ge}_2\text{Sb}_2\text{Te}_5$  to gain a comprehensive understanding of the reliability of PcRAM. The elements of crystalline  $\text{Ge}_2\text{Sb}_2\text{Te}_5$  are affected by an electric current, which is the momentum transfer between charge carriers and atoms.<sup>15</sup> EM in crystalline  $\text{Ge}_2\text{Sb}_2\text{Te}_5$  has been demonstrated to cause direct amorphization without melting, which signifies that EM in the crystalline phase has sufficient power to affect the solid-state structure.<sup>16,59</sup> As the dimensions of devices diminish, the current density is anticipated to increase,<sup>17</sup> and degradation in the crystalline state may become a significant reliability problem for a PcRAM cell.

In this chapter, we investigated EM-induced failure in crystalline  $\text{Ge}_2\text{Sb}_2\text{Te}_5$ , which has never been reported. Despite the low rate of migration in the crystalline phase, this failure exhibits a gradual increase in the resistance by nano-scale void formation. We investigated the failure mechanism of the EM-induced atomic migration in the crystalline phase of  $\text{Ge}_2\text{Sb}_2\text{Te}_5$  by applying continuous current and analyzing the microstructural changes.

## **4.2. Experiments**

Line-shaped samples, whose measurements were 20  $\mu\text{m}$  in length, 2  $\mu\text{m}$  in width and 300 nm in thickness, were employed to study the EM-induced failure in crystalline Ge<sub>2</sub>Sb<sub>2</sub>Te<sub>5</sub> as described in the **Chapter 3**. Because the as-deposited GST was in the amorphous phase, the films were annealed for 1 hour at 250 °C to crystallize the initial amorphous phase into a hexagonal phase. The initial resistivity of the hexagonal phase of GST was approximately  $8 \times 10^{-4} \Omega\cdot\text{cm}$ .

All experiments for EM used current source. A direct current (DC) stress in the range of 0.17 to 1.83 MA/cm<sup>2</sup> was applied at 200 °C using a package-leveled EM tester (Qualitau MIRA). Alternating current (AC) with a frequency of 10 MHz, generated by a pulse generator (Agilent 81110A), was also applied to confirm the polarity effect. Failure morphologies were observed via scanning electron microscopy (SEM, Hitachi SU70) and transmission electron microscopy (TEM, Technai F20). Variations in the composition were analyzed by wavelength dispersive spectroscopy using an electron probe X-ray microanalyzer (EPMA, JXA-8900R) and by energy-dispersive spectroscopy using TEM.

## **4.3. Electrical stressing in crystalline Ge<sub>2</sub>Sb<sub>2</sub>Te<sub>5</sub>**

**Figure 4.1** shows the electrical resistance and morphology changes of the Ge<sub>2</sub>Sb<sub>2</sub>Te<sub>5</sub> line during electrical stressing with respect to time and current density at 200 °C ambient temperature. The resistance and morphology changes exhibited

different behavior depending on the current density. Depending on the applied current density, the change behaviors fall into three main classes, which has not been reported.

#### **4.3.1. High current**

The resistance rapidly increased within a minute at current densities above 1.67 MA/cm<sup>2</sup>, which resulted in catastrophic failure. Large micro-scaled damage spots formed at current densities above 1.67 MA/cm<sup>2</sup>. Severe joule heating occurred when higher current density was applied, which caused instantaneous melting. In the liquid state, atomic migration is fast, and mass divergence and voids are generated by EM at a rapid rate. This phenomenon has been reported in the **Section 2.3.1**.

#### **4.3.2. Low current**

The resistance increased with time for current densities above 0.83 MA/cm<sup>2</sup>, and the rate of resistance change increased with the current density. However, no resistance and morphological change was observed below 0.83 MA/cm<sup>2</sup>, with the exception of a decrease in the initial resistance due to annealing. The resistance decrease is originated from the vacancies in the crystalline structure of Ge<sub>2</sub>Sb<sub>2</sub>Te<sub>5</sub>. As mentioned in the **Section 2.1.4**, crystalline Ge<sub>2</sub>Sb<sub>2</sub>Te<sub>5</sub> has two types of crystalline phase depending on the temperature, which are hexagonal and cubic phase. Except for this resistance decrease, current-induced degradation is not observed on the condition of current density below 0.83 MA/cm<sup>2</sup>. The detailed information in this condition will be discussed in the next chapter. (**Chapter 5**)

#### **4.3.3. Mid current**

Interestingly, a gradual increase in the resistance (on a time scale of approximately 10–20 hours) was observed under intermediate current density conditions. The failure morphology revealed that numerous nanometer-sized voids formed throughout the entire area, as shown in **Figure 4.1(b)**. This failure mode differed from the catastrophic failure caused by large voids at higher current densities, which indicates that intermediate current densities ranging from 1 to 1.5  $\text{MA}/\text{cm}^2$  induce the generation of nano-scaled voids and a gradual increase in the resistance. The compositional analysis of the sample clearly distinguished the difference between high and mid current failure modes, as shown in **Figure 4.2**. The relative intensity is the value of atomic quantity normalized to the initial quantity, which shows the mass flux of atoms. As shown in **Figure 4.2**, at the high current, demixing of the elements in the entire sample was observed. Te atoms moved to the anode, and Ge and Sb atoms moved to the cathode. This behavior is typical of electric field-induced EM in the liquid state.<sup>12,13</sup> However, at the mid current, the compositional change is quite different. The migrated amounts are small, and all elements move in the same direction, which is typical EM behavior in the crystalline phase.<sup>13,15</sup> Therefore, the gradual failure mode is caused by EM in the solid state.

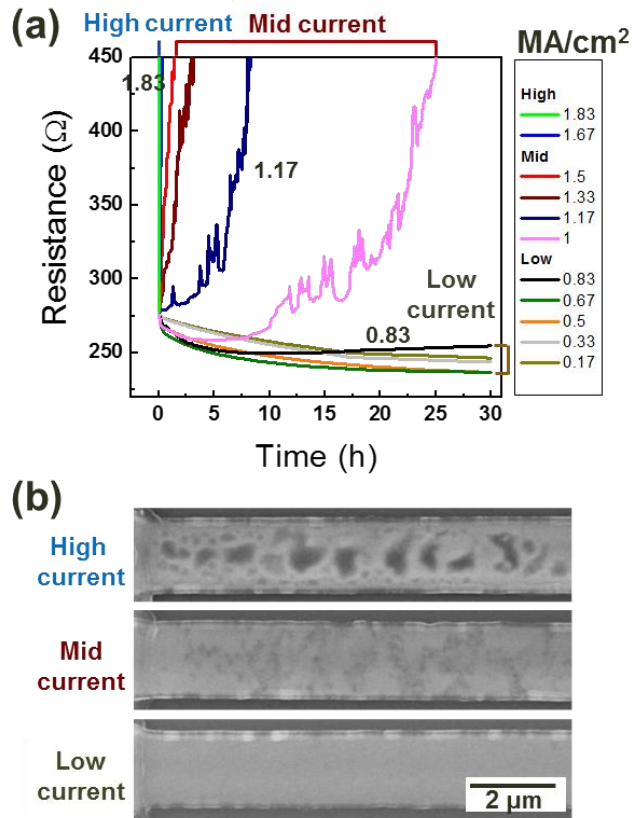


**Figure 4.1** (a) Relative resistance-time curves during constant DC current stress on  $\text{Ge}_2\text{Sb}_2\text{Te}_5$  line samples. The stress current ranged from 0.17 to 1.83 MA/cm<sup>2</sup> at 200 °C. (b) Based on the current density, different microstructures developed in the  $\text{Ge}_2\text{Sb}_2\text{Te}_5$  line samples, as shown by the SEM images. Current densities below 0.83 MA/cm<sup>2</sup>, ranging from 1 to 1.5 MA/cm<sup>2</sup> and above 1.67 MA/cm<sup>2</sup> are denoted as “low current”, “mid current” and “high current”, respectively.

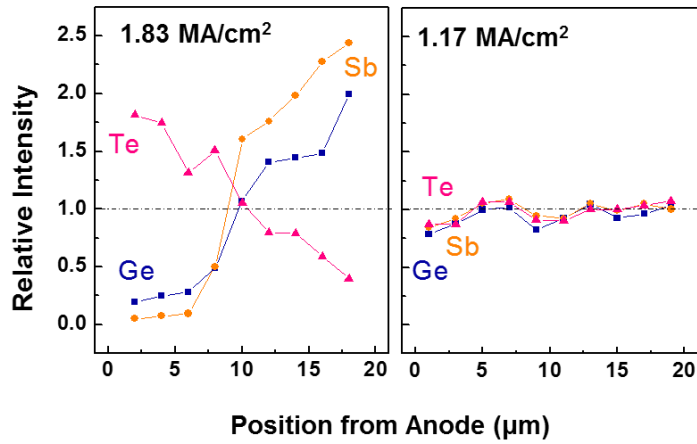


**Figure 4.2** Compositional changes of the sample after the EM stressing at a current density of  $1.83 \text{ MA/cm}^2$  (high current) and  $1.17 \text{ MA/cm}^2$  (mid current).



#### **4.4. Frequency dependence in gradual failure**

To understand the physical origin of the gradual failure in the crystalline state, we investigated the effect of bias with DC and AC. **Figure 4.3** shows the resistance change and SEM image of the line samples after the test under DC and AC conditions. The result of DC current stressing at  $1.17 \text{ MA/cm}^2$  was compared with an AC current of 10 MHz at the same current density and temperature. Unlike the DC test, neither the resistance increase nor the generation of voids was observed under AC conditions. The only difference between the DC and AC conditions is the directionality of the bias because the joule heating induced by the current is similar for DC and AC owing to their equivalent current densities. Under DC conditions, the charge carriers move in only one direction, so momentum transfer between charged carriers and atoms is accumulated while DC bias is applied. However, flux of charge carriers is variable in AC condition. 10 MHz of AC stress was used in this experiment, which means direction of bias is alternated 10 million times per second. In this case, migration rate is much slower than the speed of bias switching, thus, atoms could only pace around the own position and don't have a directionality. The migration effect is canceled out by the repetitive directional switching of AC. Therefore, electromigration works only DC condition, not AC condition. Because the joule heating of AC and DC should produce the same effect, this result indicates that the gradual failure is related to the bias dependence during current stressing.

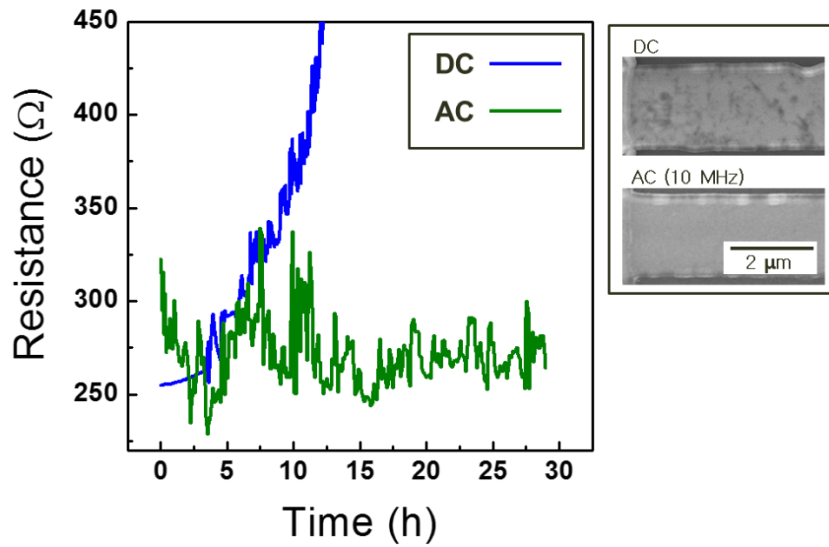


**Figure 4.3** Resistance-time curves illustrating DC and AC (frequency of 10 MHz) current stressing of  $1.17 \text{ MA/cm}^2$  at  $200^\circ\text{C}$ . The SEM image for each result is also displayed.

## 4.5. Microstructural analysis

### 4.5.1. Quantification of voids

For a more detailed examination of the relationship between EM and resistance, microstructural and compositional analyses were conducted. **Figure 4.4(a)** shows the cross-sectional TEM images of the  $\text{Ge}_2\text{Sb}_2\text{Te}_5$  line samples after testing at 1.17 MA/cm<sup>2</sup> at 200 °C (gradual failure conditions). The bright areas are  $\text{Ge}_2\text{Sb}_2\text{Te}_5$  and the dark particle-shaped areas depict the generated nanometer scale voids. Nano-scaled voids were generated not only on the surface but also inside the GST. The average size of the voids, which were well distributed, was approximately 7 nm. The resistance of the whole system is increased by the local void formation because the conducting area decreases with increasing void areas which act as an insulator.

Although we can calculate the area fraction of voids from cross-sectioned TEM image, volume fraction can't be calculated from the image exactly. To calculate volume fraction from the area fraction, some assumptions are needed. We assume that all voids have same radius with perfect sphere shape, and well distributed on the whole line. We consider a rectangular with a thickness of  $d$  which is the same with the diameter of voids. **Figure 4.5(a)** shows schematic image of the rectangular type matrix and sphere-shaped voids, and **Figure 4.5(b)** is top view of (a).  $R_r$  and  $R_p$  are actual radius and average radius in plane, respectively. TEM image in this study is a top view image as shown **Figure 4.5(b)**. Because the voids displayed in a plane are sectioned image of sphere-shaped actual voids, the value of  $R_p$  is always smaller than the value of  $R_r$ . **Figure 4.5(c)** shows calculation of area sectioned from sphere based on the y-axis distance. Because we assume voids are well-distributed particle,

distances along the y-axis have an identical probability. Average of sectioned-area can be calculated by,

$$\begin{aligned}\pi R_p^2 &= \lim_{n \rightarrow \infty} \frac{\sum_{i=0}^n \pi R_r^2 \left(1 - (i/n)^2\right)}{n} \\ &= \pi R_r^2 \cdot \lim_{n \rightarrow \infty} \frac{\left(n - \frac{n(n+1)(2n+1)}{6n^2}\right)}{n} = \frac{2}{3} \pi R_r^2\end{aligned}\quad (4.1)$$

The average radius in plane is,

$$R_p = \sqrt{2/3} R_r \quad (4.2)$$

The total number of particle of  $n$  can be calculated via,

$$n = \frac{\text{total particle area}}{\text{particle area}} = \frac{(\text{area fraction}) \times A}{\pi R_p^2} \quad (4.3)$$

where  $A$  is the area of a rectangular as depicted in **Figure 4.5(a)**. Volume fraction of voids can be calculated by ratio between volume of voids and rectangular.

$$\begin{aligned}\text{volume fraction} &= \frac{\text{Total volume of voids}}{\text{Total volume of rectangular}} \\ &= \frac{n \cdot \left(\frac{4}{3} \pi R_r^3\right)}{A \cdot d} = \frac{\frac{(\text{area fraction}) \times A}{\pi R_p^2} \cdot \left(\frac{4}{3} \pi R_r^3\right)}{A \cdot 2 R_r}\end{aligned}$$

$$= (\text{area fraction}) \quad (4.4)$$

Therefore, we can conclude that the volume fraction of voids is same to the area fraction of voids. The volume fraction of the voids, which was quantified from the images using an image analyzer, is 0.28.

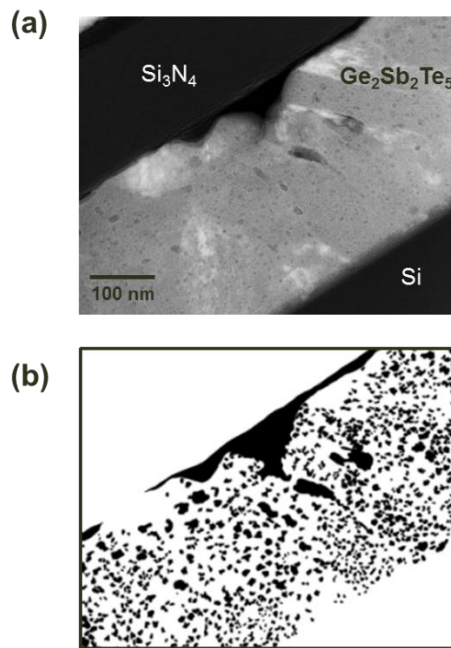


**Figure 4.4** (a) High-contrast image of the  $\text{Ge}_2\text{Sb}_2\text{Te}_5$  line sample after testing at  $1.17 \text{ MA/cm}^2$  at  $200^\circ\text{C}$ , as observed by TEM. The gray region denotes  $\text{Ge}_2\text{Sb}_2\text{Te}_5$ , and the dark areas denote defects. (b) The area analysis of the defects as measured by the image analyzer.

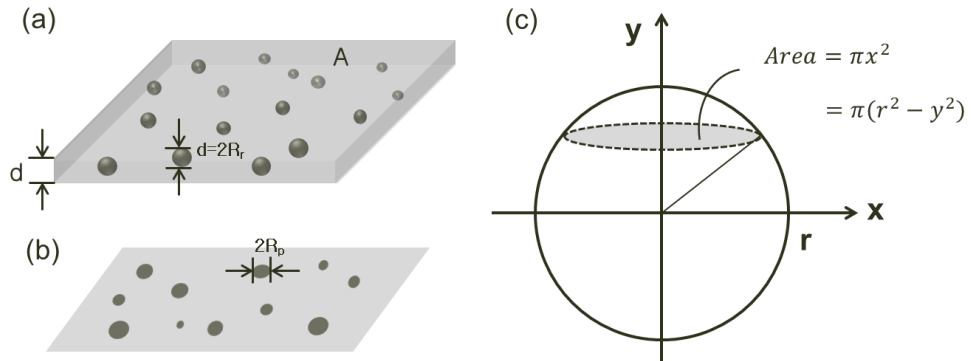


**Figure 4.5** Schematic image of homogenous particle model on the (a) rectangular type and (b) top view. (c) Calculation of area sectioned from sphere according to the y-axis distance.

#### **4.5.2. Resistivity according to void fraction**

To analyze the effect of the voids on the resistivity quantitatively, the effective resistivity was calculated using the dispersed particle model. The resistance increase is modeled by following simple assumption originally suggested by Reynolds and Hough.<sup>60</sup> They proposed the general equation of mixture rule. Because the effective resistivity of multiphase solid is closely related to the effective dielectric constant, effective thermal conductivity, etc., for a variety of the mixtures, these mixture rules are identical. We can consider a heterogeneous material that has a dispersed phase (labeled  $d$ ), in the form of particles, in a continuous phase (labeled  $c$ ) that acts as a matrix. The general equation is,

$$\frac{\sigma_{eff} - \sigma_c}{\sigma_{eff} + 2\sigma_c} = \chi \frac{\sigma_d - \sigma_c}{\sigma_d + 2\sigma_c} \quad (4.5)$$

where  $\sigma_{eff}$ ,  $\sigma_c$ , and  $\sigma_d$  are effective conductivity, conductivity of continuous phase and dispersed phase, respectively, and  $\chi$  is volume fraction of dispersed phase. If the resistivity of dispersed phase is much higher than the resistivity of continuous phase, that is  $\rho_d \gg \rho_c$ , then,

$$\sigma_{eff} = \sigma_c \frac{1 - \chi}{1 + (1/2)\chi} \quad (4.6)$$

modified according to resistivity



$$\rho_{eff} = \rho_c \frac{1 + (1/2)\chi}{1 - \chi} \quad (4.7)$$

where  $\rho_{eff}$  is the effective resistivity,  $\rho_c$  is the resistivity of the matrix and  $\chi$  is the volume fraction of the voids. From the above equation, the effective resistivity of total system increase as the volume fraction of voids increase. The simulation of relative resistance according to volume fraction of voids is shown in **Figure 4.6**.

The area analysis between the dark (void) and white (Ge<sub>2</sub>Sb<sub>2</sub>Te<sub>5</sub>) is depicted in the **Figure 4.4(b)**. As mentioned above, the volume fraction of the voids, which was quantified from the images using an image analyzer, is 0.28. The equation (4.7) illustrates that when the volume fraction of the voids is 0.28, the final resistivity is 1.6 times the initial resistance, which is similar to our results depicted in **Figure 4.1(a)** ( $R_f/R_i=1.6$ ). The experimentally determined resistance is equivalent to the calculated value from the void generation. Therefore, the main reason for the gradual increase in resistance during current stressing is the generation of highly resistive voids.

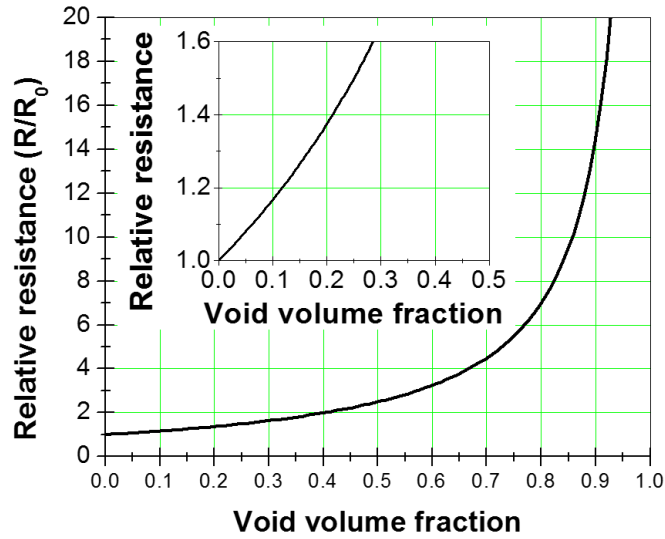


**Figure 4.6** Simulation of relative resistance according to volume fraction of voids, which is calculated using the dispersed particle model. (eq. 4.7) The expansion graph for volume fraction ranged from 0 to 0.5 is displayed in the inset image.

#### **4.5.3. Composition at the defect site**

To confirm the origin of the nano-scaled voids, a compositional analysis of the sample was performed by SEM and TEM. **Figure 4.7** includes three different quantitative results: (1) the total composition of the sample by SEM, (2) the composition of the non-voided area by TEM and (3) the composition of the void by TEM. The composition from SEM (1) and TEM of the non-voided area (2) were nearly similar to the initial composition of the  $\text{Ge}_2\text{Sb}_2\text{Te}_5$ , which was Ge:Sb:Te=2:2:5. However, the composition of the void (3) differs from the original compositions, being Ge-deficient and Sb-rich. These results show that the composition is dependent on the existence of voids and compositional variation only occurs in the void area.

The local non-stoichiometry of the void area is distinct evidence of localized melting and is explained by the phase diagram.  $\text{Ge}_2\text{Sb}_2\text{Te}_5$  is a ternary compound composed of 2:1 mixtures of GeTe and  $\text{Sb}_2\text{Te}_3$ . Based on the pseudo-binary phase diagrams of GeTe and  $\text{Sb}_2\text{Te}_3$ ,  $\text{Ge}_2\text{Sb}_2\text{Te}_5$  does not melt congruently.<sup>10</sup> Because  $\text{Ge}_2\text{Sb}_2\text{Te}_5$  has an incongruent melting region below the melting temperature, the pseudo-binary phases of  $\text{Sb}_2\text{Te}_3$  and GeTe were separated during solidification, which produced Ge-deficient and Sb-rich voids.<sup>10</sup> Therefore, the void area previously consisted of a locally molten state, and the compositional change was initiated during solidification. **Figure 4.8** shows a schematic diagram of the defect-induced melting process. Once the localized liquid phase was formed, the voids were generated by EM in milliseconds.

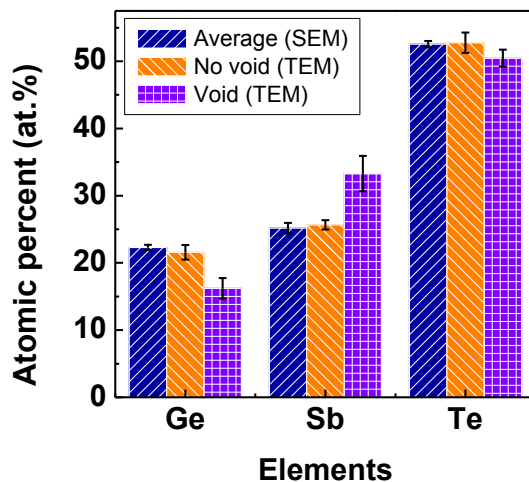


**Figure 4.7** Compositional analysis from SEM and TEM, which contain different interaction volumes. Three different quantitative results are included: the total composition of the sample by SEM, the composition of the non-voided area by TEM, and the composition of the void by TEM.

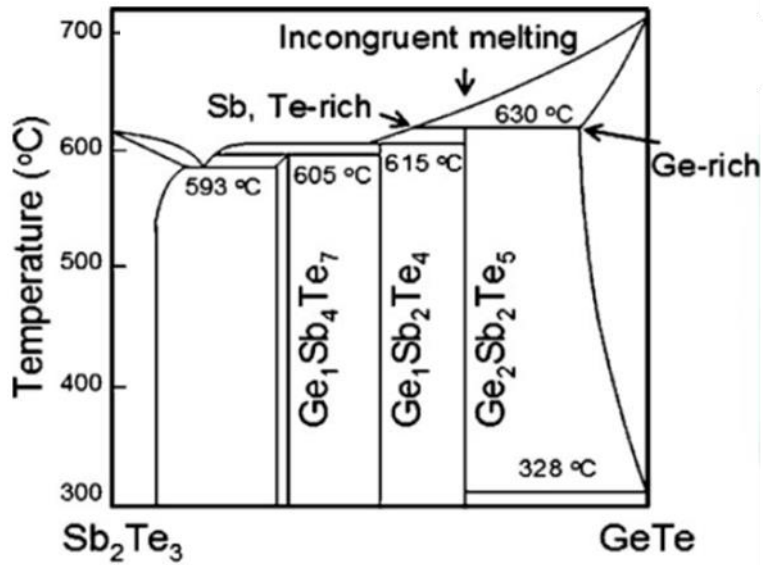


**Figure 4.8** Pseudo-binary phase diagram of  $\text{Sb}_2\text{Te}_3$  and  $\text{GeTe}$ . Molten state of  $\text{Ge}_2\text{Sb}_2\text{Te}_5$  is separated into two phase during solidification process, which are Sb-rich liquid phase and Ge-rich solid phase.

## **4.6. Mechanism of void generation**

The origin of voids is caused by EM in the crystalline state. Although EM in the crystalline phase is not sufficient to induce a catastrophic de-mixing of elements, it can induce an amorphous phase at the grain boundary or surface. It was reported that EM leads to a direct transformation from the crystalline to the amorphous phase without melting by pile-up of the dislocations in the  $\text{Ge}_2\text{Sb}_2\text{Te}_5$ .<sup>16</sup> The grain boundary or surface is the pile-up site of dislocations in the polycrystalline system. Although current flows around the amorphous phase due to its high resistivity, the amorphous phase can act as defect points and generate localized melting. The temperature of the sample increases due to joule heating under the gradual failure testing conditions, but the temperature is too low to cause melting. Under these conditions, melting can only occur locally at vulnerable points, such as a defect, through heterogeneous or defect-induced melting.<sup>61,62</sup>

In the classical thermodynamics, melting process is known as a first-order transformation occurring at the temperature which Gibbs free energies of the solid and liquid phase are same. However, numerous experimental discovered that various kinds of defect, such as grain boundary, surface, voids and other defects initiated melting process.<sup>63</sup> Solid can melt at a temperature below their melting point, because these defects act as heterogeneous nucleation sites for melt. Fecht and Johnson explored the superheating for melting by the temperature dependence of entropy change for a solid and liquid.<sup>64</sup> Fecht and Johnson point out that entropy paradox, which is similar to Kauzmann paradox, exist at a temperature above melting point.<sup>65</sup> Like the ideal glass transition temperature,  $T_g$ , defined by the isentropic condition for an undercooled liquid and crystal below melting point, the instability temperature,  $T_i^*$ , can be defined

by the isentropic temperature for a superheated crystal and liquid above melting point.

<sup>64</sup> If the instability temperature correspond with the temperature, which the volume of the liquid and the superheated crystal become equal through increasing of defect concentration, melting becomes a second-order transition. In this condition, an overall melting cannot occur even at melting point and only arises at the defect sites predominantly.

Intrinsic vacancies of the Ge<sub>2</sub>Sb<sub>2</sub>Te<sub>5</sub> produce free volume in the liquid phase, which is not filled with constituent atoms. When the constituent elements of Ge<sub>2</sub>Sb<sub>2</sub>Te<sub>5</sub> were separated by EM, agglomerated free volumes caused the formation of voids in the liquid matrix. <sup>56,66</sup> Because the liquid phase exhibits low resistivity compared with the crystalline phase, the liquid phase can be rapidly transformed to the crystalline phase by reducing the joule heating. Consequently, the gradual increase in the resistance resulted from the steady generation of localized melting spots, which is the rate determining step. The process of voids generation is shown in **Figure 4.9**.

## **4.7. Summary**

We investigated the failure mechanism of Ge<sub>2</sub>Sb<sub>2</sub>Te<sub>5</sub> in the crystalline phase under DC and AC conditions. Because this behavior only occurs when using DC, we conclude that the failure of the crystalline phase was induced by EM. Localized melting induced by EM produced compositional changes in these localized areas, which consisted of nano-scaled voids. Void generation is the predominant factor in the gradual increase in resistance. These results indicate that devices can fail due to atomic migration in both the crystalline and liquid states, which can cause fatal

reliability problems even at intermediate currents, a regime that has not been considered to cause failures.

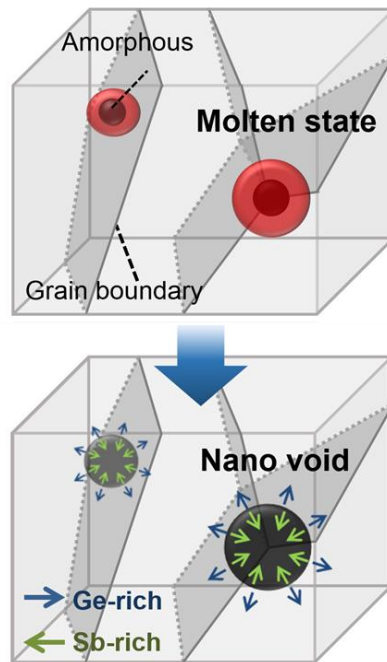


**Figure 4.9** Schematic diagram of the defect-induced melting and phase separation behavior during solidification.



## CHAPTER 5

# Formation of metallic cubic-phase Ge-Sb-Te compounds when induced by an electric current

### 5.1. Introduction

Cubic-phase Ge-Sb-Te compounds have a high degree of disorder with large numbers of structural vacancies in their lattices.<sup>4, 22, 67</sup> This structural feature of the metastable cubic phase causes the electrical properties and charge transport properties to be significantly influenced by temperature.

The resistance of  $\text{GeSb}_2\text{Te}_4$  gradually decreases with temperature, unlike GeTe, and the nature of the material changes from an insulator to a metal at high temperatures, as demonstrated by T. Siegrist et al.<sup>39</sup> Theoretical studies by W. Zhang et al., who used density functional theory calculations determined the microscopic origin of the metal-insulator transition (MIT) in cubic  $\text{GeSb}_2\text{Te}_4$ ; the rearrangement of vacancies decreases the total energy per atom, which implies that the arrangement of vacancies is critical in the electrical properties of cubic  $\text{GeSb}_2\text{Te}_4$ .<sup>48</sup> More recently, the impact of the stoichiometry was demonstrated by P. Jost et al. as a controllable parameter for the MIT of the most common compositions in the  $(\text{GeTe})_x(\text{Sb}_2\text{Te}_3)_{1-x}$  system; i.e., disorder-induced

localization results in the MIT differ according to the average vacancy concentration of various compositions.<sup>50</sup> Therefore, the behaviors of the MIT, which are controlled by the annealing temperature and stoichiometry, are critical for tailoring the charge transport properties of cubic Ge-Sb-Te compounds to increase the performance of PcRAM devices.

Although the rearrangement of vacancies in Ge-Sb-Te compounds is considered the origin of MITs, separating the vacancy effect from phase transitions is difficult because Ge-Sb-Te compounds have two phase types: an insulating cubic phase and a metallic hexagonal phase.<sup>22</sup> The phase transition from the cubic to the hexagonal phase is a high priority before the rearrangement of vacancies can be completed.<sup>39,45</sup> Therefore, the final product of Ge-Sb-Te compounds after an MIT is the hexagonal phase, and the vacancy effect on MITs has not been proven experimentally. Here, we investigated the driving force for MITs beyond the annealing temperature or stoichiometry and independent from the phase transition, specifically, the electric current. The atomic displacement from an electric current can promote the rearrangement of vacancies. MITs should be investigated under electric current stressing conditions, i.e., more device-related characteristics. During PcRAM operation (writing, erasing and reading), cubic Ge-Sb-Te compounds are exposed to various ranges of electric current stressing, and much evidence exists of changes in the structural and charge transport properties under these circumstances.<sup>68,69</sup>

The electric current effect on crystalline GST has been typically associated with a high current density of over  $10^7$  A/cm<sup>2</sup>.<sup>8,9,13,66,68</sup> Under these conditions, the electric current generates disorder or the massive displacement of atoms because the driving force for migration is sufficient to create structural changes with high current density. Disorder can be induced by a high current density in a nanowire system, creating an amorphous or insulating phase.<sup>68,16</sup> In contrast, a relatively low current density of approximately  $10^6$  A/cm<sup>2</sup> cannot generate enough structural disorder to transition to an insulating phase. The

atomic displacement by a low current is negligible compared to that from a high current because the driving force is insufficient to generate a massive flux of atoms.<sup>68</sup> An electric current in the range of  $10^6$  A/cm<sup>2</sup> only assists in the rearrangement of vacancies.

In this chapter, we demonstrate the transition from an insulator to a metal without a phase transition by using an electric current in crystalline Ge<sub>2</sub>Sb<sub>2</sub>Te<sub>5</sub>, which differs from thermal annealing. This approach is a new pathway for metallic cubic phase formation, which has not been previously reported because Ge<sub>2</sub>Sb<sub>2</sub>Te<sub>5</sub> generally has low resistivity in the hexagonal phase. The metallic cubic phase of Ge<sub>2</sub>Sb<sub>2</sub>Te<sub>5</sub> is investigated by temperature dependency and microstructural analyses. Moreover, the influence of intrinsic vacancies on MITs was investigated by comparing Ge<sub>2</sub>Sb<sub>2</sub>Te<sub>5</sub> and GeSb<sub>4</sub>Te<sub>7</sub>, which have structurally different initial vacancies.<sup>18,70</sup>

## 5.2. Experiments

Line-patterned Ge<sub>2</sub>Sb<sub>2</sub>Te<sub>5</sub> and GeSb<sub>4</sub>Te<sub>7</sub> samples, whose measurements were 20  $\mu$ m in length, 2  $\mu$ m in width and 300 nm in thickness, were subjected to an electric current or various temperatures as described in **Chapter 3**. Unlike the study in **Chapter 4**, the as-deposited Ge<sub>2</sub>Sb<sub>2</sub>Te<sub>5</sub> film was annealed for 1 hour at 200 °C to crystallize the initial amorphous phase into a cubic phase. The initial resistivity of the cubic phase of Ge<sub>2</sub>Sb<sub>2</sub>Te<sub>5</sub> was approximately  $2 \times 10^{-2}$   $\Omega$ ·cm.

The I-V characteristics of the Ge<sub>2</sub>Sb<sub>2</sub>Te<sub>5</sub> were measured by using a wafer-level tester (**Section 3.2.1**) and long-term stressing was applied to the Ge<sub>2</sub>Sb<sub>2</sub>Te<sub>5</sub> by using a package-level tester (**Section 3.2.2**)

Cross-sectional images of the current- and temperature-stressed samples were taken by using a TEM (Technai F20). The TEM samples were fabricated by using an FIB (SII NanoTechnology SMI3050SE). Microstructural analysis with X-ray diffractometry (XRD, PANalytical X'pert Pro) was also performed.

### **5.3. Current-driven electrical sweep in $\text{Ge}_2\text{Sb}_2\text{Te}_5$**

#### **5.3.1. I-V characteristics of $\text{Ge}_2\text{Sb}_2\text{Te}_5$**

A double directional mode, with a sweep from zero to the peak current and a return to zero was used, and the peak current density increased each cycle from 0.33 to 1.67  $\text{MA}/\text{cm}^2$  in 0.17  $\text{MA}/\text{cm}^2$  increments, as shown in **Figure 5.1**. The electrical resistivity of  $\text{Ge}_2\text{Sb}_2\text{Te}_5$  after a current sweep with an increasing peak current density is displayed only for 0.33 and 0.5  $\text{MA}/\text{cm}^2$  in **Figure 5.1(b)**. As shown in **Figure 5.1**, the resistivity of  $\text{Ge}_2\text{Sb}_2\text{Te}_5$  decreased with increasing current density, and a certain amount of the resistivity was unrecovered during the reverse sweep; i.e., an irreversible change in resistivity was observed. In contrast, the change in resistivity during the reverse sweep was the same as that for the forward sweep under the experienced current density; i.e., a reversible change in resistivity was displayed. These results indicate that an irreversible change in resistivity was completed during the first cycle of the applied current. The slopes of the resistivity and current density during the reverse sweep increased with the peak current density, and their signs changed from negative to positive at a peak current density of 1  $\text{MA}/\text{cm}^2$ .

A cyclic current sweep was performed with a fixed peak-current density of 1.67  $\text{MA}/\text{cm}^2$  for  $\text{Ge}_2\text{Sb}_2\text{Te}_5$ . **Figure 5.2** shows the resistivity of  $\text{Ge}_2\text{Sb}_2\text{Te}_5$  during a

current sweep from 0 to  $1.67 \text{ MA/cm}^2$  at room temperature 10 times, and the inset of **Figure 5.2** shows a range of resistivity from 0.0018 to  $0.0035 \text{ }\Omega\text{cm}$ . The first sweep (black line in **Figure 5.2**) shows a continuous decrease in resistivity to  $1.67 \text{ MA/cm}^2$  during the forward sweep and a slight change in resistivity during the reverse sweep to zero. The second to tenth sweeps, however, follow the reverse of the first sweep with some variation. Furthermore, the resistivity for a direct sweep to  $1.67 \text{ MA/cm}^2$  (**Figure 5.2**) is the same as the resistivity for sequential sweeps to  $1.67 \text{ MA/cm}^2$ , increasing in increments of  $0.17 \text{ MA/cm}^2$  (**Figure 5.1**). These results indicate that an irreversible change in resistivity was completed during the first cycle of the applied current. Once irreversibly changed, the resistivity was reversible under the experienced current density.

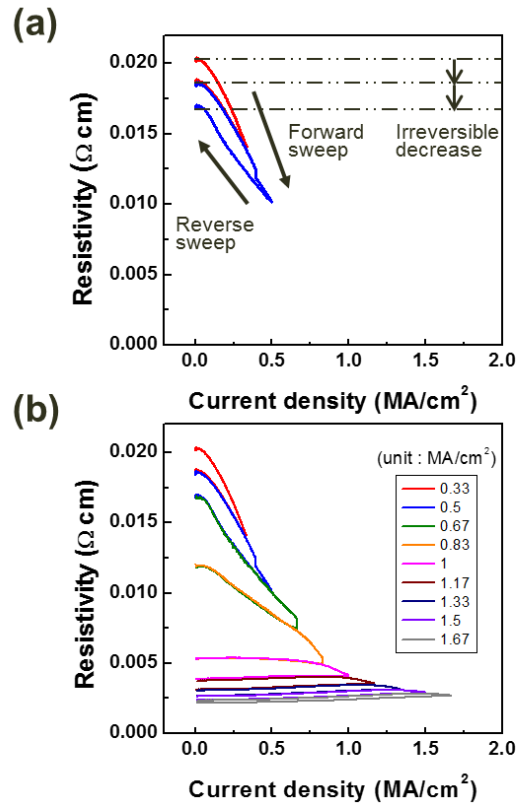


**Figure 5.1** Resistivity of  $\text{Ge}_2\text{Sb}_2\text{Te}_5$  for a current sweep using the double directional mode, with a sweep from zero to peak current and a return to zero, at room temperature for the 0.33 and 0.5  $\text{MA/cm}^2$  conditions. (b) Resistivity change for peak current densities ranging from 0.33 to 1.67  $\text{MA/cm}^2$  in increments of 0.17  $\text{MA/cm}^2$ .

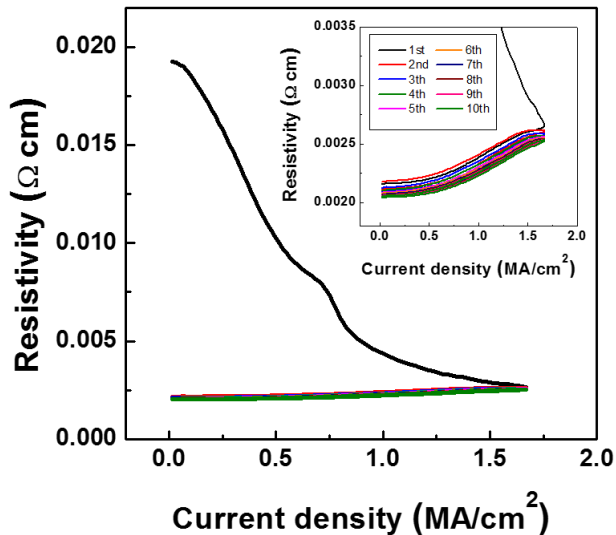


**Figure 5.2** Cyclic test for current sweep from 0 to 1.67 MA/cm<sup>2</sup> with a fixed peak-current-density of 1.67 MA/cm<sup>2</sup> at room temperature for Ge<sub>2</sub>Sb<sub>2</sub>Te<sub>5</sub>. The inset of **Figure 5.2** shows a resistivity during cyclic current sweep ranging from 0.0018 to 0.0035 Ωcm. An irreversible change in resistivity was completed during the first cycle of applied current.

### 5.3.2. TCR measurement of current-stressed $\text{Ge}_2\text{Sb}_2\text{Te}_5$

**Figure 5.3(a)** shows the resistivity of  $\text{Ge}_2\text{Sb}_2\text{Te}_5$  for temperatures from 30 to 90 °C after current stressing. A linear relationship between resistivity and temperature was observed, and their slopes decreased with increasing applied current. The slope of the resistivity and temperature provides the temperature coefficient of resistance (TCR), which is used to distinguish metallic (positive relationship) from insulating (negative relationship) behavior.<sup>39</sup> The TCR of 0.83-MA/cm<sup>2</sup>-stressed  $\text{Ge}_2\text{Sb}_2\text{Te}_5$  (yellow star) was  $-4.0 \times 10^4$  1/K, and the TCR of 1-MA/cm<sup>2</sup>-stressed  $\text{Ge}_2\text{Sb}_2\text{Te}_5$  (orange diamond) was  $6.7 \times 10^4$  1/K, as shown in **Figure 5.3(a)**.

The behavior of resistivity near 0 K is important to distinguish insulators from metals. We attempted to confirm the slope of temperature-resistance at a low temperature range by using three different samples: 0.67 MA/cm<sup>2</sup> current-stressed  $\text{Ge}_2\text{Sb}_2\text{Te}_5$  (insulating), 1 MA/cm<sup>2</sup> current-stressed  $\text{Ge}_2\text{Sb}_2\text{Te}_5$  (transient condition), and 1.5 MA/cm<sup>2</sup> current-stressed  $\text{Ge}_2\text{Sb}_2\text{Te}_5$  (metallic). Because of the limitation of our cooling system, the tendencies of the resistivity of  $\text{Ge}_2\text{Sb}_2\text{Te}_5$  and temperature were confirmed only up to 150 K. **Figure 5.3(b)** shows the resistivity of current-stressed  $\text{Ge}_2\text{Sb}_2\text{Te}_5$  for temperatures from 150 to 373 K. These results show that the behaviors of resistivity near room temperature have constant slopes up to 150 K, which is similar to the reported results of Ge-Sb-Te compounds.<sup>39,50</sup> Although the resistivity behavior near 0 K was not observed, the tendencies of the resistivity changes in the current-stressed GST were similar to annealed GST ( $\text{Ge}_2\text{Sb}_2\text{Te}_5$  with a current density below 1 MA/cm<sup>2</sup> is the same as insulating GST, and  $\text{Ge}_2\text{Sb}_2\text{Te}_5$  with a current density over 1 MA/cm<sup>2</sup> is the same as metallic GST). Therefore, current-stressed  $\text{Ge}_2\text{Sb}_2\text{Te}_5$  over 1 MA/cm<sup>2</sup>, which has a positive relationship between resistivity and temperature, is estimated to have a finite



resistivity value at 0 K. The exact confirmation of metallic behavior through an analysis near 0 K will be discussed in a future study.

**Figure 5.4** shows the resistivity slope as a function of the current density, which corresponds to the results in **Figure 5.1(b)**, and as a function of the temperature, which corresponds to the results in **Figure 5.3(a)**, according to the stress peak current density. The slopes of resistivity according to the current density during the reverse sweep and temperature are denoted as current slope and temperature slope, respectively. As shown in **Figure 5.4**, the behavior of the TCR was similar to the resistivity slope for the current density, which changed from negative to positive at the peak current density of  $1 \text{ MA/cm}^2$ . Because the resistivity change in the reverse sweep had a relationship with temperature, a reversible change in the resistivity under experienced conditions was affected by Joule heating. Therefore, the current-stressed  $\text{Ge}_2\text{Sb}_2\text{Te}_5$  was regarded to have displayed metallic behavior at current densities above  $1 \text{ MA/cm}^2$ .

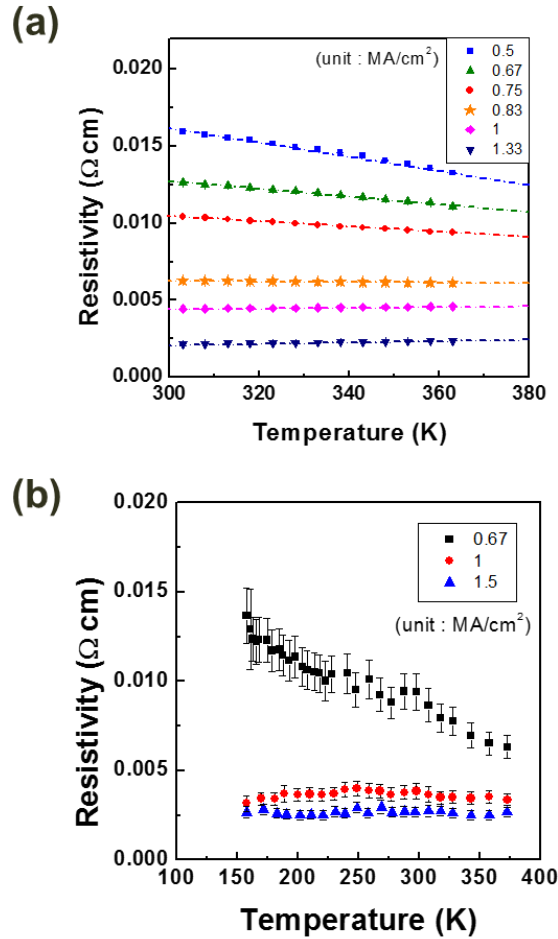


**Figure 5.3** (a) The resistivity of current-stressed  $\text{Ge}_2\text{Sb}_2\text{Te}_5$  from **Figure 5.1(b)** for temperatures ranging from 30 to 90 °C. The dotted lines are extrapolations whose slopes correspond to the temperature coefficient of resistance (TCR). (b) Resistivity of current-stressed  $\text{Ge}_2\text{Sb}_2\text{Te}_5$  for temperature ranging from 150 to 373 K. Conditions of current density were 0.67  $\text{MA/cm}^2$  (black square), 1  $\text{MA/cm}^2$  (red diamond), and 1.5  $\text{MA/cm}^2$  (blue triangle).

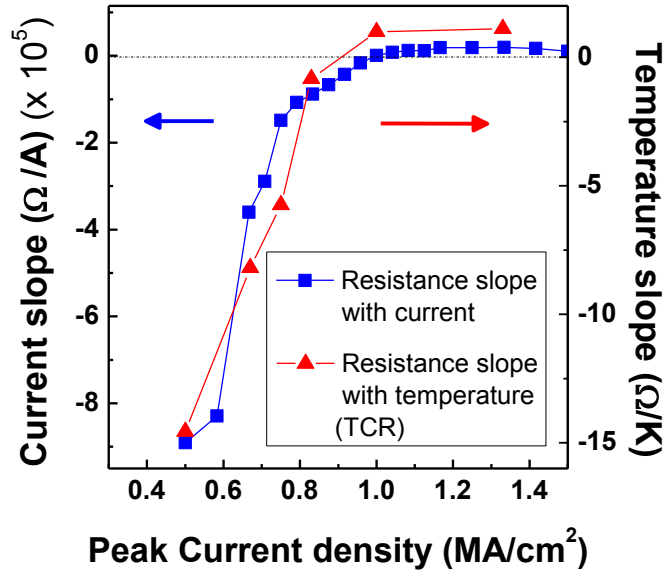


**Figure 5.4** Resistivity slope for current density and temperature according to the stress peak current density results from **Figure 5.1(b)** and **5.3(a)**, respectively. The behavior of the TCR in  $\text{Ge}_2\text{Sb}_2\text{Te}_5$  was similar to the resistivity slope for the current density, which changed from negative to positive at the peak current density of  $1 \text{ MA/cm}^2$ .

### 5.3.3. Complex effect of current and temperature in $\text{Ge}_2\text{Sb}_2\text{Te}_5$

**Figure 5.5** shows that the resistivity of  $\text{Ge}_2\text{Sb}_2\text{Te}_5$  depends on each current sweep under different temperature conditions, which are (a) room temperature, (b) 100 °C, and (c) 200 °C. **Figure 5.5(d)** illustrates how the final resistivity of  $\text{Ge}_2\text{Sb}_2\text{Te}_5$  depends on each current sweep, and **Figure 5.5(e)** shows that the slope of the resistivity depends on each current sweep for various temperatures, which are results of the current sweep at various temperatures, as referenced in **Figure 5.5(a)-(c)**. As the temperature increased, the starting point of the resistivity decreased, as depicted in **Figure 5.5(d)**. However, the resistivity for a current density over 0.7 MA/cm<sup>2</sup> showed the same results in the resistivity curve regardless of the temperature. Additionally, the sign of the resistivity slope changed from negative to positive at 1 MA/cm<sup>2</sup>, independent of the temperature, as shown in **Figure 5.5(e)**. This result implies that the resistivity of  $\text{Ge}_2\text{Sb}_2\text{Te}_5$  is only determined by the current density, regardless of the initial resistivity or external temperature.

The crystalline  $\text{Ge}_2\text{Sb}_2\text{Te}_5$  compounds had a fixed resistivity value depending on the applied current density, and the resistivity changes were irreversible. Therefore, once the initial resistivity was reduced by the temperature, the current density had no direct effect on the final resistivity until it reached the current density for the corresponding reduced resistivity. When the current density reached the corresponding resistivity, the resistivity followed the universal curve of  $\text{Ge}_2\text{Sb}_2\text{Te}_5$ , which is useful for a resistivity-based device because the resistivity can be controlled by an electric current.

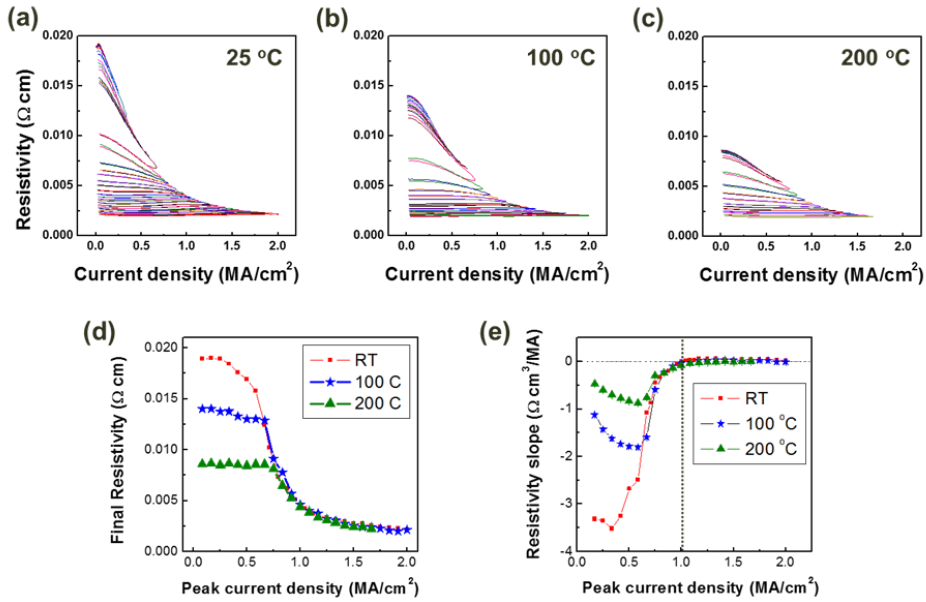


**Figure 5.5** (a)-(c) Resistivity of  $\text{Ge}_2\text{Sb}_2\text{Te}_5$  for peak-current densities ranging from  $0.17$  to  $2 \text{ MA/cm}^2$  in increments of  $0.08 \text{ MA/cm}^2$  at different temperatures which are (a) room temperature, (b)  $100^\circ\text{C}$ , and (c)  $200^\circ\text{C}$ , respectively. (d) Final resistivity and (e) slope of resistivity of  $\text{Ge}_2\text{Sb}_2\text{Te}_5$  according to peak current density at various temperature based on the results from (a)-(c).

## 5.4. Time-dependent behavior of $\text{Ge}_2\text{Sb}_2\text{Te}_5$

We investigated the influence of the current duration on the resistivity of  $\text{Ge}_2\text{Sb}_2\text{Te}_5$ , as shown in **Figure 5.6(a)**, to understand the kinetic properties of current-induced resistivity change in  $\text{Ge}_2\text{Sb}_2\text{Te}_5$ . The resistivity of  $\text{Ge}_2\text{Sb}_2\text{Te}_5$  decreased with the application of a current density, but the change only occurred during the early current stressing phase, similar to the results in **Figure 5.1(b)**. **Figure 5.6(b)** shows the initial and final resistivity values of  $\text{Ge}_2\text{Sb}_2\text{Te}_5$  with an electric current that was applied for 30 hours, according to the current density. As mentioned above, a current-induced resistivity change occurred during the first cycle of the current sweep, which indicates that an irreversible change in resistivity occurred within a few seconds. After this drastic change, the resistivity of  $\text{Ge}_2\text{Sb}_2\text{Te}_5$  remained unchanged for a long period, regardless of the current density.

We also investigated resistivity according to time annealing at various temperatures, as shown in **Figure 5.7(a)**, to compare this influence with that of electrical and thermal stress on changes in the resistivity of  $\text{Ge}_2\text{Sb}_2\text{Te}_5$ . The resistivity of  $\text{Ge}_2\text{Sb}_2\text{Te}_5$  under isothermal annealing decreased with temperature, and a continuous change was observed over a long period, as shown in **Figure 5.7(a)**. The saturated resistivity, or the time-independent point of resistivity, was inversely proportional to the ambient temperature. **Figure 5.7(b)** shows the initial and final resistivity values of  $\text{Ge}_2\text{Sb}_2\text{Te}_5$  (based on **Figure 5.7(a)**) according to the temperature. Unlike the results for an applied current, significant differences were observed between the initial and final resistivity values under annealed conditions, as shown in **Figure 5.7(b)**. These results show that the electric current has a kinetically fast effect on the resistivity compared to thermal stress, which involves a thermally activated change. Although electrical and thermal stress have different time-dependent behaviors,

they exert a similar influence on the resistivity of  $\text{Ge}_2\text{Sb}_2\text{Te}_5$  to reach a minimum resistivity state.

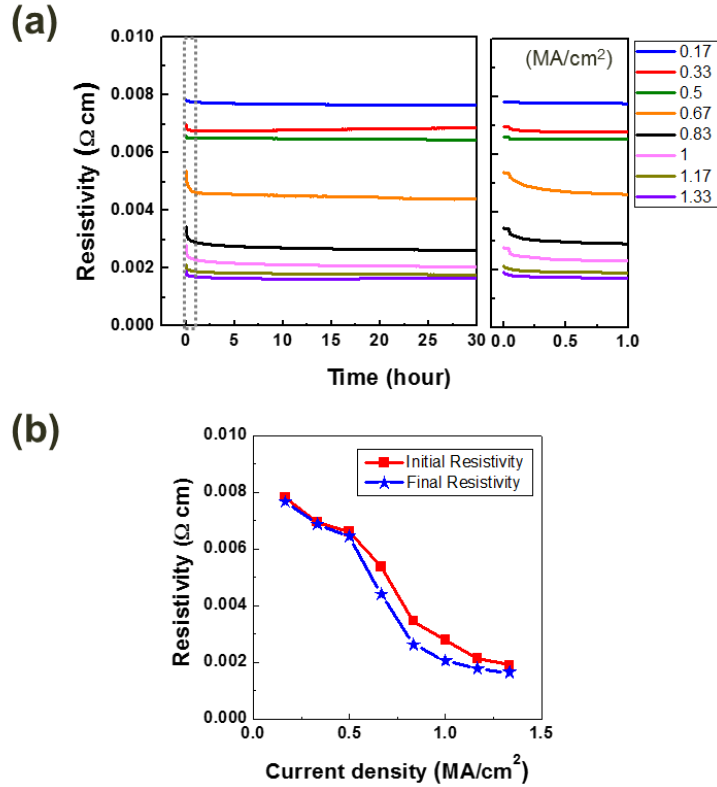


**Figure 5.6** (a) Resistivity change of  $\text{Ge}_2\text{Sb}_2\text{Te}_5$  according to the duration of applied current density, ranging from 0.17 to 1.33 MA/cm<sup>2</sup>, for 30 hours and its expansion (dotted box) from 0 to 1 hour. (b) Initial and final resistivities of  $\text{Ge}_2\text{Sb}_2\text{Te}_5$  according to the current density for the current-stressed condition result from (a).

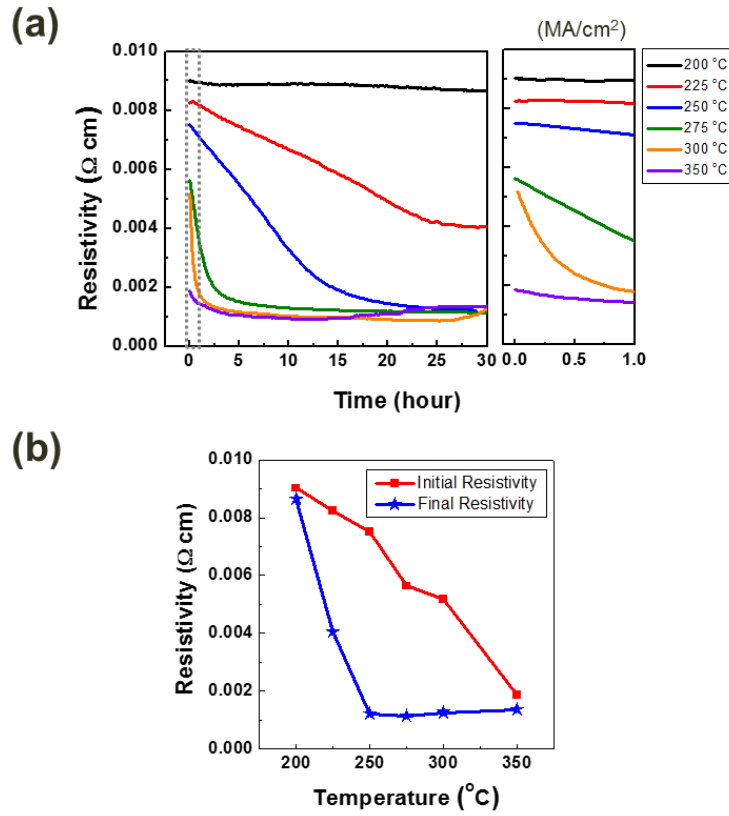


**Figure 5.7** (a) Resistivity change of  $\text{Ge}_2\text{Sb}_2\text{Te}_5$  according to the duration of applied temperature, ranging from 200 to 350  $^{\circ}\text{C}$ , for 30 hours and its expansion (dotted box) from 0 to 1 hour. (d) Initial and final resistivities of  $\text{Ge}_2\text{Sb}_2\text{Te}_5$  according to the ambient temperature for the isothermal annealing condition result from (c). The electric current has a kinetically fast effect on resistivity compared with thermal stress, which involves a thermally activated change.



## 5.5. Microstructural analysis of $\text{Ge}_2\text{Sb}_2\text{Te}_5$

### 5.5.1 Phase of current- and temperature-stressed $\text{Ge}_2\text{Sb}_2\text{Te}_5$

Microstructural analyses were conducted for a more detailed examination of the differences between electrical and thermal effects. According to **Figure 5.6** and **Figure 5.7**, the resistivity values from an electrical stress of  $1 \text{ MA/cm}^2$  and a thermal stress of  $250^\circ\text{C}$  were saturated and unchanged. The current-stressed sample for  $1 \text{ MA/cm}^2$  and the temperature-stressed sample for  $250^\circ\text{C}$  are denoted as the “current sample” and “temperature sample”, respectively.

First, a microstructural analysis of the initial sample, which was not applied with an electrical or thermal stress, is shown in **Figure 5.8**. The microstructure of the initial sample was in a polycrystalline state and the average grain size was approximately 20 nm, as indicated by the dotted line. Because of the polycrystalline state and small grain size, a ring-type diffraction pattern was observed, as shown in **Figure 5.8(b)**. According to the radii of the concentric circles, the crystalline phase of the current sample was confirmed as the face-centered cubic (FCC) phase of  $\text{Ge}_2\text{Sb}_2\text{Te}_5$ . This result is expected because the as-deposited  $\text{Ge}_2\text{Sb}_2\text{Te}_5$  was annealed at  $200^\circ\text{C}$  to transform the crystalline cubic phase.

**Figure 5.9** shows the microstructural image and diffraction pattern of a current and temperature sample of  $\text{Ge}_2\text{Sb}_2\text{Te}_5$ . As shown in **Figure 5.9(a)**, the microstructure of the current sample was in a polycrystalline state and the average grain size was approximately 20 nm, which is similar to the initial  $\text{Ge}_2\text{Sb}_2\text{Te}_5$ . The diffraction pattern was also the same as the initial  $\text{Ge}_2\text{Sb}_2\text{Te}_5$  to maintain a polycrystalline face-centered cubic (FCC) phase of  $\text{Ge}_2\text{Sb}_2\text{Te}_5$ . The calculated results of the diffraction pattern are displayed in **Table 5.1**. These results show that an electric current can reduce the resistivity by an order of magnitude when the microstructure is maintained in a cubic phase. Microstructural

analyses were conducted in various positions to represent the entire phase, and the results were independent of the position.

In contrast, large grains of more than 100 nm were observed in the temperature sample, as shown in **Figure 5.9(c)**. High temperatures increased the grain size of  $\text{Ge}_2\text{Sb}_2\text{Te}_5$ . **Figure 5.9(d)** shows the diffraction pattern for **Figure 5.9(c)**, which is a spot-type pattern because of the large grains. Based on the distance ( $3.05 \text{ \AA}$ ) and angle of the spots ( $87.5^\circ$ ), the crystalline plane of the temperature sample is determined to be in the (013) family, and the phase was confirmed as the hexagonal close packing (HCP) phase of  $\text{Ge}_2\text{Sb}_2\text{Te}_5$ . The plane indexes, whose zone axes were  $[-3 \ 3 \ 1]$ , are described in **Figure 5.10**. The initial sample, which was not stressed by a current or temperature, was not a fully crystalline phase but had a grain size of approximately 20 nm and was in the cubic phase of  $\text{Ge}_2\text{Sb}_2\text{Te}_5$ , similar to the current sample. Based on the standard phase of  $\text{Ge}_2\text{Sb}_2\text{Te}_5$  at room temperature, the only microstructural change in the current sample was crystallization. The temperature sample, however, had large grains and a different crystalline phase compared to the initial state. Interestingly, the current and temperature samples exhibited similar electrical resistivity values, although the cubic phase displayed an insulating behavior and the hexagonal phase displayed a metallic behavior. The current sample had a low resistivity, similar to the hexagonal phase, while maintaining the cubic phase. Therefore, crystalline  $\text{Ge}_2\text{Sb}_2\text{Te}_5$  possesses another primary factor for the determination of resistivity in addition to the phase.

**Table 5.1** Comparison between the calculated distance in **Figure 5.9(b)** and crystallographic distance in cubic phase of  $\text{Ge}_2\text{Sb}_2\text{Te}_5$ .

<b>(h k l)</b>	<b>d (Å)</b>	<b>Calculated distance (Å)</b>	<b>Error (%)</b>
<b>1 1 1</b>	3.481	3.477	0.1
<b>2 0 0</b>	3.050	3.037	- 0.7
<b>2 2 0</b>	2.131	2.143	- 0.5
<b>3 1 1</b>	1.818	1.869	- 2.8
<b>2 2 2</b>	1.741	1.758	- 0.8
<b>4 0 0</b>	1.507	1.522	- 1.0

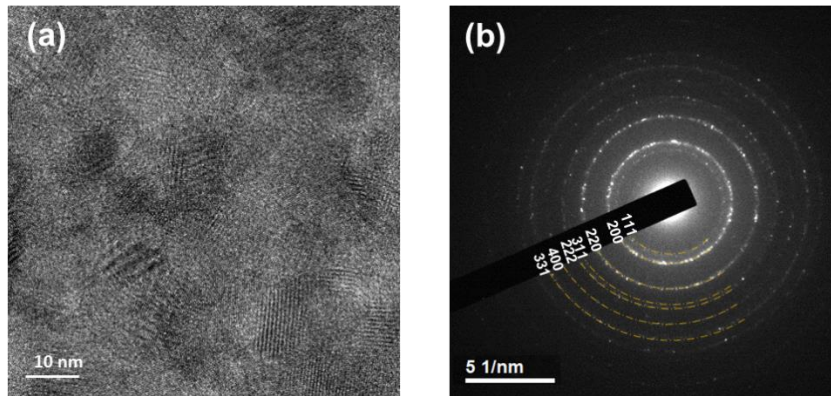


**Figure 5.8** (a) TEM image and (b) diffraction pattern of the initial  $\text{Ge}_2\text{Sb}_2\text{Te}_5$  sample, which was not applied by thermal and electrical stress. The microstructure of the current sample was in a polycrystalline cubic phase and the average grain size was approximately 20 nm.

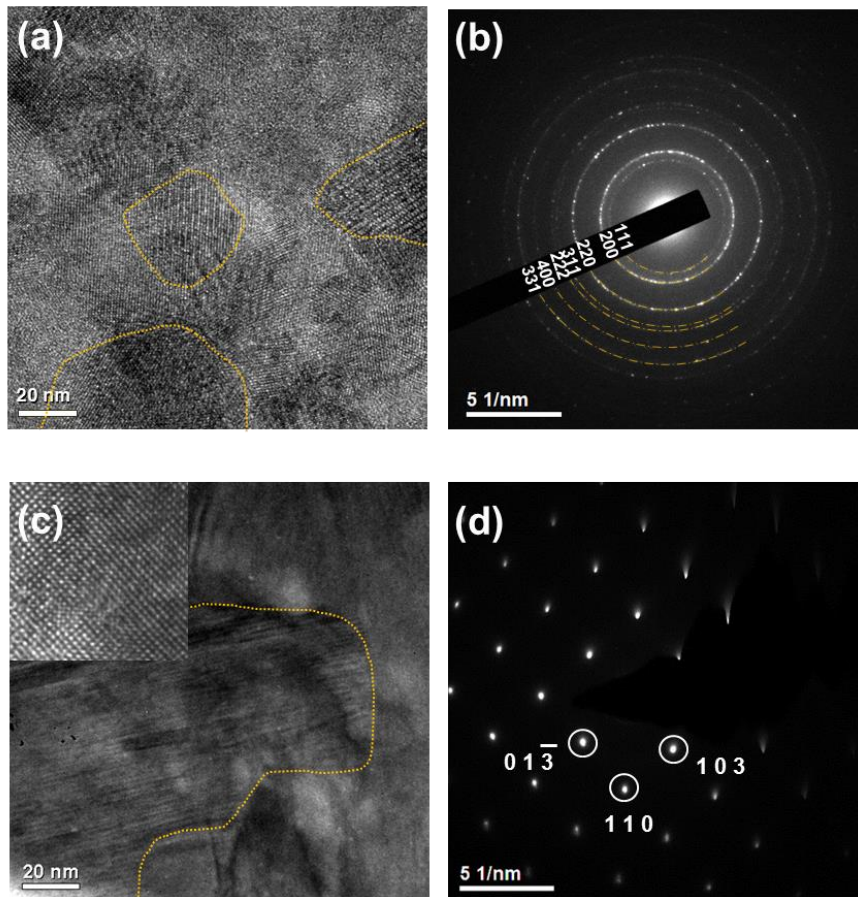


**Figure 5.9** (a) TEM image and (b) diffraction pattern of the current-stressed  $\text{Ge}_2\text{Sb}_2\text{Te}_5$  sample (Current sample:  $1 \text{ MA/cm}^2$  condition). The yellow dotted lines indicate the grain boundary. The microstructure of the current sample was in a polycrystalline cubic phase and the average grain size was approximately 20 nm. (c) TEM image and (d) diffraction pattern of the temperature-stressed  $\text{Ge}_2\text{Sb}_2\text{Te}_5$  sample (temperature sample:  $250^\circ\text{C}$  condition). An HRTEM image of a single grain is displayed in the inset of (c). Large grains of more than 100 nm in a hexagonal phase were observed in the temperature sample.

(a)

2 $\theta$	d(Å)	Intensity	h	k	l
25.5684	3.481020	136	1	1	1
29.6079	3.014650	999	2	0	0
42.3661	2.131680	635	2	2	0
50.1393	1.817900	67	3	1	1
52.5347	1.740510	189	2	2	2
61.4644	1.507320	75	4	0	0
67.6799	1.383220	27	3	3	1
69.6880	1.348190	176	4	2	0

(b)

2 $\theta$	d(Å)	Intensity	h	k	l
5.2062	16.960000	160	0	0	1
10.4233	8.480000	1	0	0	2
15.6621	5.653330	1	0	0	3
20.9341	4.240000	3	0	0	4
24.4524	3.637310	17	1	0	0
25.0173	3.556440	9	0	1	1
26.2513	3.392000	16	0	0	5
26.6449	3.342780	19	1	0	2
29.1702	3.058880	999	0	1	3
31.6267	2.826670	11	0	0	6
32.4032	2.760680	66	0	1	4
36.1798	2.480700	10	1	0	5
37.0746	2.422860	3	0	0	7
40.3780	2.231930	297	1	0	6
42.6109	2.120000	4	0	0	8
43.0368	2.100000	324	1	1	0

**Figure 5.10** JCPDS database of (a) face-centered cubic phase and (b) hexagonal close-packed phase of  $\text{Ge}_2\text{Sb}_2\text{Te}_5$ .

### **5.5.2. Gradual decrease in resistivity during thermal annealing**

**Figure 5.11** shows the XRD results for  $\text{Ge}_2\text{Sb}_2\text{Te}_5$  under different annealing conditions. The HCP transition temperature is generally near 350 °C: <sup>27</sup> the XRD results at 350 °C are shown in **Figure 5.11**. However, even at 250 °C, the hexagonal phase was transformed by long-term annealing. Because a high level of energy is required to generate a new phase, phase transitions are kinetically slow processes and are sensitive to the temperature. Therefore, the continuous decrease in the resistivity of  $\text{Ge}_2\text{Sb}_2\text{Te}_5$  during isothermal annealing, as shown in **Figure 5.7(a)**, is closely related to phase transformation.

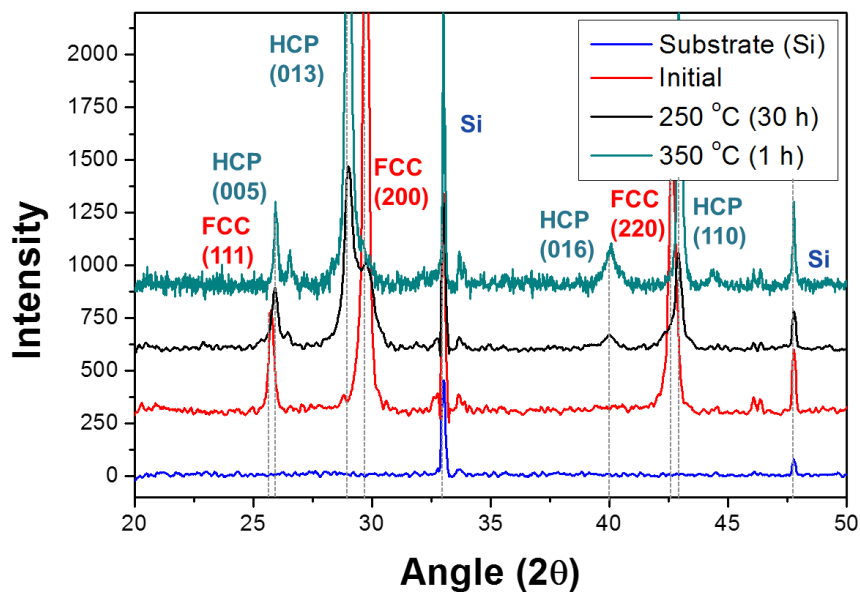


**Figure 5.11** XRD result of  $\text{Ge}_2\text{Sb}_2\text{Te}_5$  for different annealing temperatures: Si substrate (blue), pre-annealed  $\text{Ge}_2\text{Sb}_2\text{Te}_5$  (red),  $\text{Ge}_2\text{Sb}_2\text{Te}_5$  annealed at 250 °C for 30 hours (black), and  $\text{Ge}_2\text{Sb}_2\text{Te}_5$  annealed at 350 °C for 1 hour (green).



## 5.6. Comparison between $\text{Ge}_2\text{Sb}_2\text{Te}_5$ and $\text{GeSb}_4\text{Te}_7$

Because crystalline  $\text{Ge}_2\text{Sb}_2\text{Te}_5$  has a high number of intrinsic vacancies, the electrical properties of  $\text{Ge}_2\text{Sb}_2\text{Te}_5$  are governed by disorder between the constitutional atoms and vacancies.<sup>39</sup> As mentioned in **Section 2.1.2**, a rock-salt structure consists of two interpenetrating FCC sub-lattices; one sub-lattice is located at the origin and the other is located at (0.25, 0.25, 0.25). The volume of intrinsic vacancies depends on the composition because Te atoms perfectly occupy one FCC sub-lattice while Ge and Sb atoms randomly occupy the other FCC sub-lattice. **Table 5.2** shows the fraction of vacancies according to the composition of the Ge-Sb-Te compound. Similar experiments were conducted for  $\text{GeSb}_4\text{Te}_7$ , which has more vacancies than  $\text{Ge}_2\text{Sb}_2\text{Te}_5$ , to investigate the effect of intrinsic vacancies.<sup>18, 70</sup>

**Figure 5.12(a)** shows the electrical resistivity of  $\text{GeSb}_4\text{Te}_7$  after a current sweep with an increasing peak current density from 0.17 and 1.67 MA/cm<sup>2</sup> in 0.17 MA/cm<sup>2</sup> increments at room temperature. As shown in **Figure 5.12(a)**, the resistivity of  $\text{GeSb}_4\text{Te}_7$  decreased with increasing current density, and an irreversible change in resistivity was observed, which are similar to the results for  $\text{Ge}_2\text{Sb}_2\text{Te}_5$  as shown in **Figure 5.1(b)**. **Figure 5.12(b)** shows the final resistivity results for  $\text{Ge}_2\text{Sb}_2\text{Te}_5$  from **Figure 5.1(b)** and the  $\text{GeSb}_4\text{Te}_7$  results from **Figure 5.12(a)** according to the peak current density at room temperature. Although the resistivity of  $\text{Ge}_2\text{Sb}_2\text{Te}_5$  and  $\text{GeSb}_4\text{Te}_7$  decreased with the peak current density, the degree and speed of the decline in  $\text{GeSb}_4\text{Te}_7$  was much higher than that in  $\text{Ge}_2\text{Sb}_2\text{Te}_5$ . These results indicate that electric currents have a similar effect on  $\text{GeSb}_4\text{Te}_7$ , but  $\text{GeSb}_4\text{Te}_7$  is much more sensitive to electric currents than  $\text{Ge}_2\text{Sb}_2\text{Te}_5$ .

**Figure 5.13(a)** shows the resistivity of  $\text{GeSb}_4\text{Te}_7$  at temperatures from 30 to 90 °C after current stressing. The slopes of resistivity and temperature, or the TCR, increased with the

peak current density from negative to near zero. The slopes of the resistivity with current density and temperature, according to the stress current density for  $\text{Ge}_2\text{Sb}_2\text{Te}_5$  and  $\text{GeSb}_4\text{Te}_7$  are shown in **Figure 5.13(b)**, which correspond to the results for  $\text{Ge}_2\text{Sb}_2\text{Te}_5$  (**Figure 5.1(b)** and **Figure 5.3(a)**) and  $\text{GeSb}_4\text{Te}_7$  (**Figure 5.12(a)** and **Figure 5.13(a)**). As shown in **Figure 5.13(b)**, the behavior of the TCR for  $\text{Ge}_2\text{Sb}_2\text{Te}_5$  was similar to the resistivity slope for the current density, which changed from negative to positive at the peak current density of  $1 \text{ MA/cm}^2$ . Although the current and temperature slopes for  $\text{GeSb}_4\text{Te}_7$  have some differences, a similar slope change that approached zero was observed. Moreover, the current and temperature slopes for  $0.33\text{-MA/cm}^2$ -stressed  $\text{GeSb}_4\text{Te}_7$  were extremely changed compared to  $0.17\text{-MA/cm}^2$ -stressed  $\text{GeSb}_4\text{Te}_7$ , even though the difference was only  $0.17 \text{ MA/cm}^2$ . These results indicate that the current-induced resistivity change was more effective in  $\text{GeSb}_4\text{Te}_7$  than in  $\text{Ge}_2\text{Sb}_2\text{Te}_5$ , which depends on the intrinsic vacancy of materials.

Furthermore, **Figure 5.14** illustrates how the resistivity values of  $\text{GeSb}_4\text{Te}_7$  (**Figure 5.14(a)-(c)**) depend on each current sweep at various temperatures, namely, room temperature,  $100^\circ\text{C}$ , and  $200^\circ\text{C}$ . As the temperature increased, the starting point of the resistivity decreased in  $\text{GeSb}_4\text{Te}_7$  because additional thermal energy decreases the resistivity. However, resistivity at high temperatures eventually follows the same resistivity curve of that at room temperature over a certain current density, which is the corresponding point of resistivity. The resistivity of  $\text{GeSb}_4\text{Te}_7$  showed a drastic decrease in current and temperature compared to  $\text{Ge}_2\text{Sb}_2\text{Te}_5$ . The resistivity of  $\text{GeSb}_4\text{Te}_7$  was even saturated to the minimum value at  $200^\circ\text{C}$ . These results indicate that the resistivity of  $\text{GeSb}_4\text{Te}_7$  is much more sensitive to external stimuli, such as electric current and temperature, compared to  $\text{Ge}_2\text{Sb}_2\text{Te}_5$ .

**Table 5.2** Fraction of vacancies in the pseudo-binary compound of  $(\text{GeTe})_x\text{-(Sb}_2\text{Te}_3)_{1-x}$  according to  $x$ .

Compound	x	Fraction of vacancy (Ge/Sb site)	Fraction of vacancy (Entire)
<b>GeSb<sub>4</sub>Te<sub>7</sub></b>	0.33	28.6 %	14.7 %
<b>GeSb<sub>2</sub>Te<sub>4</sub></b>	0.5	25 %	12.5 %
<b>Ge<sub>2</sub>Sb<sub>2</sub>Te<sub>5</sub></b>	0.67	20 %	10 %
<b>GeTe</b>	1	0 %	0 %

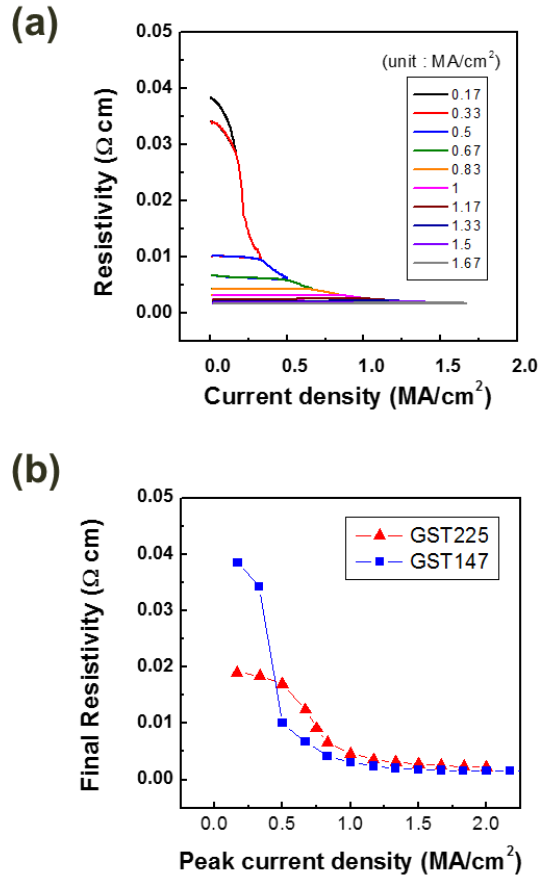


**Figure 5.12** (a) Resistivity change of  $\text{GeSb}_4\text{Te}_7$  with current densities for peak current densities ranging from 0.17 to 1.67  $\text{MA}/\text{cm}^2$  in increments of 0.17  $\text{MA}/\text{cm}^2$  at room temperature. (b) Final resistivity of  $\text{Ge}_2\text{Sb}_2\text{Te}_5$  and  $\text{GeSb}_4\text{Te}_7$  according to peak current density at room temperature (results from **Figure 5.1(b)** and **Figure 5.12(a)**, respectively).

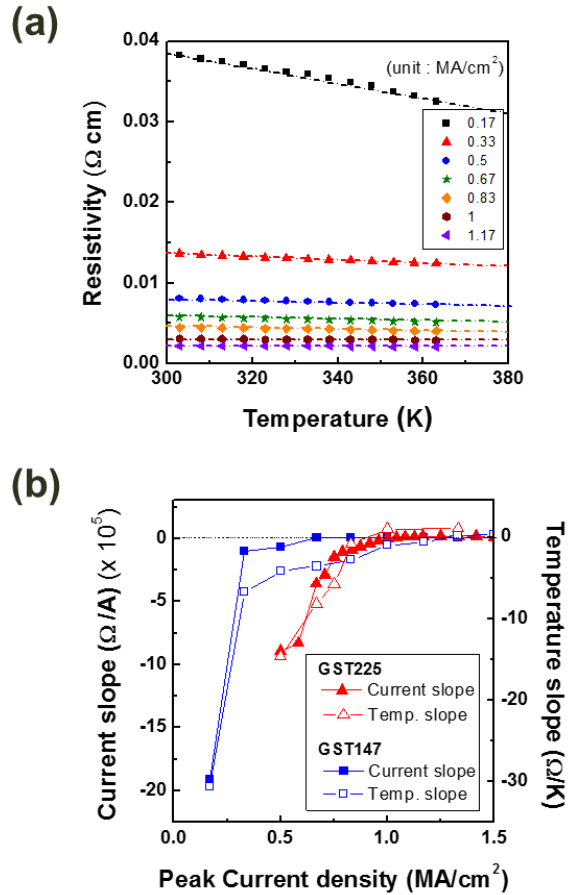


**Figure 5.13** (a) The resistivity of current-stressed  $\text{GeSb}_4\text{Te}_7$  for temperatures ranging from 30 to 90  $^\circ\text{C}$ . The dotted lines are extrapolations whose slopes correspond to the TCR. (b) Resistivity slope of  $\text{Ge}_2\text{Sb}_2\text{Te}_5$  and  $\text{GeSb}_4\text{Te}_7$  for current density and temperature according to the stressed-peak-current-density results for  $\text{Ge}_2\text{Sb}_2\text{Te}_5$  (Figure 5.1(b) and Figure 5.3(a)) and  $\text{GeSb}_4\text{Te}_7$  (Figure 5.12(a) and Figure 5.13(a)).

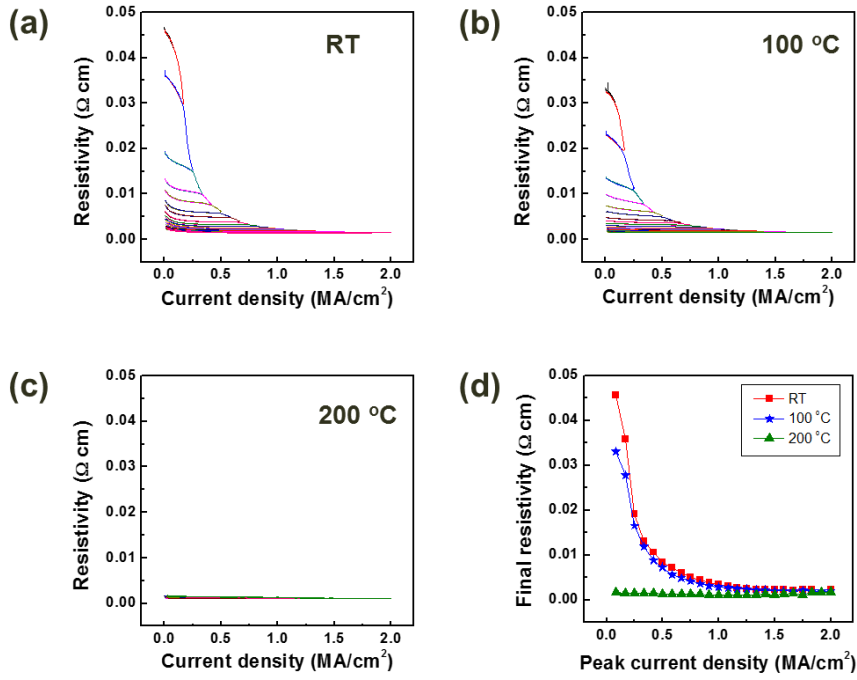


**Figure 5.14** (a)-(c) Resistivity change of GeSb<sub>4</sub>Te<sub>7</sub> for peak-current-densities ranging from 0.17 to 2 MA/cm<sup>2</sup> in increments of 0.08 MA/cm<sup>2</sup> at different temperatures: (a) room temperature, (b) 100 °C, and (c) 200 °C. (d) Final resistivity of GeSb<sub>4</sub>Te<sub>7</sub> according to the peak-current-density at various temperatures, based on the results from (a)-(c).

## **5.7. Role of electric current in vacancy rearrangement**

W. Zhang et al. calculated the total energy per atom for cubic and hexagonal Ge-Sb-Te compounds with respect to vacancy ordering.<sup>48</sup> The rearrangement of vacancies affects the degree of disorder and creates a vacancy plane in both the cubic and hexagonal phases, the latter of which is the most stable state. However, the phase transition from a cubic to hexagonal phase is a high priority before the vacancy planes can be completely formed.<sup>39</sup> Therefore, Ge<sub>2</sub>Sb<sub>2</sub>Te<sub>5</sub> has a low resistivity in the hexagonal phase, which agrees with our results for the temperature sample, as shown in **Figure 5.9(d)**. Surprisingly, the current-stressed Ge<sub>2</sub>Sb<sub>2</sub>Te<sub>5</sub> has a low resistivity, similar to the hexagonal phase, while maintaining a cubic phase. An applied current can migrate atoms by momentum transfer from the charge carriers, which is known as electromigration.<sup>15</sup> Vacancy rearrangement is not triggered by electrical currents because the process is thermodynamically spontaneous.<sup>39</sup>

A comparison between AC and DC may explain vacancy migration. Decrease in resistance under an electric current were only affected by DC as shown in **Figure 5.15**. Because the joule heating of AC and DC should produce the same effect, this result indicates that the decreases in resistance related to bias dependence during current stressing. Cumulative migration changes the resistance. No reason can explain the ordering of vacancies through electric currents because vacancy rearrangement is a thermodynamically spontaneous process.<sup>48</sup> The role of electric currents is a kinetic factor that accelerates vacancy rearrangement. Although the driving force of migration is too low to generate a massive flow of atoms for sub-MA/cm<sup>2</sup> current densities, vacancy rearrangements can be easily promoted by electromigration. Therefore, both vacancy rearrangements and phase transitions involve atomic arrangement processes. Phase transitions, however, require more energy to generate a new phase compared to vacancy

rearrangements because phase transitions are accompanied by a global change in atoms. A schematic diagram of the energy state according to vacancy rearrangement in the cubic and hexagonal phases of  $\text{Ge}_2\text{Sb}_2\text{Te}_5$  is described in **Figure 5.16**.

Because the  $\text{Ge}_2\text{Sb}_2\text{Te}_5$  line in our experiment was directly patterned on bulk Si, any generated heat spread easily because of the high thermal conductivity and heat capacity of Si. Furthermore, the resistivity of  $\text{Ge}_2\text{Sb}_2\text{Te}_5$  was independent of the frequency and voltage under an alternating current (AC), unlike under a direct current (DC) as shown in **Figure 5.15**. Because the joule heating of AC and DC should produce the same effect, this result indicates that the resistivity decrease is related to bias dependence during current stressing. Therefore, a current can accelerate vacancy rearrangements without a phase transition.



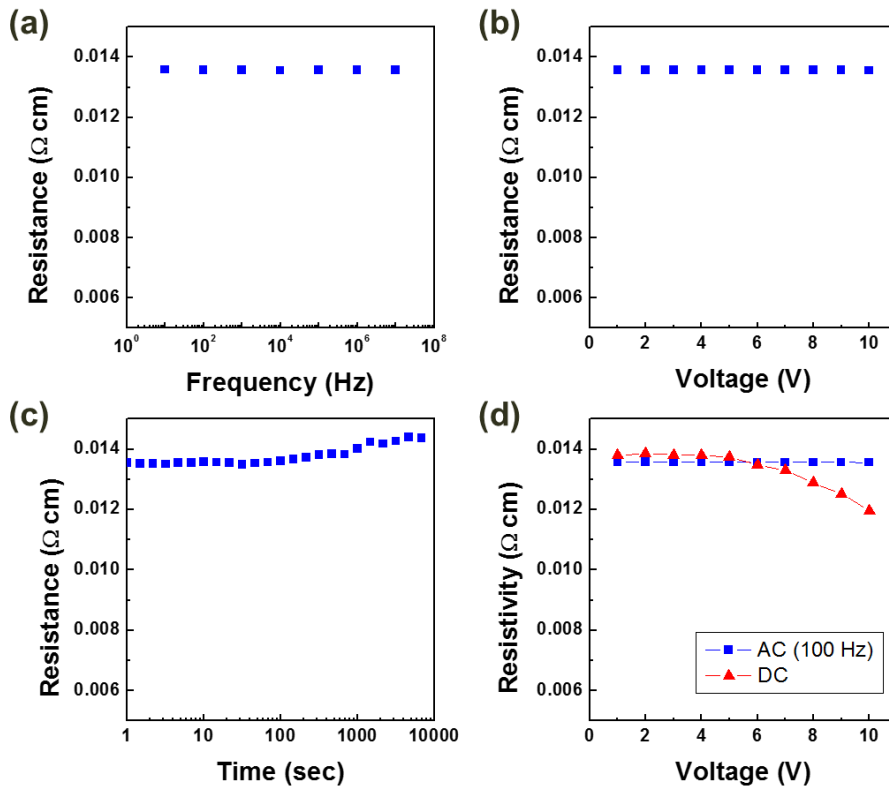


**Figure 5.15** Resistivity of  $\text{Ge}_2\text{Sb}_2\text{Te}_5$  affected by alternating current (AC) and direct current (DC). (a) Resistivity of  $\text{Ge}_2\text{Sb}_2\text{Te}_5$  according to AC frequency from  $10^2$  to  $10^7$  Hz with 1 sec of duration time and 10 V of voltage. (b) Resistivity of  $\text{Ge}_2\text{Sb}_2\text{Te}_5$  according to AC voltage from 1 to 10 V with 1 sec of duration time and 100 Hz of frequency. (c) Resistivity of  $\text{Ge}_2\text{Sb}_2\text{Te}_5$  according to AC time from 0 to 3 hours with voltage of 10 V and frequency of 100 Hz. (d) Resistivity of  $\text{Ge}_2\text{Sb}_2\text{Te}_5$  according to DC and 100 Hz of AC from 1 to 10 V with 1 sec of duration time.

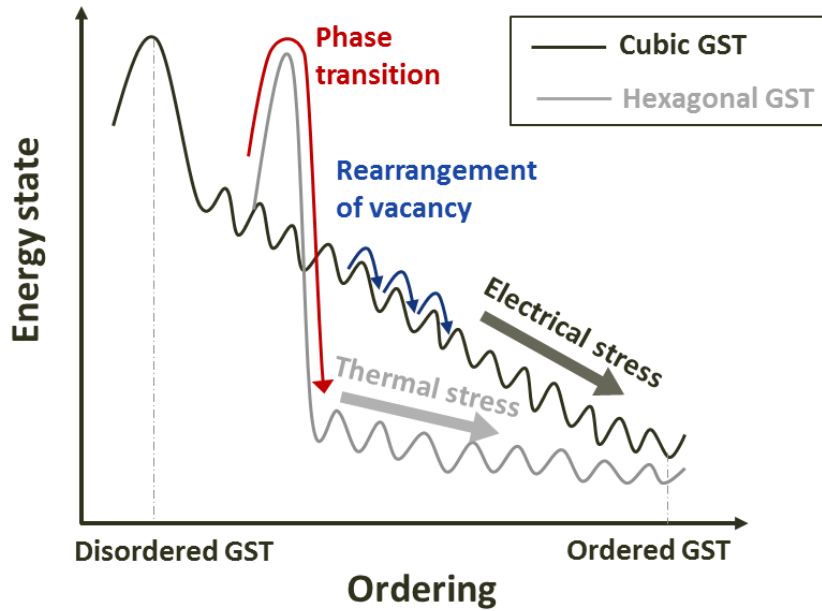


**Figure 5.16** The schematic diagram of the energy states according to the vacancy rearrangement in the cubic and hexagonal phases of Ge-Sb-Te compound. The energy state decreases with vacancy ordering, which is a stable state. The energy barrier for the phase transition from the cubic to the hexagonal phase is much higher than the energy barrier for the rearrangement of vacancies.

## **5.8. Summary**

In summary, we investigated the resistivity of  $\text{Ge}_2\text{Sb}_2\text{Te}_5$  and  $\text{GeSb}_4\text{Te}_7$  under an applied electric current for a range of temperatures. The resistivity is determined by the current density, regardless of the initial resistivity. Without a phase transition, the minimum resistivity can be achieved kinetically quickly by applying a current density, which differs significantly from thermal annealing. This phenomenon depends on the initial vacancy of the materials. This work provides a new pathway for promoting vacancy rearrangements by using an electric current and deepens our understanding of the material physics of phase-change materials.

## CHAPTER 6

# Divergence of failure mechanisms with current and temperature in crystalline chalcogenide

### 6.1. Introduction

Current-induced changes in crystalline phases of  $\text{Ge}_2\text{Sb}_2\text{Te}_5$  have been described in **Chapter 4** and **Chapter 5**. As mentioned in **Chapter 4**, the failure mechanism of  $\text{Ge}_2\text{Sb}_2\text{Te}_5$  changes with the current density. Depending on the applied current density, the behaviors of these changes fall into three main classes. However, this phenomenon has a close relationship with both the current density and temperature. In this chapter, we describe the divergence of mechanisms in chalcogenide materials, including  $\text{Ge}_2\text{Sb}_2\text{Te}_5$  and  $\text{Bi}_2\text{Te}_3$ , with electric current and ambient temperature. Because electric currents create a thermal effect from Joule heating, separating electrical and thermal effects from current-induced degradation is difficult. Thus, we observed the differences in the mechanisms by changing the ambient temperature to confirm the role of the temperature. Furthermore, a mechanism map is proposed from the behavioral differences according to the external conditions, which can provide guidelines for device design.

## **6.2. Experiments**

Line-shaped samples, whose measurements were 20  $\mu\text{m}$  in length, 2  $\mu\text{m}$  in width and 300 nm in thickness, were employed to study the mechanism differences in crystalline chalcogenide with current and temperature, as described in **Chapter 3**.  $\text{Bi}_2\text{Te}_3$  and  $\text{Bi}_{35}\text{Te}_{65}$ , which are Te-rich compositions compared to intermetallic  $\text{Bi}_2\text{Te}_3$ , and  $\text{Ge}_2\text{Sb}_2\text{Te}_5$  were chosen to confirm the effect of stoichiometry on the failure mechanism. Because the as-deposited chalcogenide films were in the amorphous phase, the films were annealed for 1 hour at 200  $^{\circ}\text{C}$  to crystallize the initial amorphous phase into a crystalline phase. The initial  $\text{Ge}_2\text{Sb}_2\text{Te}_5$  was in a cubic phase before the current stressing.

A direct current (DC) stress from 0.17 to 1.83  $\text{MA}/\text{cm}^2$  was applied, and the ambient temperature was changed from room temperature to 200  $^{\circ}\text{C}$  by using a package-leveled EM tester (Qualitau MIRA). Failure morphologies were observed via scanning electron microscopy (SEM, Hitachi SU70) and transmission electron microscopy (TEM, Technai F20).

## **6.3. Limitations of the mechanism map for $\text{Ge}_2\text{Sb}_2\text{Te}_5$**

**Figure 6.1** shows the resistance changes with time according to the current density and ambient temperature. The initial resistance of  $\text{Ge}_2\text{Sb}_2\text{Te}_5$  was approximately 3000  $\Omega$  and the phase was the cubic phase of  $\text{Ge}_2\text{Sb}_2\text{Te}_5$ . The resistance of  $\text{Ge}_2\text{Sb}_2\text{Te}_5$  at the starting time commonly decreases with current density. However, gradual decreases

and increases along with constant behavior in the resistance of  $\text{Ge}_2\text{Sb}_2\text{Te}_5$  were observed at different current and temperature conditions. As mentioned in **Section 4.3**, the criteria for a mechanism include the behavior of the resistance and morphological changes. At a high current density, the resistance of  $\text{Ge}_2\text{Sb}_2\text{Te}_5$  rapidly increased within a minute, which resulted in catastrophic failure. Micro-scale agglomerated voids were observed under these conditions. This phenomenon is melting from Joule heating, which is denoted as “abrupt failure”. The resistance of  $\text{Ge}_2\text{Sb}_2\text{Te}_5$  gradually increased for tens of hours and nano-scale voids formed under an intermediate current density. Voids were generated by defect-induced melting, which continuously degraded the conductivity of  $\text{Ge}_2\text{Sb}_2\text{Te}_5$ , as described in **Chapter 4**. This phenomenon is denoted as “gradual failure”. Although no morphological changes occurred under at low current density, the resistance of  $\text{Ge}_2\text{Sb}_2\text{Te}_5$  decreased with current density. This phenomenon originates from vacancy rearrangement in the Ge-Sb-Te system, which is described in **Chapter 5**. Because electrical failure does not occur under a low current despite the resistance change, this phenomenon is denoted as “no failure”.

However, the behavior of the resistance and the morphology are inappropriate criteria for examining the mechanisms in  $\text{Ge}_2\text{Sb}_2\text{Te}_5$  because the factors that can increase and decrease the resistance operate at the same time. **Figure 6.2** shows an SEM image of the  $\text{Ge}_2\text{Sb}_2\text{Te}_5$  line after current stressing for 30 hours at 30 °C, which is the result from the 30 °C test in **Figure 6.1**. Voids are observed under a current density over  $1.17 \text{ MA/cm}^2$ , and the melting of the  $\text{Ge}_2\text{Sb}_2\text{Te}_5$  line is observed over  $1.83 \text{ MA/cm}^2$ . Based on the morphological behavior, current densities below  $1.17 \text{ MA/cm}^2$  are labeled “no failure”, current densities from  $1.17$  to  $1.67 \text{ MA/cm}^2$  are labeled “gradual failure”, and current densities over  $1.83 \text{ MA/cm}^2$  are labeled “abrupt failure”. On the other hand, the resistance initially decreases with the current density,

while time-dependent changes are not observed for a current density below 1.67 MA/cm<sup>2</sup>. This phenomenon is determined to be “no failure” based on the resistance criteria. For example, the resistance of Ge<sub>2</sub>Sb<sub>2</sub>Te<sub>5</sub> when applied with a 1.17 MA/cm<sup>2</sup> current density at 30 °C shows constant behavior over 30 hours, while voids were generated under these conditions. Therefore, the factors that influenced the degradation in Ge<sub>2</sub>Sb<sub>2</sub>Te<sub>5</sub> were confounded and must be classified. **Figure 6.3** shows the mechanism map of Ge<sub>2</sub>Sb<sub>2</sub>Te<sub>5</sub> according to the current density and temperature based only on the morphological behavior.

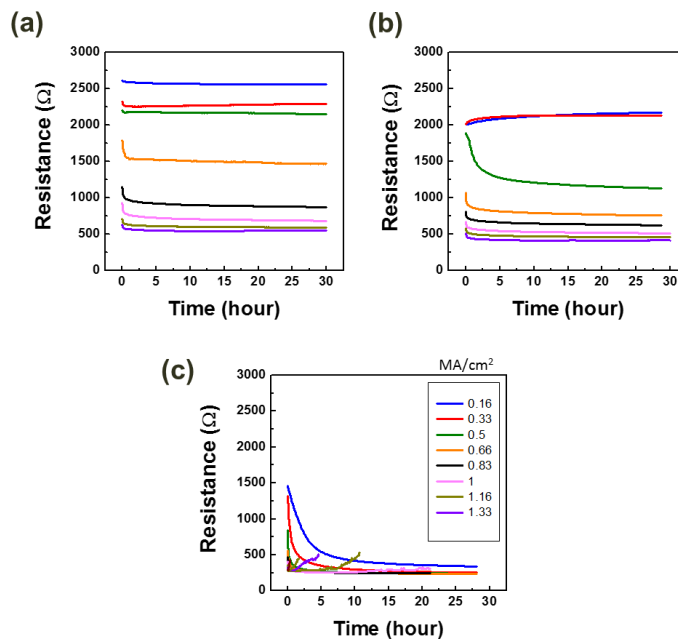


**Figure 6.1** Resistivity change of Ge<sub>2</sub>Sb<sub>2</sub>Te<sub>5</sub> according to the duration of applied current density, ranging from 0.17 to 1.33 MA/cm<sup>2</sup>, for 30 hours at the different ambient temperature: (a) room temperature, (b) 100 °C, and (c) 200 °C



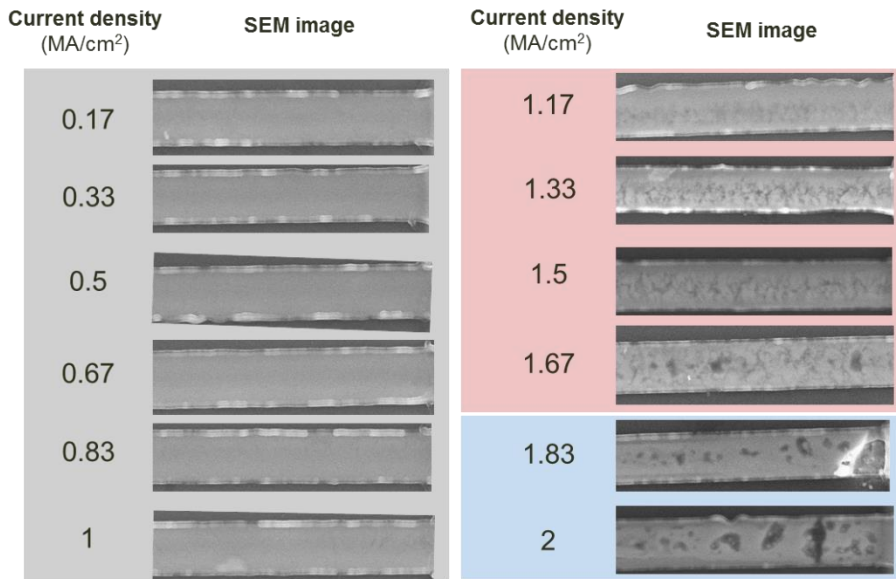


**Figure 6.2** SEM image of Ge<sub>2</sub>Sb<sub>2</sub>Te<sub>5</sub> line after current stressing test for 30 hours at room temperature, which are shown in **Figure 6.1(a)**. Background color means the group of failure behavior based on the morphological image. Current density below 1.17 MA/cm<sup>2</sup> is determined to “no failure” (gray), current density ranged from 1.17 to 1.67 MA/cm<sup>2</sup> is determined to “gradual failure” (red), and current density over 1.83 MA/cm<sup>2</sup> is determined to “abrupt failure” (blue).

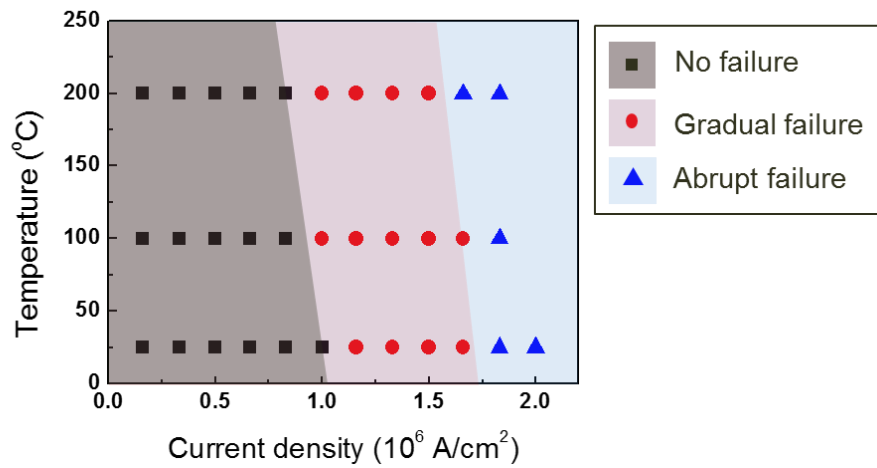


**Figure 6.3** Mechanism map of  $\text{Ge}_2\text{Sb}_2\text{Te}_5$  according to current density and temperature based only on the morphological behavior. All solid point are experiment results and failure mechanisms are expressed by background color. Black square shows “no failure”, red circle shows “gradual failure”, and blue triangle shows “abrupt failure”.

## 6.4. Mechanism map for chalcogenide materials

### 6.4.1. Resistivity behavior in ternary and binary chalcogenide

**Figure 6.4** shows the change in resistance with  $0.33 \text{ MA/cm}^2$  of current stressing over 30 hours in various Te-based chalcogenide materials, including  $\text{Bi}_2\text{Te}_3$ ,  $\text{Sb}_2\text{Te}_3$ ,  $\text{GeTe}$ , and  $\text{Ge}_2\text{Sb}_2\text{Te}_5$ . All the materials were fabricated to a line-shaped structure, and an electric current was applied by using a package-level tester. The relative resistance in **Figure 6.4** means that the resistance value was divided by the initial resistance of each material. According to the results, only the resistance of  $\text{Ge}_2\text{Sb}_2\text{Te}_5$  changed, with a huge and consistent reduction over 30 hours, while the other materials, i.e.,  $\text{Bi}_2\text{Te}_3$ ,  $\text{Sb}_2\text{Te}_3$ , and  $\text{GeTe}$ , remained at their initial resistance values. This result is also shown in **Figure 6.1**.

Crystalline  $\text{Ge}_2\text{Sb}_2\text{Te}_5$  has two types of structures, which are cubic and hexagonal, as mentioned in **Section 2.1**. Although the stable state of crystalline  $\text{Ge}_2\text{Sb}_2\text{Te}_5$  is the hexagonal phase, the cubic phase of  $\text{Ge}_2\text{Sb}_2\text{Te}_5$ , which is a metastable state of crystalline  $\text{Ge}_2\text{Sb}_2\text{Te}_5$ , exists under low temperature. Furthermore, crystalline  $\text{Ge}_2\text{Sb}_2\text{Te}_5$  has a high fraction of structural vacancies. The arrangement of vacancies affects the degree of disorder and the band structure, as mentioned in **Chapter 5**. The gradual decrease in the resistance of crystalline  $\text{Ge}_2\text{Sb}_2\text{Te}_5$  originates from these factors. However, binary chalcogenides, e.g.,  $\text{Bi}_2\text{Te}_3$ ,  $\text{Sb}_2\text{Te}_3$ , and  $\text{GeTe}$ , have a single crystalline phase and no structural vacancies. For example, crystalline  $\text{GeTe}$  forms in a rhombohedral structure with space group  $R3m$  as a distorted rock-salt structure with Ge and Te uniquely located on the each FCC sub-lattice.<sup>71</sup> Because each FCC sub-lattice is perfectly occupied with Ge and Te considering the stoichiometry of  $\text{GeTe}$ , an ideal  $\text{GeTe}$  structure has no structural vacancies.

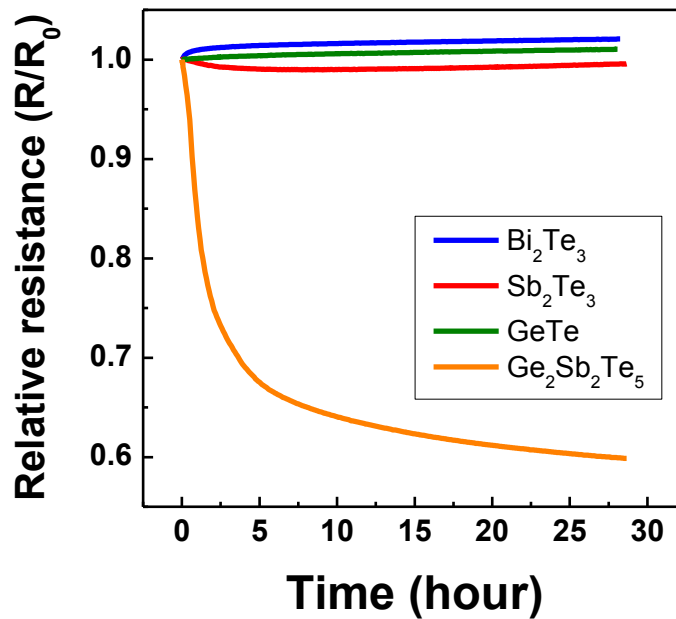


**Figure 6.4** Resistivity change with applying current density of 0.33 MA/cm<sup>2</sup> for 30 hours at 100 °C according to different Te-based chalcogenide materials, which are  $\text{Bi}_2\text{Te}_3$ ,  $\text{Sb}_2\text{Te}_3$ ,  $\text{GeTe}$ , and  $\text{Ge}_2\text{Sb}_2\text{Te}_5$ . The relative resistance means that value of resistance is divided by the initial resistance of each material.

#### **6.4.2. Mechanism behavior in crystalline $\text{Bi}_2\text{Te}_3$**

Bismuth telluride ( $\text{Bi}_2\text{Te}_3$ ) is the binary compound of Bi and Te, which is a well-known thermoelectric material.<sup>72</sup> A thin film super-lattice with  $\text{Bi}_2\text{Te}_3$  and antimony telluride ( $\text{Sb}_2\text{Te}_3$ ) was recently formed, and these materials showed the highest value of thermoelectric efficiency.<sup>73</sup> Understanding electrical and thermal stability of thermoelectric materials is important for reliability because high current density and temperature are inevitable to thermoelectric devices.

$\text{Bi}_2\text{Te}_3$  is a layered semiconductor that crystallizes in a rhombohedral structure in single unit cells, where each layer consists of Te-Bi-Te-Bi-Te. **Figure 6.5** shows the phase diagram of Bi and Te, which contains various intermetallic compounds, e.g.,  $\text{Bi}_2\text{Te}_3$ ,  $\text{Bi}_4\text{Te}_5$ , BiTe, and so on. Among the stoichiometric compounds,  $\text{Bi}_2\text{Te}_3$  is the most promising material for thermoelectric application.

**Figure 6.6** shows the resistance of  $\text{Bi}_2\text{Te}_3$  according to applied current densities from 0.33 to 1.33  $\text{MA}/\text{cm}^2$  over 30 hours at 100 °C. Three different failure modes could be determined for the current stress tests of  $\text{Bi}_2\text{Te}_3$  line specimens, namely, abrupt failure, gradual failure, and no failure in the resistance and morphological changes according to its current density. The sample with high current density (over 1.17  $\text{MA}/\text{cm}^2$ ) failed in a short amount of time, with largely agglomerated voids forming in a molten state, while the sample with low current density (below 0.83  $\text{MA}/\text{cm}^2$ ) exhibited no failure and no voids. Unlike the two-failure mode, a gradual increase in the resistance during current stressing was observed under an intermediate current density. Nano-scale voids (approximately 10 nm), which were responsible for the gradual change in resistance, were observed in the sample with an intermediate current density. These results are similar to the current-induced behavior in  $\text{Ge}_2\text{Sb}_2\text{Te}_5$  as shown in **Chapter 4**. However, the resistance of  $\text{Bi}_2\text{Te}_3$  did not decrease with the

electric current, unlike  $\text{Ge}_2\text{Sb}_2\text{Te}_5$ . Therefore, the behaviors of the resistance and morphology are simultaneously applicable for the criteria of the mechanisms in  $\text{Bi}_2\text{Te}_3$ .

The three failure modes according to the electric current were observed at different temperatures, namely, room temperature, 100 °C, and 200 °C, which confirms a temperature dependency. The resistance behaviors according to the electric current and temperature are shown in the mechanism map in **Figure 6.7**. As the temperature increased, abrupt failure and gradual failure were observed at a low current density because these failures have a close relationship with the melting temperature. The total thermal effect on  $\text{Bi}_2\text{Te}_3$  was the sum of the ambient temperature and Joule heating from the electric current. An abrupt failure (melting) can be initiated from the electric current or temperature, while a gradual failure cannot be initiated only from the temperature. Because gradual failure originates from current-induced defects, as mentioned in **Chapter 4**, an electric current must be applied even near the melting temperature.

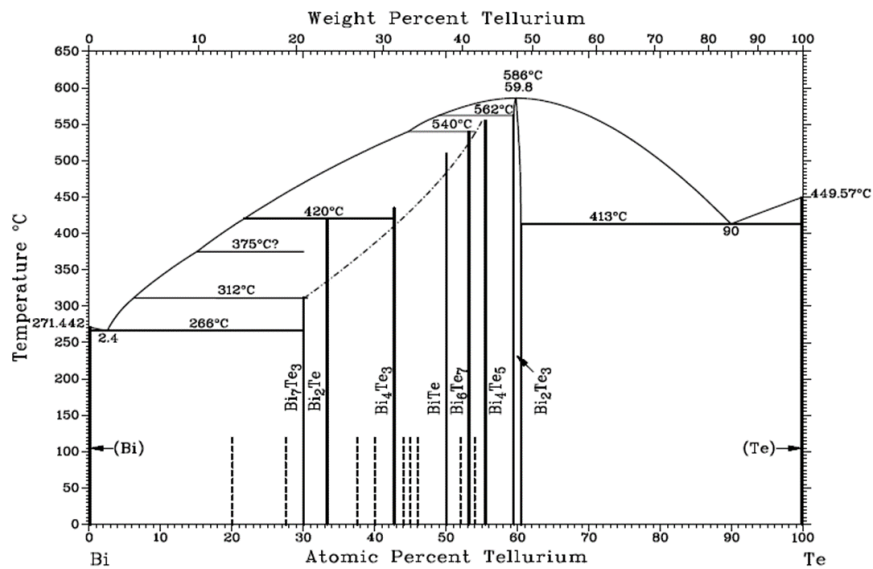


**Figure 6.5** Phase diagram of bismuth and tellurium according to atomic percent of tellurium.

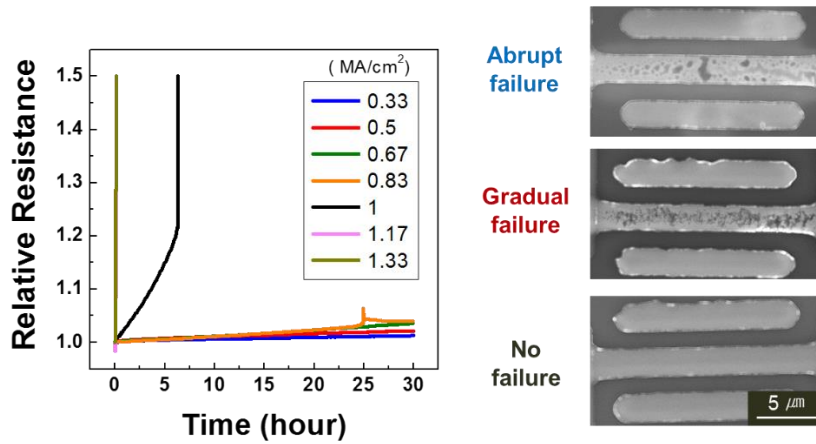


**Figure 6.6** Relative resistance of  $\text{Bi}_2\text{Te}_3$  according to current density ranged from 0.33 to 1.33  $\text{MA}/\text{cm}^2$  for 30 hours at 100 °C, and their SEM image. Current densities below 0.83  $\text{MA}/\text{cm}^2$ , ranging from 0.83 to 1.17  $\text{MA}/\text{cm}^2$  and above 1.17  $\text{MA}/\text{cm}^2$  are denoted as “no failure”, “gradual failure” and “abrupt failure”, respectively.



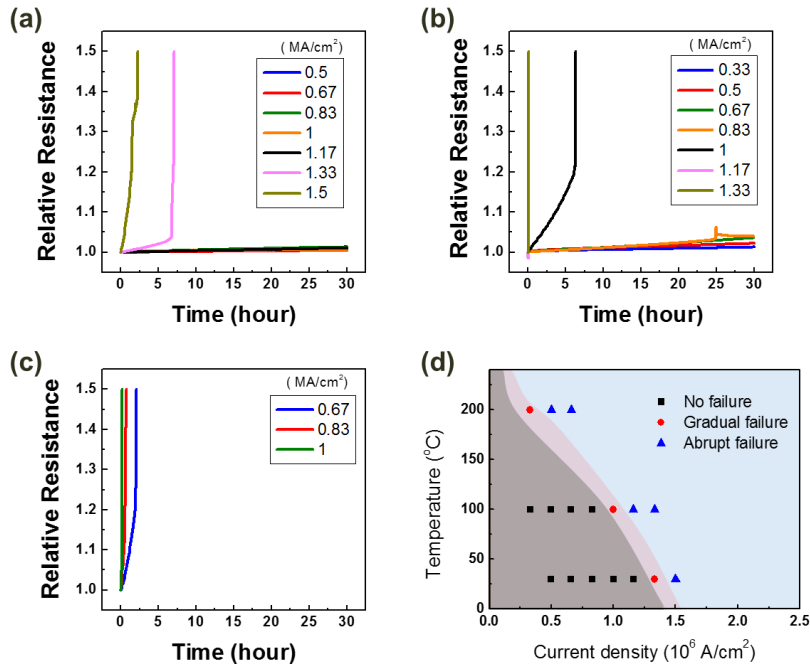


**Figure 6.7** Relative resistance of  $\text{Bi}_2\text{Te}_3$  according to current density ranged from 0.33 to 1.5  $\text{MA}/\text{cm}^2$  for 30 hours at (a) room temperature, (b) 100 °C, and (c) 200 °C. (d) The mechanism map according to current density and temperature, which is the merging of the results from (a)-(c).

#### **6.4.3. Failure criteria with respect to the stoichiometric effect**

Although intermetallic compounds of chalcogenide are widely used in various fields, matching the stoichiometric composition is very difficult because of close interval ranges in the composition. Continuously matching the stoichiometry with chemical vapor deposition (CVD) or wet processes is becoming increasingly difficult, so the reliability of non-stoichiometric materials will become more important. We focused on the failure mechanism in  $\text{Bi}_{35}\text{Te}_{65}$ , which has a composition difference of 5 at. % from the intermetallic composition of stoichiometric  $\text{Bi}_2\text{Te}_3$ .

**Figure 6.8** shows the resistance behavior of  $\text{Bi}_{35}\text{Te}_{65}$  when applying an electric current from 0.33 to 1.17 MA/cm<sup>2</sup> for 30 hours at room temperature, 100 °C, 150 °C and 200 °C. A mechanism map based on the current density and temperature, which merges the results from different temperatures, is displayed in **Figure 6.8**. The major difference between  $\text{Bi}_2\text{Te}_3$  and  $\text{Bi}_{35}\text{Te}_{65}$  is the “no failure” region. Gradual increases in the resistance of the constituent materials and catastrophic failure with melting are critical reliability problems in electrical device. Therefore, only the “no failure” mode is a safe condition for operating these devices. The “no failure” region in  $\text{Bi}_{35}\text{Te}_{65}$  is much smaller than that in  $\text{Bi}_2\text{Te}_3$ , as depicted in **Figure 6.7** and **Figure 6.8**. This result indicates that  $\text{Bi}_2\text{Te}_3$  is more stable under an electric current than  $\text{Bi}_{35}\text{Te}_{65}$ .

The reduction in the reliability of non-stoichiometric compounds originates from structural vacancies. Ideally, the crystalline structure of stoichiometric compounds is perfectly located and contains no structural vacancies. The crystalline structure of non-stoichiometric compounds, however, is deficient or contains excess atoms compared to a perfect crystal, which generates structural vacancies and acts as defect sites for gradual failure. Furthermore, phase separation in non-stoichiometric systems occurs below melting temperature with coexisting solid and liquid phases. According to the

phase diagram of Bi and Te in **Figure 6.5**, the melting temperature of  $\text{Bi}_2\text{Te}_3$  is 586 °C, while the melting temperature of eutectic  $\text{BiTe}_9$  is 413 °C. The solid phase of  $\text{Bi}_2\text{Te}_3$  and the liquid phase of  $\text{BiTe}_9$  coexist in a temperature range from 413 to 586 °C. This means that liquid phases in  $\text{Bi}_{35}\text{Te}_{65}$  can be obtained at much lower temperatures compared to  $\text{Bi}_2\text{Te}_3$ . Local liquid phases from phase separation will turn into voids by electromigration through “abrupt failure”. TEM analysis showed that the void area was a Te-rich phase, which has a low melting temperature.

## 6.5. Summary

The behaviors of resistance and morphology are criteria for current-induced failure modes, which include “no failure”, “gradual failure”, and “abrupt failure”. These criteria are applicable in binary chalcogenides but are inappropriate criteria for failure modes in ternary chalcogenides, e.g.,  $\text{Ge}_2\text{Sb}_2\text{Te}_5$ .

The failure mode depends on the electric current and temperature, so a mechanism map can be suggested. The mechanism maps of  $\text{Bi}_2\text{Te}_3$  and  $\text{Bi}_{35}\text{Te}_{65}$  show that the “no failure” area in  $\text{Bi}_2\text{Te}_3$  is far wider than that in  $\text{Bi}_{35}\text{Te}_{65}$ . This result indicates that  $\text{Bi}_2\text{Te}_3$  is more stable for current-induced failure than  $\text{Bi}_{35}\text{Te}_{65}$ . In conclusion, non-stoichiometry in materials seriously reduces the reliability of devices and should be considered in terms of device failure. This result suggests that small composition changes of only 5 at.% from stoichiometry can greatly impede the reliability of devices and that matching an accurate composition is important. Moreover, this result suggests that the guidelines for designing devices should consider the non-stoichiometry of chalcogenide materials by using a mechanism map.

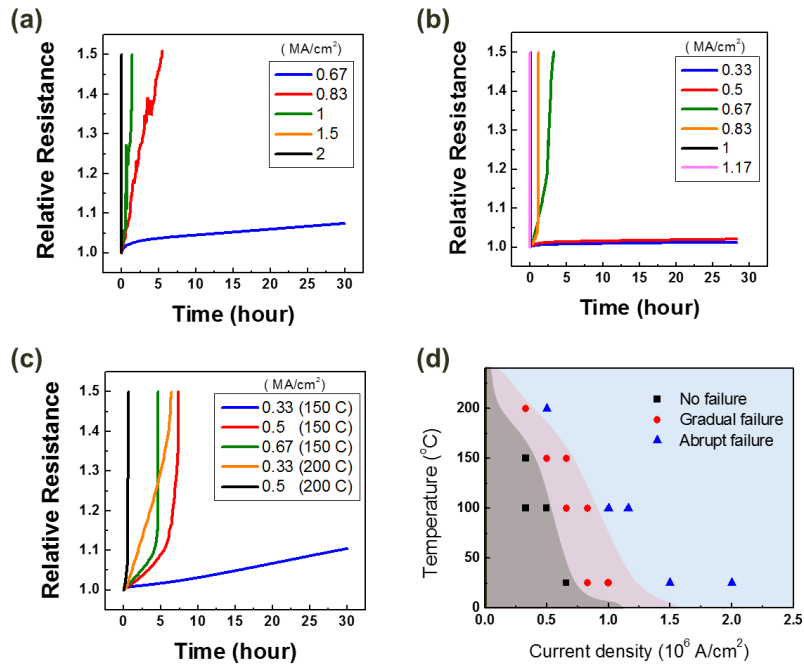


**Figure 6.8** Relative resistance of  $\text{Bi}_{35}\text{Te}_{65}$  according to current density ranged from 0.33 to 1.5  $\text{MA/cm}^2$  for 30 hours at (a) room temperature, (b) 100 °C, (c) 150, and 200 °C. (d) The mechanism map according to current density and temperature, which is the merging of the results from (a)-(c).

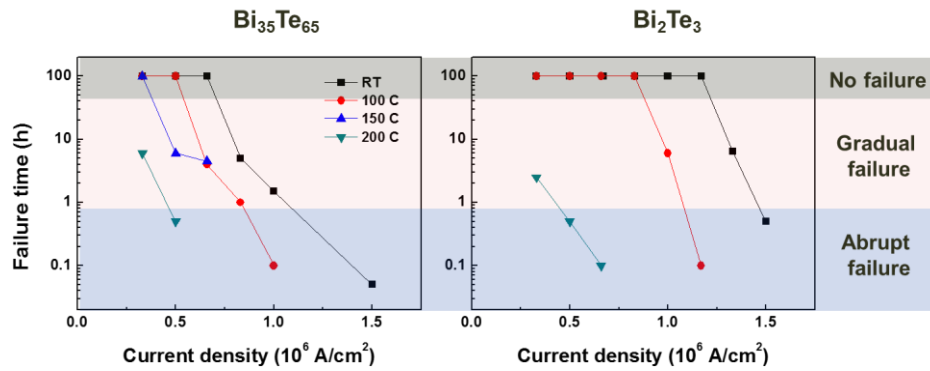


**Figure 6.9** The failure time according to current density and temperature in the  $\text{Bi}_{35}\text{Te}_{65}$  and  $\text{Bi}_2\text{Te}_3$ . Failure time is displayed in the log-scale.

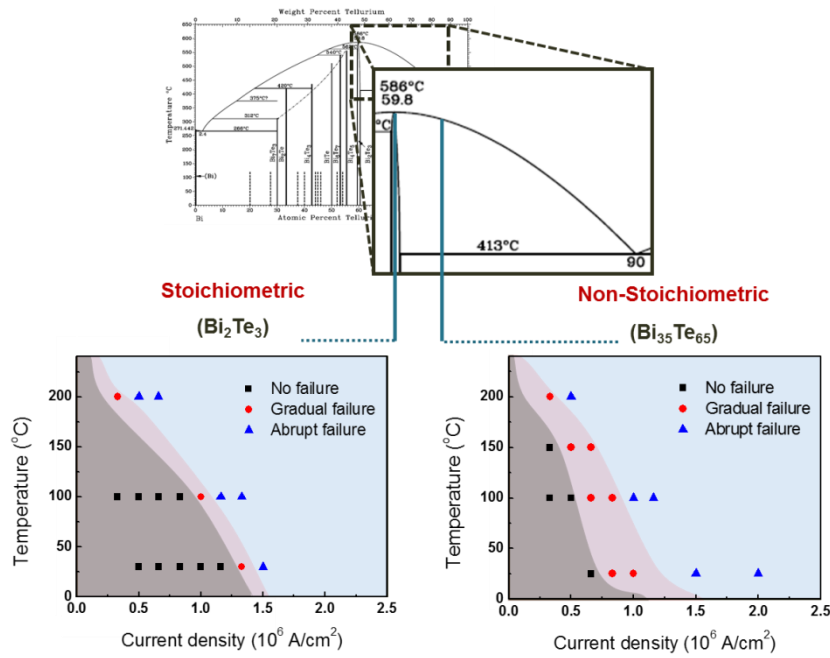


**Figure 6.10** Expanded phase diagram of Bi and Te with atomic percent of Te ranged from 60 to 90 at. %, and mechanism map of stoichiometric Bi<sub>2</sub>Te<sub>3</sub> (Te : 60 at. %) and non-stoichiometric Bi<sub>35</sub>Te<sub>65</sub> (Te : 65 at. %).

## **CHAPTER 7**

### **Conclusions**

#### **7.1. Summary of results**

This study investigated the degradation behavior that was induced by electric currents in phase-change materials by using a simple line-shaped structure, instead of PcRAM cells. The atomic displacement from a low current of approximately  $10^6$  A/cm<sup>2</sup> is negligible compared to that from a high current because the driving force for migration at low currents is insufficient to generate a massive flux of atoms. Although no catastrophic failure is induced by electric currents in crystalline phase-change materials, various phenomena that have not been reported were observed in crystalline Ge-Sb-Te compounds.

We chose Ge-Sb-Te compounds, which are commonly used materials for phase change memory, and applied electric currents on these materials to investigate the effect of electric current on crystalline phase-change materials. The resistivity and morphology of crystalline Ge<sub>2</sub>Sb<sub>2</sub>Te<sub>5</sub> were changed by electric currents and time with three different behaviors. At a high current density, greater than approximately 1 MA/cm<sup>2</sup>, the resistivity rapidly increased within a minute after the formation of micro-

scaled agglomerated voids. This catastrophic failure is electromigration in a molten state that is caused by severe Joule heating. In this case, the compositional de-mixing of constituent elements and voids originated from the free volume of  $\text{Ge}_2\text{Sb}_2\text{Te}_5$  after current stressing. At a low current density, less than approximately  $1 \text{ MA/cm}^2$ , no resistivity or morphological changes were observed with the exception of a decrease in the initial resistance. This decrease in resistivity originated from the ordering of the initial vacancies in  $\text{Ge}_2\text{Sb}_2\text{Te}_5$ . Interestingly, a gradual increase in the resistivity over 10-20 hours was observed under intermediate current density conditions of approximately  $1 \text{ MA/cm}^2$ . The failure morphology revealed that numerous nanometer-sized voids formed throughout the entire area. We can denote these phenomena according to current density as “abrupt failure”, “no failure”, and “gradual failure”, respectively.

A gradual degradation in resistivity was only observed under DC bias, while resistivity and morphological changes were not observed under AC bias. Because the only difference between DC and AC bias is the directionality of the electric current, gradual failure is related to the bias dependence during current stressing, which is electromigration. The local composition near nano-scale voids exhibited a Ge-deficient and Sb-excess composition, while the total composition was maintained at the initial state. The local non-stoichiometry of these void areas is distinct evidence of localized melting. Based on the pseudo-binary phase diagram of  $\text{Sb}_2\text{Te}_3$  and  $\text{GeTe}$ , the Sb-excess liquid phase and Ge-excess solid phase were separated during solidification, which produced Ge-deficient and Sb-excess compositions at the void areas. The origin of these voids was electromigration in the crystalline state. Although electromigration in crystalline phases is not sufficient to induce a catastrophic de-mixing of elements, this process can induce an amorphous phase at the grain boundary



or surface. This amorphous phase can act as defect points and generate localized melting, which is called defect-induced melting. Void generation is a prominent factor in this gradual increase in resistivity. These results indicate that devices can fail because of atomic migration in the crystalline phase and in liquid states. Although catastrophic failure is not induced by electric currents in the crystalline states of phase-change materials, the degradation of crystalline phases is cumulative in the non-active regions of PcRAM devices, which can be a fatal reliability problem even at intermediate currents.

A decrease in resistivity in crystalline  $\text{Ge}_2\text{Sb}_2\text{Te}_5$  at low currents is called the metal-insulator transition. From the theoretical literature, the origin of this phenomenon is known to be the rearrangement of vacancies. We first demonstrated a resistivity change in the cubic phase of  $\text{Ge}_2\text{Sb}_2\text{Te}_5$  by using an electric current of approximately  $1 \text{ MA/cm}^2$ . The final resistivity is determined by the current density regardless of the initial resistivity. The material property of  $\text{Ge}_2\text{Sb}_2\text{Te}_5$  changed from an insulator to a metal under a current density of  $1 \text{ MA/cm}^2$ , which was analyzed from the slope change of the resistivity versus temperature. The time-dependent behavior of the resistivity shows that the change only occurred during the early current stressing phase, while a continuous change was observed over long periods under isothermal annealing. The major difference between electrical and thermal stress is the microstructure. The current stressed  $\text{Ge}_2\text{Sb}_2\text{Te}_5$ , which had a current density of  $1 \text{ MA/cm}^2$ , had a small grain size of approximately 20 nm and maintained a cubic phase, similar to unstressed  $\text{Ge}_2\text{Sb}_2\text{Te}_5$ . The temperature stressed  $\text{Ge}_2\text{Sb}_2\text{Te}_5$ , however, had a grain size that was greater than 100 nm and transformed to a hexagonal phase. The origin of the difference between electrical and thermal stress is the migration energy. The rearrangement of vacancies is a thermodynamically spontaneous process. The

role of electric currents is a kinetic factor that accelerates vacancy rearrangement. Phase transitions, however, require more energy to generate a new phase compared to vacancy rearrangements because phase transitions are accompanied by a global change in atoms. Therefore, the minimum resistivity of cubic phases can be achieved kinetically quickly by applying a current density without a phase transition.  $\text{GeSb}_4\text{Te}_7$  shows the same behavior as  $\text{Ge}_2\text{Sb}_2\text{Te}_5$ , while  $\text{GeSb}_4\text{Te}_7$  is much more sensitive to electric currents compared to  $\text{Ge}_2\text{Sb}_2\text{Te}_5$ .  $\text{GeSb}_4\text{Te}_7$  and  $\text{Ge}_2\text{Sb}_2\text{Te}_5$  have different intrinsic vacancy fractions, specifically, 14.7 % and 10 %, respectively. Therefore, current-induced resistivity changes are determined by the intrinsic vacancy of materials.

The failure mode depends on the electric current and temperature, so a mechanism map can be suggested. The mechanism maps of  $\text{Bi}_2\text{Te}_3$  and  $\text{Bi}_{35}\text{Te}_{65}$  show that the “no failure” area in  $\text{Bi}_2\text{Te}_3$  is far wider than that in  $\text{Bi}_{35}\text{Te}_{65}$ . This result indicates that  $\text{Bi}_2\text{Te}_3$  is more stable for current-induced failure than  $\text{Bi}_{35}\text{Te}_{65}$ . In conclusion, the non-stoichiometry of materials seriously reduces the reliability of devices and should be considered for device failure. This result suggests that small composition changes of only 5 at.% from stoichiometry can greatly impede the reliability of devices and that matching an accurate composition is important. Moreover, this result suggests guidelines for designing devices that consider the non-stoichiometry of chalcogenide materials by using mechanism map.

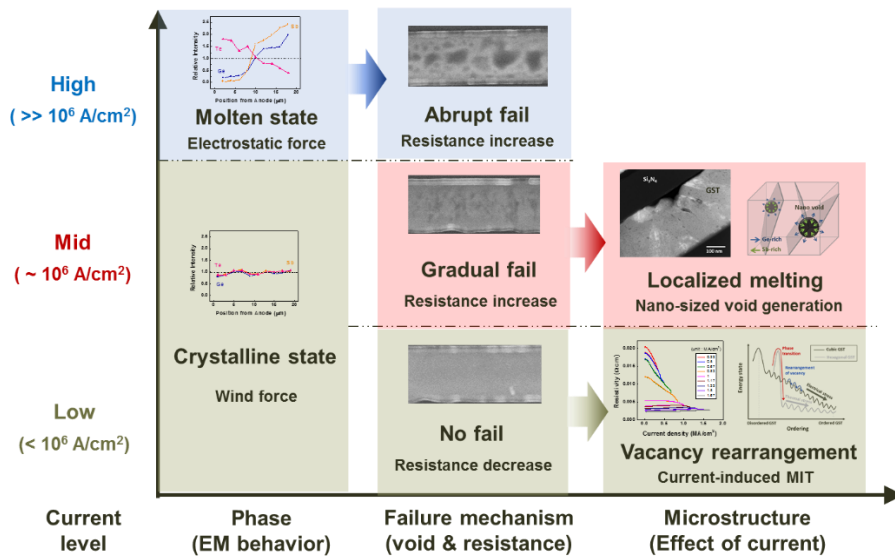


**Figure 7.1** Summary of behavior in phase change materials according to current density.

## **7.2. Future works and suggested research**

In this study, the slope of the TCR, which is obtained from the relationship between resistivity and temperature, was used to distinguish metallic and insulating behavior. A positive TCR relationship implies metallic behavior, while a negative TCR relationship implies insulating behavior. However, the behavior of resistivity near zero Kelvin is a more powerful method for confirming electrical characteristics compared to TCR measurements. The conductivity of insulators vanishes as the temperature approaches zero Kelvin, while metals maintain finite conductivity. The conductivity of current-stressed  $\text{Ge}_2\text{Sb}_2\text{Te}_5$  will be analyzed near zero Kelvin to confirm the transition to metal under electrical stress. In addition, we are scheduled to study the dependence of the dimensions on the current-induced metal transition. An electric current generates a current path, so not all materials can be affected by electric currents. In this case, current-induced transitions can be determined from the dimensions of the materials.

A sample structure with a line shape was used for a model study in this study. By using a line structure, we could clearly identify the various degradation mechanisms and structural changes in phase-change materials depending on the current density. However, the factors that influence a material's structure and environment are mixed in actual devices. Device level studies will be considered to identify suitable application. For example, crystalline  $\text{Ge}_2\text{Sb}_2\text{Te}_5$  had a fixed resistivity value depending on the applied current density in our work. When the current density reached the corresponding resistivity, the resistivity followed the universal curve of  $\text{Ge}_2\text{Sb}_2\text{Te}_5$ , which can be applicable for a crystalline-based device because the resistivity was controlled by an electric current.

A mechanism map for various materials will help guide device operation. Based on the failure mode, gradual increases in resistance in the constituent materials and catastrophic failure with melting are critical reliability problems. The “no failure” mode is the only safe condition for operating devices. We believe that this work provides new insight into the electrical reliability of the crystalline phase of chalcogenides and offers design rules and guidelines for chalcogenide-based devices.

## Reference

- 1 Bedeschi, F., Resta, C., Khouri, O., Buda, E., Costa, L., Ferraro, M., Pellizzer, F., Ottogalli, F., Pirovano, A., Tosi, M., Bez, R., Gastaldi, R., and Casagrande, G., *IEEE Symposium on VLSI Circuits, Digest of Technical Papers*. CIRCUITS SYMP. edn 442-445 (2004).
- 2 Pirovano, A., Lacaita, A. L., Benvenuti, A., Pellizzer, F., and Bez, R. *IEEE Transactions on Electron Devices* **51**(3), 452-459 (2004).
- 3 Lai, S. *Technical Digest - International Electron Devices Meeting*, 255-258 (2003).
- 4 Wuttig, M., and Yamada, N., *Nature Materials* **6**(11), 824-832 (2007).
- 5 Ielmini, D., Lacaita, A. L., Pirovano, A., Pellizzer, F., and Bez, R., *IEEE Electron Device Letters* **25**(7), 507-509 (2004).
- 6 Cho, W. Y., Cho, B. H., Choi, B. G., Oh, H. R., Kang, S., Kim, K. S., Kim, K. H., Kim, D. E., Kwak, C. K., Byun, H. G., Hwang, Y., Ahn, S., Koh, G. H., Jeong, G., Jeong, H., and Kim, K., *IEEE Journal of Solid-State Circuits* **40**(1), 293-298 (2005).
- 7 Kim, K., and Ahn, S. J., *IEEE International Reliability Physics Symposium Proceedings*. 157-162 (2005).

- 8 Yoon, S. M., Choi, K. J., Lee, N. Y., Lee, S. Y., Park, Y. S., and Yu, B. G., *Applied Surface Science* **254**(1), 316-320 (2007).
- 9 Park, J. B., Park, G. S., Baik, H. S., Lee, J. H., Jeong, H., and Kim, K., *Journal of the Electrochemical Society* **154**(3), H139-H141 (2007).
- 10 Nam, S. W., Kim, C., Kwon, M. H., Lee, H. S., Wi, J. S., Lee, D., Lee, T. Y., Khang, Y., and Kim, K. B., *Applied Physics Letters* **92**(11), 111913 (2008).
- 11 Kang, D., Lee, D., Kim, H. M., Nam, S. W., Kwon, M. H., and Kim, K. B., *Applied Physics Letters* **95**(1), 011904 (2009).
- 12 Nam, S. W., Lee, D., Kwon, M. H., Kang, D., Kim, C., Lee, T. Y., Heo, S., Park, Y. W., Lim, K., Lee, H. S., Wi, J. S., Yi, K. W., Khang, Y., and Kim, K. B., *Electrochemical and Solid-State Letters* **12**(4), H155-H159 (2009).
- 13 Yang, T. Y., Park, I. M., Kim, B. J., and Joo, Y. C., *Applied Physics Letters* **95**(3), 032104 (2009).
- 14 Chen, C. F., Schrott, A., Lee, M. H., Raoux, S., Shin, Y. H., Breitwisch, M., Baumann, F. H., Lai, E. K., Shaw, T. M., Flaitz, P., Cheek, R., Joseph, E. A., Chen, S. H., Rajendran, B., Lung, H. L., and Lam, C., *IEEE International Memory Workshop*, 5090589 (2009)
- 15 Huntington, H. B., and Grone, A. R. *Journal of Physics and Chemistry of Solids* **20**(1), 76-87 (1961).

- 16 Nam, S. W., Chung, H. S., Lo, Y. C., Qi, L., Li, J., Lu, Y., Johnson, A. T. C., Jung, Y., Nukala, P., and Agarwal, R., *Science* **336**(6088), 1561-1566 (2012).
- 17 Cheong, B. K., Lee, S., Jeong, J. H., Park, S., Hang, S., Wu, Z., and Ahn, D. H., *Physica Status Solidi (B) Basic Research* **249**(10), 1985-1991 (2012).
- 18 Yamada, N., and Matsunaga, T. *Journal of Applied Physics* **88**(12), 7020-7028 (2000).
- 19 Ovshinsky, S. R., *Physical Review Letters* **21**(20), 1450-1453 (1968).
- 20 Abrikosov, N. K., and DANILOVA, D. *IZV AKAD NAUK SSSR NEORGAN MATERIALY* **1**(2), 204-207 (1965).
- 21 Bordas, S., Clavaguer-Mora, M. T., Legendre, B., and Hancheng, C., *Thermochimica Acta* **107**(C), 239-265 (1986).
- 22 Yamada, N., Ohno, E., Nishiuchi, K., Akahira, N., and Takao, M., *Journal of Applied Physics* **69**(5), 2849-2856 (1991).
- 23 Yamada, N., Nishiuchi, K., Sanai, S., Nagata, K., Takao, M., and Akahira, N., *National technical report* **35**(2), 12-19 (1989).
- 24 Kuypers, S., van Tendeloo, G., van Landuyt, J., and Amelinckx, S., *Journal of Solid State Chemistry* **76**(1), 102-108 (1988).
- 25 Karpinsky, O. G., Shelimova, L. E., Kretova, M. A., and Fleurial, J. P., *Journal of Alloys and Compounds* **268**(1), 112-117 (1998).



- 26 Shelimova, L. E., Karpinskii, O. G., Konstantinov, P. P., Kretova, M. A., Avilov, E. S., and Zemskov, V. S., *Inorganic Materials* **37**(4), 342-348 (2001).
- 27 Friedrich, I., Weidenhof, V., Njoroge, W., Franz, P., and Wuttig, M., *Journal of Applied Physics* **87**(9), 4130-4134 (2000).
- 28 WeŁnic, W., Pamungkas, A., Detemple, R., Steimer, C., Blügel, S., and Wuttig, M., *Nature Materials* **5**(1), 56-62 (2006).
- 29 Wuttig, M., Lüsebrink, D., Wamwangi, D., WeŁnic, W., Gilleen, M., and Dronskowski, R., *Nature Materials* **6**(2), 122-128 (2007).
- 30 Zhou, J., Sun, Z., Pan, Y., Song, Z., and Ahuja, R., *Europhysics Letters* **95**(2), 27002 (2011).
- 31 Petrov, I. I., and Imamov, R. M., *Ussr* **13**(3), 339 (1968).
- 32 Sun, Z., Zhou, J., and Ahuja, R., *Physical Review Letters* **96**(5), 055507 (2006).
- 33 Kooi, B. J., and De Hosson, J. T. M., *Journal of Applied Physics* **92**(7), 3584-3590 (2002).
- 34 Kolobov, A. V., Fons, P., Frenkel, A. I., Ankudinov, A. L., Tominaga, J., and Uruga, T., *Nature Materials* **3**(10), 703-708 (2004).
- 35 Kolobov, A. V., Haines, J., Pradel, A., Ribes, M., Fons, P., Tominaga, J., Katayama, Y., Hammouda, T., and Uruga, T., *Physical Review Letters* **97**(3),

- 035701 (2006).
- 36 Fons, P., Kolobov, A. V., Tominaga, J., and Katayama, Y., *Nuclear Instruments and Methods in Physics Research, Section B: Beam Interactions with Materials and Atoms* **238**(1), 160-162 (2005).
  - 37 Kolobov, A. V., Haines, J., Pradel, A., Ribes, M., Fons, P., Tominaga, J., Steimer, C., Aquilanti, G., and Pascarelli, S., *Applied Physics Letters* **91**(2), 021911 (2007).
  - 38 Lyeo, H. K., Cahill, D. G., Lee, B. S., Abelson, J. R., Kwon, M. H., Kim, K. B., Bishop, S. G., and Cheong, B. G., *Applied Physics Letters* **89**(15), 151904 (2006).
  - 39 Siegrist, T., Jost, P., Volker, H., Woda, M., Merkelbach, P., Schlockermann, C., and Wuttig, M., *Nature Materials* **10**(3), 202-208 (2011).
  - 40 Mott, N. *Proceedings of the Royal Society of London A: Mathematical, Physical and Engineering Sciences*. 1-24 (1982).
  - 41 Anderson, P. W. *Physical review* **109**(5), 1492 (1958).
  - 42 Lee, P. A., and Ramakrishnan, T. V., *Reviews of Modern Physics* **57**(2), 287-337 (1985).
  - 43 Belitz, D., and Kirkpatrick, T. R., *Reviews of Modern Physics* **66**(2), 261-380 (1994).

- 44 Denteneer, P. J. H., Scalettar, R. T., and Trivedi, N., *Physical Review Letters* **87**(14), 146401 (2001).
- 45 Siegrist, T., Merkelbach, P., and Wuttig, M., *Annual Review of Condensed Matter Physics* **3**(1), 215-237 (2012).
- 46 Lee, B. S., Abelson, J. R., Bishop, S. G., Kang, D. H., Cheong, B. K., and Kim, K. B., *Journal of Applied Physics* **97**(9), 093509 (2005).
- 47 Kato, T., and Tanaka, K., *Japanese Journal of Applied Physics, Part 1: Regular Papers and Short Notes and Review Papers* **44**(10), 7340-7344 (2005).
- 48 Zhang, W., Thiess, A., Zalden, P., Zeller, R., Dederichs, P. H., Rat, J. Y., Wuttig, M., Blugel, S., and Mazzarello, R., *Nature Materials* **11**(11), 952-956 (2012).
- 49 Shportko, K., Kremers, S., Woda, M., Lencer, D., Rovertson, J., and Wuttig, M., *Nature Materials* **7**(8), 653-658 (2008).
- 50 Jost, P., Volker, H., Poitz, A., Poltorak, C., Zalden, P., Schäfer, T., Lange, F. R. L., Schmidt, R. M., Holländer, B., Wirtsohn, M. R., and Wuttig, M. *Advanced Functional Materials* **25**(40), 6399-6406 (2015).
- 51 Fiks, V., *Soviet Physics-Solid State* **1**(1), 14-28 (1959).
- 52 Pearson, R. G., *Inorganic Chemistry* **27**(4), 734-740 (1988).

- 53 Nix, W. D., and Arzt, E., *Metallurgical transactions. A, Physical metallurgy and materials science* **23A**(7), 2007-2013 (1992).
- 54 Smigelskas, A., and Kirkendall, E. *Trans. Aime* **171**, 130-142 (1947).
- 55 Ragone, D. V., *Thermodynamics of materials*. Wiley (1995).
- 56 Yang, T.-Y., Cho, J.-Y., Park, Y.-J., and Joo, Y.-C. *Current Applied Physics* **13**(7), 1426-1432 (2013).
- 57 Lloyd, J. R., Polcari, M. R., and MacKenzie, G. A., *Applied Physics Letters* **36**(6), 428-430 (1980).
- 58 Yoon, S. M., Lee, S. Y., Jung, S. W., Park, Y. S., and Yu, B. G., *Solid-State Electronics* **53**(5), 557-561 (2009).
- 59 Nardone, M., Simon, M., Karpov, I. V., and Karpov, V. G. *Journal of Applied Physics* **112**(7), 071101 (2012).
- 60 Reynolds, J. A., and Hough, J. M., *Proceedings of the Physical Society. Section B* **70**(8), 769-775 (1957).
- 61 Ivanov, D. S., and Zhigilei, L. V., *Physical Review Letters* **98**(19), 195701 (2007).
- 62 Mei, Q. S., and Lu, K., *Progress in Materials Science* **52**(8), 1175-1262 (2007).
- 63 Dash, J., *Reviews of Modern Physics* **71**(5), 1737 (1999).

- 64 Fecht, H., and Johnson, W., *Nature* **334**(6177), 50-51 (1988).
- 65 Kauzmann, W., *Chemical Reviews* **43**(2), 219-256 (1948).
- 66 Yang, T. Y., Cho, J. Y., Park, Y. J., and Joo, Y. C., *Acta Materialia* **60**(5), 2021-2030 (2012).
- 67 Lencer, D., Salanga, M., and Wuttig, M., *Advanced Materials* **23**(18), 2030-2058 (2011).
- 68 Park, Y. J., Yang, T. Y., Cho, J. Y., Lee, S. Y., and Joo, Y. C. *Applied Physics Letters* **103**(7), 073503 (2013).
- 69 Nukala, P., Agarwal, R., Qian, X., Jang, M. H., Dhara, S., Kumar, K., Johnson, A. T. C., Li, J., and Agarwal, R., *Nano Letters* **14**(4), 2201-2209 (2014).
- 70 Sun, Z., Kyrsta, S., Music, D., Ahuja, R., and Schneider, J. M., *Solid State Communications* **143**(4), 240-244 (2007).
- 71 Gaspard, J. P., Pellegatti, A., Marinelli, F., and Bichara, C., *Philosophical Magazine B: Physics of Condensed Matter; Statistical Mechanics, Electronic, Optical and Magnetic Properties* **77**(3), 727-744 (1998).
- 72 Goldsmid, H., and Douglas, R., *British Journal of Applied Physics* **5**(11), 386 (1954).
- 73 Venkatasubramanian, R., Siivola, E., Colpitts, T., and O'quinn, B., *Nature* **413**(6856), 597-602 (2001).

## 요약(국문초록)

상변화 메모리(PcRAM)는 높은 온도 및 전류밀도라는 가혹한 동작 조건에 의해 재료 내부에 공동(void) 형성과 같은 심각한 신뢰성 문제가 존재한다. 전류밀도에 상변화 물질에 미치는 영향에 대해 지금까지 많은 연구가 진행되어 왔지만 대부분의 파손기구에 관한 연구는 용융상에 한정되어 있다. 용융상 내의 원자의 확산은 결정상에 비해 매우 빠르게 이루어 지기 때문에 재료의 파손은 용융상에서 주도적으로 발생하고 결정상은 상대적으로 전류에 안정한 상으로 지금까지 알려져 왔다. 본 연구에서는 결정상 상변화 물질에서 발생하는 전류에 의한 전도도의 증가 또는 감소 현상을 최초로 발견하였고 선형 형태의 간단한 구조의 모사실험을 통해 실제 소자에서 발생할 수 있는 다양한 외적 요인을 배제시켰다.

결정상  $\text{Ge}_2\text{Sb}_2\text{Te}_5$  물질에 전류를 인가할 시 전류밀도에 따라 크게 3 가지의 다른 현상이 발생한다. 이때의 기준은 재료의 저항 변화 양상과 공동의 형태를 들 수 있다. 결정상  $\text{Ge}_2\text{Sb}_2\text{Te}_5$  물질에 약  $1 \sim 1.5 \text{ MA/cm}^2$ 의 전류 인가시 저항은 수십 시간동안 지속적으로 증가하고 내부에 나노 사이즈의 공동을 형성시키는 데, 이러한 현상은 기존에 보고된 용융상에서 발생하는 파손기구와는 확연히 다른 양상이다. 결정상에서 발생하는 열화현상은 전류에 의한 원자이동 (electro-migration)에 의한 것으로, 교류 전류 하에서는 본 현상이 발생하지 않는 것을 통해 확인이 가능하다. 원자이동에 의해 발생한 결함에서 국소적인 용융이 발생하게 되는데 이러한 용융상이 공동으로 형성된다. 이러한 현상을 결함 유도 용융 (defect-induced melting)이라고 한다. 지속적인 저항의 증가는 내부에 발생하는 나노 공동에 의해 발생한다.

1 MA/cm<sup>2</sup> 이하의 전류밀도 인가시 발생하는 저항의 감소는 재료 내부의 고유 공공(intrinsic vacancy)의 재배열에 기인 한다. 전류와 온도 모두 결정상 Ge<sub>2</sub>Sb<sub>2</sub>Te<sub>5</sub>의 물질 특성을 절연체에서 금속성으로 변화시키는 데 이를 금속-절연체 전이(metal-insulator transition)라고 한다. 하지만 전류를 인가할 경우 금속성을 띄지만 면심 입방 구조를 유지하는 Ge<sub>2</sub>Sb<sub>2</sub>Te<sub>5</sub>를 최초로 얻을 수 있었으며, 이는 육방 밀집 구조로의 상변화를 수반하는 열에 의한 전이와는 매우 다른 현상이다. 전류에 의한 저항 감소는 가장 높은 전류밀도 (peak current density)에 의존하고 초기의 저항이나 온도와는 무관하게 결정된다. 또한 전류에 의한 본 변화는 고유 공공 농도가 다른 GeSb<sub>4</sub>Te<sub>7</sub>와 Ge<sub>2</sub>Sb<sub>2</sub>Te<sub>5</sub>에서 다르게 발생하는 데, 이를 통해 본 현상이 고유 공공에 의존하여 발생함을 확인할 수 있다.

본 연구는 소자가 작아질수록 결정상에 흐르는 전류가 높아질 경우 발생 가능한 새로운 형태의 문제를 시사한다. 상변화 메모리에서 상변화가 발생하는 부분은 하부 전극과 맞닿은 일부의 영역에 한정된다. 따라서 상변화가 발생하지 않는 영역에서는 용융에 의한 회복이 없기 때문에 전류에 의한 영향이 계속해서 누적된다. 결정상에서의 저항의 변화는 SET 상태의 신뢰성과 매우 밀접한 관계를 가지고 있으며 다중 레벨 셀 (multi level cell)로 변화하는 현재 추세에 따라 더욱 중요해질 것으로 생각된다.

본 연구는 결정상 상변화 물질에서 발생하는 전기적인 불안정성에 관한 기준을 처음으로 규명함으로써 높은 신뢰성을 위한 상변화 메모리 소자의 설계 규칙 (design rule) 및 새로운 형태의 소자로의 응용 가능성을 제시하였다.

**표제어:** 상변화 메모리, 일렉트로마이그레이션, 결정상 칼코지나이드, 파손기구 분류, 전류 유도 금속-절연체 전이

학 번: 2010-20602





## 저작자표시-비영리-변경금지 2.0 대한민국

이용자는 아래의 조건을 따르는 경우에 한하여 자유롭게

- 이 저작물을 복제, 배포, 전송, 전시, 공연 및 방송할 수 있습니다.

다음과 같은 조건을 따라야 합니다:



저작자표시. 귀하는 원저작자를 표시하여야 합니다.



비영리. 귀하는 이 저작물을 영리 목적으로 이용할 수 없습니다.



변경금지. 귀하는 이 저작물을 개작, 변형 또는 가공할 수 없습니다.

- 귀하는, 이 저작물의 재이용이나 배포의 경우, 이 저작물에 적용된 이용허락조건을 명확하게 나타내어야 합니다.
- 저작권자로부터 별도의 허가를 받으면 이러한 조건들은 적용되지 않습니다.

저작권법에 따른 이용자의 권리는 위의 내용에 의하여 영향을 받지 않습니다.

이것은 [이용허락규약\(Legal Code\)](#)을 이해하기 쉽게 요약한 것입니다.

[Disclaimer](#)

공학박사학위논문

Instability in Crystalline Phase of  
Chalcogenide Materials under  
Electric Current for  
Phase Change Memory

결정상 상변화 물질의 전류 인가에 따른  
불안정성 연구

2016년 2월

서울대학교 대학원

재료공학부

박 용 진

결정상 상변화 물질의 전류 인가에 따른  
불안정성 연구

INSTABILITY IN CRYSTALLINE PHASE OF  
CHALCOGENIDE MATERIALS UNDER ELECTRIC CURRENT FOR  
PHASE CHANGE MEMORY

지도교수: 주 영 창

이 논문을 공학박사 학위논문으로 제출함

2016년 1월

서울대학교 대학원

재료공학부

박 용 진

박 용 진의 박사학위 논문을 인준함

2016년 1월

위 원 장	김 기 범	(인)
-------	-------	-----

부 위 원 장	주 영 창	(인)
---------	-------	-----

위 원	한 승 우	(인)
-----	-------	-----

위 원	양 철 웅	(인)
-----	-------	-----

위 원	안 동 호	(인)
-----	-------	-----

## **ABSTRACT**

### **Instability in crystalline phase of chalcogenide materials under electric current for phase change memory**

Yong-Jin Park

Department of Materials Science and Engineering

The Graduate School

Seoul National University

Reliability problems such as void formation have been reported in phase change random access memory (PcRAM), which originates from harsh operating conditions and high temperatures and current density. Previous research has examined the migration behavior of phase-change materials when induced by electric currents, while most studies of failure mechanisms have only focused on liquid states. Crystalline phase have been considered a stable state for electric currents because the diffusivity of atoms in a liquid phase is much faster than that in a crystalline phase.

Here, we observe the mechanism behaviors in crystalline chalcogenide materials, which noticeably degrade or upgrade the conductivity. A simple structure with a line shape is used for a model study to avoid the side effects

from the structure and environment of the actual device.

Three different behaviors with respect to the electric current are observed in crystalline  $\text{Ge}_2\text{Sb}_2\text{Te}_5$ . The criteria for mechanism divergence include the resistivity behavior and evolution of voids. Continuous increase in the resistivity over tens of hours and nano-scaled voids are generated at a current density that ranges from 1 to  $1.5 \text{ MA/cm}^2$ ; this behavior is completely different from previous results regarding molten phase failure. This phenomenon develops from electromigration, because alternating (AC) bias cannot trigger this behavior. Localized melting that occurs at the defect site is induced by electromigration, and the molten phase becomes the void area; this phenomenon is called defect-induced melting. The homogeneous nano-voids explains the gradual increase in quantitative resistivity.

Decrease in resistance below a current density of  $1 \text{ MA/cm}^2$  originate from the rearrangement of vacancies. The nature of the material changes from an insulator to a metal, i.e., metal-insulator transition, which is affected by the electric current and temperature. However, the metallic cubic phase of  $\text{Ge}_2\text{Sb}_2\text{Te}_5$  is first demonstrated by using an electric current of  $1 \text{ MA/cm}^2$ , which differs significantly from the thermal annealing accompanying phase transition to a hexagonal phase. The final resistivity of  $\text{Ge}_2\text{Sb}_2\text{Te}_5$  varies according to the peak current density, regardless of the initial resistivity and temperature, which implies that the conductivity can be modulated by an

electric current. Furthermore, a current-induced metal transition is more effective in  $\text{GeSb}_4\text{Te}_7$  than  $\text{Ge}_2\text{Sb}_2\text{Te}_5$ , which depends on the intrinsic vacancy of the materials.

This work represents a possible side effect of device shrinkage, which increases the current density within the crystalline phase. Because only the active region, which is the limited zone near the heater, can be transformed into a liquid phase, the effect of atomic migration in non-active region is cumulative without recovery by melting. Resistivity changes in crystalline phases affect the reliability of the *SET* state of PcRAM devices, which becomes more significant in multi-level cell (MLC) devices. We believe that this work provides new insight regarding electrical reliability in the crystalline phase of chalcogenide, which offers the design rules and applications for reliable PcRAM devices. Scientifically, this work adds to the fundamental knowledge of the influence of electric currents on the crystalline phase of chalcogenide materials.

---

**Keywords:** phase change random access memory (PcRAM), electromigration, crystalline chalcogenide, categorization of mechanism, current-induced metal insulator transition (MIT)

***Student Number:*** 2010-20602



# Table of Contents

---

<b>Abstract.....</b>	<b>i</b>
<b>Table of contents.....</b>	<b>iv</b>
<b>List of Tables.....</b>	<b>viii</b>
<b>List of Figures.....</b>	<b>ix</b>

## **Chapter 1. Introduction**

---

1.1. Phase change random access memory (PcRAM) .....	1
1.2. Reliability issues in PcRAM .....	5
1.2.1. Endurance problem .....	5
1.2.2. Migration behavior in PcRAM .....	6
1.3. Objective of the thesis .....	10
1.4. Organization of the thesis .....	13

## **Chapter 2. Theoretical Background**

---

2.1. Physical properties of phase-change materials .....	14
2.1.1. Ge-Sb-Te alloys .....	15
2.1.2. Crystalline structure of Ge-Sb-Te compounds .....	17
2.1.3. Temperature dependence of resistivity .....	22



2.1.4. Metal-insulator transition in Ge-Sb-Te alloys .....	25
2.2. Theory of electromigration .....	30
2.2.1. Electromigration .....	30
2.2.2. Driving forces for electromigration .....	31
2.3. Mass transport in phase-change materials .....	34
2.3.1. Electromigration behaviors in molten phase $\text{Ge}_2\text{Sb}_2\text{Te}_5$ .....	35
2.3.2. Electromigration behaviors in crystalline phase $\text{Ge}_2\text{Sb}_2\text{Te}_5$ ..	41

### **Chapter 3. Experimental Procedures**

---

3.1. Sample preparation .....	44
3.2. Electrical stressing method .....	49
3.2.1. Wafer-level test .....	49
3.2.2. Package-level test .....	52
3.3. Compositional analysis .....	55

### **Chapter 4. Gradual degradation in the crystalline $\text{Ge}_2\text{Sb}_2\text{Te}_5$ under electric current**

---

4.1. Introduction .....	57
4.2. Experiments .....	59
4.3. Electrical stressing in crystalline $\text{Ge}_2\text{Sb}_2\text{Te}_5$ .....	59
4.3.1. High current .....	60
4.3.2. Low current .....	60

4.3.2. Mid current .....	61
4.4. Frequency dependence in gradual failure .....	64
4.5. Microstructural analysis .....	66
4.5.1. Quantification of voids .....	66
4.5.2. Resistivity according to void fraction .....	71
4.5.3. Composition at the defect site .....	74
4.6. Mechanism for the void generation .....	77
4.7. Summary .....	78

## **Chapter 5. Formation of metallic cubic-phase Ge-Sb-Te compounds when induced by an electric current**

---

5.1. Introduction .....	80
5.2. Experiments .....	82
5.3. Current-driven electrical sweep in $\text{Ge}_2\text{Sb}_2\text{Te}_5$ .....	83
5.3.1. I-V characteristics of $\text{Ge}_2\text{Sb}_2\text{Te}_5$ .....	83
5.3.2. TCR measurement of current-stressed $\text{Ge}_2\text{Sb}_2\text{Te}_5$ .....	87
5.3.3. Complex effect of current and temperature in $\text{Ge}_2\text{Sb}_2\text{Te}_5$ ...	91
5.4. Time-dependent behavior of $\text{Ge}_2\text{Sb}_2\text{Te}_5$ .....	93
5.5. Microstructural analysis of $\text{Ge}_2\text{Sb}_2\text{Te}_5$ .....	96
5.5.1. Phase of current- and temperature-stressed $\text{Ge}_2\text{Sb}_2\text{Te}_5$ .....	96
5.5.2. Gradual decrease in resistivity during thermal annealing ...	102
5.6. Comparison between $\text{Ge}_2\text{Sb}_2\text{Te}_5$ and $\text{GeSb}_4\text{Te}_7$ .....	104
5.7. Role of electric current in vacancy rearrangement .....	110

5.8. Summary .....	114
--------------------	-----

## **Chapter 6. Divergence of failure mechanisms with current and temperature in crystalline chalcogenide**

---

6.1. Introduction .....	115
6.2. Experiments .....	116
6.3. Limitations of the mechanism map for $\text{Ge}_2\text{Sb}_2\text{Te}_5$ .....	116
6.4. Mechanism map for chalcogenide materials .....	122
6.4.1. Resistivity behavior in ternary and binary chalcogenide .....	122
6.4.2. Mechanism behavior in crystalline $\text{Bi}_2\text{Te}_3$ .....	124
6.4.3. Failure criteria with respect to the stoichiometric effect .....	129
6.5. Summary .....	130

## **Chapter 7. Conclusions**

---

7.1. Summary of results .....	134
7.2. Future works and suggested research .....	139

<b>References</b> .....	141
-------------------------	-----

<b>Abstract (In Korean)</b> .....	149
-----------------------------------	-----

<b>Curriculum Vitae</b> .....	151
-------------------------------	-----



## LIST OF TABLES

- Table 3.1** Detailed sputtering conditions for deposition of chalcogenide materials.
- Table 5.1** Comparison between the calculated distance in **Figure 5.9(b)** and crystallographic distance in cubic phase of  $\text{Ge}_2\text{Sb}_2\text{Te}_5$ .
- Table 5.2** Fraction of vacancies in the pseudo-binary compound of  $(\text{GeTe})_x(\text{Sb}_2\text{Te}_3)_{1-x}$  according to  $x$ .

## LIST OF FIGURES

- Figure 1.1** A graphical representation of material phases and principle of operation in PcRAM device. The crystalline phase is denoted as *SET* state, and the amorphous phase is denoted as *RESET* state. The phase transformation is caused by Joule heating with modulating the power and time of pulse.
- Figure 1.2** Schematic image for a PcRAM cell of the *SET* state (left) and the *RESET* state (right), where the phase change material (PCM) is in a crystalline or amorphous phase. PcRAM storage element is conceptually a tunable resistor, usually realized by connecting the PCM layer with a metallic electrode, called a heater, that forces high current density; a Joule heating-induced phase change then occurs in the phase change volume.

**Figure 1.3** (a) STEM image of PcRAM cell and EDS line profiles show the non-stoichiometric composition on vertical line 1. Sb accumulated in the phase change volume. [9] (b) An EDS mapping shows Sb accumulated in the phase change volume and Ge diffused out of the phase change volume after cycling.

**Figure 1.4** (a) Void generated at the interface between the phase change volume (blue dotted line) and bottom electrode after cyclic operation in PcRAM. [14] (b) Void generation in the inside of phase change material with *RESET-stuck* failure. [8]

**Figure 1.5** Reported results of current-induced change in phase change materials with respect to current density level. The behavior of applying current density ranged approximately  $10^6$  A/cm<sup>2</sup> has not been reported yet.

**Figure 2.1** Equilibrium phase diagram for alloys along the pseudo-binary tie-line GeTe-Sb<sub>2</sub>Te<sub>3</sub> (adapted from references [20, 21]. In the lower section of the figure, the existence of metastable phases is also shown. Reprinted with permission from [22].

**Figure 2.2** (a) Atomic arrangement for metastable rock-salt  $\text{Ge}_2\text{Sb}_2\text{Te}_5$  structure built based on (111) planes along the [111] direction. (b) Atomic arrangement for stable hexagonal  $\text{Ge}_2\text{Sb}_2\text{Te}_5$  structure built based on (0001) planes along the [0001] direction. [32]

**Figure 2.3** (a) Pressure-induced changes of the XRD pattern of  $\text{Ge}_2\text{Sb}_2\text{Te}_5$  upon compression. The peaks marked by \* are the corresponding peaks of the NaCl marker. (b) Volume of unit cell according to pressure (solid point) and fitting using Birch-Murnaghan EOS (solid line). [35]

**Figure 2.4** (a) Sheet resistance of 80 nm thin  $\text{Ge}_2\text{Sb}_2\text{Te}_5$  film measured with increasing temperature. Sharp drops accompany the amorphous-FCC transformation at  $T_1$  and the FCC-HCP transformation at  $T_2$ . (b) Sheet resistance upon subsequent cooling. The resistance of the FCC phase (Curve 1) increases with cooling, whereas that of the HCP phase (Curve 2) decreases. [27]

**Figure 2.5** (a) Temperature dependence of the sheet resistance on GeTe. (b) Temperature dependence of the sheet resistance on  $\text{GeSb}_2\text{Te}_4$ . [45]

**Figure 2.6** Total energy per atoms,  $E_{\text{diff}}$ , of the metastable cubic  $\text{GeSb}_2\text{Te}_4$  and stable hexagonal  $\text{GeSb}_2\text{Te}_4$  with respect to vacancy layer formation. [48]



**Figure 2.7** (a) Compositional profiles in  $\text{Ge}_2\text{Sb}_2\text{Te}_5$  line from WDS analysis shown as atomic concentration and their SEM image. [13] (b) Image of the capped pattern of  $\text{Ge}_2\text{Sb}_2\text{Te}_5$  after voltage sweeping. Mass depleted regions were blackened out in the individual element mapping. [11]

**Figure 2.8** (a) Cell structure of the real device (mushroom-structure). (b) Current density and (c) temperature profile in  $\text{Ge}_2\text{Sb}_2\text{Te}_5$  layer of structure (a). (d) Compositional profiles after pulse stressing with various duration time for Ge, Sb, and Te calculated from the finite differential method (FDM). [55]

**Figure 2.9** (a) atomic concentration and (b) relative intensity showing the atomic diffusion from the anode to the cathode in crystalline  $\text{Ge}_2\text{Sb}_2\text{Te}_5$  line after the DC stressing.

**Figure 3.1** (a) SEM Images and (b) schematic of cross-section image of the line-shaped structure of chalcogenide material for electromigration test, which dimension is 20  $\mu\text{m}$  in length, 2  $\mu\text{m}$  in width and 300 nm in thickness. The chalcogenide materials were isolated by Mo contact pads and passivated with a silicon nitride film 100 nm in thickness.

**Figure 3.2** Schematic diagram of the system for electromigration test using electrical pulse stressing in the wafer-level.

**Figure 3.3** The electromigration tester for package-level test (Qualitau MIRA EM tester). Two EM modules are housed in one MIRA mainframe, with each module providing a capability of running experiments on up to 60 devices under test (DUTs), each at different stress conditions. This equipment was automatically controlled by a commercial program (Qualitau Co.)

**Figure 4.1** (a) Relative resistance-time curves during constant DC current stress on  $\text{Ge}_2\text{Sb}_2\text{Te}_5$  line samples. The stress current ranged from 0.17 to 1.83  $\text{MA}/\text{cm}^2$  at 200 °C. (b) Based on the current density, different microstructures developed in the  $\text{Ge}_2\text{Sb}_2\text{Te}_5$  line samples, as shown by the SEM images. Current densities below 0.83  $\text{MA}/\text{cm}^2$ , ranging from 1 to 1.5  $\text{MA}/\text{cm}^2$  and above 1.67  $\text{MA}/\text{cm}^2$  are denoted as “low current”, “mid current” and “high current”, respectively.

**Figure 4.2** Compositional changes of the sample after the EM stressing at a current density of 1.83  $\text{MA}/\text{cm}^2$  (high current) and 1.17  $\text{MA}/\text{cm}^2$  (mid current).

**Figure 4.3** Resistance-time curves illustrating DC and AC (frequency of 10 MHz) current stressing of  $1.17 \text{ MA/cm}^2$  at  $200^\circ\text{C}$ . The SEM image for each result is also displayed.

**Figure 4.4** (a) High-contrast image of the  $\text{Ge}_2\text{Sb}_2\text{Te}_5$  line sample after testing at  $1.17 \text{ MA/cm}^2$  at  $200^\circ\text{C}$ , as observed by TEM. The gray region denotes  $\text{Ge}_2\text{Sb}_2\text{Te}_5$ , and the dark areas denote defects. (b) The area analysis of the defects as measured by the image analyzer.

**Figure 4.5** Schematic image of homogenous particle model on the (a) rectangular type and (b) top view. (c) Calculation of area sectioned from sphere according to the y-axis distance.

**Figure 4.6** Simulation of relative resistance according to volume fraction of voids, which is calculated using the dispersed particle model. (eq. 4.7) The expansion graph for volume fraction ranged from 0 to 0.5 is displayed in the inset image.

**Figure 4.7** Compositional analysis from SEM and TEM, which contain different interaction volumes. Three different quantitative results are included: the total composition of the sample by SEM, the composition of the non-voided area by TEM, and the composition of the void by TEM.

**Figure 4.8** Pseudo-binary phase diagram of  $\text{Sb}_2\text{Te}_3$  and  $\text{GeTe}$ . Molten state of  $\text{Ge}_2\text{Sb}_2\text{Te}_5$  is separated into two phase during solidification process, which are Sb-rich liquid phase and Ge-rich solid phase.

**Figure 4.9** Schematic diagram of the defect-induced melting and phase separation behavior during solidification.

**Figure 5.1** Resistivity of  $\text{Ge}_2\text{Sb}_2\text{Te}_5$  for a current sweep using the double directional mode, with a sweep from zero to peak current and a return to zero, at room temperature for the 0.33 and 0.5  $\text{MA}/\text{cm}^2$  conditions. (b) Resistivity change for peak current densities ranging from 0.33 to 1.67  $\text{MA}/\text{cm}^2$  in increments of 0.17  $\text{MA}/\text{cm}^2$ .

**Figure 5.2** Cyclic test for current sweep from 0 to 1.67  $\text{MA}/\text{cm}^2$  with a fixed peak-current-density of 1.67  $\text{MA}/\text{cm}^2$  at room temperature for  $\text{Ge}_2\text{Sb}_2\text{Te}_5$ . The inset of **Figure 5.2** shows a resistivity during cyclic current sweep ranging from 0.0018 to 0.0035  $\Omega\text{cm}$ . An irreversible change in resistivity was completed during the first cycle of applied current.

**Figure 5.3** (a) The resistivity of current-stressed  $\text{Ge}_2\text{Sb}_2\text{Te}_5$  from **Figure 5.1(b)** for temperatures ranging from 30 to 90 °C. The dotted lines are extrapolations whose slopes correspond to the temperature coefficient of resistance (TCR). (b) Resistivity of current-stressed  $\text{Ge}_2\text{Sb}_2\text{Te}_5$  for temperature ranging from 150 to 373 K. Conditions of current density were 0.67 MA/cm<sup>2</sup> (black square), 1 MA/cm<sup>2</sup> (red diamond), and 1.5 MA/cm<sup>2</sup> (blue triangle).

**Figure 5.4** Resistivity slope for current density and temperature according to the stress peak current density results from **Figure 5.1(b)** and **5.3(a)**, respectively. The behavior of the TCR in  $\text{Ge}_2\text{Sb}_2\text{Te}_5$  was similar to the resistivity slope for the current density, which changed from negative to positive at the peak current density of 1 MA/cm<sup>2</sup>.

**Figure 5.5** (a)-(c) Resistivity of  $\text{Ge}_2\text{Sb}_2\text{Te}_5$  for peak-current densities ranging from 0.17 to 2 MA/cm<sup>2</sup> in increments of 0.08 MA/cm<sup>2</sup> at different temperatures which are (a) room temperature, (b) 100 °C, and (c) 200 °C, respectively. (d) Final resistivity and (e) slope of resistivity of  $\text{Ge}_2\text{Sb}_2\text{Te}_5$  according to peak current density at various temperature based on the results from (a)-(c).

**Figure 5.6** (a) Resistivity change of  $\text{Ge}_2\text{Sb}_2\text{Te}_5$  according to the duration of applied current density, ranging from 0.17 to 1.33  $\text{MA}/\text{cm}^2$ , for 30 hours and its expansion (dotted box) from 0 to 1 hour. (b) Initial and final resistivities of  $\text{Ge}_2\text{Sb}_2\text{Te}_5$  according to the current density for the current-stressed condition result from (a).

**Figure 5.7** (a) Resistivity change of  $\text{Ge}_2\text{Sb}_2\text{Te}_5$  according to the duration of applied temperature, ranging from 200 to 350  $^{\circ}\text{C}$ , for 30 hours and its expansion (dotted box) from 0 to 1 hour. (d) Initial and final resistivities of  $\text{Ge}_2\text{Sb}_2\text{Te}_5$  according to the ambient temperature for the isothermal annealing condition result from (c). The electric current has a kinetically fast effect on resistivity compared with thermal stress, which involves a thermally activated change.

**Figure 5.8** (a) TEM image and (b) diffraction pattern of the initial  $\text{Ge}_2\text{Sb}_2\text{Te}_5$  sample, which was not applied by thermal and electrical stress. The microstructure of the current sample was in a polycrystalline cubic phase and the average grain size was approximately 20 nm.

**Figure 5.9** (a) TEM image and (b) diffraction pattern of the current-stressed  $\text{Ge}_2\text{Sb}_2\text{Te}_5$  sample (Current sample:  $1 \text{ MA/cm}^2$  condition). The yellow dotted lines indicate the grain boundary. The microstructure of the current sample was in a polycrystalline cubic phase and the average grain size was approximately 20 nm. (c) TEM image and (d) diffraction pattern of the temperature-stressed  $\text{Ge}_2\text{Sb}_2\text{Te}_5$  sample (temperature sample:  $250^\circ\text{C}$  condition). An HRTEM image of a single grain is displayed in the inset of (c). Large grains of more than 100 nm in a hexagonal phase were observed in the temperature sample.

**Figure 5.10** JCPDS database of (a) face-centered cubic phase and (b) hexagonal close-packed phase of  $\text{Ge}_2\text{Sb}_2\text{Te}_5$ .

**Figure 5.11** XRD result of  $\text{Ge}_2\text{Sb}_2\text{Te}_5$  for different annealing temperatures: Si substrate (blue), pre-annealed  $\text{Ge}_2\text{Sb}_2\text{Te}_5$  (red),  $\text{Ge}_2\text{Sb}_2\text{Te}_5$  annealed at  $250^\circ\text{C}$  for 30 hours (black), and  $\text{Ge}_2\text{Sb}_2\text{Te}_5$  annealed at  $350^\circ\text{C}$  for 1 hour (green).

**Figure 5.12** (a) Resistivity change of GeSb<sub>4</sub>Te<sub>7</sub> with current densities for peak current densities ranging from 0.17 to 1.67 MA/cm<sup>2</sup> in increments of 0.17 MA/cm<sup>2</sup> at room temperature. (b) Final resistivity of Ge<sub>2</sub>Sb<sub>2</sub>Te<sub>5</sub> and GeSb<sub>4</sub>Te<sub>7</sub> according to peak current density at room temperature (results from **Figure 5.1(b)** and **Figure 5.12(a)**, respectively).

**Figure 5.13** (a) The resistivity of current-stressed GeSb<sub>4</sub>Te<sub>7</sub> for temperatures ranging from 30 to 90 °C. The dotted lines are extrapolations whose slopes correspond to the TCR. (b) Resistivity slope of Ge<sub>2</sub>Sb<sub>2</sub>Te<sub>5</sub> and GeSb<sub>4</sub>Te<sub>7</sub> for current density and temperature according to the stressed-peak-current-density results for Ge<sub>2</sub>Sb<sub>2</sub>Te<sub>5</sub> (**Figure 5.1(b)** and **Figure 5.3(a)**) and GeSb<sub>4</sub>Te<sub>7</sub> (**Figure 5.12(a)** and **Figure 5.13(a)**).

**Figure 5.13** (a)-(c) Resistivity change of GeSb<sub>4</sub>Te<sub>7</sub> for peak-current-densities ranging from 0.17 to 2 MA/cm<sup>2</sup> in increments of 0.08 MA/cm<sup>2</sup> at different temperatures: (a) room temperature, (b) 100 °C, and (c) 200 °C. (d) Final resistivity of GeSb<sub>4</sub>Te<sub>7</sub> according to the peak-current-density at various temperatures, based on the results from (a)-(c).



**Figure 5.14** Resistivity of  $\text{Ge}_2\text{Sb}_2\text{Te}_5$  affected by alternating current (AC) and direct current (DC). (a) Resistivity of  $\text{Ge}_2\text{Sb}_2\text{Te}_5$  according to AC frequency from  $10^2$  to  $10^7$  Hz with 1 sec of duration time and 10 V of voltage. (b) Resistivity of  $\text{Ge}_2\text{Sb}_2\text{Te}_5$  according to AC voltage from 1 to 10 V with 1 sec of duration time and 100 Hz of frequency. (c) Resistivity of  $\text{Ge}_2\text{Sb}_2\text{Te}_5$  according to AC time from 0 to 3 hours with voltage of 10 V and frequency of 100 Hz. (d) Resistivity of  $\text{Ge}_2\text{Sb}_2\text{Te}_5$  according to DC and 100 Hz of AC from 1 to 10 V with 1 sec of duration time.

**Figure 5.15** The schematic diagram of the energy states according to the vacancy rearrangement in the cubic and hexagonal phases of Ge-Sb-Te compound. The energy state decreases with vacancy ordering, which is a stable state. The energy barrier for the phase transition from the cubic to the hexagonal phase is much higher than the energy barrier for the rearrangement of vacancies.

**Figure 6.1** Resistivity change of  $\text{Ge}_2\text{Sb}_2\text{Te}_5$  according to the duration of applied current density, ranging from 0.17 to  $1.33 \text{ MA/cm}^2$ , for 30 hours at the different ambient temperature: (a) room temperature, (b)  $100^\circ\text{C}$ , and (c)  $200^\circ\text{C}$

**Figure 6.2** SEM image of  $\text{Ge}_2\text{Sb}_2\text{Te}_5$  line after current stressing test for 30 hours at room temperature, which are shown in **Figure 6.1(a)**. Background color means the group of failure behavior based on the morphological image. Current density below  $1.17 \text{ MA/cm}^2$  is determined to “no fail” (gray), current density ranged from  $1.17$  to  $1.67 \text{ MA/cm}^2$  is determined to “gradual fail” (red), and current density over  $1.83 \text{ MA/cm}^2$  is determined to “abrupt fail” (blue).

**Figure 6.3** Mechanism map of  $\text{Ge}_2\text{Sb}_2\text{Te}_5$  according to current density and temperature based only on the morphological behavior. All solid point are experiment results and failure mechanisms are expressed by background color. Black square shows “no fail”, red circle shows “gradual fail”, and blue triangle shows “abrupt fail”.

**Figure 6.4** Resistivity change with applying current density of  $0.33 \text{ MA/cm}^2$  for 30 hours at  $100^\circ\text{C}$  according to different Te-based chalcogenide materials, which are  $\text{Bi}_2\text{Te}_3$ ,  $\text{Sb}_2\text{Te}_3$ ,  $\text{GeTe}$ , and  $\text{Ge}_2\text{Sb}_2\text{Te}_5$ . The relative resistance means that value of resistance is divided by the initial resistance of each material.

**Figure 6.5** Phase diagram of bismuth and tellurium according to atomic percent of tellurium.

**Figure 6.6** Relative resistance of  $\text{Bi}_2\text{Te}_3$  according to current density ranged from 0.33 to 1.33  $\text{MA}/\text{cm}^2$  for 30 hours at 100 °C, and their SEM image. Current densities below 0.83  $\text{MA}/\text{cm}^2$ , ranging from 0.83 to 1.17  $\text{MA}/\text{cm}^2$  and above 1.17  $\text{MA}/\text{cm}^2$  are denoted as “no fail”, “gradual fail” and “abrupt fail”, respectively.

**Figure 6.7** Relative resistance of  $\text{Bi}_2\text{Te}_3$  according to current density ranged from 0.33 to 1.5  $\text{MA}/\text{cm}^2$  for 30 hours at (a) room temperature, (b) 100 °C, and (c) 200 °C. (d) The mechanism map according to current density and temperature, which is the merging of the results from (a)-(c).

**Figure 6.8** Relative resistance of  $\text{Bi}_{35}\text{Te}_{65}$  according to current density ranged from 0.33 to 1.5  $\text{MA}/\text{cm}^2$  for 30 hours at (a) room temperature, (b) 100 °C, (c) 150, and 200 °C. (d) The mechanism map according to current density and temperature, which is the merging of the results from (a)-(c).

**Figure 6.9** The failure time according to current density and temperature in the  $\text{Bi}_{35}\text{Te}_{65}$  and  $\text{Bi}_2\text{Te}_3$ . Failure time is displayed in the log-scale.

**Figure 6.10** Expanded phase diagram of Bi and Te with atomic percent of Te ranged from 60 to 90 at. %, and mechanism map of stoichiometric  $\text{Bi}_2\text{Te}_3$  (Te : 60 at. %) and non-stoichiometric  $\text{Bi}_{35}\text{Te}_{65}$  (Te : 65 at. %).

**Figure 7.1** Summary of behavior in phase change materials according to current density.

# CHAPTER 1

## Introduction

### 1.1. Phase change random access memory (PcRAM)

Phase change random access memory (PcRAM) is a promising device for non-volatile memory that uses a reversible transition between a material's phases.<sup>1,2,3</sup> PcRAM uses two types of phases to store information: amorphous and crystalline phases. **Figure 1.1** shows a graphical representation of the material phases in PcRAM devices. The crystal structure exhibits regularity over long distances in the crystal lattice, which is called long-range ordering. In this phase, the material has high electrical conductivity and high reflectivity. In contrast, the crystal structure of amorphous phases is disordered and randomly distributed with atomic-scale regularity, which is called short-range ordering. In this phase, the material has low electrical conductivity and low reflectivity compared to the crystalline phase. The difference in resistivity between crystalline and amorphous phases is approximately three orders of magnitude.<sup>2</sup> Thus, these phases can be easily recognized by an electrical signal, such as a current or voltage, in the device system, which enables a PcRAM device to store information.<sup>4</sup>

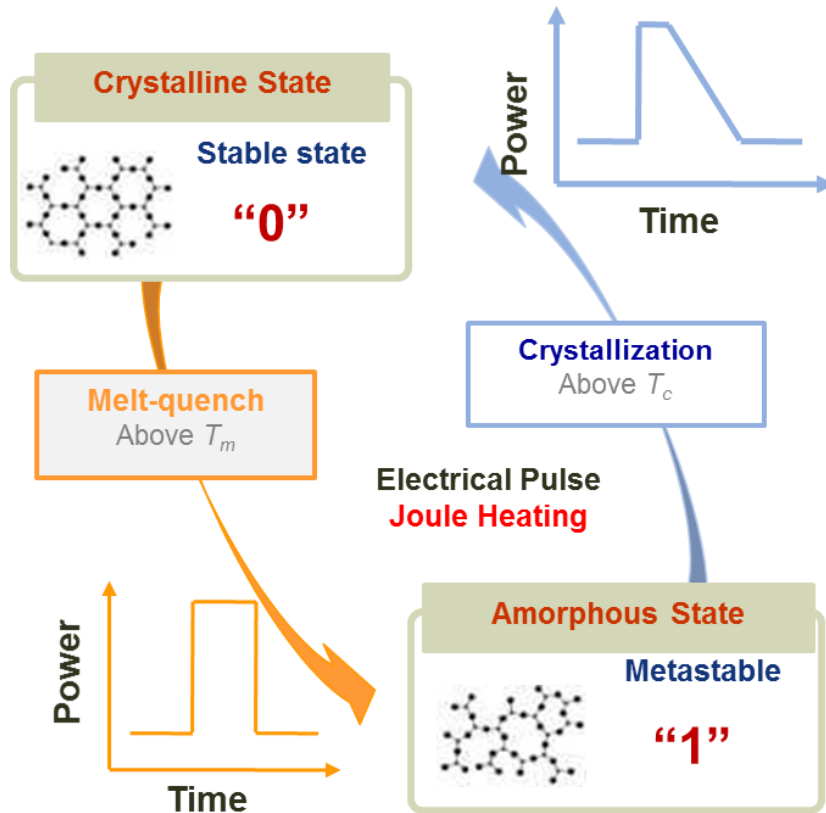


**Figure 1.1** A graphical representation of material phases and principle of operation in PcRAM device. The crystalline phase is denoted as *SET* state, and the amorphous phase is denoted as *RESET* state. The phase transformation is caused by Joule heating with modulating the power and time of pulse.

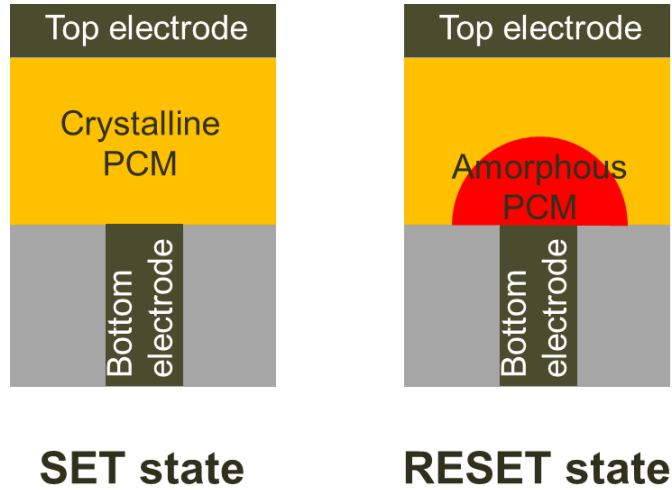


**Figure 1.2** Schematic image for a PcRAM cell of the *SET* state (left) and the *RESET* state (right), where the phase change material (PCM) is in a crystalline or amorphous phase. PcRAM storage element is conceptually a tunable resistor, usually realized by connecting the PCM layer with a metallic electrode, called a heater, that forces high current density; a Joule heating-induced phase change then occurs in the phase change volume.

The phases of phase-change materials can be altered by applying an electric pulse ( $\sim 10^8$  A/cm<sup>2</sup>). A high current density generates localized heat from Joule heating. The material states that form from Joule heating are influenced by the current density and duration of the electric pulse. A high-density electric pulse applies enough Joule heating to raise the temperature above the melting temperature ( $T_m$ ) to change the phase of a material, thus allowing a transformation to a liquid phase during the pulse. This liquid phase is an intermediate state. To transform an amorphous phase into a crystalline phase, the electric pulse is reduced for a sufficient amount of time to allow the crystallization of a liquid phase, which is referred to as the *SET* operation in PcRAM and ranges from 100 ns to 1  $\mu$ s.<sup>5</sup> To transform a crystalline phase into an amorphous phase, however, the electric pulse is reduced quickly enough to quench the liquid phase, which is referred to as the *RESET* operation in a PcRAM device. Strong confinement of the heat and electric current are required for efficient Joule heating in the cell. This condition is usually satisfied by a narrow bottom electrode, which is known as the heater. Therefore, only a portion of the volume of the phase-change material is melted and transformed into an amorphous phase. The amorphous phase occupies a typical dome-shaped volume, which is called a mushroom cell structure.

PcRAM has various advantages for application in memory devices, including fast programming speed<sup>1</sup>, high endurance<sup>2</sup>, and high scalability<sup>3</sup>. Theoretically, phase change mechanisms occur at the nanometer scale.<sup>3</sup> In addition, PcRAM cells have a 1T1R (one transistor and one resistor) structure, which is a very simple structure.<sup>6</sup> Using this simple cell structure facilitates the integration of PcRAM cells into conventional CMOS process technology for conventional memory devices such as DRAM and FLASH, which is a huge advantage for device integration with respect to cost.

However, PcRAM should overcome reliability problems that originate from extrinsically harsh operating conditions. To employ PcRAM as the main memory device, its endurance characteristic should achieve  $10^{16}$  cycles. However, recently developed PcRAM devices typically exhibit only  $10^8 \sim 10^9$  cycles. The reliability issues in PcRAM will be considered in the next section.

## 1.2. Reliability issues in PcRAM

### 1.2.1. Endurance problem

After many *SET-RESET* cycles, PcRAM cells end up with one of two types of failure: *SET-stuck* failure and *RESET-stuck* failure.<sup>7</sup> This practical problem in PcRAM devices originates from high current density. In a *SET-stuck* problem, the resistance of the phase-change material is degraded and fixed at a low resistance value. Switching from a crystalline to amorphous phase is prohibited despite any *RESET* operation. *SET-stuck* problems originate from compositional changes in the phase-change material in the phase change region. Recent studies have shown that  $\text{Ge}_2\text{Sb}_2\text{Te}_5$  (GST) materials-based PcRAM cells tend to show depletion in germanium (Ge) and enrichment in antimony (Sb) inside the active volume of the  $\text{Ge}_2\text{Sb}_2\text{Te}_5$ .<sup>7,8</sup> Park et al. reported that enrichment in Sb and depletion in tellurium (Te) were observed at the bottom electrode. The behavior of Ge was not observed in this study.<sup>9</sup> Although the directions of elements are controversial issues, compositional changes and atomic demixing are obvious results after cyclic switching, which is related to *SET-stuck* failure. Previous reports on the origin of compositional changes in  $\text{Ge}_2\text{Sb}_2\text{Te}_5$  suggested that incongruent melting<sup>10</sup>, thermal diffusion<sup>9</sup>, and mass flow



were enhanced by electric fields.<sup>11,12,13</sup>

In a *RESET*-stuck problem, the resistance of the phase-change material is fixed at a high resistance value, which is the amorphous phase. Switching from an amorphous to a crystalline phase is prohibited despite any *SET* operation. *RESET*-stuck problems originate from delamination at the bottom electrode, which is related to the formation of voids in the phase-change material.<sup>7, 8, 14</sup> These endurance problems originate from the migration of atoms.

### 1.2.2. Migration behavior in PcRAM

As the memory density increases, the phase-change material experiences harsher operating conditions, such as high current density and temperature, which cause reliability issues and failure. Compositional changes and void formation in phase-change materials are major reliability problems in PcRAM.<sup>8,9</sup> These durability problems are caused by the mass transport of compositional elements including electric and thermal stress. First, an electric stress results in the mass transport of constituent atoms, including the electric current of the field, which is known as electromigration (EM). Previous research has focused on the liquid phase, which is the intermediate state of transformation between crystalline and amorphous phases during PcRAM operation. For example, the separation of elements in  $\text{Ge}_2\text{Sb}_2\text{Te}_5$  has been observed during high current stressing in the liquid phase.<sup>12,13</sup> During current stressing, the ionized elements of liquid GST are affected by the electric field and their direction depends on the charge of the ion.

Thermal stress also influences the migration of atoms in PcRAM.  $\text{Ge}_2\text{Sb}_2\text{Te}_5$ , which is one of the most promising materials for PcRAM, should be separately phased to a liquid phase and a solid phase because Ge-Sb-Te compounds do not melt congruently.

<sup>10</sup> The temperature range from 630 to 650 °C is the region of incongruent melting,

which contains liquid and solid phases simultaneously. The problem is the composition difference between the liquid phase and solid phase in the incongruent region, namely, a Sb and Te-rich liquid phase and Ge-rich solid phase. This phase separation occurs with the formation of a Ge-rich solid phase at the heat sink during the solidification of the phase-change material. Phase transformation in phase-change materials generates mechanical stress because of density differences. Various phases exist in Ge-Sb-Te compounds, including amorphous, cubic crystalline, and hexagonal crystalline phases. The difference in density between the amorphous phase and hexagonal crystalline phase is theoretically approximately 10 %. <sup>14</sup> This difference in density causes volume shrinkage for the *SET* state, which generates large tensile stress at the active region in the phase-change material. Repeating these thermal operations during programming causes the coalescence of voids and eventually results in cell failure.

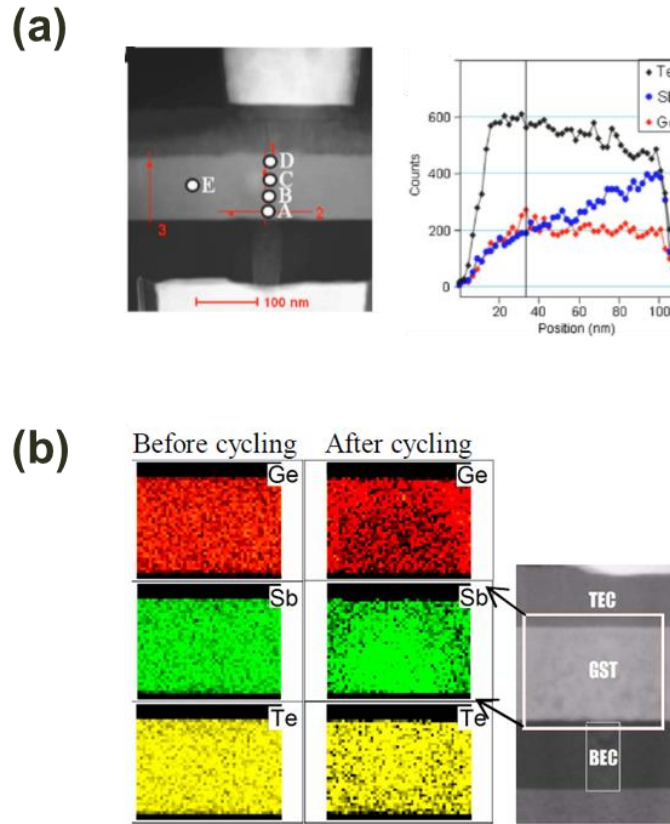


**Figure 1.3** (a) STEM image of PcRAM cell and EDS line profiles show the non-stoichiometric composition on vertical line 1. Sb accumulated in the phase change volume. [9] (b) An EDS mapping shows Sb accumulated in the phase change volume and Ge diffused out of the phase change volume after cycling.

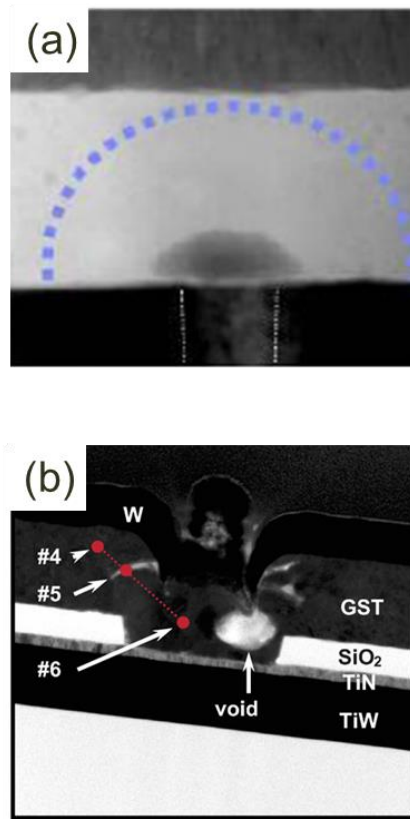


**Figure 1.4** (a) Void generated at the interface between the phase change volume (blue dotted line) and bottom electrode after cyclic operation in PcRAM. [14]  
(b) Void generation in the inside of phase change material with *RESET-stuck* failure. [8]

### **1.3 Objective of the thesis**

As mentioned above, previous research regarding PcRAM reliability predominantly focused on liquid phases. Because the atomic diffusivity of liquid phases is much faster than the atomic diffusivity in crystalline phases,<sup>13</sup> electric field-induced failures predominantly occur in the liquid phase. Therefore, the effect of a current density below  $10^7$  A/cm<sup>2</sup> on phase-change materials has not been reported and crystalline phases have been considered a stable state for electromigration.

However, not all regions of a phase-change material experience melting during PcRAM operation. Only the active region, which is the limited zone near the heater, can be transformed into a liquid phase. The alternate region remains a crystalline phase without melting, despite repeated PcRAM operation. The effect of atomic migration in the crystalline regions is cumulative, whereas the effect that evolves in the active region can be recovered through melting and solidification processes. This cumulative effect on the crystalline phase can affect the reliability of the *SET* state of the phase-change material, which becomes more significant in multi-level cell (MLC) devices. Therefore, investigating the migration behavior of the crystalline phase of Ge<sub>2</sub>Sb<sub>2</sub>Te<sub>5</sub> is important to gain a comprehensive understanding of the reliability of phase-change materials. The elements of crystalline GST are affected by an electric current, which is the momentum transfer between charge carriers and atoms.<sup>15</sup> EM in crystalline GST has been demonstrated to cause direct amorphization without melting, which signifies that EM in the crystalline phase has sufficient power to affect the solid-state structure.<sup>16</sup> As the dimensions of devices diminish, the current density is anticipated to increase,<sup>17</sup> and degradation in the crystalline state may become a significant reliability problem for a PcRAM cell.

The objective of this thesis is to clearly identify the effect of electric currents on the crystalline phase of phase-change materials and to provide the guidelines for improving their endurance. The atomic displacement from a low current, approximately  $10^6$  A/cm<sup>2</sup>, is negligible compared to that from a high current because the driving force is insufficient to generate a massive flux of atoms. Although no catastrophic failure is induced by an electric current in crystalline phase-change materials, various phenomena that have not been reported are observed in crystalline Ge<sub>2</sub>Sb<sub>2</sub>Te<sub>5</sub>. The resistance of phase-change materials, especially Ge-Sb-Te compounds, is very sensitive to external signals such as thermal stress and electric stress because phase-change materials have various phases, such as cubic and hexagonal structures.<sup>18</sup> Therefore, investigating the migration behavior of the crystalline phase of Ge<sub>2</sub>Sb<sub>2</sub>Te<sub>5</sub> is important to gain a comprehensive understanding of the reliability of phase-change materials. To achieve this objective, a simple structure with a line shape is used for a model study instead of a PcRAM cell structure. Because the factors that influence the material structure and environment are mixed in the actual device, we cannot distinguish the effect of electric currents from those of other factors. In addition, actual devices are too small to investigate the degradation behaviors in phase-change materials. By using a line structure for a model study, we can clearly identify the various mechanisms that are related to degradation or structural changes in phase-change materials, depending on the current density. We believe that this work provides new insight regarding electrical reliability in the crystalline phase of phase-change materials, which offers new design rules and applications for crystalline-based PcRAM devices. Scientifically, this work adds to the fundamental understanding of the influence of electric currents on the crystalline phase of chalcogenide materials.





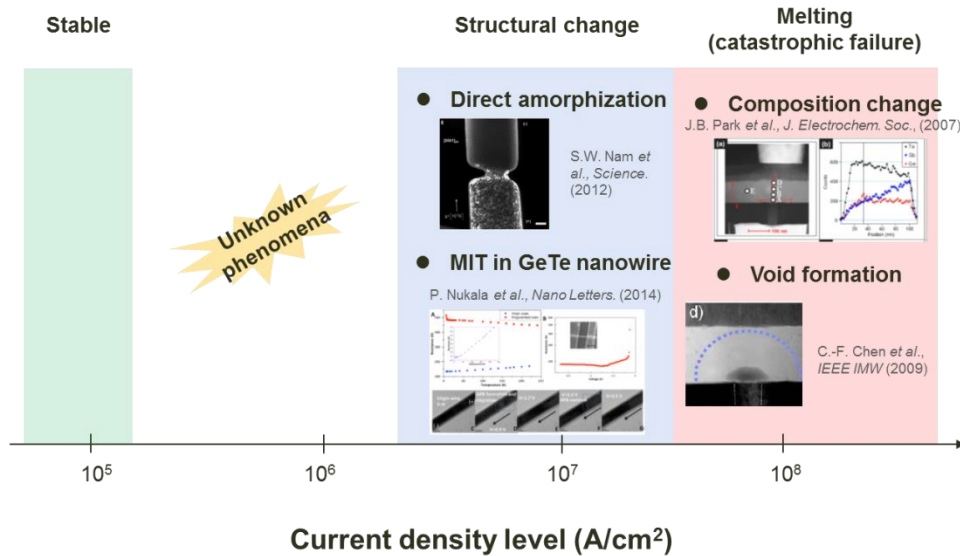


**Figure 1.5** Reported results of current-induced change in phase change materials with respect to current density level. The behavior of applying current density ranged approximately  $10^6 A/cm^2$  has not been reported yet.

## **1.4. Organization of the thesis**

This thesis consists of seven chapters. In **Chapter 2**, the physical properties of phase change material is reviewed. The previous research of current effect on GST is also explained in **Chapter 2**. The basic theory of mass transport induced by electric stress, electromigration is discussed in detail. **Chapter 3** describes the experimental procedure, including the fabrication of samples. In **Chapter 4**, gradual degradation in the crystalline  $\text{Ge}_2\text{Sb}_2\text{Te}_5$  under electric current is explained, which has never been reported. **Chapter 5** discusses the metal-insulator transition induced by electric current without phase transition. This phenomenon differs significantly from the thermal annealing accompanying phase transition. **Chapter 6** describes mechanism change with respect to the current density and temperature. **Chapter 7** summarizes the results of this study and suggests a method for the improvement of PcRAM reliability.

## CHAPTER 2

### Theoretical background

#### 2.1. Physical properties of phase-change materials

Over the past forty years, many materials have been investigated for their suitability as phase change materials.  $\text{Te}_{48}\text{As}_{30}\text{Si}_{12}\text{Ge}_{10}$  and  $\text{Te}_{81}\text{Ge}_{15}\text{Sb}_2\text{S}_2$  are the materials that Ovshinsky used for his first electrical and optical switching experiments, respectively.

<sup>19</sup> Variations of  $\text{Ge}_2\text{Sb}_2\text{Te}_5$ , Ag or In doped  $\text{Sb}_{69}\text{Te}_{31}$  and Ge-In-Sn-Sb are currently used in various optical recording formats. Phase-change materials should be able to form glasses, which are characterized by a sufficiently low melting point, for the successful application of electrical devices. Furthermore, these materials should have a stable amorphous phase that is characterized by high activation energy toward crystallization and should be able to crystallize rapidly. A high contrast between the amorphous and crystalline states is also important for electrical devices. Chalcogenide alloys, which contain various chalcogen atoms (e.g., sulfur, selenium, and tellurium), show a large contrast in electrical conductivity and optical reflectivity between their crystalline and amorphous phases. In particular, materials that are composed of antimony, tellurium and germanium in various ratios fulfill all these requirements and

are major materials that are used in PcRAM devices. Compositions are usually determined by means of a “composition triangle”, as depicted in **Figure 2.1**. In this chapter, we review the physical properties of phase-change materials with a focus on Ge-Sb-Te compounds.

### 2.1.1. Ge-Sb-Te alloys

Some of the most promising materials for optical devices and phase change memory include phase-change material alloys from the Ge-Sb-Te phase diagram. These materials are mainly focused along the pseudo-binary tie line between GeTe and Sb<sub>2</sub>Te<sub>3</sub>, although other parts of the phase diagram are being investigated as well. **Figure 2.1** shows the pseudo-binary phase diagram along the tie line between GeTe and Sb<sub>2</sub>Te<sub>3</sub> with respect to equilibrium alloys.<sup>20,21</sup> The properties of Ge-Sb-Te alloys were first researched in the former Soviet Union at the end of the 1960s.<sup>19</sup>

At the beginning of the 1990s, Yamada *et al.* recognized that GeSb<sub>2</sub>Te<sub>4</sub> and Ge<sub>2</sub>Sb<sub>2</sub>Te<sub>5</sub> alloys show long-term stability at ambient temperatures and a low crystallization time (approximately 50 ns) under the influence of fast laser irradiation. These properties were advantageous for optical recording. Under the influence of laser irradiation, these alloys transformed into a simple and high-symmetry phase such as a face-centered cubic (FCC) shape, and not into an equilibrium hexagonal close-packed (HCP) crystalline phase.<sup>22</sup> Longer crystalline times would be required to obtain a nine-layer hexagonal structure.

Although the three intermetallic phases GeSb<sub>4</sub>Te<sub>7</sub>, GeSb<sub>2</sub>Te<sub>4</sub>, and Ge<sub>2</sub>Sb<sub>2</sub>Te<sub>5</sub> were possible candidates for phase change material alloys in PcRAM devices, the Ge<sub>2</sub>Sb<sub>2</sub>Te<sub>5</sub> composition exhibited the greatest stability in the amorphous to crystalline

transition with an activation energy of approximately 2.2 eV, as determined by a Kissinger analysis of differential scanning calorimetry (DSC) data.<sup>23</sup>

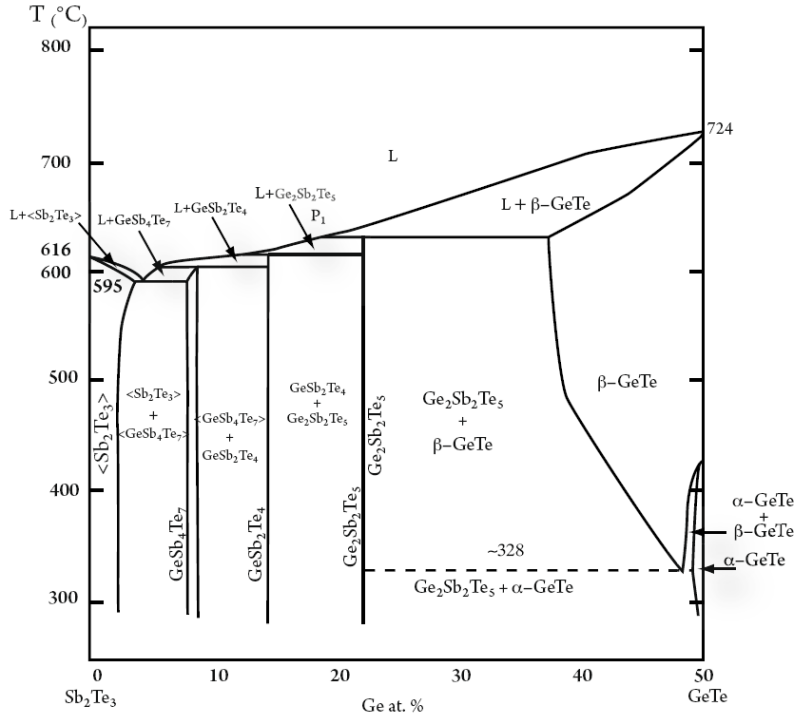


**Figure 2.1** Equilibrium phase diagram for alloys along the pseudo-binary tie-line GeTe-Sb<sub>2</sub>Te<sub>3</sub> (adapted from references [20, 21]. In the lower section of the figure, the existence of metastable phases is also shown. Reprinted with permission from [22].

### 2.1.2 Crystalline structure of Ge-Sb-Te compounds

The equilibrium structure of GeTe-Sb<sub>2</sub>Te<sub>3</sub> pseudo-binary alloys has been examined since the 1980s. The number of layers is listed in the unit cell by the expression (GeTe)<sub>n</sub>(Sb<sub>2</sub>Te<sub>3</sub>)<sub>m</sub> for homologous compounds. For example, the space groups of GeSb<sub>4</sub>Te<sub>7</sub> (n=1, m=2), GeSb<sub>2</sub>Te<sub>4</sub> (n=1, m=1), and Ge<sub>2</sub>Sb<sub>2</sub>Te<sub>5</sub> (n=2, m=1) are *P3m1*, *R3m*, *P3m1*, respectively.<sup>24, 25, 26</sup> The existence of these series has been confirmed for a wide range of compositions with  $n \leq 4$  and  $m \leq 4$ . However, extremely long unit cells such as GeSb<sub>8</sub>Te<sub>13</sub> (n=1, m=4) are difficult to form because they require long thermal annealing to allow for sufficient diffusion time.

The crystalline structures of Ge-Sb-Te alloys show two different crystalline phases. Ge-Sb-Te alloys first crystallize into a metastable rock-salt structure at low temperature and then into a stable hexagonal structure at higher temperature during heating.<sup>27</sup> **Figure 2.2(a)** shows a metastable rock-salt structure, which forms over 150 °C. The crystalline structures of GeSb<sub>4</sub>Te<sub>7</sub>, GeSb<sub>2</sub>Te<sub>4</sub>, and Ge<sub>2</sub>Sb<sub>2</sub>Te<sub>5</sub>, which were determined by diffraction-based investigation, formed in the rock-salt structure. The rock-salt structure consists of two interpenetrating FCC sub-lattices; one sub-lattice is located at the origin and the other is located at (0.25, 0.25, 0.25). Te atoms perfectly occupy one FCC sub-lattice, while Ge and Sb atoms randomly occupy the other FCC sub-lattice with an amount of vacancies that depends on the composition, which are 28.6 % for GeSb<sub>4</sub>Te<sub>7</sub>, 25 % for GeSb<sub>2</sub>Te<sub>4</sub>, and 20 % for Ge<sub>2</sub>Sb<sub>2</sub>Te<sub>5</sub>.<sup>18</sup> The presence of Peierls like distortion in the Ge-Sb-Te alloys was subsequently shown both theoretically and experimentally from x-ray diffraction.<sup>28, 29</sup>

**Figure 2.2(b)** shows the stable hexagonal phase of Ge<sub>2</sub>Sb<sub>2</sub>Te<sub>5</sub>, which forms a approximately 300 °C depending on the cooling rate.<sup>27</sup> Density functional theory (DFT) total energy calculations on Ge<sub>2</sub>Sb<sub>2</sub>Te<sub>5</sub> were performed to identify the

structural properties of hexagonal  $\text{Ge}_2\text{Sb}_2\text{Te}_5$  because the stacking order of atoms was hard to deduce from experimental results. *Ab-initio* simulations on  $\text{Ge}_2\text{Sb}_2\text{Te}_5$  alloys by Zhou *et al.* showed that stable hexagonal phases contain intrinsic vacancies within the Te-Te layers.<sup>30</sup> The stable hexagonal  $\text{Ge}_2\text{Sb}_2\text{Te}_5$  alloys consist of nine layers of atoms following the ABC stacking sequence Te-Ge-Te-Sb-Te-Te-Sb-Te-Ge along the [0001] direction in the unit cell.<sup>31, 32</sup> The DFT total energy calculations show that the most stable configuration is the model that was proposed by Kooi and De Hosson, which is Te-Ge-Te-Sb-Te-v-Te-Sb-Te-Ge.<sup>33</sup> This model added a vacancy layer, which is labeled 'v'. The vacancy layers are highly ordered and lie along the [0001] direction between the weak Te-Te layers. Hexagonal phases can exist in PcRAM devices because of the temperature of the fabrication process but are not observed in optical discs.

The concentration of vacancies and their role in the metastable structures of  $\text{GeSb}_4\text{Te}_7$ ,  $\text{GeSb}_2\text{Te}_4$ , and  $\text{Ge}_2\text{Sb}_2\text{Te}$  have been shown to be a necessity based on extended X-ray absorption fine structure (EXAFS) determination of local structures.<sup>34</sup> Vacancies are an intrinsic part of structures. In rock-salt structures, six saturated covalent bonds are populated by two electrons. For this phenomenon to occur, each atom must have six valence electrons, with the number of required electrons differing among elements: Sb needs one additional electron, while Ge needs two additional electrons. These missing electrons are donated to Ge and Sb from Te orbitals that point into vacancies to saturate all octahedral bonds. Therefore, vacancies are a significant factor in the formation of crystalline structures. Pressure has also been suggested to affect the formation of amorphous phases in phase-change materials. Actually, the phase-change materials in PcRAM devices generate 5-6 GPa of pressure because of the volume mismatch between amorphous and crystalline phases.

Diamond-anvil diffraction experiments showed that the hydrostatic compression of  $\text{Ge}_2\text{Sb}_2\text{Te}_5$  results in amorphization, which is a pressure-induced transformation.<sup>35</sup>

**Figure 2.3** shows a series of x-ray diffraction patterns of the metastable crystalline phase of  $\text{Ge}_2\text{Sb}_2\text{Te}_5$  as a function of applied pressure. The crystalline peaks vanished at a pressure over 22 GPa. EXAFS results showed that amorphization initiated at approximately 10 GPa when the Sb atoms in the distorted rock-salt structure reached the center of the cell, leaving vacancies to be compressed.<sup>36</sup> Furthermore, the  $\text{GeSb}_2\text{Te}_4$  phase was amorphized under a lower pressure than the  $\text{Ge}_2\text{Sb}_2\text{Te}_5$  phase. This result means that the concentration of vacancies affects pressure-induced amorphization. Near-edge x-ray absorption measurements also suggested that the local order in the laser-quenched and pressure amorphized phases were similar.<sup>37</sup>



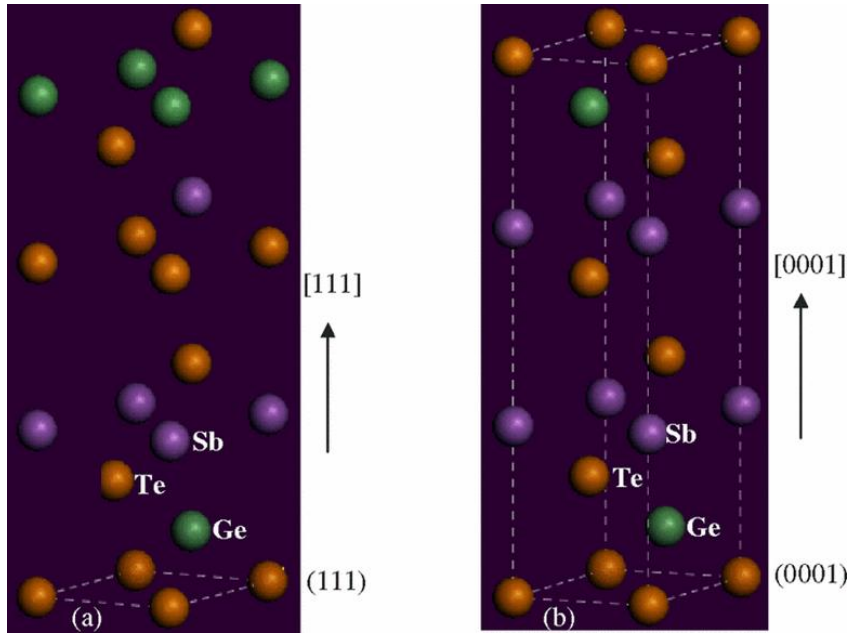


**Figure 2.2** (a) Atomic arrangement for metastable rock-salt  $\text{Ge}_2\text{Sb}_2\text{Te}_5$  structure built based on (111) planes along the [111] direction. (b) Atomic arrangement for stable hexagonal  $\text{Ge}_2\text{Sb}_2\text{Te}_5$  structure built based on (0001) planes along the [0001] direction. [32]

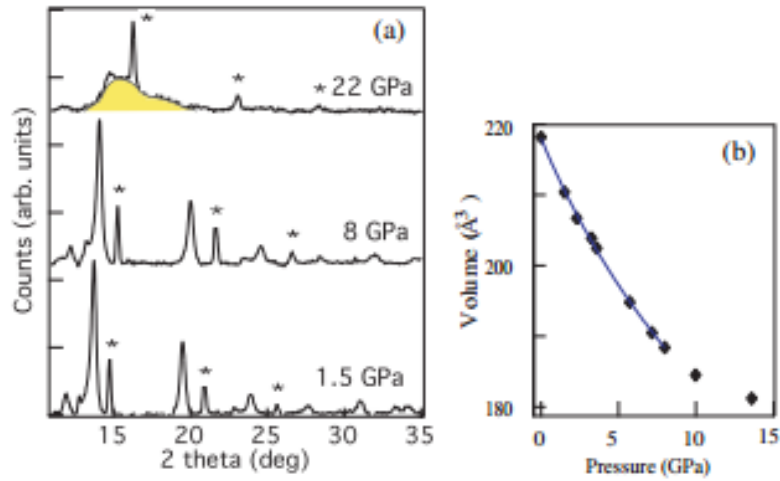


**Figure 2.3** (a) Pressure-induced changes of the XRD pattern of  $\text{Ge}_2\text{Sb}_2\text{Te}_5$  upon compression. The peaks marked by \* are the corresponding peaks of the NaCl marker. (b) Volume of unit cell according to pressure (solid point) and fitting using Birch-Murnaghan EOS (solid line). [35]

### 2.1.3. Temperature dependence of resistivity

The temperature dependence of the sheet resistance of a thin film of  $\text{Ge}_2\text{Sb}_2\text{Te}_5$  is shown in **Figure 2.4**. A 2-3 orders of magnitude drop in sheet resistance was observed at a  $T_1$  temperature near 150 °C, which marks the transformation from an amorphous to FCC crystalline phase.<sup>27</sup> This contrast in resistivity is the major feature of PcRAM devices. The transformation of a very small volume creates a sufficient resistance contrast, which enables the device to electrically read the digital signal. At a higher temperature  $T_2$ , which is approximately 300 °C depending on the sample's characteristics, the metastable FCC phase transformed into a stable hexagonal phase, as mentioned in **Section 2.1.2**. As shown in **Figure 2.4**, the resistances of both amorphous and crystalline phases continuously decrease with temperature, but the origins of these resistance changes are different for each phase. In amorphous  $\text{Ge}_2\text{Sb}_2\text{Te}_5$ , the number of excited carriers increases with temperature, which exponentially decreases the resistance. Because this process is reversible, the resistance returns to its original value when the temperature decreases. Decreases in the resistance of crystalline  $\text{Ge}_2\text{Sb}_2\text{Te}_5$ , however, mainly occur because of an increase in mobility rather than carrier concentration.<sup>38</sup> Declines in scattering at grain boundaries result from grain growth, which increases the mobility of carriers in crystalline  $\text{Ge}_2\text{Sb}_2\text{Te}_5$ . Because this process is irreversible, resistance is maintained at low values when the temperature decreases. During cooling, the FCC phase becomes slightly more resistive while the hexagonal phase becomes more conductive, which will be discussed in the next section.

The heat of crystallization is generated by electrical Joule heating in a PcRAM cell, which actually involves a very interesting electronic switching phenomenon. As the voltage that is applied across an amorphous region increases, the current also increases

but the magnitude is small because of the large resistivity. However, when the voltage exceeds a certain threshold, the material suddenly exhibits a negative differential resistance, which allows a high current. Consequently, the Joule heat from this high current can crystallize the amorphous region.

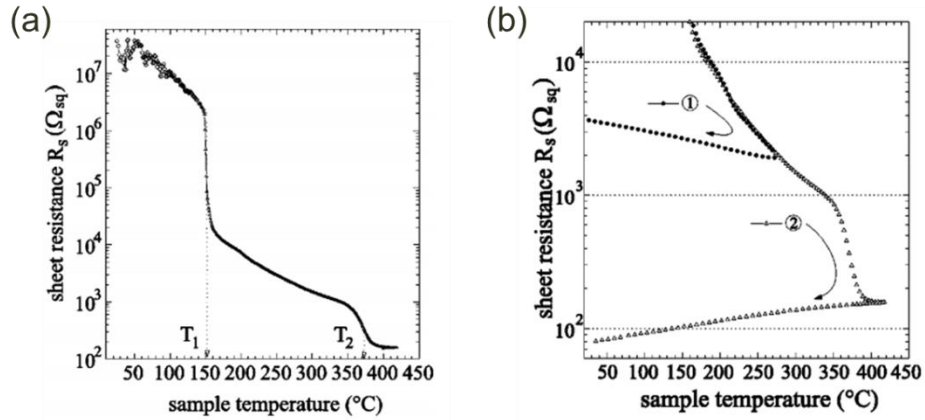


**Figure 2.4** (a) Sheet resistance of 80 nm thin  $\text{Ge}_2\text{Sb}_2\text{Te}_5$  film measured with increasing temperature. Sharp drops accompany the amorphous-FCC transformation at  $T_1$  and the FCC-HCP transformation at  $T_2$ . (b) Sheet resistance upon subsequent cooling. The resistance of the FCC phase (Curve 1) increases with cooling, whereas that of the HCP phase (Curve 2) decreases. [27]

### **2.1.4. Metal-insulator transition in Ge-Sb-Te alloys**

Two different types of solids are distinguished by the relationship between temperature and conductivity. The temperature coefficient of resistivity (TCR) is used as the criterion of this relationship. Experimentally, materials with metallic behavior have positive TCR values and materials with insulating behavior have negative TCR values.<sup>39</sup> Theoretical studies have shown that the limit of resistivity at low temperature (approaching zero Kelvin) is a more accurate criterion for classifying material types. The resistivity of insulators diverges to infinity as the temperature approaches zero Kelvin, while metals maintain a finite resistivity.

Although many models of a metal-insulator transition (MIT) explain changes in the crystal structure and properties, Mott and Anderson's models are representative models for property transitions without a phase change. Mott argued that an MIT occurs when the electron interaction energy exceeds the Fermi energy.<sup>40</sup> On the other hands, Anderson showed that increasing disorder generates a localized state at the Fermi energy.<sup>41</sup> The properties of solids are strongly influenced by the interaction between electrons and the presence of disorder.<sup>42</sup> Both Coulomb correlations (electron) and randomness (disorder) are driving forces behind MITs and involve the localization and delocalization of particles. Although one might be a dominant driving force for MITs, this phenomenon is not always necessarily true. For example, weak disorder weakens the effect of correlation because it redistributes states into the Mott gap and may thus turn an insulator into a metal. Therefore, the interplay between disorder and interaction leads to many subtle body effects, which poses fundamental challenges for theories and experiments.<sup>43,44</sup>

The occurrence of MIT in crystalline Ge-Sb-Te alloys has been recently reported.<sup>39,</sup>  
<sup>45</sup> **Figure 2.5** shows that resistivity measurements of as-deposited films of GeTe and

$\text{GeSb}_2\text{Te}_4$  depend on the ambient temperature. The resistivity of amorphous GeTe suddenly drops by several orders of magnitude at crystallization, while the resistivity of crystalline phases does not depend on temperature. The resistivity of  $\text{GeSb}_2\text{Te}_4$ , however, shows a pronounced temperature dependence. Furthermore, the value of TCR changes from negative to positive with increasing temperature, which means that the nature of  $\text{GeSb}_2\text{Te}_4$  changes from an insulator to a metal, as mentioned above. This result is also observed in other Ge-Sb-Te alloys.<sup>46,47</sup> Interestingly, the nature of  $\text{GeSb}_2\text{Te}_4$  changes from an insulator to a metal at 275 °C, while the phase transition from rock-salt to a hexagonal phase occurs at 225 °C. Thus, a transition in the crystallographic phase has no relationship with the transport mechanism. However, a hexagonal  $\text{GeSb}_2\text{Te}_4$  phase is a degenerate semiconductor, that is, the Fermi energy lies within the valence band, which results in metal-like behavior. Consequently, the hexagonal phase of  $\text{GeSb}_2\text{Te}_4$  shows positive TCR values.

Theoretical studies that used density functional theory (DFT) provided the microscopic origin of MIT in crystalline  $\text{GeSb}_2\text{Te}_4$ .<sup>48</sup> The transition from an insulator to a metal has been attributed to increasing order in the crystalline phase. This property is related to the resonance bonding of the p electrons in crystalline Ge-Sb-Te alloys. This unique bonding results in a high static dielectric constant and very weak effective electron interaction.<sup>49</sup> Furthermore, atomic displacements that are induced by Peierls distortions and the statistical distributions of vacancies and Ge and Sb atoms affect the electronic properties.<sup>29</sup> **Figure 2.6** shows the total energy per atom of the models of metastable cubic  $\text{GeSb}_2\text{Te}_4$  and stable hexagonal  $\text{GeSb}_2\text{Te}_4$  with respect to the ordering of vacancies and Ge/Sb atoms. Three factors play an important role in the MIT: the distribution of vacancies, the disordering of Ge/Sb, and the crystalline phase. The rearrangement of vacancies affects the degree of disorder and creates a

vacancy plane in both cubic and hexagonal planes. The hexagonal phase becomes lower in energy than the corresponding cubic structure with sufficiently high vacancy layer formation. Therefore, the phase transition from a cubic to hexagonal phase is a high priority before the rearrangements of vacancies can be completed. Consequently, the final product of Ge-Sb-Te alloys after MIT is a hexagonal phase, and the vacancy effect on the MIT is hard to prove experimentally. Although the substitutional disorder of Ge and Sb atoms also affects the total energy of the Ge-Sb-Te system, the energy differences are quite small compared to vacancy ordering.

More recently, the impact of stoichiometry was demonstrated by P. Jost et al. as a controllable parameter for the MIT of the most common compositions in the  $(\text{GeTe})_x\text{-(Sb}_2\text{Te}_3)_{1-x}$  system; i.e., disorder-induced localization results in MITs differ according to the average vacancy concentration of various compositions.<sup>50</sup> Therefore, the behaviors of MITs, which are controlled by the annealing temperature and the stoichiometry, are critical for tailoring the charge transport properties of cubic GST to increase the performance of PcRAM devices.



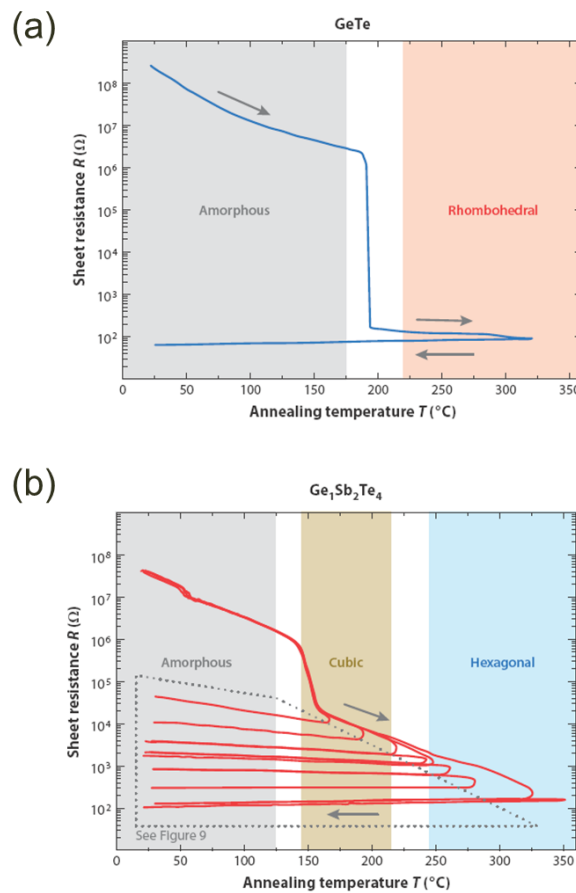


**Figure 2.5** (a) Temperature dependence of the sheet resistance on GeTe. (b) Temperature dependence of the sheet resistance on  $\text{GeSb}_2\text{Te}_4$ . [45]

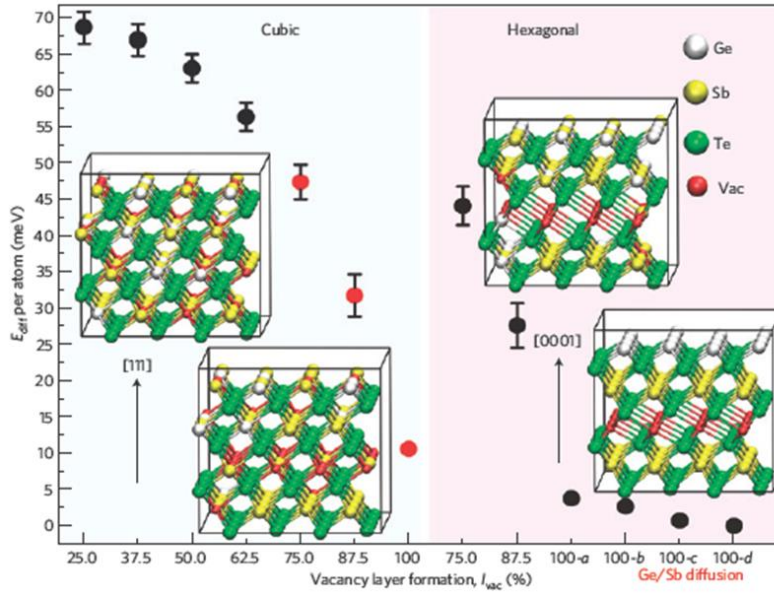


**Figure 2.6** Total energy per atoms,  $E_{\text{diff}}$ , of the metastable cubic  $\text{GeSb}_2\text{Te}_4$  and stable hexagonal  $\text{GeSb}_2\text{Te}_4$  with respect to vacancy layer formation. [48]

## **2.2. Theory of electromigration**

Endurance failures in PcRAM occur because of compositional changes and void formation in phase-change materials, as presented in **Section 1.2.1**. Both mechanisms of endurance failure are generated by mass transport in phase-change materials. When the atomic flux of constituent elements is different, the stoichiometry of multi-component alloys is broken. Voids are also generated by flux divergence because mass transport is dominant in one direction. Therefore, understanding mass transport in phase-change materials is essential to understand the failure mechanisms in PcRAM devices. This section will describe the theory of atomic migration phenomena and will discuss previous research on phase-change materials.

### **2.2.1. Electromigration**

Electromigration is the phenomenon of interconnecting metal self-diffusion along an interconnect when a high current density passes through the section. Voids form on some parts of the interconnect because of constituent atomic movement, and hillocks form on the other side because of the accumulation of atoms. The presence of voids increases the resistance of interconnects. The presence of hillocks causes short circuits between adjacent interconnects if these hillocks develop side-ways and between different levels of interconnects if these hillocks develop vertically and punch through the dielectric.

Electromigration has been a subject of scientific study for over 100 years, but the interest remained academic until it became a major failure mechanism for integrated circuits (IC) in 1959, when thin and narrow metal films began to be used as interconnects. Indeed, electromigration was the one of the first failure mechanisms

that were found in ICs. Unlike bulk conductors, which melt from Joule heating at high current density (above  $10^4$  A/cm<sup>2</sup>), the metallization in ICs can sustain current densities that are greater than  $10^7$  A/cm<sup>2</sup> because of the good thermal contact with the silicon substrate. This high current density significantly increases the effect of electromigration.

In addition, thin-film interconnects in ICs possess small grain sizes and high surface or interfacial area to volume ratios with many high mobility diffusion paths, which allows the mass transport of self-diffused metal atoms at low temperature. When these diffusion paths intersect with one another and when each path has different mobility, atoms accumulate or voids nucleate at the intersection. This combination of a high driving force for electromigration and the availability of inhomogeneous high-mobility diffusion paths makes thin-film conductors susceptible to electromigration damage.

### 2.2.2. Driving forces for electromigration

The driving force for electromigration has two major parts according to the direction of atomic migration. One is the direct action of an electrostatic field on the diffusing atoms, and the other is momentum exchange between charge carriers and diffusing atoms. For simplicity, the effective charge number ( $Z^*$ ) is introduced in the following manner:

$$F_{EM} = Z^* eE = (Z_{el}^* + Z_{wd}^*)eE, \quad (2.1)$$

where  $Z_{el}^*$  can be regarded as the nominal valence of the diffusion ion. Diffusing atoms are forced to migrate because of the direct electrostatic action of the electric

field, which is commonly called the electrostatic force.  $Z_{wd}^*$  is the charge number, which represents the momentum exchange effect and is commonly called the electron wind force.  $Z_{wd}^*$  has generally been shown to be approximately 10 in metallic systems, so the momentum exchange effect is much larger than the electrostatic field effect for electromigration in metals.

Although the physical meaning of  $Z_{el}^*$  is the valence charge of the diffusion ion, the evaluation of the quantity has been a prolific subject of controversy because of the shielding effect of conduction carriers. For metals,  $Z_{el}^*$  is usually much smaller than  $Z_{wd}^*$  because the valence charges of atoms in metal are blocked by free electrons.

The evaluation of  $Z_{wd}^*$  is more complex. The intuitive picture one forms from the classical model of momentum exchange in a continuous electronic fluid is too simple to illustrate the quantum mechanical phenomena between diffusing atoms and electrons. Several efforts in quantum mechanics have been made to estimate the electron wind force, yet no result has been widely accepted. The difficulty lies in conducting the proper and complete treatment of the scattering of electrons by a diffusing atom and its surrounding atoms. In the following, we discuss ballistic approaches to the scattering process, which were provided by Fiks<sup>51</sup> and by Huntington and Grone<sup>15</sup>.

The idea that was conceived by Fiks assumes that the diffusing atoms have an intrinsic cross-section  $\sigma_e$  for collision with electrons and that conduction electrons have an average velocity  $v$ , with  $n$  being the concentration of conduction electrons per unit volume.<sup>51</sup> The number of collisions per unit time between electrons and a moving atom is  $nv\sigma_e$ . For each collision, an electron conducts the average momentum it acquires during the relaxation time  $\tau_e$ ,  $F_x^1\tau_e = eE\tau_e$ , where the subscript  $x$  indicates that the electrical field and the force are acting along the  $x$ -direction. The total change

in momentum per unit time, i.e., the wind force, is the product of the number of collisions per unit time and the momentum exchange per collision,

$$F_x = -(nv\sigma_e)(eE_x\tau_e) = -eE_x n\lambda_e\sigma_e, \quad (2.2)$$

where  $\lambda_e = v\tau_e$  is the mean free path of scattering. This expression has been extended to cover the situation in which both electrons and holes are involved in the transport process:

$$Z_{wd}^* = -n_e\lambda_e\sigma_e + n_h\lambda_h\sigma_h. \quad (2.3)$$

The semi-classical model that was developed by Huntington and Grone postulates a transition probability per unit time from one free-electron state to another free-electron state because of scattering by diffusion atoms. A formal expression has been developed to describe the momentum transfer per unit time by treating electrons as free particles. Subsequently, this approach has been modified by considering the electron pseudo-momentum of electronic states. The force is calculated by summing over the initial and final states of the scattered electrons or by integrating a transition probability over the jumping path of the diffusing atoms. The force that acts on the diffusing atom is not constant along the jumping path, but the calculation is simplified by assuming that the electron reciprocal relaxation time that arises from collision with moving atoms is constant. The result shows that the effective charge number can be provided in terms of the specific resistivity,

$$Z_{wd}^* = -Z \frac{\rho_d / C_d}{\rho / C} \frac{m_0}{m^*}, \quad (2.4)$$

where  $Z$  is the electron-atom ratio;  $\rho = m_0 / ne^2\tau$  and  $\rho_d = m^* / ne^2\tau_d$  are the resistivity of the lattice atoms and the diffusing atoms, respectively, and  $m_0$  and  $m^*$  are the free electron mass and effective electron mass, respectively.

In an FCC lattice, 12 equivalent jump paths are present along the  $\langle 110 \rangle$  directions. For a given current, the average specific resistivity of a diffusing atom must be corrected by a factor of one-half. Therefore, if we consider both  $Z_{el}^*$  and  $Z_{wd}^*$ ,

$$Z^* = -Z \left[ \frac{1}{2} \frac{\rho_d / C_d}{\rho / C} \frac{m_0}{m^*} - 1 \right]. \quad (2.5)$$

The direction of the electron wind force, the first term in Eq. (2.5), appears to depend on the sign of the charge carriers. For electrons that interact with positive ions, the term is opposite to the electrostatic force; the direction of mass transport is determined by the relative magnitudes of these two forces. For holes that interact with positive ions, both forces are of the same sign; therefore, mass transport should always be toward the cathode.

### **2.3. Mass transport in phase-change materials**

Electromigration in multi-component alloys such as phase-change materials is quite different from that of metal interconnects. This difference is caused by the physical properties of materials and operating conditions of the device. For example, metals are good conductors with high concentrations of charge carriers, while phase-change

materials are poor conductors with relatively low concentrations of charge carriers. Furthermore, the mass transport behavior in phase-change materials changes with the current density because the material transforms into a molten state under severe Joule heating at a high current density (above  $10^7$  A/cm<sup>2</sup>). This operation condition is vulnerable to migration because the mobility of atoms in a molten state is some orders of magnitude faster than that in a solid state. Previous research regarding electromigration behavior in phase-change materials with respect to the phase is briefly introduced in this section.

### 2.3.1. Electromigration behaviors in molten-phase Ge<sub>2</sub>Sb<sub>2</sub>Te<sub>5</sub>

**Figure 2.7** shows the atomic concentration profile in the Ge<sub>2</sub>Sb<sub>2</sub>Te<sub>5</sub> line along the longitudinal direction after applying a single electric pulse with duration times on the scale of milliseconds.<sup>13</sup> The composition of Ge<sub>2</sub>Sb<sub>2</sub>Te<sub>5</sub> abruptly changed and the directions of the atoms differed among the elements. Ge and Sb atoms migrated to the anode, while Te atoms migrated to the cathode. This result was also shown in an EDS compositional map that was analyzed by TEM.<sup>11</sup> The driving force for the atomic migration is the electrostatic force that was exerted on the ionized atoms in the molten state. As mentioned in **Section 2.2**, electromigration has two driving force, namely, electron wind force and electrostatic force. Generally, the wind force is much higher than electrostatic force in solid-state electromigration. In a molten state, however, the electrostatic force becomes the dominant factor for electromigration because of the ionization of atoms. Each element has different ionicity when the materials are molten depending on the electronegativity. Therefore, atoms in a molten state donate or accept electrons and are ionized depending on their electronegativity. Because the



electronegativity of Te is much larger than that of Ge and Sb, Te becomes an anionic ion, and Ge and Sb become cationic ions.<sup>52</sup>

The atomic flux refers to the quantity of migrated atoms through a certain area over a unit time, which is the rate of electromigration. The atomic flux of electromigration can be written as

$$J^{EM} = \frac{CD}{RT} Z^* eE, \quad (2.6)$$

The electric field (E) and temperature (T) are determined by the operating conditions. If the dimensions of the sample and operating conditions are fixed, the atomic flux is determined by the effective charge number ( $Z^*$ ) and diffusion coefficient (D). The value of  $DZ^*$ , which is the product of the effective charge number and diffusion coefficient, can be used to quantify the electromigration rate. The  $DZ^*$  value of each element is calculated from the quantity of migrated atoms that can be measured by compositional analysis. The assumption is that the electric field and the number of atoms per volume are constant along the whole sample, and temperature is fixed to 900 K, which is the melting temperature. The  $DZ^*$  values of Ge, Sb, and Te were calculated to be 2.56, 3.02, and  $-2.13 \times 10^{-5} \text{ cm}^2\text{s}^{-1}$ , respectively.<sup>13</sup> A negative  $DZ^*$  value means that the mass flux of atoms is in the opposite direction compared to a positive value. These  $DZ^*$  values are a few orders of magnitudes larger than those of metal interconnects in semiconductors and are based on the large coefficient of diffusion in the molten state. Therefore, electrical stressing during *RESET* switching is critical to endurance failure in PcRAM devices.

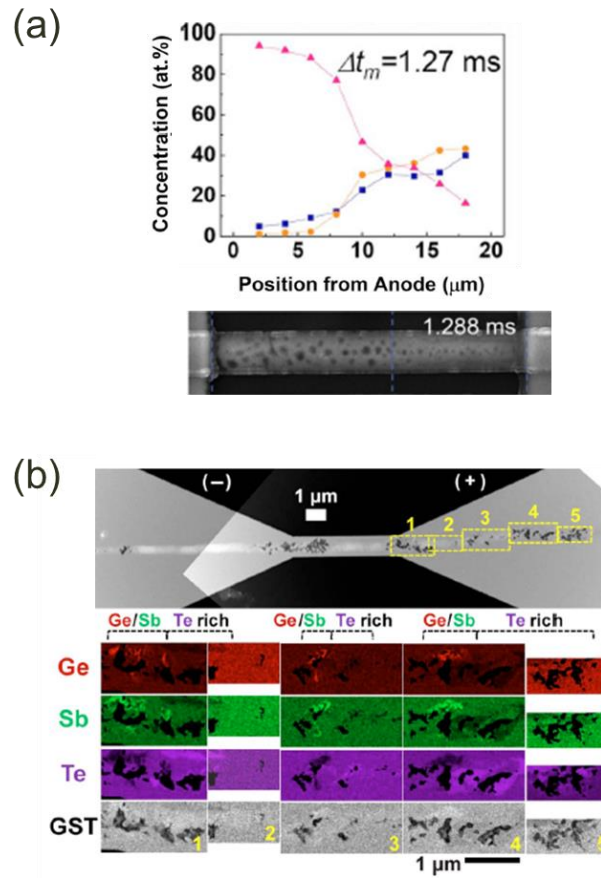


**Figure 2.7** (a) Compositional profiles in  $\text{Ge}_2\text{Sb}_2\text{Te}_5$  line from WDS analysis shown as atomic concentration and their SEM image. [13] (b) Image of the capped pattern of  $\text{Ge}_2\text{Sb}_2\text{Te}_5$  after voltage sweeping. Mass depleted regions were blackened out in the individual element mapping. [11]

After catastrophic atomic de-mixing in  $\text{Ge}_2\text{Sb}_2\text{Te}_5$ , voids are observed at the anode contact as shown in **Figure 2.7**. These voids are uniformly generated along the whole line during the as-melted state. As the duration time increase, however, voids that are near the cathode begin to disappear, and voids that are near the anode grow through agglomeration. These observations indicate that small voids are generated during the initial stage of electromigration and that voids migrate toward the anode upon coalescence. Void formation during electromigration has also been reported in metal interconnects, in which voids are generated at the point of flux divergence, such as material interfaces.<sup>53</sup> Atoms are depleted at this point because the incoming flux of atoms is different from the outgoing flux of atoms. The depletion of atoms leads to tensile stress in the cathode, which is the driving force for void nucleation. Although no point of flux divergence exists in molten  $\text{Ge}_2\text{Sb}_2\text{Te}_5$ , atomic fluxes are different among elements. Moreover, the crystalline structure of  $\text{Ge}_2\text{Sb}_2\text{Te}_5$  has many sites of intrinsic vacancies, as mentioned in **Section 2.1**, which results in the formation of free volume in the molten state. Free volume refers to a volume that was not occupied by constituent atoms in the liquid state. Under non-uniform atomic flux, vacancies migrate along the direction of lower atomic flux. Therefore, the flux of voids during electromigration is toward the anode because the total atomic flux is dominantly toward the cathode. This phenomenon is similar to the Kirkendall effect regarding inter-diffusion in complex metal systems.<sup>54</sup>

The electromigration behavior in line structures of  $\text{Ge}_2\text{Sb}_2\text{Te}_5$  cannot completely explain the failure behavior in actual PcRAM devices. The main difference in these devices because of the line structure is the distribution of the electric field and temperature, which leads to a divergence in the atomic flux. Furthermore, the temperature gradient is also a critical driving force for atomic migration in phase-

change materials, which is called thermomigration.<sup>55</sup> The driving forces for migration contain not only external factors, such as electric fields and temperature, but also internal factors that result from atomic migration. In a real system, a large amount of atomic accumulation generates compressive stress, which prevent high values of atomic density. An additional atomic flux is generated by the stress field from compressive to tensile regions to achieve equilibrium with electromigration. Atomic accumulation also generates a spontaneous diffusion flux to dissipate the concentration profile. According to the various driving forces for migration, mass fluxes in actual PcRAM devices can be explained by simulations and matched with experimental results.<sup>56</sup>

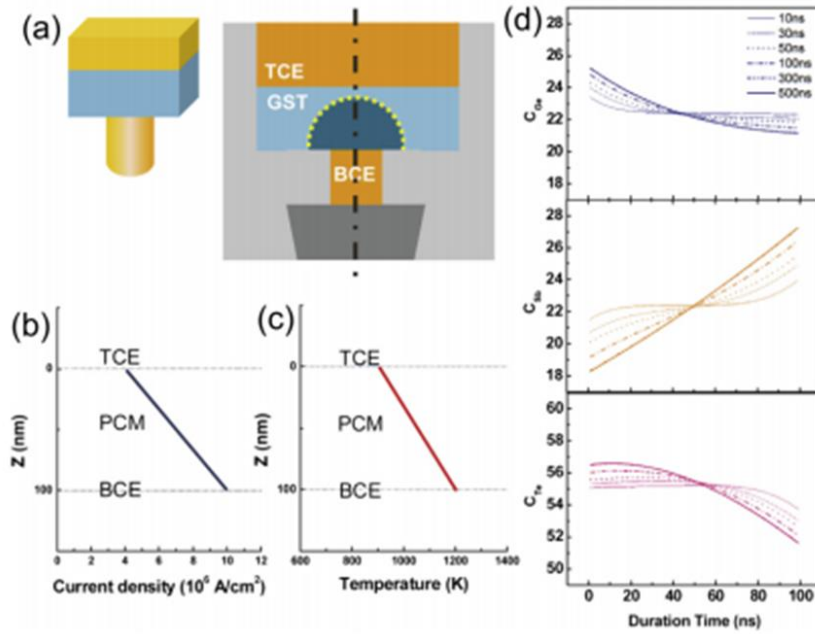


**Figure 2.8** (a) Cell structure of the real device (mushroom-structure). (b) Current density and (c) temperature profile in Ge<sub>2</sub>Sb<sub>2</sub>Te<sub>5</sub> layer of structure (a). (d) Compositional profiles after pulse stressing with various duration time for Ge, Sb, and Te calculated from the finite differential method (FDM). [55]

### 2.3.2. Electromigration behaviors in crystalline phase $\text{Ge}_2\text{Sb}_2\text{Te}_5$

As mentioned above, previous research has predominantly focused on the migration behavior in molten state of phase-change materials, because the mobility of atoms in molten states is some orders of magnitude faster than that in solid states. Obviously, the catastrophic failures in actual PcRAM devices have a close relationship with migration in molten states compared with that in solid states. However, except for kinetic differences, the mechanism of electromigration in solid states is different from that in liquid states.

**Figure 2.9** shows the atomic concentration profiles in crystalline  $\text{Ge}_2\text{Sb}_2\text{Te}_5$  line after electrical stressing.<sup>13</sup> Because the sum of the concentrations of constituent elements is fixed to 100 at. %, the concentration is expressed by relative values. The absolute mass according to the position is calculated from a comparison with the initial X-ray intensity of the atoms to verify the atomic flux. In the plot of the relative intensity, all the elements migrate from the anode to the cathode, which is different from the migration behavior in a molten state. The mass transport of all the elements to the cathode originates from the wind force of electromigration. This wind-force-induced electromigration results in the same directional migration regardless of the elements, while electrostatic-force-induced electromigration results in migration in various directions according to the ionicity of the elements.

The driving force for electromigration in crystalline structures is the wind force, which involves atomic migration by momentum transfer from conducting carriers. Because the wind force in metals is affected by electrons, which are the majority carrier, atoms migrate from the cathode to the anode, similar to the electron. However, the wind force in crystalline  $\text{Ge}_2\text{Sb}_2\text{Te}_5$  occurs in the opposite direction compared to that in metals. The sign of  $Z^*$  is determined by the sign of the effective mass of charge

carriers, as mentioned in **Section 2.2**. Crystalline  $\text{Ge}_2\text{Sb}_2\text{Te}_5$  is *p*-type semiconductor, i.e., the majority carriers are holes. The dependence of  $Z^*$  on the majority carriers has been observed in electromigration tests of doped Si.<sup>57</sup> After current stressing, catastrophic failure was observed in doped-Si, with differences in the behavior depending on their types. Voids were generated near the cathode in the *n*-type Si sample and near the anode in the *p*-type Si sample. No failure was observed in the AC pulse conditions even after 24 hours of stressing. These results are direct evidence that the sign of  $Z^*$  is determined by the majority carriers in materials.

Although crystalline  $\text{Ge}_2\text{Sb}_2\text{Te}_5$  is affected by the hole wind force, the quantity of migrated atoms is much smaller than that of molten  $\text{Ge}_2\text{Sb}_2\text{Te}_5$ , which is affected by the electrostatic force. Therefore, the compositional changes of phase-change materials in actual PcRAM devices are mainly affected by atomic migration in the molten state, and the effect of electromigration in the crystalline phase has been thought to be insignificant.

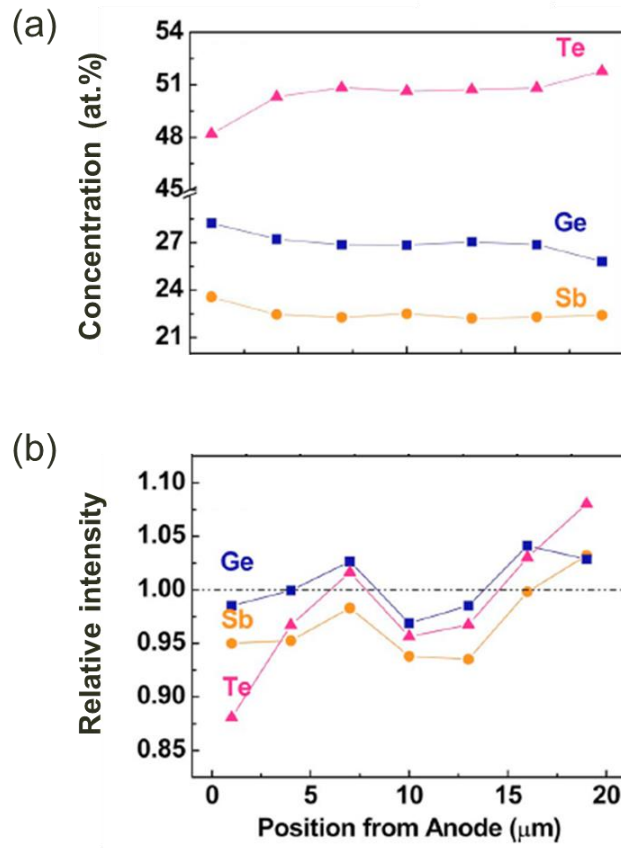


**Figure 2.9** (a) atomic concentration and (b) relative intensity showing the atomic diffusion from the anode to the cathode in crystalline  $\text{Ge}_2\text{Sb}_2\text{Te}_5$  line after the DC stressing.



## CHAPTER 3

### Experimental procedures

#### 3.1. Sample preparation

Line-patterned samples were used to apply an electric current. **Figure 3.1** shows the structure for the electromigration tests in this study. The dimensions of the line were 20  $\mu\text{m}$  in length, 2  $\mu\text{m}$  in width and 300 nm in thickness, which are much larger (micro scale) than those in actual devices (nano scale). The line structure in this study has many advantages for electromigration tests because microstructural and compositional changes from applying a current could be analyzed by SEM-level studies. PcRAM devices are too small to observe failure phenomena and analyze their mechanisms. In addition, failure mechanisms in PcRAM devices become confounded by the dispersion of the current density and temperature gradient because of a narrow bottom contact, which makes it difficult to concretely identify the failure mechanism. Various mechanisms are mixed into actual devices. The line structure in this study, however, was easy to analyze for failure phenomena

with a model study. The temperature and current density were more uniform in this structure compared to actual devices.

The chalcogenide materials that were used in this study are listed in **Table 3.1** with the deposition conditions.  $\text{Ge}_2\text{Sb}_2\text{Te}_5$  was the main materials that was used in this study, and Te-based chalcogenides were used for comparison. Thin films of chalcogenide were deposited by using a direct current (DC) magnetron sputtering on a 10-nm silicon oxide wafer. A single sputtering target with fixed composition was used to deposit thin films. The base pressure was approximately  $8 \times 10^{-8}$  torr and the working pressure was  $3 \times 10^{-3}$  torr with an argon ambient. The deposition conditions were fixed with 80 W of DC power and 20 sccm of  $\text{N}_2$  gas. Because a thick layer of oxide could interrupt thermal dispersion, 10-nm oxide was chosen as the maximum thickness for the dielectric layer. An AZ5214 photoresist was patterned by a photoaligner (Karl-Suss MA-6 II) and a lift-off method was performed to form line-shaped chalcogenide material. The as-deposited films were an amorphous phase.

Large molybdenum pads that were 500  $\mu\text{m}$  by 500  $\mu\text{m}$  were located on the end of the line-shaped chalcogenide materials for contact. Because the molybdenum pad was not affected by an electric current, these materials could act as boundaries for the atomic migration of chalcogenide materials. A highly accurate quantitative analysis can thus be conducted. To prevent the evaporation and oxidation of the chalcogenide materials, a 100 nm-thick film of silicon nitride ( $\text{Si}_3\text{N}_4$ ) was deposited on the chalcogenide line by using plasma-enhanced chemical vapor deposition (PECVD) at 200 °C. The chalcogenide materials crystallized during the passivation process because the process temperature was higher than the crystallization temperature of the chalcogenide materials.

### *Chapter 3: Experimental procedures*

---

The Pad opening process was conducted with a dry etcher (AMK P-5000 IV, Ar 10 sccm, CF<sub>4</sub> 10 sccm, CHF<sub>3</sub> 15 sccm, O<sub>2</sub> 8 sccm, 100 mtorr, radio frequency 600 W, and magnetic field 30 gauss for 25 sec). Silicon nitride films on the molybdenum pad were removed with a dry etcher for electrical contacts.

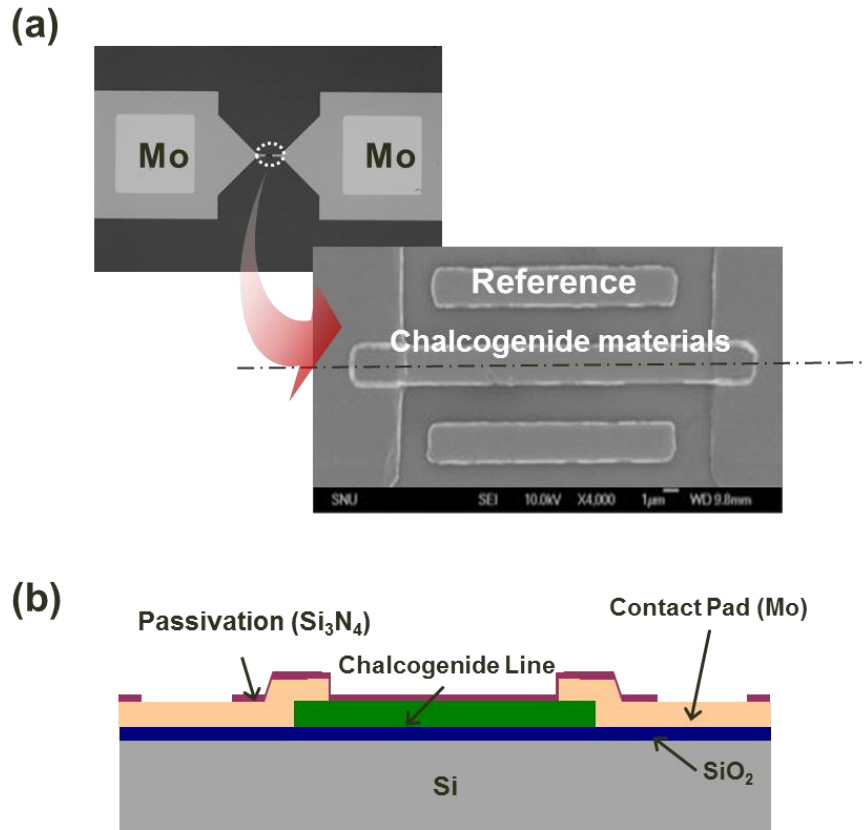


**Figure 3.1** (a) SEM Images and (b) schematic of cross-section image of the line-shaped structure of chalcogenide material for electromigration test, which dimension is 20  $\mu\text{m}$  in length, 2  $\mu\text{m}$  in width and 300 nm in thickness. The chalcogenide materials were isolated by Mo contact pads and passivated with a silicon nitride film 100 nm in thickness.

**Table 3.1** Detailed sputtering conditions for deposition of chalcogenide materials.

	Target	Power	Sputtering gas flow
<b>Ge<sub>2</sub>Sb<sub>2</sub>Te<sub>5</sub></b>	Ge <sub>2</sub> Sb <sub>2</sub> Te <sub>5</sub>	80 W	Ar: 20 sccm
<b>GeSb<sub>4</sub>Te<sub>7</sub></b>	GeSb <sub>4</sub> Te <sub>7</sub>	80 W	Ar: 20 sccm
<b>Bi<sub>2</sub>Te<sub>3</sub></b>	Bi <sub>2</sub> Te <sub>3</sub>	80 W	Ar: 20 sccm
<b>Bi<sub>35</sub>Te<sub>65</sub></b>	Bi <sub>2</sub> Te <sub>3</sub>	100 W	Ar: 20 sccm
	Te	10 W	

Base pressure:  $8.0 \times 10^{-8}$  Torr

Working pressure:  $3.0 \times 10^{-3}$  Torr

Temperature: room temperature

## **3.2. Electrical stressing method**

The methods that were used to characterize electromigration in chalcogenide materials were wafer-level electrical stressing on a hot-chuck-equipped probe station and package-level electrical stressing on an oven system. The former was a single-type test with various functional analysis, and the latter was a batch-type test with fixed conditions. In this section, the pulse dependency and IV sweep test were analyzed by using the wafer-level test, and the influences of temperature, current density, and time were analyzed by using the package-level test.

### **3.2.1. Wafer-level test**

IV sweep is the method for monitoring voltage by applying a current on the test sample. A DC current was applied to the test sample by a parameter analyzer (Agilent 4156C) under ambient air. A double-directional mode with a sweep from zero to the peak current and a return to zero was used, and the peak current density increased each cycle from 0.33 to 2 MA/cm<sup>2</sup> in 0.17 MA/cm<sup>2</sup> increments. A current density over 2 MA/cm<sup>2</sup> results in the melting of the chalcogenide materials because of severe Joule heating. Therefore, a current density under 2 MA/cm<sup>2</sup> was used in this study to maintain a crystalline phase. The ambient temperature could be changed by a hot chuck controller, which ranges from room temperature to 200 °C.

An alternating current (AC) was also applied to the chalcogenide sample by using a pulse generator (Agilent 81110A) under ambient air, which was equipped in the same probe station. The current pulse was identified from the voltage, which was measured by an oscilloscope (Agilent 54833D) with a 50 Ω input impedance. The resistance change in the sample during the test was monitored by a parameter tester (Keithley

2400). The pulse generator and the parameter tester were connected to the sample through a switching system (Keithley 7001) to switch between electrical stressing and resistance measurement. This equipment was automatically controlled by a program with LabVIEW (National Instruments). The maximum frequency that was applicable in this system was 10 MHz (minimum period of the pulse was 100 ns).

First, the parameter tester was connected to the sample through a switching system, and the resistance of the sample was measured by the parameter tester. Then, the switching system changed connection from the parameter tester to the pulse generator and oscilloscope. The pulse generator applied an electric current to the chalcogenide sample considering the resistance of the sample as measured by the parameter tester. The oscilloscope simultaneously measured the pulse shape and applied voltage. After applying a pulse current for 5 min, the connection of the sample was changed to the parameter tester by using the switching system, and the parameter tester measured and recorded the resistance of the sample again. This series of processes was repeated until the end of the experiment.

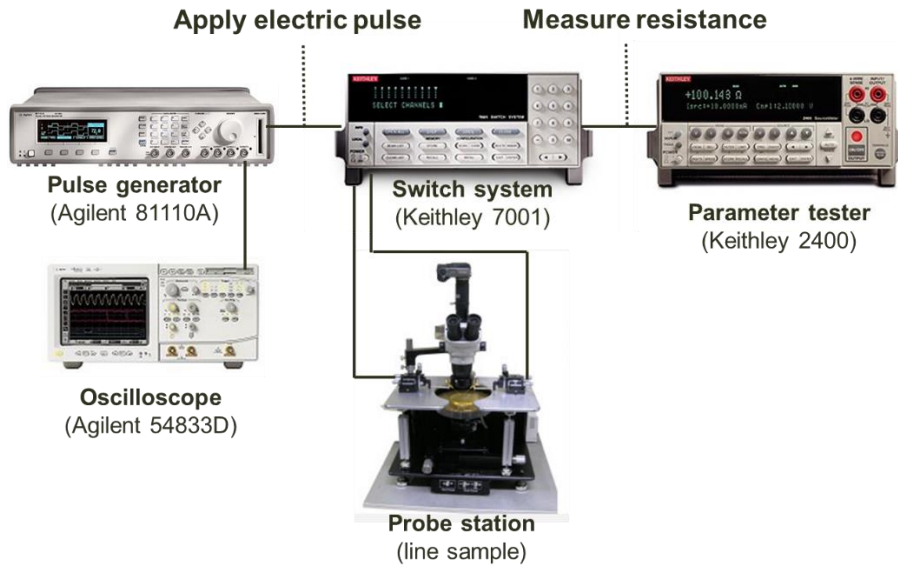


**Figure 3.2** Schematic diagram of the system for electromigration test using electrical pulse stressing in the wafer-level.



### **3.2.2. Package-level test**

Although wafer-level tests have the merits of precise and various functional analysis, only a single sample can be tested at one time. To determine the effect of various conditions, many experiments with various conditions must be conducted and compared. Wafer-level tests are limited in this case, and package-level tests are an alternative to experiments with various conditions. **Figure 3.3** shows the package-level tester (Qualitau MIRA EM test) that we used in this study.

The EM tester contains the MIRA mainframe with EM modules and controller, temperature chambers, an AC power distribution unit, and cooling fan trays. Several EM racks may be networked together and monitored by a workstation. The EM modules contain precision current sources and measurement circuits. Two EM modules are housed in one MIRA mainframe, with each module capable of running experiments on up to 60 devices under testing (DUTs), each at different stress conditions. The outputs of the current sources, which are controlled by the MIRA mainframe controller, are routed to the DUTs in the temperature chambers. The system measures the resulting current through and voltage across the DUTs by using separate sensor wires. For package-level testing, DUTs are housed in zero insertion force (ZIF) sockets, which are located on DUT boards in the temperature chambers. The devices must be packaged in a 28-pin (or less) dual in-line package (DIP). Each DUT package can contain one DUT line, one reference line and up to four independent extrusion monitors, which measure the leakage to adjacent lines. The equipment has three temperature chambers, which makes it possible to control the temperature with an individual temperature chamber. Each temperature chamber contains one DUT board, which includes 20 DUTs; therefore, the electric current can be stressed to 60 samples with different experimental conditions at the same time.

This equipment was automatically controlled by a commercial program (Qualitau Co.).

The sequence of this experiment involves two phases, which are the temperature coefficient of resistance (TCR) phase and stress phase. During the TCR phase, the resistance of each DUT is measured as a function of temperature. The purpose of the TCR phase is to generate a curve fit of these data so that the DUT line temperature can be determined. The line temperature is greater than the oven temperature during stress, because of the stress current and the effects of Joule heating. The first and lowest temperature the system can reach is 50 °C, which is the lowest temperature the oven can control without cooling from liquid nitrogen. The maximum temperature the oven can reach is the stress temperature as specified in the test conditions. The number of intermediate temperatures the oven can reach is generally three steps in this study. At the end of the TCR phase, the oven is at the stress temperature and the temperature has stabilized for one hour.

The system can also measure the actual stress current through each DUT for high-precision resistance measurements. For a standard EM module, this value amounts to approximately 10  $\mu$ A. At the stress phase, electrical tests are conducted for every sample by simultaneously monitoring their resistances.



**Figure 3.3** The electromigration tester for package-level test (Qualitau MIRA EM tester). Two EM modules are housed in one MIRA mainframe, with each module providing a capability of running experiments on up to 60 devices under test (DUTs), each at different stress conditions. This equipment was automatically controlled by a commercial program (Qualitau Co.)

### **3.3. Compositional analysis**

Compositional changes that were induced by electromigration were analyzed by wavelength dispersive X-ray spectroscopy (WDS) under a scanning electron microscope (SEM) and by energy dispersive X-ray spectroscopy (EDS) under a transmission electron microscope (TEM). Because electromigration is mass transport that is induced by electric currents, the concentration of atoms can change depending on the position and element. Compositional analysis under SEMs and TEMs is similar, but the interaction volumes of each method are different.

The interaction volume of WDS electrons under the SEM was probably approximately 2  $\mu\text{m}$  with a hemispherical shape at the detection point. The dimensions of the chalcogenide line in this study were 20  $\mu\text{m}$  in length and 2  $\mu\text{m}$  in width. Therefore, 10 compositional analysis points were available in the direction of the line without overlap. We can quantify the composition of the chalcogenide materials, which depends on the line position. **Figure 3.1** shows the structure for the electromigration test in this study as mentioned above. Three independent chalcogenide lines were located between metal pads, but only one chalcogenide line was connected with the metal pad. The connected chalcogenide line was an actual test line, which was applied by an electric current. The rest of the lines without any connections, which were denoted by the reference line, experienced the same process and thermal history as the test line. Because the reference line did not experience electrical stress, the composition of reference line can be used as a standard to analyze the mass flux of chalcogenide materials after current stressing. The absolute quantity of each element was calculated from the results of pure elements. For example, 99.99 %

pure Ge, Sb, and Te samples were used to conduct a quantitative analysis of  $\text{Ge}_2\text{Sb}_2\text{Te}_5$ .

The interaction volume of EDS electrons under the TEM, however, was probably approximately 100 nm at the detection point because of the thickness of the sample. Compared to WDS under an SEM, EDS analysis under a TEM has low resolution and high precision with the location. The TEM samples were fabricated by using a focused ion beam (FIB).

## **CHAPTER 4**

# **Gradual degradation in the crystalline $\text{Ge}_2\text{Sb}_2\text{Te}_5$ under electric current**

### **4.1. Introduction**

Chalcogenides are used as phase-change materials in PcRAM.<sup>4,19</sup> As the memory density increases, PcRAM experiences harsher operating conditions, such as high current density and temperature, which can cause reliability issues and failure induced by compositional change and void formation.<sup>9, 58</sup> These durability problems are caused by the mass transport of compositional elements, including electric current or field-induced migration, also known as electromigration (EM). Previous research predominantly focused on the liquid phase, which is the intermediate state of transformation between the crystalline and amorphous phases during PcRAM operation. Because the atomic diffusivity of the liquid phase is much faster than the atomic diffusivity of the crystalline phase,<sup>13</sup> electric field-induced failures predominantly occur in the liquid phase; the crystalline phase has thus been considered the stable state for electromigration.

However, not all regions of the phase-change material experience the melting process during PcRAM operation. Only the active region, which is the limited zone near the heater, can be transformed into the liquid phase. The alternate region remains as a crystalline phase without melting, despite repeated device operation. The effect of atomic migration in the crystalline regions is cumulative, whereas the effect that evolves at the active region can be recovered through the melting and solidification process. This cumulative effect on the crystalline phase can affect the instability of the SET resistance. Therefore, it is important to investigate the migration behavior of the crystalline phase of  $\text{Ge}_2\text{Sb}_2\text{Te}_5$  to gain a comprehensive understanding of the reliability of PcRAM. The elements of crystalline  $\text{Ge}_2\text{Sb}_2\text{Te}_5$  are affected by an electric current, which is the momentum transfer between charge carriers and atoms.<sup>15</sup> EM in crystalline  $\text{Ge}_2\text{Sb}_2\text{Te}_5$  has been demonstrated to cause direct amorphization without melting, which signifies that EM in the crystalline phase has sufficient power to affect the solid-state structure.<sup>16,59</sup> As the dimensions of devices diminish, the current density is anticipated to increase,<sup>17</sup> and degradation in the crystalline state may become a significant reliability problem for a PcRAM cell.

In this chapter, we investigated EM-induced failure in crystalline  $\text{Ge}_2\text{Sb}_2\text{Te}_5$ , which has never been reported. Despite the low rate of migration in the crystalline phase, this failure exhibits a gradual increase in the resistance by nano-scale void formation. We investigated the failure mechanism of the EM-induced atomic migration in the crystalline phase of  $\text{Ge}_2\text{Sb}_2\text{Te}_5$  by applying continuous current and analyzing the microstructural changes.

## **4.2. Experiments**

Line-shaped samples, whose measurements were 20  $\mu\text{m}$  in length, 2  $\mu\text{m}$  in width and 300 nm in thickness, were employed to study the EM-induced failure in crystalline Ge<sub>2</sub>Sb<sub>2</sub>Te<sub>5</sub> as described in the **Chapter 3**. Because the as-deposited GST was in the amorphous phase, the films were annealed for 1 hour at 250 °C to crystallize the initial amorphous phase into a hexagonal phase. The initial resistivity of the hexagonal phase of GST was approximately  $8 \times 10^{-4} \Omega\cdot\text{cm}$ .

All experiments for EM used current source. A direct current (DC) stress in the range of 0.17 to 1.83 MA/cm<sup>2</sup> was applied at 200 °C using a package-leveled EM tester (Qualitau MIRA). Alternating current (AC) with a frequency of 10 MHz, generated by a pulse generator (Agilent 81110A), was also applied to confirm the polarity effect. Failure morphologies were observed via scanning electron microscopy (SEM, Hitachi SU70) and transmission electron microscopy (TEM, Technai F20). Variations in the composition were analyzed by wavelength dispersive spectroscopy using an electron probe X-ray microanalyzer (EPMA, JXA-8900R) and by energy-dispersive spectroscopy using TEM.

## **4.3. Electrical stressing in crystalline Ge<sub>2</sub>Sb<sub>2</sub>Te<sub>5</sub>**

**Figure 4.1** shows the electrical resistance and morphology changes of the Ge<sub>2</sub>Sb<sub>2</sub>Te<sub>5</sub> line during electrical stressing with respect to time and current density at 200 °C ambient temperature. The resistance and morphology changes exhibited



different behavior depending on the current density. Depending on the applied current density, the change behaviors fall into three main classes, which has not been reported.

#### **4.3.1. High current**

The resistance rapidly increased within a minute at current densities above 1.67 MA/cm<sup>2</sup>, which resulted in catastrophic failure. Large micro-scaled damage spots formed at current densities above 1.67 MA/cm<sup>2</sup>. Severe joule heating occurred when higher current density was applied, which caused instantaneous melting. In the liquid state, atomic migration is fast, and mass divergence and voids are generated by EM at a rapid rate. This phenomenon has been reported in the **Section 2.3.1**.

#### **4.3.2. Low current**

The resistance increased with time for current densities above 0.83 MA/cm<sup>2</sup>, and the rate of resistance change increased with the current density. However, no resistance and morphological change was observed below 0.83 MA/cm<sup>2</sup>, with the exception of a decrease in the initial resistance due to annealing. The resistance decrease is originated from the vacancies in the crystalline structure of Ge<sub>2</sub>Sb<sub>2</sub>Te<sub>5</sub>. As mentioned in the **Section 2.1.4**, crystalline Ge<sub>2</sub>Sb<sub>2</sub>Te<sub>5</sub> has two types of crystalline phase depending on the temperature, which are hexagonal and cubic phase. Except for this resistance decrease, current-induced degradation is not observed on the condition of current density below 0.83 MA/cm<sup>2</sup>. The detailed information in this condition will be discussed in the next chapter. (**Chapter 5**)

#### **4.3.3. Mid current**

Interestingly, a gradual increase in the resistance (on a time scale of approximately 10–20 hours) was observed under intermediate current density conditions. The failure morphology revealed that numerous nanometer-sized voids formed throughout the entire area, as shown in **Figure 4.1(b)**. This failure mode differed from the catastrophic failure caused by large voids at higher current densities, which indicates that intermediate current densities ranging from 1 to 1.5 MA/cm<sup>2</sup> induce the generation of nano-scaled voids and a gradual increase in the resistance. The compositional analysis of the sample clearly distinguished the difference between high and mid current failure modes, as shown in **Figure 4.2**. The relative intensity is the value of atomic quantity normalized to the initial quantity, which shows the mass flux of atoms. As shown in **Figure 4.2**, at the high current, demixing of the elements in the entire sample was observed. Te atoms moved to the anode, and Ge and Sb atoms moved to the cathode. This behavior is typical of electric field-induced EM in the liquid state.<sup>12,13</sup> However, at the mid current, the compositional change is quite different. The migrated amounts are small, and all elements move in the same direction, which is typical EM behavior in the crystalline phase.<sup>13,15</sup> Therefore, the gradual failure mode is caused by EM in the solid state.

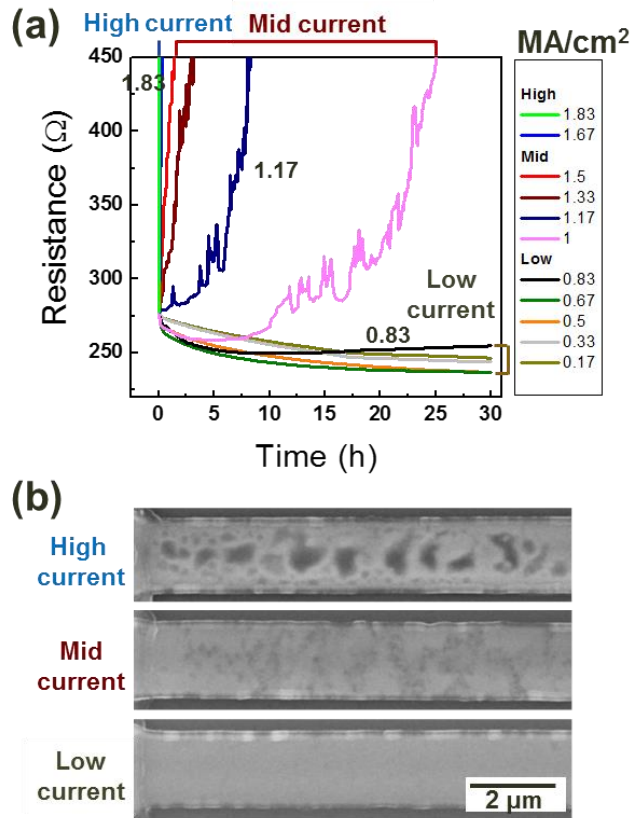


**Figure 4.1** (a) Relative resistance-time curves during constant DC current stress on  $\text{Ge}_2\text{Sb}_2\text{Te}_5$  line samples. The stress current ranged from 0.17 to 1.83 MA/cm<sup>2</sup> at 200 °C. (b) Based on the current density, different microstructures developed in the  $\text{Ge}_2\text{Sb}_2\text{Te}_5$  line samples, as shown by the SEM images. Current densities below 0.83 MA/cm<sup>2</sup>, ranging from 1 to 1.5 MA/cm<sup>2</sup> and above 1.67 MA/cm<sup>2</sup> are denoted as “low current”, “mid current” and “high current”, respectively.

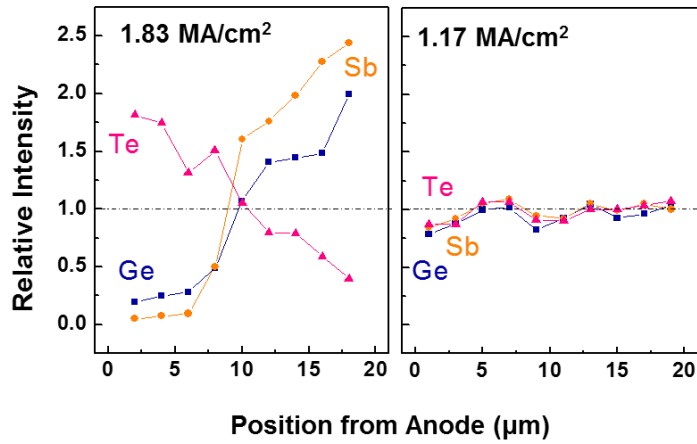


**Figure 4.2** Compositional changes of the sample after the EM stressing at a current density of  $1.83 \text{ MA/cm}^2$  (high current) and  $1.17 \text{ MA/cm}^2$  (mid current).

#### **4.4. Frequency dependence in gradual failure**

To understand the physical origin of the gradual failure in the crystalline state, we investigated the effect of bias with DC and AC. **Figure 4.3** shows the resistance change and SEM image of the line samples after the test under DC and AC conditions. The result of DC current stressing at  $1.17 \text{ MA/cm}^2$  was compared with an AC current of 10 MHz at the same current density and temperature. Unlike the DC test, neither the resistance increase nor the generation of voids was observed under AC conditions. The only difference between the DC and AC conditions is the directionality of the bias because the joule heating induced by the current is similar for DC and AC owing to their equivalent current densities. Under DC conditions, the charge carriers move in only one direction, so momentum transfer between charged carriers and atoms is accumulated while DC bias is applied. However, flux of charge carriers is variable in AC condition. 10 MHz of AC stress was used in this experiment, which means direction of bias is alternated 10 million times per second. In this case, migration rate is much slower than the speed of bias switching, thus, atoms could only pace around the own position and don't have a directionality. The migration effect is canceled out by the repetitive directional switching of AC. Therefore, electromigration works only DC condition, not AC condition. Because the joule heating of AC and DC should produce the same effect, this result indicates that the gradual failure is related to the bias dependence during current stressing.

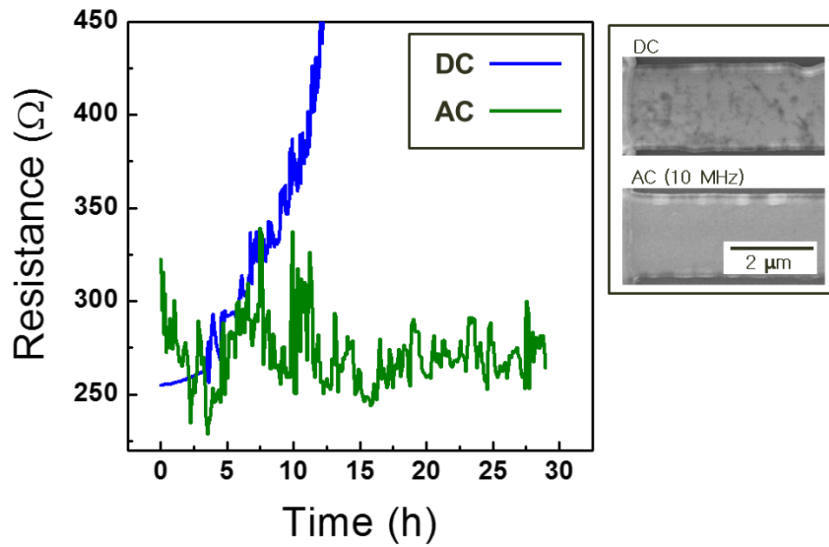


**Figure 4.3** Resistance-time curves illustrating DC and AC (frequency of 10 MHz) current stressing of  $1.17 \text{ MA/cm}^2$  at  $200^\circ\text{C}$ . The SEM image for each result is also displayed.

## 4.5. Microstructural analysis

### 4.5.1. Quantification of voids

For a more detailed examination of the relationship between EM and resistance, microstructural and compositional analyses were conducted. **Figure 4.4(a)** shows the cross-sectional TEM images of the  $\text{Ge}_2\text{Sb}_2\text{Te}_5$  line samples after testing at 1.17 MA/cm<sup>2</sup> at 200 °C (gradual failure conditions). The bright areas are  $\text{Ge}_2\text{Sb}_2\text{Te}_5$  and the dark particle-shaped areas depict the generated nanometer scale voids. Nano-scaled voids were generated not only on the surface but also inside the GST. The average size of the voids, which were well distributed, was approximately 7 nm. The resistance of the whole system is increased by the local void formation because the conducting area decreases with increasing void areas which act as an insulator.

Although we can calculate the area fraction of voids from cross-sectioned TEM image, volume fraction can't be calculated from the image exactly. To calculate volume fraction from the area fraction, some assumptions are needed. We assume that all voids have same radius with perfect sphere shape, and well distributed on the whole line. We consider a rectangular with a thickness of  $d$  which is the same with the diameter of voids. **Figure 4.5(a)** shows schematic image of the rectangular type matrix and sphere-shaped voids, and **Figure 4.5(b)** is top view of (a).  $R_r$  and  $R_p$  are actual radius and average radius in plane, respectively. TEM image in this study is a top view image as shown **Figure 4.5(b)**. Because the voids displayed in a plane are sectioned image of sphere-shaped actual voids, the value of  $R_p$  is always smaller than the value of  $R_r$ . **Figure 4.5(c)** shows calculation of area sectioned from sphere based on the y-axis distance. Because we assume voids are well-distributed particle,

distances along the y-axis have an identical probability. Average of sectioned-area can be calculated by,

$$\begin{aligned}\pi R_p^2 &= \lim_{n \rightarrow \infty} \frac{\sum_{i=0}^n \pi R_r^2 \left(1 - (i/n)^2\right)}{n} \\ &= \pi R_r^2 \cdot \lim_{n \rightarrow \infty} \frac{\left(n - \frac{n(n+1)(2n+1)}{6n^2}\right)}{n} = \frac{2}{3} \pi R_r^2\end{aligned}\quad (4.1)$$

The average radius in plane is,

$$R_p = \sqrt{2/3} R_r \quad (4.2)$$

The total number of particle of  $n$  can be calculated via,

$$n = \frac{\text{total particle area}}{\text{particle area}} = \frac{(\text{area fraction}) \times A}{\pi R_p^2} \quad (4.3)$$

where  $A$  is the area of a rectangular as depicted in **Figure 4.5(a)**. Volume fraction of voids can be calculated by ratio between volume of voids and rectangular.

$$\begin{aligned}\text{volume fraction} &= \frac{\text{Total volume of voids}}{\text{Total volume of rectangular}} \\ &= \frac{n \cdot \left(\frac{4}{3} \pi R_r^3\right)}{A \cdot d} = \frac{\frac{(\text{area fraction}) \times A}{\pi R_p^2} \cdot \left(\frac{4}{3} \pi R_r^3\right)}{A \cdot 2 R_r}\end{aligned}$$



$$= (\text{area fraction}) \quad (4.4)$$

Therefore, we can conclude that the volume fraction of voids is same to the area fraction of voids. The volume fraction of the voids, which was quantified from the images using an image analyzer, is 0.28.

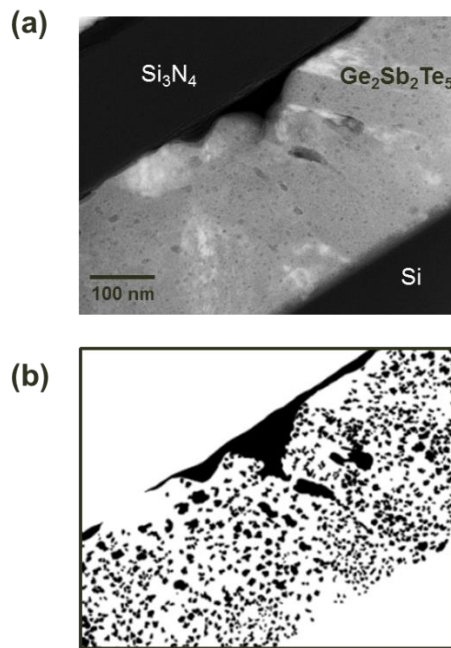


**Figure 4.4** (a) High-contrast image of the  $\text{Ge}_2\text{Sb}_2\text{Te}_5$  line sample after testing at  $1.17 \text{ MA/cm}^2$  at  $200^\circ\text{C}$ , as observed by TEM. The gray region denotes  $\text{Ge}_2\text{Sb}_2\text{Te}_5$ , and the dark areas denote defects. (b) The area analysis of the defects as measured by the image analyzer.

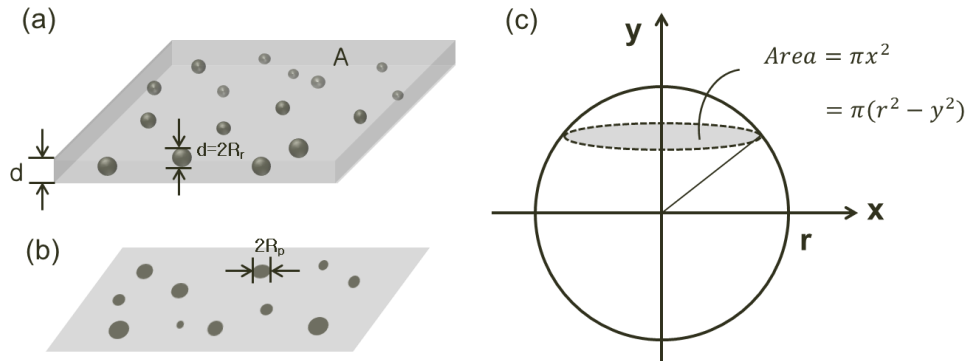


**Figure 4.5** Schematic image of homogenous particle model on the (a) rectangular type and (b) top view. (c) Calculation of area sectioned from sphere according to the y-axis distance.

#### **4.5.2. Resistivity according to void fraction**

To analyze the effect of the voids on the resistivity quantitatively, the effective resistivity was calculated using the dispersed particle model. The resistance increase is modeled by following simple assumption originally suggested by Reynolds and Hough.<sup>60</sup> They proposed the general equation of mixture rule. Because the effective resistivity of multiphase solid is closely related to the effective dielectric constant, effective thermal conductivity, etc., for a variety of the mixtures, these mixture rules are identical. We can consider a heterogeneous material that has a dispersed phase (labeled  $d$ ), in the form of particles, in a continuous phase (labeled  $c$ ) that acts as a matrix. The general equation is,

$$\frac{\sigma_{eff} - \sigma_c}{\sigma_{eff} + 2\sigma_c} = \chi \frac{\sigma_d - \sigma_c}{\sigma_d + 2\sigma_c} \quad (4.5)$$

where  $\sigma_{eff}$ ,  $\sigma_c$ , and  $\sigma_d$  are effective conductivity, conductivity of continuous phase and dispersed phase, respectively, and  $\chi$  is volume fraction of dispersed phase. If the resistivity of dispersed phase is much higher than the resistivity of continuous phase, that is  $\rho_d \gg \rho_c$ , then,

$$\sigma_{eff} = \sigma_c \frac{1 - \chi}{1 + (1/2)\chi} \quad (4.6)$$

modified according to resistivity

$$\rho_{eff} = \rho_c \frac{1 + (1/2)\chi}{1 - \chi} \quad (4.7)$$

where  $\rho_{eff}$  is the effective resistivity,  $\rho_c$  is the resistivity of the matrix and  $\chi$  is the volume fraction of the voids. From the above equation, the effective resistivity of total system increase as the volume fraction of voids increase. The simulation of relative resistance according to volume fraction of voids is shown in **Figure 4.6**.

The area analysis between the dark (void) and white ( $\text{Ge}_2\text{Sb}_2\text{Te}_5$ ) is depicted in the **Figure 4.4(b)**. As mentioned above, the volume fraction of the voids, which was quantified from the images using an image analyzer, is 0.28. The equation (4.7) illustrates that when the volume fraction of the voids is 0.28, the final resistivity is 1.6 times the initial resistance, which is similar to our results depicted in **Figure 4.1(a)** ( $R_f/R_i=1.6$ ). The experimentally determined resistance is equivalent to the calculated value from the void generation. Therefore, the main reason for the gradual increase in resistance during current stressing is the generation of highly resistive voids.

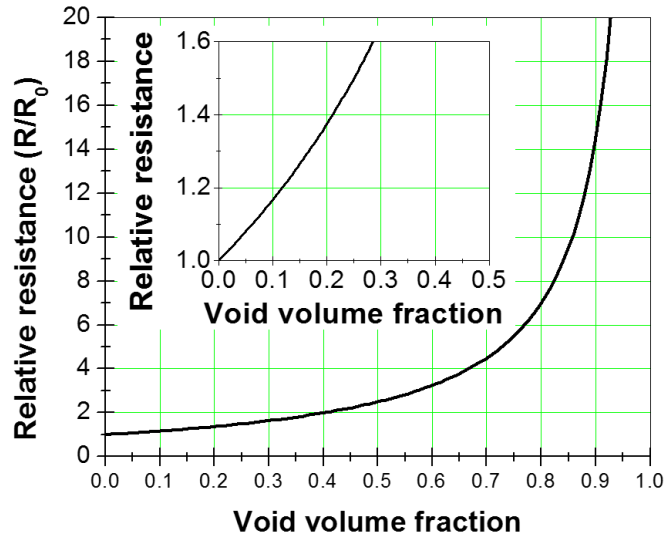


**Figure 4.6** Simulation of relative resistance according to volume fraction of voids, which is calculated using the dispersed particle model. (eq. 4.7) The expansion graph for volume fraction ranged from 0 to 0.5 is displayed in the inset image.

#### **4.5.3. Composition at the defect site**

To confirm the origin of the nano-scaled voids, a compositional analysis of the sample was performed by SEM and TEM. **Figure 4.7** includes three different quantitative results: (1) the total composition of the sample by SEM, (2) the composition of the non-voided area by TEM and (3) the composition of the void by TEM. The composition from SEM (1) and TEM of the non-voided area (2) were nearly similar to the initial composition of the  $\text{Ge}_2\text{Sb}_2\text{Te}_5$ , which was Ge:Sb:Te=2:2:5. However, the composition of the void (3) differs from the original compositions, being Ge-deficient and Sb-rich. These results show that the composition is dependent on the existence of voids and compositional variation only occurs in the void area.

The local non-stoichiometry of the void area is distinct evidence of localized melting and is explained by the phase diagram.  $\text{Ge}_2\text{Sb}_2\text{Te}_5$  is a ternary compound composed of 2:1 mixtures of GeTe and  $\text{Sb}_2\text{Te}_3$ . Based on the pseudo-binary phase diagrams of GeTe and  $\text{Sb}_2\text{Te}_3$ ,  $\text{Ge}_2\text{Sb}_2\text{Te}_5$  does not melt congruently.<sup>10</sup> Because  $\text{Ge}_2\text{Sb}_2\text{Te}_5$  has an incongruent melting region below the melting temperature, the pseudo-binary phases of  $\text{Sb}_2\text{Te}_3$  and GeTe were separated during solidification, which produced Ge-deficient and Sb-rich voids.<sup>10</sup> Therefore, the void area previously consisted of a locally molten state, and the compositional change was initiated during solidification. **Figure 4.8** shows a schematic diagram of the defect-induced melting process. Once the localized liquid phase was formed, the voids were generated by EM in milliseconds.

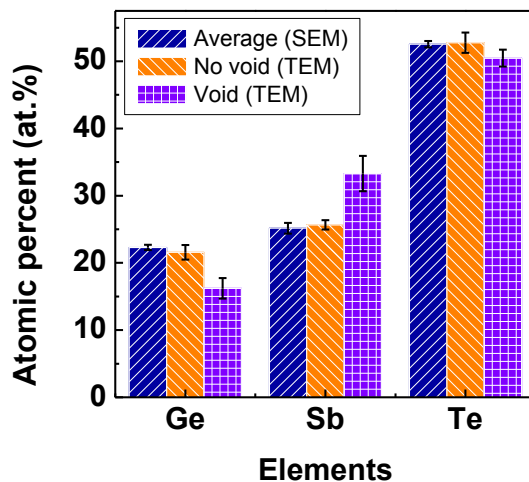


**Figure 4.7** Compositional analysis from SEM and TEM, which contain different interaction volumes. Three different quantitative results are included: the total composition of the sample by SEM, the composition of the non-voided area by TEM, and the composition of the void by TEM.



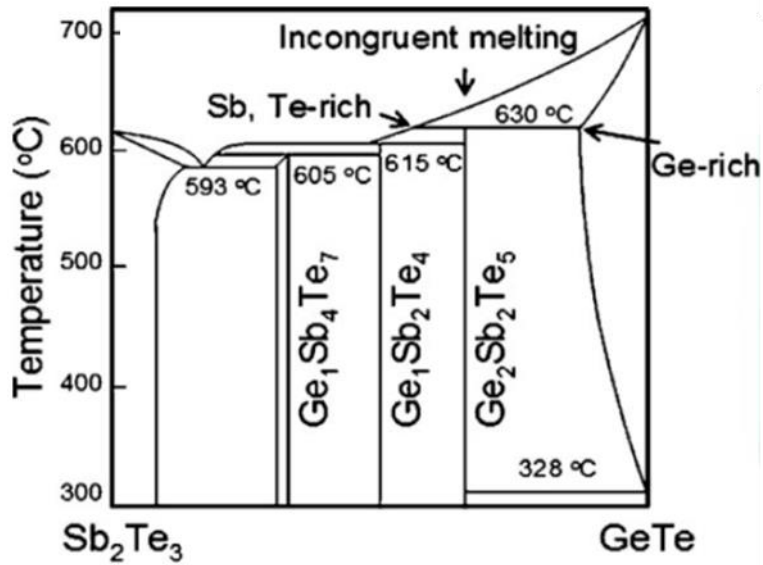


**Figure 4.8** Pseudo-binary phase diagram of  $\text{Sb}_2\text{Te}_3$  and  $\text{GeTe}$ . Molten state of  $\text{Ge}_2\text{Sb}_2\text{Te}_5$  is separated into two phase during solidification process, which are Sb-rich liquid phase and Ge-rich solid phase.

## **4.6. Mechanism of void generation**

The origin of voids is caused by EM in the crystalline state. Although EM in the crystalline phase is not sufficient to induce a catastrophic de-mixing of elements, it can induce an amorphous phase at the grain boundary or surface. It was reported that EM leads to a direct transformation from the crystalline to the amorphous phase without melting by pile-up of the dislocations in the  $\text{Ge}_2\text{Sb}_2\text{Te}_5$ .<sup>16</sup> The grain boundary or surface is the pile-up site of dislocations in the polycrystalline system. Although current flows around the amorphous phase due to its high resistivity, the amorphous phase can act as defect points and generate localized melting. The temperature of the sample increases due to joule heating under the gradual failure testing conditions, but the temperature is too low to cause melting. Under these conditions, melting can only occur locally at vulnerable points, such as a defect, through heterogeneous or defect-induced melting.<sup>61,62</sup>

In the classical thermodynamics, melting process is known as a first-order transformation occurring at the temperature which Gibbs free energies of the solid and liquid phase are same. However, numerous experimental discovered that various kinds of defect, such as grain boundary, surface, voids and other defects initiated melting process.<sup>63</sup> Solid can melt at a temperature below their melting point, because these defects act as heterogeneous nucleation sites for melt. Fecht and Johnson explored the superheating for melting by the temperature dependence of entropy change for a solid and liquid.<sup>64</sup> Fecht and Johnson point out that entropy paradox, which is similar to Kauzmann paradox, exist at a temperature above melting point.<sup>65</sup> Like the ideal glass transition temperature,  $T_g$ , defined by the isentropic condition for an undercooled liquid and crystal below melting point, the instability temperature,  $T_i^*$ , can be defined

by the isentropic temperature for a superheated crystal and liquid above melting point.

<sup>64</sup> If the instability temperature correspond with the temperature, which the volume of the liquid and the superheated crystal become equal through increasing of defect concentration, melting becomes a second-order transition. In this condition, an overall melting cannot occur even at melting point and only arises at the defect sites predominantly.

Intrinsic vacancies of the  $\text{Ge}_2\text{Sb}_2\text{Te}_5$  produce free volume in the liquid phase, which is not filled with constituent atoms. When the constituent elements of  $\text{Ge}_2\text{Sb}_2\text{Te}_5$  were separated by EM, agglomerated free volumes caused the formation of voids in the liquid matrix. <sup>56,66</sup> Because the liquid phase exhibits low resistivity compared with the crystalline phase, the liquid phase can be rapidly transformed to the crystalline phase by reducing the joule heating. Consequently, the gradual increase in the resistance resulted from the steady generation of localized melting spots, which is the rate determining step. The process of voids generation is shown in **Figure 4.9**.

## **4.7. Summary**

We investigated the failure mechanism of  $\text{Ge}_2\text{Sb}_2\text{Te}_5$  in the crystalline phase under DC and AC conditions. Because this behavior only occurs when using DC, we conclude that the failure of the crystalline phase was induced by EM. Localized melting induced by EM produced compositional changes in these localized areas, which consisted of nano-scaled voids. Void generation is the predominant factor in the gradual increase in resistance. These results indicate that devices can fail due to atomic migration in both the crystalline and liquid states, which can cause fatal

reliability problems even at intermediate currents, a regime that has not been considered to cause failures.

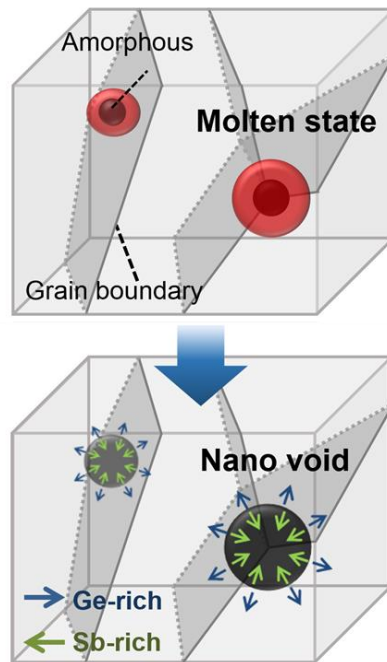


**Figure 4.9** Schematic diagram of the defect-induced melting and phase separation behavior during solidification.

## CHAPTER 5

# Formation of metallic cubic-phase Ge-Sb-Te compounds when induced by an electric current

### 5.1. Introduction

Cubic-phase Ge-Sb-Te compounds have a high degree of disorder with large numbers of structural vacancies in their lattices.<sup>4, 22, 67</sup> This structural feature of the metastable cubic phase causes the electrical properties and charge transport properties to be significantly influenced by temperature.

The resistance of  $\text{GeSb}_2\text{Te}_4$  gradually decreases with temperature, unlike GeTe, and the nature of the material changes from an insulator to a metal at high temperatures, as demonstrated by T. Siegrist et al.<sup>39</sup> Theoretical studies by W. Zhang et al., who used density functional theory calculations determined the microscopic origin of the metal-insulator transition (MIT) in cubic  $\text{GeSb}_2\text{Te}_4$ ; the rearrangement of vacancies decreases the total energy per atom, which implies that the arrangement of vacancies is critical in the electrical properties of cubic  $\text{GeSb}_2\text{Te}_4$ .<sup>48</sup> More recently, the impact of the stoichiometry was demonstrated by P. Jost et al. as a controllable parameter for the MIT of the most common compositions in the  $(\text{GeTe})_x(\text{Sb}_2\text{Te}_3)_{1-x}$  system; i.e., disorder-induced

localization results in the MIT differ according to the average vacancy concentration of various compositions.<sup>50</sup> Therefore, the behaviors of the MIT, which are controlled by the annealing temperature and stoichiometry, are critical for tailoring the charge transport properties of cubic Ge-Sb-Te compounds to increase the performance of PcRAM devices.

Although the rearrangement of vacancies in Ge-Sb-Te compounds is considered the origin of MITs, separating the vacancy effect from phase transitions is difficult because Ge-Sb-Te compounds have two phase types: an insulating cubic phase and a metallic hexagonal phase.<sup>22</sup> The phase transition from the cubic to the hexagonal phase is a high priority before the rearrangement of vacancies can be completed.<sup>39,45</sup> Therefore, the final product of Ge-Sb-Te compounds after an MIT is the hexagonal phase, and the vacancy effect on MITs has not been proven experimentally. Here, we investigated the driving force for MITs beyond the annealing temperature or stoichiometry and independent from the phase transition, specifically, the electric current. The atomic displacement from an electric current can promote the rearrangement of vacancies. MITs should be investigated under electric current stressing conditions, i.e., more device-related characteristics. During PcRAM operation (writing, erasing and reading), cubic Ge-Sb-Te compounds are exposed to various ranges of electric current stressing, and much evidence exists of changes in the structural and charge transport properties under these circumstances.<sup>68,69</sup>

The electric current effect on crystalline GST has been typically associated with a high current density of over  $10^7$  A/cm<sup>2</sup>.<sup>8,9,13,66,68</sup> Under these conditions, the electric current generates disorder or the massive displacement of atoms because the driving force for migration is sufficient to create structural changes with high current density. Disorder can be induced by a high current density in a nanowire system, creating an amorphous or insulating phase.<sup>68,16</sup> In contrast, a relatively low current density of approximately  $10^6$  A/cm<sup>2</sup> cannot generate enough structural disorder to transition to an insulating phase. The

atomic displacement by a low current is negligible compared to that from a high current because the driving force is insufficient to generate a massive flux of atoms.<sup>68</sup> An electric current in the range of  $10^6$  A/cm<sup>2</sup> only assists in the rearrangement of vacancies.

In this chapter, we demonstrate the transition from an insulator to a metal without a phase transition by using an electric current in crystalline Ge<sub>2</sub>Sb<sub>2</sub>Te<sub>5</sub>, which differs from thermal annealing. This approach is a new pathway for metallic cubic phase formation, which has not been previously reported because Ge<sub>2</sub>Sb<sub>2</sub>Te<sub>5</sub> generally has low resistivity in the hexagonal phase. The metallic cubic phase of Ge<sub>2</sub>Sb<sub>2</sub>Te<sub>5</sub> is investigated by temperature dependency and microstructural analyses. Moreover, the influence of intrinsic vacancies on MITs was investigated by comparing Ge<sub>2</sub>Sb<sub>2</sub>Te<sub>5</sub> and GeSb<sub>4</sub>Te<sub>7</sub>, which have structurally different initial vacancies.<sup>18,70</sup>

## 5.2. Experiments

Line-patterned Ge<sub>2</sub>Sb<sub>2</sub>Te<sub>5</sub> and GeSb<sub>4</sub>Te<sub>7</sub> samples, whose measurements were 20  $\mu$ m in length, 2  $\mu$ m in width and 300 nm in thickness, were subjected to an electric current or various temperatures as described in **Chapter 3**. Unlike the study in **Chapter 4**, the as-deposited Ge<sub>2</sub>Sb<sub>2</sub>Te<sub>5</sub> film was annealed for 1 hour at 200 °C to crystallize the initial amorphous phase into a cubic phase. The initial resistivity of the cubic phase of Ge<sub>2</sub>Sb<sub>2</sub>Te<sub>5</sub> was approximately  $2 \times 10^{-2}$   $\Omega$ ·cm.

The I-V characteristics of the Ge<sub>2</sub>Sb<sub>2</sub>Te<sub>5</sub> were measured by using a wafer-level tester (**Section 3.2.1**) and long-term stressing was applied to the Ge<sub>2</sub>Sb<sub>2</sub>Te<sub>5</sub> by using a package-level tester (**Section 3.2.2**)

Cross-sectional images of the current- and temperature-stressed samples were taken by using a TEM (Technai F20). The TEM samples were fabricated by using an FIB (SII NanoTechnology SMI3050SE). Microstructural analysis with X-ray diffractometry (XRD, PANalytical X'pert Pro) was also performed.

### **5.3. Current-driven electrical sweep in $\text{Ge}_2\text{Sb}_2\text{Te}_5$**

#### **5.3.1. I-V characteristics of $\text{Ge}_2\text{Sb}_2\text{Te}_5$**

A double directional mode, with a sweep from zero to the peak current and a return to zero was used, and the peak current density increased each cycle from 0.33 to 1.67  $\text{MA}/\text{cm}^2$  in 0.17  $\text{MA}/\text{cm}^2$  increments, as shown in **Figure 5.1**. The electrical resistivity of  $\text{Ge}_2\text{Sb}_2\text{Te}_5$  after a current sweep with an increasing peak current density is displayed only for 0.33 and 0.5  $\text{MA}/\text{cm}^2$  in **Figure 5.1(b)**. As shown in **Figure 5.1**, the resistivity of  $\text{Ge}_2\text{Sb}_2\text{Te}_5$  decreased with increasing current density, and a certain amount of the resistivity was unrecovered during the reverse sweep; i.e., an irreversible change in resistivity was observed. In contrast, the change in resistivity during the reverse sweep was the same as that for the forward sweep under the experienced current density; i.e., a reversible change in resistivity was displayed. These results indicate that an irreversible change in resistivity was completed during the first cycle of the applied current. The slopes of the resistivity and current density during the reverse sweep increased with the peak current density, and their signs changed from negative to positive at a peak current density of 1  $\text{MA}/\text{cm}^2$ .

A cyclic current sweep was performed with a fixed peak-current density of 1.67  $\text{MA}/\text{cm}^2$  for  $\text{Ge}_2\text{Sb}_2\text{Te}_5$ . **Figure 5.2** shows the resistivity of  $\text{Ge}_2\text{Sb}_2\text{Te}_5$  during a



current sweep from 0 to 1.67 MA/cm<sup>2</sup> at room temperature 10 times, and the inset of **Figure 5.2** shows a range of resistivity from 0.0018 to 0.0035 Ωcm. The first sweep (black line in **Figure 5.2**) shows a continuous decrease in resistivity to 1.67 MA/cm<sup>2</sup> during the forward sweep and a slight change in resistivity during the reverse sweep to zero. The second to tenth sweeps, however, follow the reverse of the first sweep with some variation. Furthermore, the resistivity for a direct sweep to 1.67 MA/cm<sup>2</sup> (**Figure 5.2**) is the same as the resistivity for sequential sweeps to 1.67 MA/cm<sup>2</sup>, increasing in increments of 0.17 MA/cm<sup>2</sup> (**Figure 5.1**). These results indicate that an irreversible change in resistivity was completed during the first cycle of the applied current. Once irreversibly changed, the resistivity was reversible under the experienced current density.

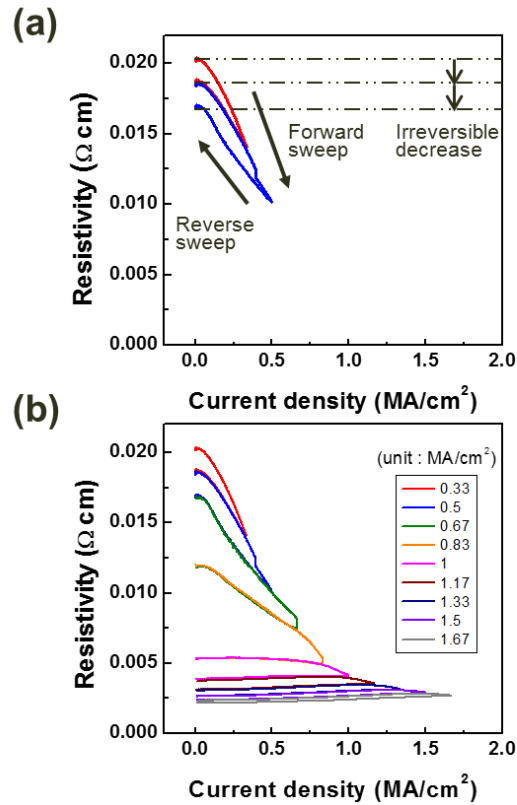


**Figure 5.1** Resistivity of  $\text{Ge}_2\text{Sb}_2\text{Te}_5$  for a current sweep using the double directional mode, with a sweep from zero to peak current and a return to zero, at room temperature for the 0.33 and 0.5  $\text{MA/cm}^2$  conditions. (b) Resistivity change for peak current densities ranging from 0.33 to 1.67  $\text{MA/cm}^2$  in increments of 0.17  $\text{MA/cm}^2$ .

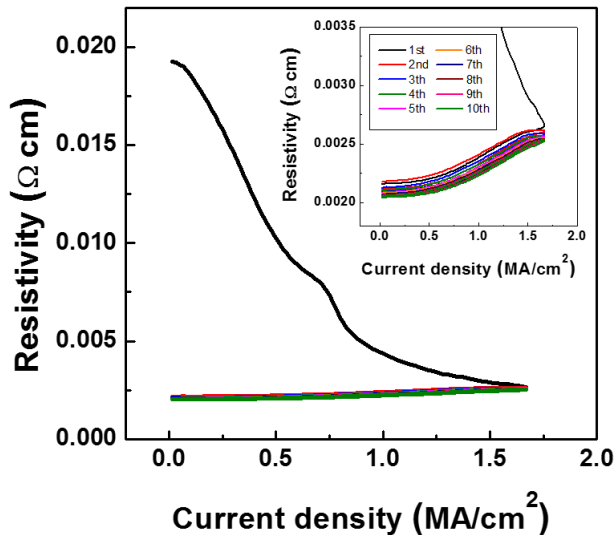


**Figure 5.2** Cyclic test for current sweep from 0 to 1.67 MA/cm<sup>2</sup> with a fixed peak-current-density of 1.67 MA/cm<sup>2</sup> at room temperature for Ge<sub>2</sub>Sb<sub>2</sub>Te<sub>5</sub>. The inset of **Figure 5.2** shows a resistivity during cyclic current sweep ranging from 0.0018 to 0.0035 Ωcm. An irreversible change in resistivity was completed during the first cycle of applied current.

### 5.3.2. TCR measurement of current-stressed $\text{Ge}_2\text{Sb}_2\text{Te}_5$

**Figure 5.3(a)** shows the resistivity of  $\text{Ge}_2\text{Sb}_2\text{Te}_5$  for temperatures from 30 to 90 °C after current stressing. A linear relationship between resistivity and temperature was observed, and their slopes decreased with increasing applied current. The slope of the resistivity and temperature provides the temperature coefficient of resistance (TCR), which is used to distinguish metallic (positive relationship) from insulating (negative relationship) behavior.<sup>39</sup> The TCR of 0.83-MA/cm<sup>2</sup>-stressed  $\text{Ge}_2\text{Sb}_2\text{Te}_5$  (yellow star) was  $-4.0 \times 10^4$  1/K, and the TCR of 1-MA/cm<sup>2</sup>-stressed  $\text{Ge}_2\text{Sb}_2\text{Te}_5$  (orange diamond) was  $6.7 \times 10^4$  1/K, as shown in **Figure 5.3(a)**.

The behavior of resistivity near 0 K is important to distinguish insulators from metals. We attempted to confirm the slope of temperature-resistance at a low temperature range by using three different samples: 0.67 MA/cm<sup>2</sup> current-stressed  $\text{Ge}_2\text{Sb}_2\text{Te}_5$  (insulating), 1 MA/cm<sup>2</sup> current-stressed  $\text{Ge}_2\text{Sb}_2\text{Te}_5$  (transient condition), and 1.5 MA/cm<sup>2</sup> current-stressed  $\text{Ge}_2\text{Sb}_2\text{Te}_5$  (metallic). Because of the limitation of our cooling system, the tendencies of the resistivity of  $\text{Ge}_2\text{Sb}_2\text{Te}_5$  and temperature were confirmed only up to 150 K. **Figure 5.3(b)** shows the resistivity of current-stressed  $\text{Ge}_2\text{Sb}_2\text{Te}_5$  for temperatures from 150 to 373 K. These results show that the behaviors of resistivity near room temperature have constant slopes up to 150 K, which is similar to the reported results of Ge-Sb-Te compounds.<sup>39,50</sup> Although the resistivity behavior near 0 K was not observed, the tendencies of the resistivity changes in the current-stressed GST were similar to annealed GST ( $\text{Ge}_2\text{Sb}_2\text{Te}_5$  with a current density below 1 MA/cm<sup>2</sup> is the same as insulating GST, and  $\text{Ge}_2\text{Sb}_2\text{Te}_5$  with a current density over 1 MA/cm<sup>2</sup> is the same as metallic GST). Therefore, current-stressed  $\text{Ge}_2\text{Sb}_2\text{Te}_5$  over 1 MA/cm<sup>2</sup>, which has a positive relationship between resistivity and temperature, is estimated to have a finite

resistivity value at 0 K. The exact confirmation of metallic behavior through an analysis near 0 K will be discussed in a future study.

**Figure 5.4** shows the resistivity slope as a function of the current density, which corresponds to the results in **Figure 5.1(b)**, and as a function of the temperature, which corresponds to the results in **Figure 5.3(a)**, according to the stress peak current density. The slopes of resistivity according to the current density during the reverse sweep and temperature are denoted as current slope and temperature slope, respectively. As shown in **Figure 5.4**, the behavior of the TCR was similar to the resistivity slope for the current density, which changed from negative to positive at the peak current density of  $1 \text{ MA/cm}^2$ . Because the resistivity change in the reverse sweep had a relationship with temperature, a reversible change in the resistivity under experienced conditions was affected by Joule heating. Therefore, the current-stressed  $\text{Ge}_2\text{Sb}_2\text{Te}_5$  was regarded to have displayed metallic behavior at current densities above  $1 \text{ MA/cm}^2$ .

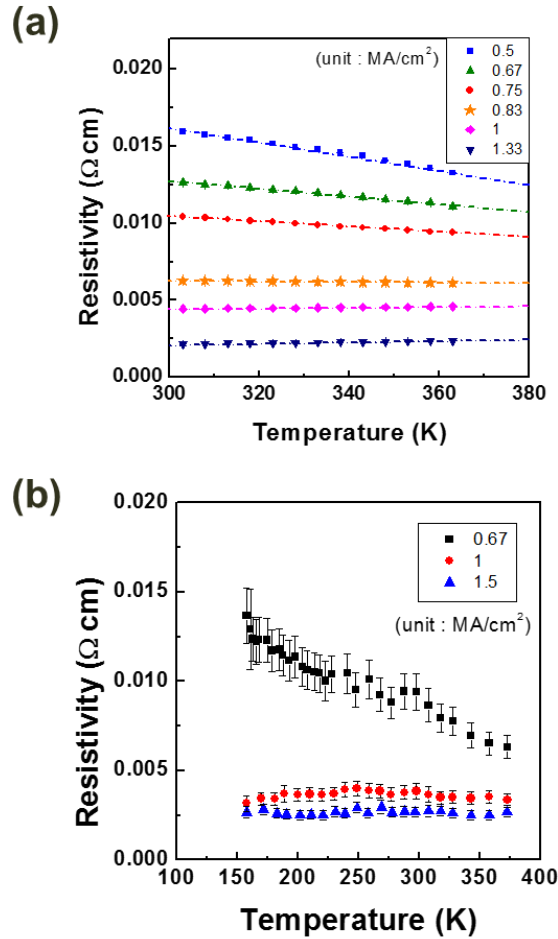


**Figure 5.3** (a) The resistivity of current-stressed  $\text{Ge}_2\text{Sb}_2\text{Te}_5$  from **Figure 5.1(b)** for temperatures ranging from 30 to 90 °C. The dotted lines are extrapolations whose slopes correspond to the temperature coefficient of resistance (TCR). (b) Resistivity of current-stressed  $\text{Ge}_2\text{Sb}_2\text{Te}_5$  for temperature ranging from 150 to 373 K. Conditions of current density were 0.67  $\text{MA/cm}^2$  (black square), 1  $\text{MA/cm}^2$  (red diamond), and 1.5  $\text{MA/cm}^2$  (blue triangle).

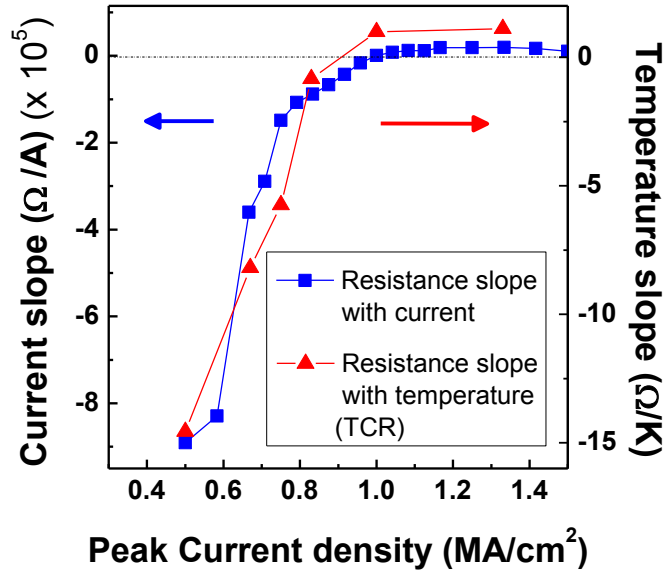


**Figure 5.4** Resistivity slope for current density and temperature according to the stress peak current density results from **Figure 5.1(b)** and **5.3(a)**, respectively. The behavior of the TCR in  $\text{Ge}_2\text{Sb}_2\text{Te}_5$  was similar to the resistivity slope for the current density, which changed from negative to positive at the peak current density of  $1 \text{ MA/cm}^2$ .

### 5.3.3. Complex effect of current and temperature in $\text{Ge}_2\text{Sb}_2\text{Te}_5$

**Figure 5.5** shows that the resistivity of  $\text{Ge}_2\text{Sb}_2\text{Te}_5$  depends on each current sweep under different temperature conditions, which are (a) room temperature, (b) 100 °C, and (c) 200 °C. **Figure 5.5(d)** illustrates how the final resistivity of  $\text{Ge}_2\text{Sb}_2\text{Te}_5$  depends on each current sweep, and **Figure 5.5(e)** shows that the slope of the resistivity depends on each current sweep for various temperatures, which are results of the current sweep at various temperatures, as referenced in **Figure 5.5(a)-(c)**. As the temperature increased, the starting point of the resistivity decreased, as depicted in **Figure 5.5(d)**. However, the resistivity for a current density over 0.7 MA/cm<sup>2</sup> showed the same results in the resistivity curve regardless of the temperature. Additionally, the sign of the resistivity slope changed from negative to positive at 1 MA/cm<sup>2</sup>, independent of the temperature, as shown in **Figure 5.5(e)**. This result implies that the resistivity of  $\text{Ge}_2\text{Sb}_2\text{Te}_5$  is only determined by the current density, regardless of the initial resistivity or external temperature.

The crystalline  $\text{Ge}_2\text{Sb}_2\text{Te}_5$  compounds had a fixed resistivity value depending on the applied current density, and the resistivity changes were irreversible. Therefore, once the initial resistivity was reduced by the temperature, the current density had no direct effect on the final resistivity until it reached the current density for the corresponding reduced resistivity. When the current density reached the corresponding resistivity, the resistivity followed the universal curve of  $\text{Ge}_2\text{Sb}_2\text{Te}_5$ , which is useful for a resistivity-based device because the resistivity can be controlled by an electric current.



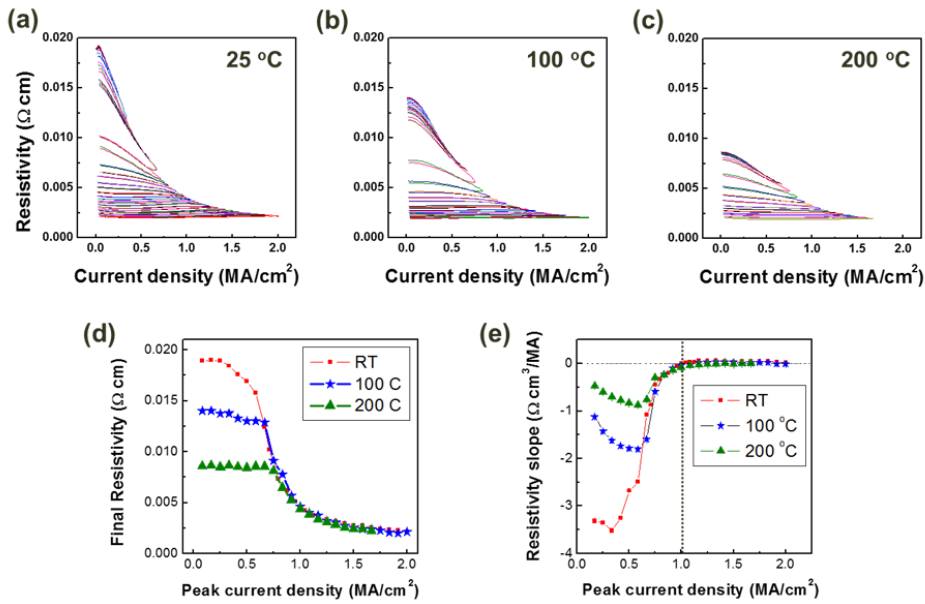


**Figure 5.5** (a)-(c) Resistivity of  $\text{Ge}_2\text{Sb}_2\text{Te}_5$  for peak-current densities ranging from 0.17 to 2  $\text{MA/cm}^2$  in increments of 0.08  $\text{MA/cm}^2$  at different temperatures which are (a) room temperature, (b) 100 °C, and (c) 200 °C, respectively. (d) Final resistivity and (e) slope of resistivity of  $\text{Ge}_2\text{Sb}_2\text{Te}_5$  according to peak current density at various temperature based on the results from (a)-(c).

## **5.4. Time-dependent behavior of $\text{Ge}_2\text{Sb}_2\text{Te}_5$**

We investigated the influence of the current duration on the resistivity of  $\text{Ge}_2\text{Sb}_2\text{Te}_5$ , as shown in **Figure 5.6(a)**, to understand the kinetic properties of current-induced resistivity change in  $\text{Ge}_2\text{Sb}_2\text{Te}_5$ . The resistivity of  $\text{Ge}_2\text{Sb}_2\text{Te}_5$  decreased with the application of a current density, but the change only occurred during the early current stressing phase, similar to the results in **Figure 5.1(b)**. **Figure 5.6(b)** shows the initial and final resistivity values of  $\text{Ge}_2\text{Sb}_2\text{Te}_5$  with an electric current that was applied for 30 hours, according to the current density. As mentioned above, a current-induced resistivity change occurred during the first cycle of the current sweep, which indicates that an irreversible change in resistivity occurred within a few seconds. After this drastic change, the resistivity of  $\text{Ge}_2\text{Sb}_2\text{Te}_5$  remained unchanged for a long period, regardless of the current density.

We also investigated resistivity according to time annealing at various temperatures, as shown in **Figure 5.7(a)**, to compare this influence with that of electrical and thermal stress on changes in the resistivity of  $\text{Ge}_2\text{Sb}_2\text{Te}_5$ . The resistivity of  $\text{Ge}_2\text{Sb}_2\text{Te}_5$  under isothermal annealing decreased with temperature, and a continuous change was observed over a long period, as shown in **Figure 5.7(a)**. The saturated resistivity, or the time-independent point of resistivity, was inversely proportional to the ambient temperature. **Figure 5.7(b)** shows the initial and final resistivity values of  $\text{Ge}_2\text{Sb}_2\text{Te}_5$  (based on **Figure 5.7(a)**) according to the temperature. Unlike the results for an applied current, significant differences were observed between the initial and final resistivity values under annealed conditions, as shown in **Figure 5.7(b)**. These results show that the electric current has a kinetically fast effect on the resistivity compared to thermal stress, which involves a thermally activated change. Although electrical and thermal stress have different time-dependent behaviors,

they exert a similar influence on the resistivity of  $\text{Ge}_2\text{Sb}_2\text{Te}_5$  to reach a minimum resistivity state.

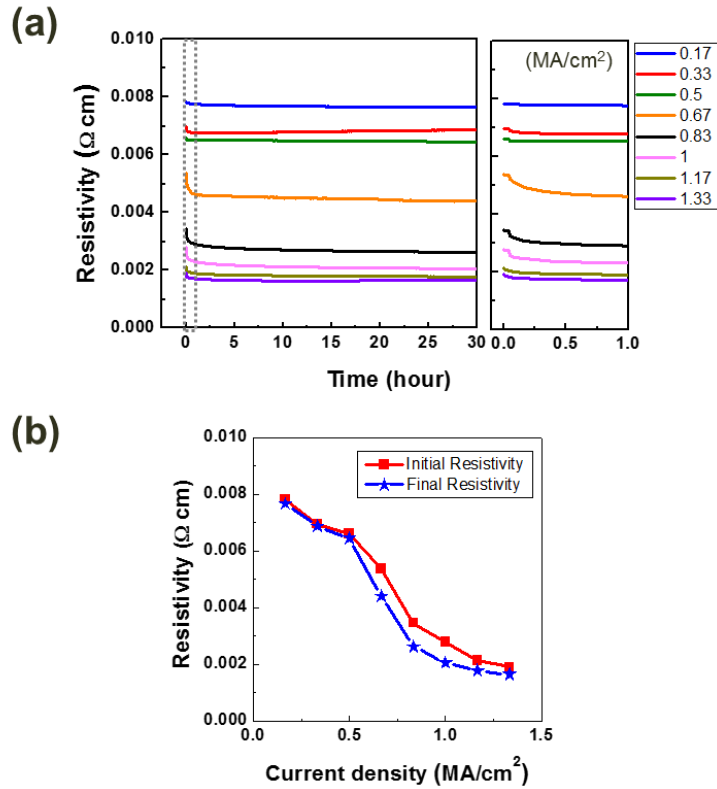


**Figure 5.6** (a) Resistivity change of  $\text{Ge}_2\text{Sb}_2\text{Te}_5$  according to the duration of applied current density, ranging from 0.17 to 1.33 MA/cm<sup>2</sup>, for 30 hours and its expansion (dotted box) from 0 to 1 hour. (b) Initial and final resistivities of  $\text{Ge}_2\text{Sb}_2\text{Te}_5$  according to the current density for the current-stressed condition result from (a).

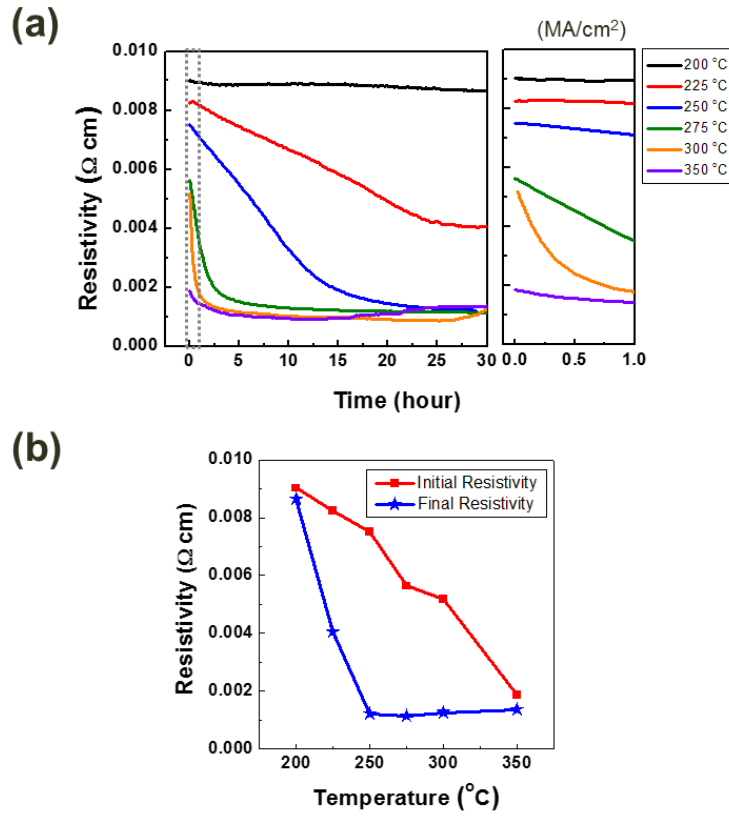


**Figure 5.7** (a) Resistivity change of  $\text{Ge}_2\text{Sb}_2\text{Te}_5$  according to the duration of applied temperature, ranging from 200 to 350  $^{\circ}\text{C}$ , for 30 hours and its expansion (dotted box) from 0 to 1 hour. (d) Initial and final resistivities of  $\text{Ge}_2\text{Sb}_2\text{Te}_5$  according to the ambient temperature for the isothermal annealing condition result from (c). The electric current has a kinetically fast effect on resistivity compared with thermal stress, which involves a thermally activated change.

## 5.5. Microstructural analysis of $\text{Ge}_2\text{Sb}_2\text{Te}_5$

### 5.5.1 Phase of current- and temperature-stressed $\text{Ge}_2\text{Sb}_2\text{Te}_5$

Microstructural analyses were conducted for a more detailed examination of the differences between electrical and thermal effects. According to **Figure 5.6** and **Figure 5.7**, the resistivity values from an electrical stress of  $1 \text{ MA/cm}^2$  and a thermal stress of  $250 \text{ }^\circ\text{C}$  were saturated and unchanged. The current-stressed sample for  $1 \text{ MA/cm}^2$  and the temperature-stressed sample for  $250 \text{ }^\circ\text{C}$  are denoted as the “current sample” and “temperature sample”, respectively.

First, a microstructural analysis of the initial sample, which was not applied with an electrical or thermal stress, is shown in **Figure 5.8**. The microstructure of the initial sample was in a polycrystalline state and the average grain size was approximately  $20 \text{ nm}$ , as indicated by the dotted line. Because of the polycrystalline state and small grain size, a ring-type diffraction pattern was observed, as shown in **Figure 5.8(b)**. According to the radii of the concentric circles, the crystalline phase of the current sample was confirmed as the face-centered cubic (FCC) phase of  $\text{Ge}_2\text{Sb}_2\text{Te}_5$ . This result is expected because the as-deposited  $\text{Ge}_2\text{Sb}_2\text{Te}_5$  was annealed at  $200 \text{ }^\circ\text{C}$  to transform the crystalline cubic phase.

**Figure 5.9** shows the microstructural image and diffraction pattern of a current and temperature sample of  $\text{Ge}_2\text{Sb}_2\text{Te}_5$ . As shown in **Figure 5.9(a)**, the microstructure of the current sample was in a polycrystalline state and the average grain size was approximately  $20 \text{ nm}$ , which is similar to the initial  $\text{Ge}_2\text{Sb}_2\text{Te}_5$ . The diffraction pattern was also the same as the initial  $\text{Ge}_2\text{Sb}_2\text{Te}_5$  to maintain a polycrystalline face-centered cubic (FCC) phase of  $\text{Ge}_2\text{Sb}_2\text{Te}_5$ . The calculated results of the diffraction pattern are displayed in **Table 5.1**. These results show that an electric current can reduce the resistivity by an order of magnitude when the microstructure is maintained in a cubic phase. Microstructural

analyses were conducted in various positions to represent the entire phase, and the results were independent of the position.

In contrast, large grains of more than 100 nm were observed in the temperature sample, as shown in **Figure 5.9(c)**. High temperatures increased the grain size of  $\text{Ge}_2\text{Sb}_2\text{Te}_5$ . **Figure 5.9(d)** shows the diffraction pattern for **Figure 5.9(c)**, which is a spot-type pattern because of the large grains. Based on the distance ( $3.05 \text{ \AA}$ ) and angle of the spots ( $87.5^\circ$ ), the crystalline plane of the temperature sample is determined to be in the (013) family, and the phase was confirmed as the hexagonal close packing (HCP) phase of  $\text{Ge}_2\text{Sb}_2\text{Te}_5$ . The plane indexes, whose zone axes were  $[-3 \ 3 \ 1]$ , are described in **Figure 5.10**. The initial sample, which was not stressed by a current or temperature, was not a fully crystalline phase but had a grain size of approximately 20 nm and was in the cubic phase of  $\text{Ge}_2\text{Sb}_2\text{Te}_5$ , similar to the current sample. Based on the standard phase of  $\text{Ge}_2\text{Sb}_2\text{Te}_5$  at room temperature, the only microstructural change in the current sample was crystallization. The temperature sample, however, had large grains and a different crystalline phase compared to the initial state. Interestingly, the current and temperature samples exhibited similar electrical resistivity values, although the cubic phase displayed an insulating behavior and the hexagonal phase displayed a metallic behavior. The current sample had a low resistivity, similar to the hexagonal phase, while maintaining the cubic phase. Therefore, crystalline  $\text{Ge}_2\text{Sb}_2\text{Te}_5$  possesses another primary factor for the determination of resistivity in addition to the phase.

**Table 5.1** Comparison between the calculated distance in **Figure 5.9(b)** and crystallographic distance in cubic phase of  $\text{Ge}_2\text{Sb}_2\text{Te}_5$ .

<b>(h k l)</b>	<b>d (Å)</b>	<b>Calculated distance (Å)</b>	<b>Error (%)</b>
<b>1 1 1</b>	3.481	3.477	0.1
<b>2 0 0</b>	3.050	3.037	- 0.7
<b>2 2 0</b>	2.131	2.143	- 0.5
<b>3 1 1</b>	1.818	1.869	- 2.8
<b>2 2 2</b>	1.741	1.758	- 0.8
<b>4 0 0</b>	1.507	1.522	- 1.0

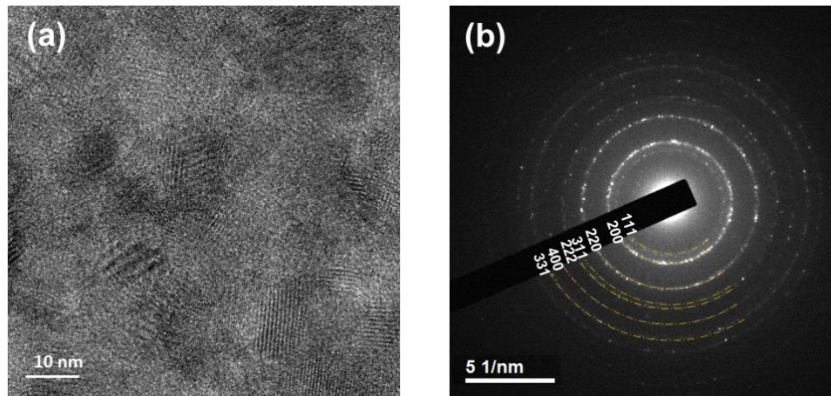


**Figure 5.8** (a) TEM image and (b) diffraction pattern of the initial  $\text{Ge}_2\text{Sb}_2\text{Te}_5$  sample, which was not applied by thermal and electrical stress. The microstructure of the current sample was in a polycrystalline cubic phase and the average grain size was approximately 20 nm.



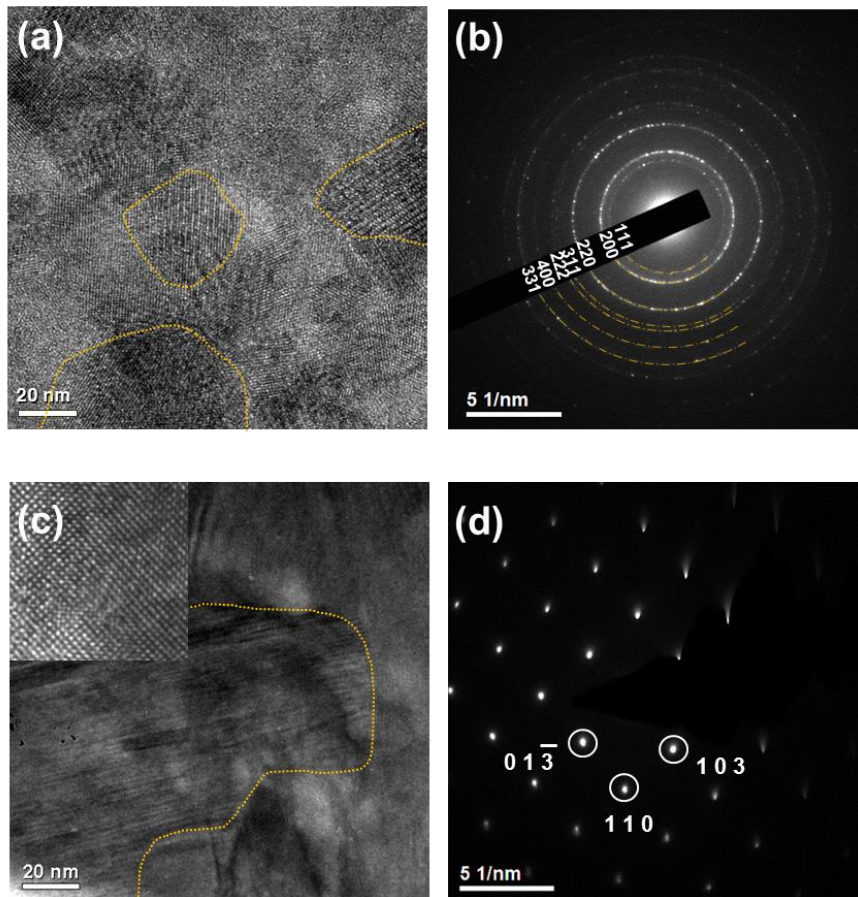


**Figure 5.9** (a) TEM image and (b) diffraction pattern of the current-stressed  $\text{Ge}_2\text{Sb}_2\text{Te}_5$  sample (Current sample:  $1 \text{ MA/cm}^2$  condition). The yellow dotted lines indicate the grain boundary. The microstructure of the current sample was in a polycrystalline cubic phase and the average grain size was approximately 20 nm. (c) TEM image and (d) diffraction pattern of the temperature-stressed  $\text{Ge}_2\text{Sb}_2\text{Te}_5$  sample (temperature sample:  $250^\circ\text{C}$  condition). An HRTEM image of a single grain is displayed in the inset of (c). Large grains of more than 100 nm in a hexagonal phase were observed in the temperature sample.

(a)

2 $\theta$	d(Å)	Intensity	h	k	l
25.5684	3.481020	136	1	1	1
29.6079	3.014650	999	2	0	0
42.3661	2.131680	635	2	2	0
50.1393	1.817900	67	3	1	1
52.5347	1.740510	189	2	2	2
61.4644	1.507320	75	4	0	0
67.6799	1.383220	27	3	3	1
69.6880	1.348190	176	4	2	0

(b)

2 $\theta$	d(Å)	Intensity	h	k	l
5.2062	16.960000	160	0	0	1
10.4233	8.480000	1	0	0	2
15.6621	5.653330	1	0	0	3
20.9341	4.240000	3	0	0	4
24.4524	3.637310	17	1	0	0
25.0173	3.556440	9	0	1	1
26.2513	3.392000	16	0	0	5
26.6449	3.342780	19	1	0	2
29.1702	3.058880	999	0	1	3
31.6267	2.826670	11	0	0	6
32.4032	2.760680	66	0	1	4
36.1798	2.480700	10	1	0	5
37.0746	2.422860	3	0	0	7
40.3780	2.231930	297	1	0	6
42.6109	2.120000	4	0	0	8
43.0368	2.100000	324	1	1	0

**Figure 5.10** JCPDS database of (a) face-centered cubic phase and (b) hexagonal close-packed phase of  $\text{Ge}_2\text{Sb}_2\text{Te}_5$ .

### **5.5.2. Gradual decrease in resistivity during thermal annealing**

**Figure 5.11** shows the XRD results for  $\text{Ge}_2\text{Sb}_2\text{Te}_5$  under different annealing conditions. The HCP transition temperature is generally near 350 °C: <sup>27</sup> the XRD results at 350 °C are shown in **Figure 5.11**. However, even at 250 °C, the hexagonal phase was transformed by long-term annealing. Because a high level of energy is required to generate a new phase, phase transitions are kinetically slow processes and are sensitive to the temperature. Therefore, the continuous decrease in the resistivity of  $\text{Ge}_2\text{Sb}_2\text{Te}_5$  during isothermal annealing, as shown in **Figure 5.7(a)**, is closely related to phase transformation.

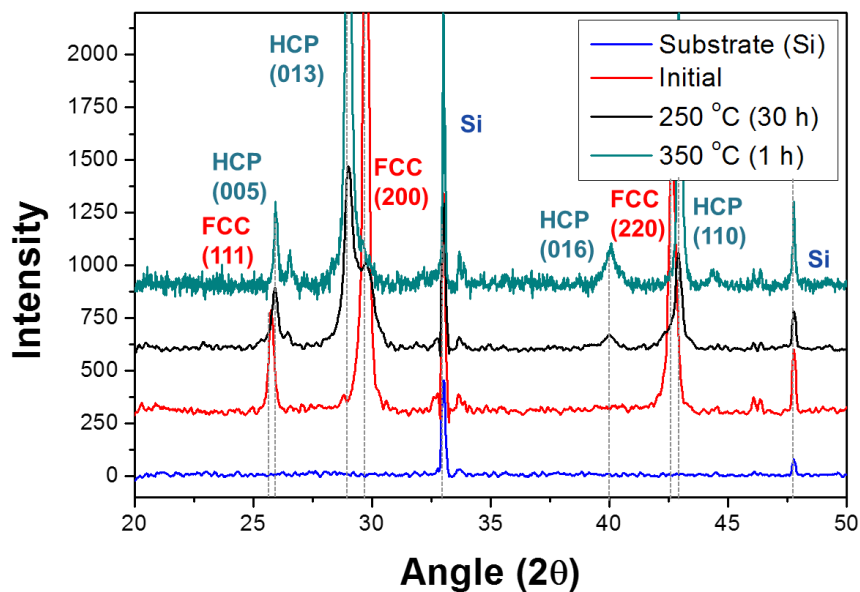


**Figure 5.11** XRD result of  $\text{Ge}_2\text{Sb}_2\text{Te}_5$  for different annealing temperatures: Si substrate (blue), pre-annealed  $\text{Ge}_2\text{Sb}_2\text{Te}_5$  (red),  $\text{Ge}_2\text{Sb}_2\text{Te}_5$  annealed at 250 °C for 30 hours (black), and  $\text{Ge}_2\text{Sb}_2\text{Te}_5$  annealed at 350 °C for 1 hour (green).

## 5.6. Comparison between $\text{Ge}_2\text{Sb}_2\text{Te}_5$ and $\text{GeSb}_4\text{Te}_7$

Because crystalline  $\text{Ge}_2\text{Sb}_2\text{Te}_5$  has a high number of intrinsic vacancies, the electrical properties of  $\text{Ge}_2\text{Sb}_2\text{Te}_5$  are governed by disorder between the constitutional atoms and vacancies.<sup>39</sup> As mentioned in **Section 2.1.2**, a rock-salt structure consists of two interpenetrating FCC sub-lattices; one sub-lattice is located at the origin and the other is located at (0.25, 0.25, 0.25). The volume of intrinsic vacancies depends on the composition because Te atoms perfectly occupy one FCC sub-lattice while Ge and Sb atoms randomly occupy the other FCC sub-lattice. **Table 5.2** shows the fraction of vacancies according to the composition of the Ge-Sb-Te compound. Similar experiments were conducted for  $\text{GeSb}_4\text{Te}_7$ , which has more vacancies than  $\text{Ge}_2\text{Sb}_2\text{Te}_5$ , to investigate the effect of intrinsic vacancies.<sup>18, 70</sup>

**Figure 5.12(a)** shows the electrical resistivity of  $\text{GeSb}_4\text{Te}_7$  after a current sweep with an increasing peak current density from 0.17 and 1.67 MA/cm<sup>2</sup> in 0.17 MA/cm<sup>2</sup> increments at room temperature. As shown in **Figure 5.12(a)**, the resistivity of  $\text{GeSb}_4\text{Te}_7$  decreased with increasing current density, and an irreversible change in resistivity was observed, which are similar to the results for  $\text{Ge}_2\text{Sb}_2\text{Te}_5$  as shown in **Figure 5.1(b)**. **Figure 5.12(b)** shows the final resistivity results for  $\text{Ge}_2\text{Sb}_2\text{Te}_5$  from **Figure 5.1(b)** and the  $\text{GeSb}_4\text{Te}_7$  results from **Figure 5.12(a)** according to the peak current density at room temperature. Although the resistivity of  $\text{Ge}_2\text{Sb}_2\text{Te}_5$  and  $\text{GeSb}_4\text{Te}_7$  decreased with the peak current density, the degree and speed of the decline in  $\text{GeSb}_4\text{Te}_7$  was much higher than that in  $\text{Ge}_2\text{Sb}_2\text{Te}_5$ . These results indicate that electric currents have a similar effect on  $\text{GeSb}_4\text{Te}_7$ , but  $\text{GeSb}_4\text{Te}_7$  is much more sensitive to electric currents than  $\text{Ge}_2\text{Sb}_2\text{Te}_5$ .

**Figure 5.13(a)** shows the resistivity of  $\text{GeSb}_4\text{Te}_7$  at temperatures from 30 to 90 °C after current stressing. The slopes of resistivity and temperature, or the TCR, increased with the

peak current density from negative to near zero. The slopes of the resistivity with current density and temperature, according to the stress current density for  $\text{Ge}_2\text{Sb}_2\text{Te}_5$  and  $\text{GeSb}_4\text{Te}_7$  are shown in **Figure 5.13(b)**, which correspond to the results for  $\text{Ge}_2\text{Sb}_2\text{Te}_5$  (**Figure 5.1(b)** and **Figure 5.3(a)**) and  $\text{GeSb}_4\text{Te}_7$  (**Figure 5.12(a)** and **Figure 5.13(a)**). As shown in **Figure 5.13(b)**, the behavior of the TCR for  $\text{Ge}_2\text{Sb}_2\text{Te}_5$  was similar to the resistivity slope for the current density, which changed from negative to positive at the peak current density of  $1 \text{ MA/cm}^2$ . Although the current and temperature slopes for  $\text{GeSb}_4\text{Te}_7$  have some differences, a similar slope change that approached zero was observed. Moreover, the current and temperature slopes for  $0.33\text{-MA/cm}^2$ -stressed  $\text{GeSb}_4\text{Te}_7$  were extremely changed compared to  $0.17\text{-MA/cm}^2$ -stressed  $\text{GeSb}_4\text{Te}_7$ , even though the difference was only  $0.17 \text{ MA/cm}^2$ . These results indicate that the current-induced resistivity change was more effective in  $\text{GeSb}_4\text{Te}_7$  than in  $\text{Ge}_2\text{Sb}_2\text{Te}_5$ , which depends on the intrinsic vacancy of materials.

Furthermore, **Figure 5.14** illustrates how the resistivity values of  $\text{GeSb}_4\text{Te}_7$  (**Figure 5.14(a)-(c)**) depend on each current sweep at various temperatures, namely, room temperature,  $100^\circ\text{C}$ , and  $200^\circ\text{C}$ . As the temperature increased, the starting point of the resistivity decreased in  $\text{GeSb}_4\text{Te}_7$  because additional thermal energy decreases the resistivity. However, resistivity at high temperatures eventually follows the same resistivity curve of that at room temperature over a certain current density, which is the corresponding point of resistivity. The resistivity of  $\text{GeSb}_4\text{Te}_7$  showed a drastic decrease in current and temperature compared to  $\text{Ge}_2\text{Sb}_2\text{Te}_5$ . The resistivity of  $\text{GeSb}_4\text{Te}_7$  was even saturated to the minimum value at  $200^\circ\text{C}$ . These results indicate that the resistivity of  $\text{GeSb}_4\text{Te}_7$  is much more sensitive to external stimuli, such as electric current and temperature, compared to  $\text{Ge}_2\text{Sb}_2\text{Te}_5$ .

**Table 5.2** Fraction of vacancies in the pseudo-binary compound of  $(\text{GeTe})_x\text{-(Sb}_2\text{Te}_3)_{1-x}$  according to x.

Compound	x	Fraction of vacancy (Ge/Sb site)	Fraction of vacancy (Entire)
<b>GeSb<sub>4</sub>Te<sub>7</sub></b>	0.33	28.6 %	14.7 %
<b>GeSb<sub>2</sub>Te<sub>4</sub></b>	0.5	25 %	12.5 %
<b>Ge<sub>2</sub>Sb<sub>2</sub>Te<sub>5</sub></b>	0.67	20 %	10 %
<b>GeTe</b>	1	0 %	0 %

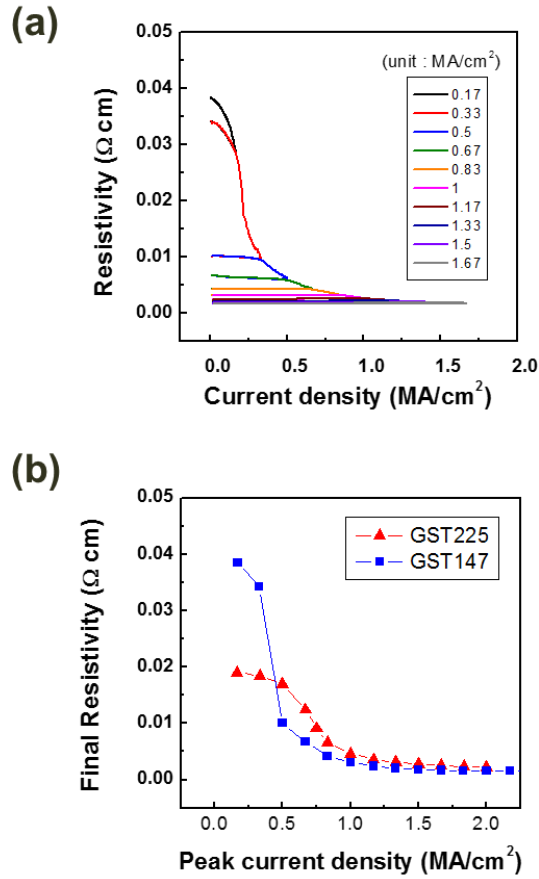


**Figure 5.12** (a) Resistivity change of  $\text{GeSb}_4\text{Te}_7$  with current densities for peak current densities ranging from 0.17 to 1.67  $\text{MA}/\text{cm}^2$  in increments of 0.17  $\text{MA}/\text{cm}^2$  at room temperature. (b) Final resistivity of  $\text{Ge}_2\text{Sb}_2\text{Te}_5$  and  $\text{GeSb}_4\text{Te}_7$  according to peak current density at room temperature (results from **Figure 5.1(b)** and **Figure 5.12(a)**, respectively).



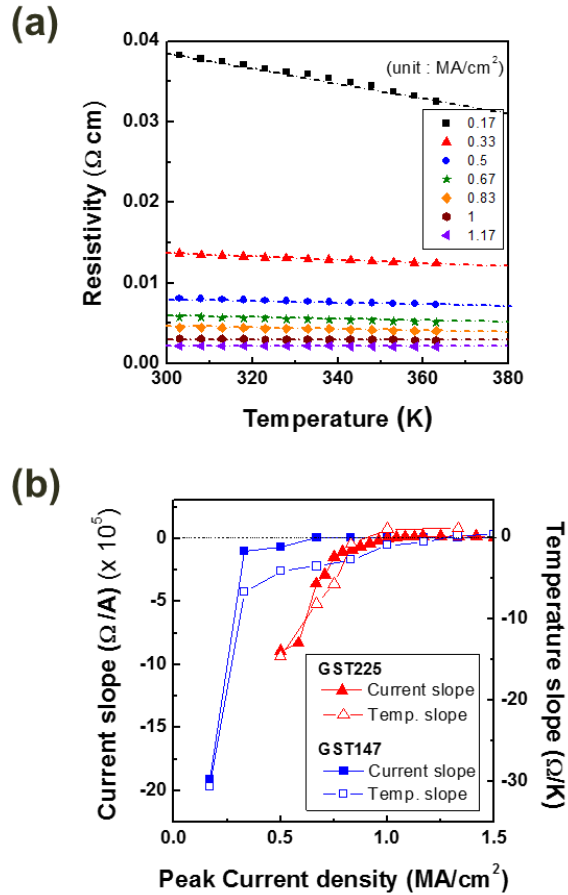


**Figure 5.13** (a) The resistivity of current-stressed  $\text{GeSb}_4\text{Te}_7$  for temperatures ranging from 30 to 90 °C. The dotted lines are extrapolations whose slopes correspond to the TCR. (b) Resistivity slope of  $\text{Ge}_2\text{Sb}_2\text{Te}_5$  and  $\text{GeSb}_4\text{Te}_7$  for current density and temperature according to the stressed-peak-current-density results for  $\text{Ge}_2\text{Sb}_2\text{Te}_5$  (Figure 5.1(b) and Figure 5.3(a)) and  $\text{GeSb}_4\text{Te}_7$  (Figure 5.12(a) and Figure 5.13(a)).

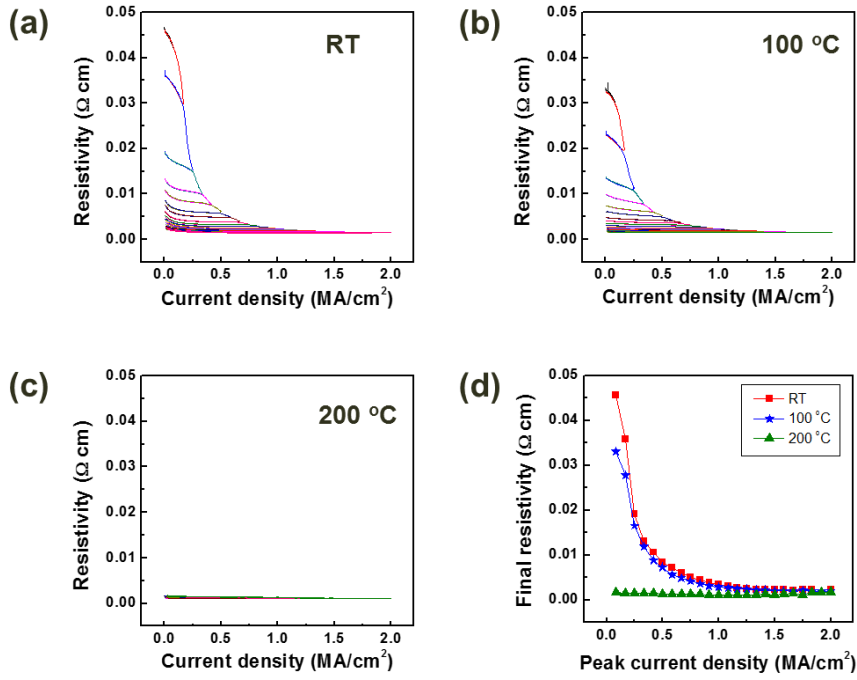


**Figure 5.14** (a)-(c) Resistivity change of GeSb<sub>4</sub>Te<sub>7</sub> for peak-current-densities ranging from 0.17 to 2 MA/cm<sup>2</sup> in increments of 0.08 MA/cm<sup>2</sup> at different temperatures: (a) room temperature, (b) 100 °C, and (c) 200 °C. (d) Final resistivity of GeSb<sub>4</sub>Te<sub>7</sub> according to the peak-current-density at various temperatures, based on the results from (a)-(c).

## **5.7. Role of electric current in vacancy rearrangement**

W. Zhang et al. calculated the total energy per atom for cubic and hexagonal Ge-Sb-Te compounds with respect to vacancy ordering.<sup>48</sup> The rearrangement of vacancies affects the degree of disorder and creates a vacancy plane in both the cubic and hexagonal phases, the latter of which is the most stable state. However, the phase transition from a cubic to hexagonal phase is a high priority before the vacancy planes can be completely formed.<sup>39</sup> Therefore, Ge<sub>2</sub>Sb<sub>2</sub>Te<sub>5</sub> has a low resistivity in the hexagonal phase, which agrees with our results for the temperature sample, as shown in **Figure 5.9(d)**. Surprisingly, the current-stressed Ge<sub>2</sub>Sb<sub>2</sub>Te<sub>5</sub> has a low resistivity, similar to the hexagonal phase, while maintaining a cubic phase. An applied current can migrate atoms by momentum transfer from the charge carriers, which is known as electromigration.<sup>15</sup> Vacancy rearrangement is not triggered by electrical currents because the process is thermodynamically spontaneous.<sup>39</sup>

A comparison between AC and DC may explain vacancy migration. Decrease in resistance under an electric current were only affected by DC as shown in **Figure 5.15**. Because the joule heating of AC and DC should produce the same effect, this result indicates that the decreases in resistance related to bias dependence during current stressing. Cumulative migration changes the resistance. No reason can explain the ordering of vacancies through electric currents because vacancy rearrangement is a thermodynamically spontaneous process.<sup>48</sup> The role of electric currents is a kinetic factor that accelerates vacancy rearrangement. Although the driving force of migration is too low to generate a massive flow of atoms for sub-MA/cm<sup>2</sup> current densities, vacancy rearrangements can be easily promoted by electromigration. Therefore, both vacancy rearrangements and phase transitions involve atomic arrangement processes. Phase transitions, however, require more energy to generate a new phase compared to vacancy

rearrangements because phase transitions are accompanied by a global change in atoms. A schematic diagram of the energy state according to vacancy rearrangement in the cubic and hexagonal phases of  $\text{Ge}_2\text{Sb}_2\text{Te}_5$  is described in **Figure 5.16**.

Because the  $\text{Ge}_2\text{Sb}_2\text{Te}_5$  line in our experiment was directly patterned on bulk Si, any generated heat spread easily because of the high thermal conductivity and heat capacity of Si. Furthermore, the resistivity of  $\text{Ge}_2\text{Sb}_2\text{Te}_5$  was independent of the frequency and voltage under an alternating current (AC), unlike under a direct current (DC) as shown in **Figure 5.15**. Because the joule heating of AC and DC should produce the same effect, this result indicates that the resistivity decrease is related to bias dependence during current stressing. Therefore, a current can accelerate vacancy rearrangements without a phase transition.

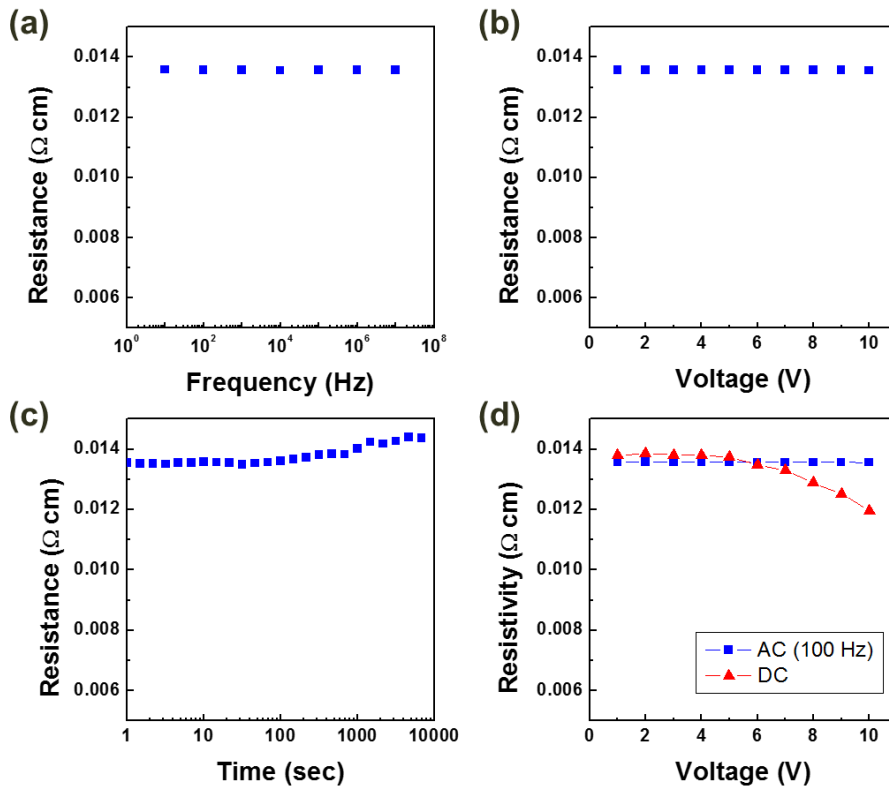


**Figure 5.15** Resistivity of  $\text{Ge}_2\text{Sb}_2\text{Te}_5$  affected by alternating current (AC) and direct current (DC). (a) Resistivity of  $\text{Ge}_2\text{Sb}_2\text{Te}_5$  according to AC frequency from  $10^2$  to  $10^7$  Hz with 1 sec of duration time and 10 V of voltage. (b) Resistivity of  $\text{Ge}_2\text{Sb}_2\text{Te}_5$  according to AC voltage from 1 to 10 V with 1 sec of duration time and 100 Hz of frequency. (c) Resistivity of  $\text{Ge}_2\text{Sb}_2\text{Te}_5$  according to AC time from 0 to 3 hours with voltage of 10 V and frequency of 100 Hz. (d) Resistivity of  $\text{Ge}_2\text{Sb}_2\text{Te}_5$  according to DC and 100 Hz of AC from 1 to 10 V with 1 sec of duration time.

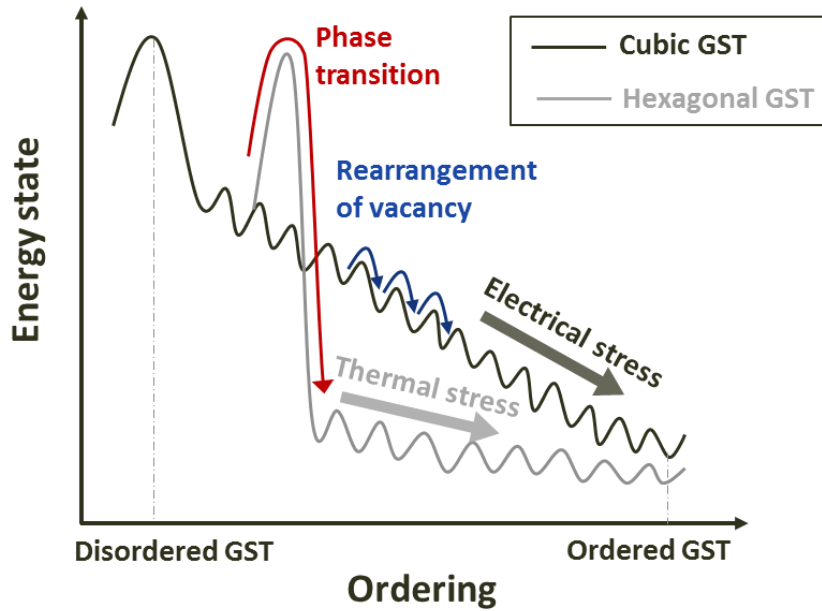


**Figure 5.16** The schematic diagram of the energy states according to the vacancy rearrangement in the cubic and hexagonal phases of Ge-Sb-Te compound. The energy state decreases with vacancy ordering, which is a stable state. The energy barrier for the phase transition from the cubic to the hexagonal phase is much higher than the energy barrier for the rearrangement of vacancies.

## **5.8. Summary**

In summary, we investigated the resistivity of  $\text{Ge}_2\text{Sb}_2\text{Te}_5$  and  $\text{GeSb}_4\text{Te}_7$  under an applied electric current for a range of temperatures. The resistivity is determined by the current density, regardless of the initial resistivity. Without a phase transition, the minimum resistivity can be achieved kinetically quickly by applying a current density, which differs significantly from thermal annealing. This phenomenon depends on the initial vacancy of the materials. This work provides a new pathway for promoting vacancy rearrangements by using an electric current and deepens our understanding of the material physics of phase-change materials.

## CHAPTER 6

# Divergence of failure mechanisms with current and temperature in crystalline chalcogenide

### 6.1. Introduction

Current-induced changes in crystalline phases of  $\text{Ge}_2\text{Sb}_2\text{Te}_5$  have been described in **Chapter 4** and **Chapter 5**. As mentioned in **Chapter 4**, the failure mechanism of  $\text{Ge}_2\text{Sb}_2\text{Te}_5$  changes with the current density. Depending on the applied current density, the behaviors of these changes fall into three main classes. However, this phenomenon has a close relationship with both the current density and temperature. In this chapter, we describe the divergence of mechanisms in chalcogenide materials, including  $\text{Ge}_2\text{Sb}_2\text{Te}_5$  and  $\text{Bi}_2\text{Te}_3$ , with electric current and ambient temperature. Because electric currents create a thermal effect from Joule heating, separating electrical and thermal effects from current-induced degradation is difficult. Thus, we observed the differences in the mechanisms by changing the ambient temperature to confirm the role of the temperature. Furthermore, a mechanism map is proposed from the behavioral differences according to the external conditions, which can provide guidelines for device design.



## **6.2. Experiments**

Line-shaped samples, whose measurements were 20  $\mu\text{m}$  in length, 2  $\mu\text{m}$  in width and 300 nm in thickness, were employed to study the mechanism differences in crystalline chalcogenide with current and temperature, as described in **Chapter 3**.  $\text{Bi}_2\text{Te}_3$  and  $\text{Bi}_{35}\text{Te}_{65}$ , which are Te-rich compositions compared to intermetallic  $\text{Bi}_2\text{Te}_3$ , and  $\text{Ge}_2\text{Sb}_2\text{Te}_5$  were chosen to confirm the effect of stoichiometry on the failure mechanism. Because the as-deposited chalcogenide films were in the amorphous phase, the films were annealed for 1 hour at 200  $^\circ\text{C}$  to crystallize the initial amorphous phase into a crystalline phase. The initial  $\text{Ge}_2\text{Sb}_2\text{Te}_5$  was in a cubic phase before the current stressing.

A direct current (DC) stress from 0.17 to 1.83  $\text{MA}/\text{cm}^2$  was applied, and the ambient temperature was changed from room temperature to 200  $^\circ\text{C}$  by using a package-leveled EM tester (Qualitau MIRA). Failure morphologies were observed via scanning electron microscopy (SEM, Hitachi SU70) and transmission electron microscopy (TEM, Technai F20).

## **6.3. Limitations of the mechanism map for $\text{Ge}_2\text{Sb}_2\text{Te}_5$**

**Figure 6.1** shows the resistance changes with time according to the current density and ambient temperature. The initial resistance of  $\text{Ge}_2\text{Sb}_2\text{Te}_5$  was approximately 3000  $\Omega$  and the phase was the cubic phase of  $\text{Ge}_2\text{Sb}_2\text{Te}_5$ . The resistance of  $\text{Ge}_2\text{Sb}_2\text{Te}_5$  at the starting time commonly decreases with current density. However, gradual decreases

and increases along with constant behavior in the resistance of  $\text{Ge}_2\text{Sb}_2\text{Te}_5$  were observed at different current and temperature conditions. As mentioned in **Section 4.3**, the criteria for a mechanism include the behavior of the resistance and morphological changes. At a high current density, the resistance of  $\text{Ge}_2\text{Sb}_2\text{Te}_5$  rapidly increased within a minute, which resulted in catastrophic failure. Micro-scale agglomerated voids were observed under these conditions. This phenomenon is melting from Joule heating, which is denoted as “abrupt failure”. The resistance of  $\text{Ge}_2\text{Sb}_2\text{Te}_5$  gradually increased for tens of hours and nano-scale voids formed under an intermediate current density. Voids were generated by defect-induced melting, which continuously degraded the conductivity of  $\text{Ge}_2\text{Sb}_2\text{Te}_5$ , as described in **Chapter 4**. This phenomenon is denoted as “gradual failure”. Although no morphological changes occurred under at low current density, the resistance of  $\text{Ge}_2\text{Sb}_2\text{Te}_5$  decreased with current density. This phenomenon originates from vacancy rearrangement in the Ge-Sb-Te system, which is described in **Chapter 5**. Because electrical failure does not occur under a low current despite the resistance change, this phenomenon is denoted as “no failure”.

However, the behavior of the resistance and the morphology are inappropriate criteria for examining the mechanisms in  $\text{Ge}_2\text{Sb}_2\text{Te}_5$  because the factors that can increase and decrease the resistance operate at the same time. **Figure 6.2** shows an SEM image of the  $\text{Ge}_2\text{Sb}_2\text{Te}_5$  line after current stressing for 30 hours at 30 °C, which is the result from the 30 °C test in **Figure 6.1**. Voids are observed under a current density over  $1.17 \text{ MA/cm}^2$ , and the melting of the  $\text{Ge}_2\text{Sb}_2\text{Te}_5$  line is observed over  $1.83 \text{ MA/cm}^2$ . Based on the morphological behavior, current densities below  $1.17 \text{ MA/cm}^2$  are labeled “no failure”, current densities from  $1.17$  to  $1.67 \text{ MA/cm}^2$  are labeled “gradual failure”, and current densities over  $1.83 \text{ MA/cm}^2$  are labeled “abrupt failure”. On the other hand, the resistance initially decreases with the current density,

while time-dependent changes are not observed for a current density below 1.67 MA/cm<sup>2</sup>. This phenomenon is determined to be “no failure” based on the resistance criteria. For example, the resistance of Ge<sub>2</sub>Sb<sub>2</sub>Te<sub>5</sub> when applied with a 1.17 MA/cm<sup>2</sup> current density at 30 °C shows constant behavior over 30 hours, while voids were generated under these conditions. Therefore, the factors that influenced the degradation in Ge<sub>2</sub>Sb<sub>2</sub>Te<sub>5</sub> were confounded and must be classified. **Figure 6.3** shows the mechanism map of Ge<sub>2</sub>Sb<sub>2</sub>Te<sub>5</sub> according to the current density and temperature based only on the morphological behavior.

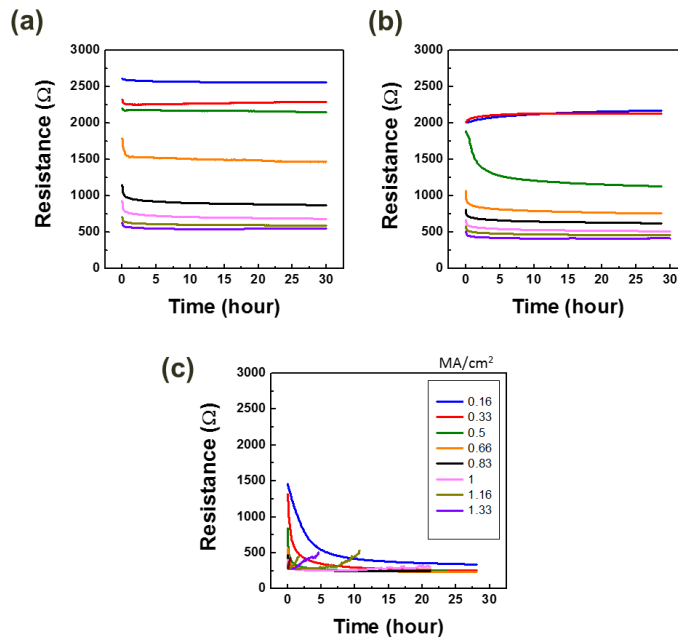


**Figure 6.1** Resistivity change of Ge<sub>2</sub>Sb<sub>2</sub>Te<sub>5</sub> according to the duration of applied current density, ranging from 0.17 to 1.33 MA/cm<sup>2</sup>, for 30 hours at the different ambient temperature: (a) room temperature, (b) 100 °C, and (c) 200 °C

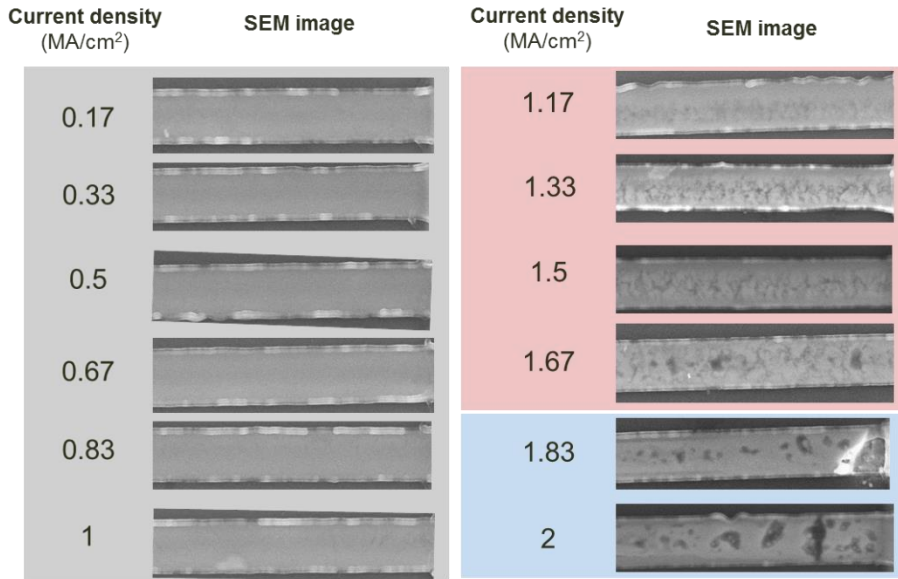


**Figure 6.2** SEM image of Ge<sub>2</sub>Sb<sub>2</sub>Te<sub>5</sub> line after current stressing test for 30 hours at room temperature, which are shown in **Figure 6.1(a)**. Background color means the group of failure behavior based on the morphological image. Current density below 1.17 MA/cm<sup>2</sup> is determined to “no failure” (gray), current density ranged from 1.17 to 1.67 MA/cm<sup>2</sup> is determined to “gradual failure” (red), and current density over 1.83 MA/cm<sup>2</sup> is determined to “abrupt failure” (blue).

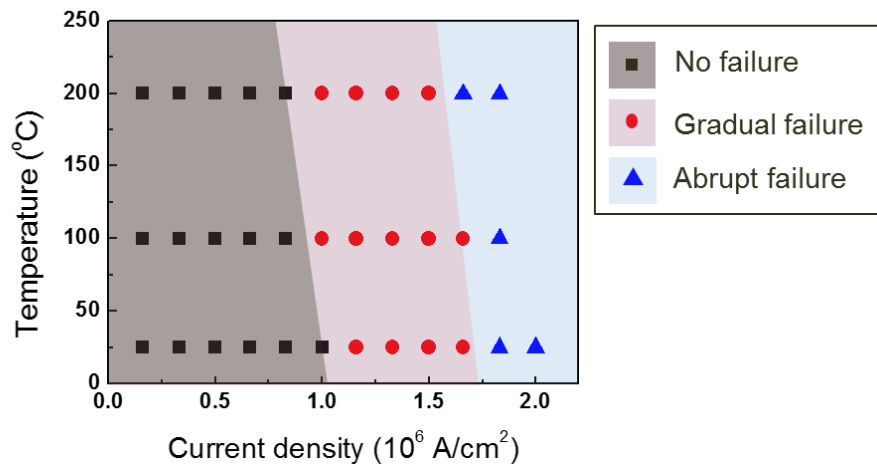


**Figure 6.3** Mechanism map of  $\text{Ge}_2\text{Sb}_2\text{Te}_5$  according to current density and temperature based only on the morphological behavior. All solid point are experiment results and failure mechanisms are expressed by background color. Black square shows “no failure”, red circle shows “gradual failure”, and blue triangle shows “abrupt failure”.

## 6.4. Mechanism map for chalcogenide materials

### 6.4.1. Resistivity behavior in ternary and binary chalcogenide

**Figure 6.4** shows the change in resistance with  $0.33 \text{ MA/cm}^2$  of current stressing over 30 hours in various Te-based chalcogenide materials, including  $\text{Bi}_2\text{Te}_3$ ,  $\text{Sb}_2\text{Te}_3$ ,  $\text{GeTe}$ , and  $\text{Ge}_2\text{Sb}_2\text{Te}_5$ . All the materials were fabricated to a line-shaped structure, and an electric current was applied by using a package-level tester. The relative resistance in **Figure 6.4** means that the resistance value was divided by the initial resistance of each material. According to the results, only the resistance of  $\text{Ge}_2\text{Sb}_2\text{Te}_5$  changed, with a huge and consistent reduction over 30 hours, while the other materials, i.e.,  $\text{Bi}_2\text{Te}_3$ ,  $\text{Sb}_2\text{Te}_3$ , and  $\text{GeTe}$ , remained at their initial resistance values. This result is also shown in **Figure 6.1**.

Crystalline  $\text{Ge}_2\text{Sb}_2\text{Te}_5$  has two types of structures, which are cubic and hexagonal, as mentioned in **Section 2.1**. Although the stable state of crystalline  $\text{Ge}_2\text{Sb}_2\text{Te}_5$  is the hexagonal phase, the cubic phase of  $\text{Ge}_2\text{Sb}_2\text{Te}_5$ , which is a metastable state of crystalline  $\text{Ge}_2\text{Sb}_2\text{Te}_5$ , exists under low temperature. Furthermore, crystalline  $\text{Ge}_2\text{Sb}_2\text{Te}_5$  has a high fraction of structural vacancies. The arrangement of vacancies affects the degree of disorder and the band structure, as mentioned in **Chapter 5**. The gradual decrease in the resistance of crystalline  $\text{Ge}_2\text{Sb}_2\text{Te}_5$  originates from these factors. However, binary chalcogenides, e.g.,  $\text{Bi}_2\text{Te}_3$ ,  $\text{Sb}_2\text{Te}_3$ , and  $\text{GeTe}$ , have a single crystalline phase and no structural vacancies. For example, crystalline  $\text{GeTe}$  forms in a rhombohedral structure with space group  $R3m$  as a distorted rock-salt structure with Ge and Te uniquely located on the each FCC sub-lattice.<sup>71</sup> Because each FCC sub-lattice is perfectly occupied with Ge and Te considering the stoichiometry of  $\text{GeTe}$ , an ideal  $\text{GeTe}$  structure has no structural vacancies.

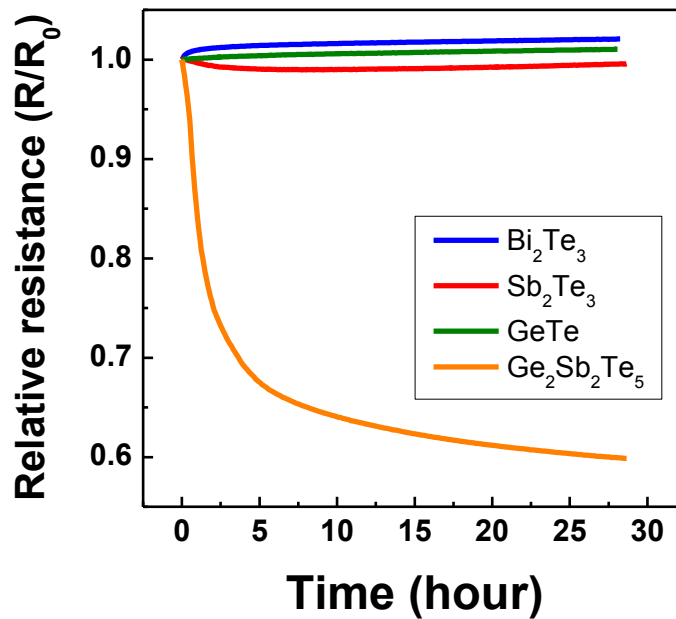


**Figure 6.4** Resistivity change with applying current density of 0.33 MA/cm<sup>2</sup> for 30 hours at 100 °C according to different Te-based chalcogenide materials, which are  $\text{Bi}_2\text{Te}_3$ ,  $\text{Sb}_2\text{Te}_3$ ,  $\text{GeTe}$ , and  $\text{Ge}_2\text{Sb}_2\text{Te}_5$ . The relative resistance means that value of resistance is divided by the initial resistance of each material.



#### **6.4.2. Mechanism behavior in crystalline Bi<sub>2</sub>Te<sub>3</sub>**

Bismuth telluride (Bi<sub>2</sub>Te<sub>3</sub>) is the binary compound of Bi and Te, which is a well-known thermoelectric material.<sup>72</sup> A thin film super-lattice with Bi<sub>2</sub>Te<sub>3</sub> and antimony telluride (Sb<sub>2</sub>Te<sub>3</sub>) was recently formed, and these materials showed the highest value of thermoelectric efficiency.<sup>73</sup> Understanding electrical and thermal stability of thermoelectric materials is important for reliability because high current density and temperature are inevitable to thermoelectric devices.

Bi<sub>2</sub>Te<sub>3</sub> is a layered semiconductor that crystallizes in a rhombohedral structure in single unit cells, where each layer consists of Te-Bi-Te-Bi-Te. **Figure 6.5** shows the phase diagram of Bi and Te, which contains various intermetallic compounds, e.g., Bi<sub>2</sub>Te<sub>3</sub>, Bi<sub>4</sub>Te<sub>5</sub>, BiTe, and so on. Among the stoichiometric compounds, Bi<sub>2</sub>Te<sub>3</sub> is the most promising material for thermoelectric application.

**Figure 6.6** shows the resistance of Bi<sub>2</sub>Te<sub>3</sub> according to applied current densities from 0.33 to 1.33 MA/cm<sup>2</sup> over 30 hours at 100 °C. Three different failure modes could be determined for the current stress tests of Bi<sub>2</sub>Te<sub>3</sub> line specimens, namely, abrupt failure, gradual failure, and no failure in the resistance and morphological changes according to its current density. The sample with high current density (over 1.17 MA/cm<sup>2</sup>) failed in a short amount of time, with largely agglomerated voids forming in a molten state, while the sample with low current density (below 0.83 MA/cm<sup>2</sup>) exhibited no failure and no voids. Unlike the two-failure mode, a gradual increase in the resistance during current stressing was observed under an intermediate current density. Nano-scale voids (approximately 10 nm), which were responsible for the gradual change in resistance, were observed in the sample with an intermediate current density. These results are similar to the current-induced behavior in Ge<sub>2</sub>Sb<sub>2</sub>Te<sub>5</sub> as shown in **Chapter 4**. However, the resistance of Bi<sub>2</sub>Te<sub>3</sub> did not decrease with the

electric current, unlike  $\text{Ge}_2\text{Sb}_2\text{Te}_5$ . Therefore, the behaviors of the resistance and morphology are simultaneously applicable for the criteria of the mechanisms in  $\text{Bi}_2\text{Te}_3$ .

The three failure modes according to the electric current were observed at different temperatures, namely, room temperature, 100 °C, and 200 °C, which confirms a temperature dependency. The resistance behaviors according to the electric current and temperature are shown in the mechanism map in **Figure 6.7**. As the temperature increased, abrupt failure and gradual failure were observed at a low current density because these failures have a close relationship with the melting temperature. The total thermal effect on  $\text{Bi}_2\text{Te}_3$  was the sum of the ambient temperature and Joule heating from the electric current. An abrupt failure (melting) can be initiated from the electric current or temperature, while a gradual failure cannot be initiated only from the temperature. Because gradual failure originates from current-induced defects, as mentioned in **Chapter 4**, an electric current must be applied even near the melting temperature.

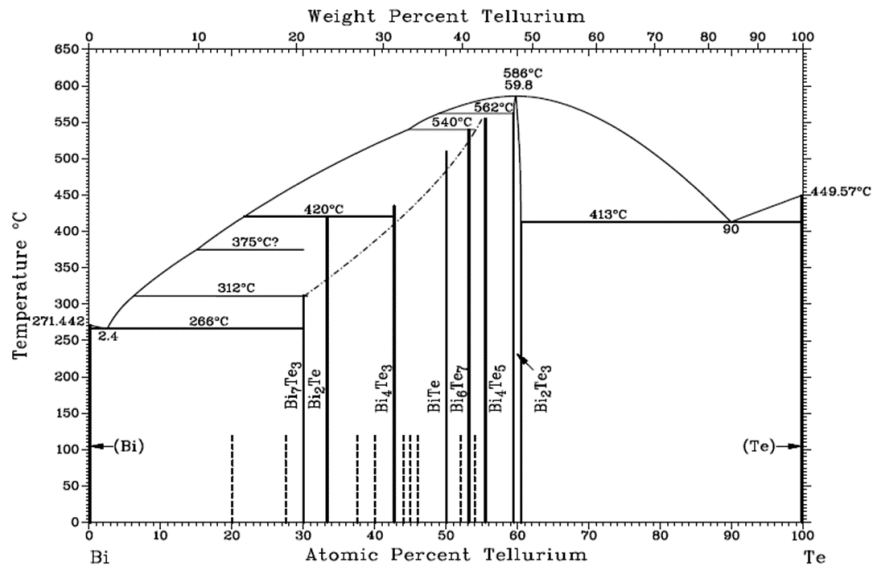


**Figure 6.5** Phase diagram of bismuth and tellurium according to atomic percent of tellurium.

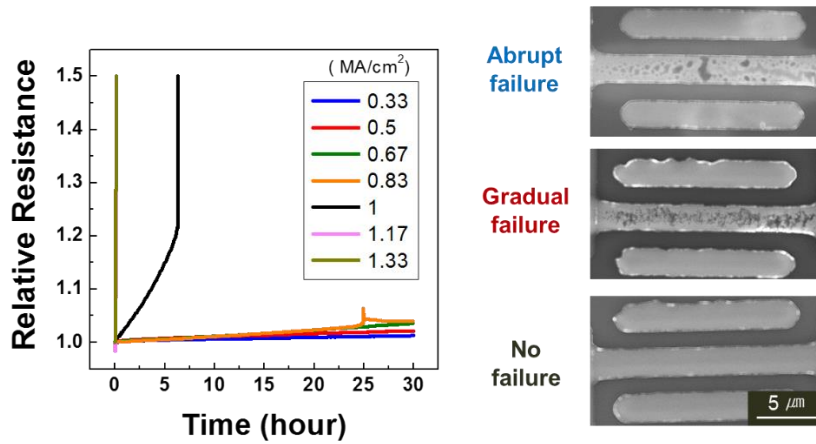


**Figure 6.6** Relative resistance of  $\text{Bi}_2\text{Te}_3$  according to current density ranged from 0.33 to 1.33  $\text{MA}/\text{cm}^2$  for 30 hours at 100 °C, and their SEM image. Current densities below 0.83  $\text{MA}/\text{cm}^2$ , ranging from 0.83 to 1.17  $\text{MA}/\text{cm}^2$  and above 1.17  $\text{MA}/\text{cm}^2$  are denoted as “no failure”, “gradual failure” and “abrupt failure”, respectively.

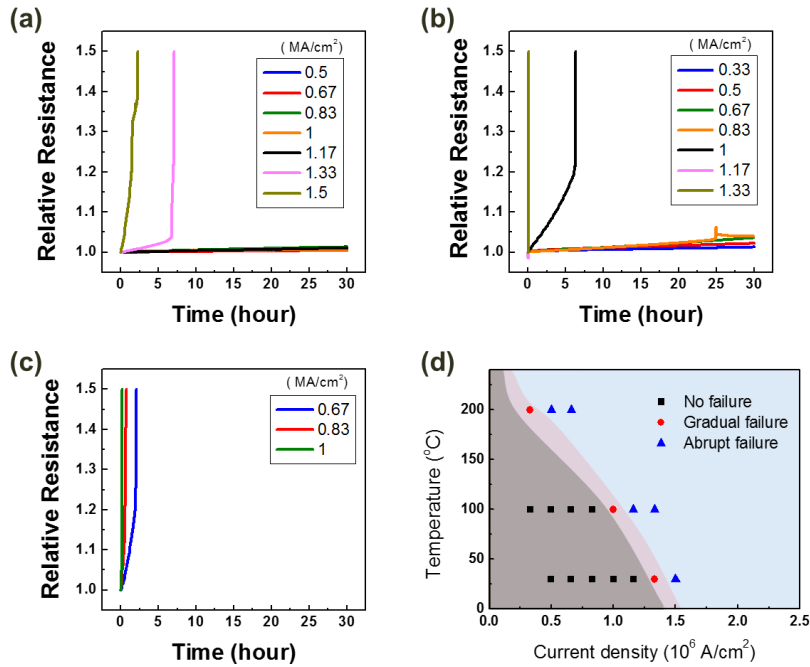


**Figure 6.7** Relative resistance of  $\text{Bi}_2\text{Te}_3$  according to current density ranged from 0.33 to 1.5  $\text{MA/cm}^2$  for 30 hours at (a) room temperature, (b) 100 °C, and (c) 200 °C. (d) The mechanism map according to current density and temperature, which is the merging of the results from (a)-(c).

#### **6.4.3. Failure criteria with respect to the stoichiometric effect**

Although intermetallic compounds of chalcogenide are widely used in various fields, matching the stoichiometric composition is very difficult because of close interval ranges in the composition. Continuously matching the stoichiometry with chemical vapor deposition (CVD) or wet processes is becoming increasingly difficult, so the reliability of non-stoichiometric materials will become more important. We focused on the failure mechanism in  $\text{Bi}_{35}\text{Te}_{65}$ , which has a composition difference of 5 at. % from the intermetallic composition of stoichiometric  $\text{Bi}_2\text{Te}_3$ .

**Figure 6.8** shows the resistance behavior of  $\text{Bi}_{35}\text{Te}_{65}$  when applying an electric current from 0.33 to 1.17 MA/cm<sup>2</sup> for 30 hours at room temperature, 100 °C, 150 °C and 200 °C. A mechanism map based on the current density and temperature, which merges the results from different temperatures, is displayed in **Figure 6.8**. The major difference between  $\text{Bi}_2\text{Te}_3$  and  $\text{Bi}_{35}\text{Te}_{65}$  is the “no failure” region. Gradual increases in the resistance of the constituent materials and catastrophic failure with melting are critical reliability problems in electrical device. Therefore, only the “no failure” mode is a safe condition for operating these devices. The “no failure” region in  $\text{Bi}_{35}\text{Te}_{65}$  is much smaller than that in  $\text{Bi}_2\text{Te}_3$ , as depicted in **Figure 6.7** and **Figure 6.8**. This result indicates that  $\text{Bi}_2\text{Te}_3$  is more stable under an electric current than  $\text{Bi}_{35}\text{Te}_{65}$ .

The reduction in the reliability of non-stoichiometric compounds originates from structural vacancies. Ideally, the crystalline structure of stoichiometric compounds is perfectly located and contains no structural vacancies. The crystalline structure of non-stoichiometric compounds, however, is deficient or contains excess atoms compared to a perfect crystal, which generates structural vacancies and acts as defect sites for gradual failure. Furthermore, phase separation in non-stoichiometric systems occurs below melting temperature with coexisting solid and liquid phases. According to the

phase diagram of Bi and Te in **Figure 6.5**, the melting temperature of  $\text{Bi}_2\text{Te}_3$  is 586 °C, while the melting temperature of eutectic  $\text{BiTe}_9$  is 413 °C. The solid phase of  $\text{Bi}_2\text{Te}_3$  and the liquid phase of  $\text{BiTe}_9$  coexist in a temperature range from 413 to 586 °C. This means that liquid phases in  $\text{Bi}_{35}\text{Te}_{65}$  can be obtained at much lower temperatures compared to  $\text{Bi}_2\text{Te}_3$ . Local liquid phases from phase separation will turn into voids by electromigration through “abrupt failure”. TEM analysis showed that the void area was a Te-rich phase, which has a low melting temperature.

## 6.5. Summary

The behaviors of resistance and morphology are criteria for current-induced failure modes, which include “no failure”, “gradual failure”, and “abrupt failure”. These criteria are applicable in binary chalcogenides but are inappropriate criteria for failure modes in ternary chalcogenides, e.g.,  $\text{Ge}_2\text{Sb}_2\text{Te}_5$ .

The failure mode depends on the electric current and temperature, so a mechanism map can be suggested. The mechanism maps of  $\text{Bi}_2\text{Te}_3$  and  $\text{Bi}_{35}\text{Te}_{65}$  show that the “no failure” area in  $\text{Bi}_2\text{Te}_3$  is far wider than that in  $\text{Bi}_{35}\text{Te}_{65}$ . This result indicates that  $\text{Bi}_2\text{Te}_3$  is more stable for current-induced failure than  $\text{Bi}_{35}\text{Te}_{65}$ . In conclusion, non-stoichiometry in materials seriously reduces the reliability of devices and should be considered in terms of device failure. This result suggests that small composition changes of only 5 at.% from stoichiometry can greatly impede the reliability of devices and that matching an accurate composition is important. Moreover, this result suggests that the guidelines for designing devices should consider the non-stoichiometry of chalcogenide materials by using a mechanism map.

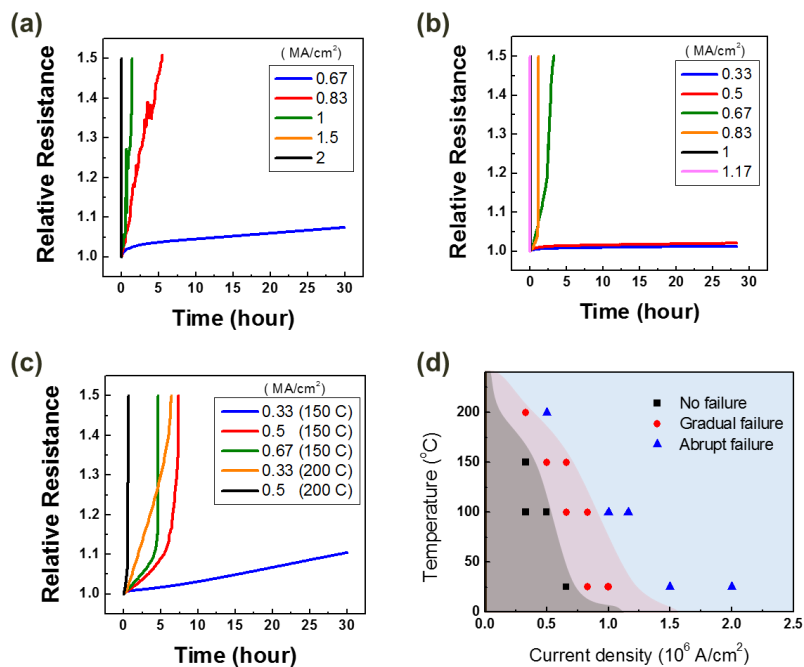


**Figure 6.8** Relative resistance of  $\text{Bi}_{35}\text{Te}_{65}$  according to current density ranged from 0.33 to 1.5  $\text{MA/cm}^2$  for 30 hours at (a) room temperature, (b) 100 °C, (c) 150, and 200 °C. (d) The mechanism map according to current density and temperature, which is the merging of the results from (a)-(c).



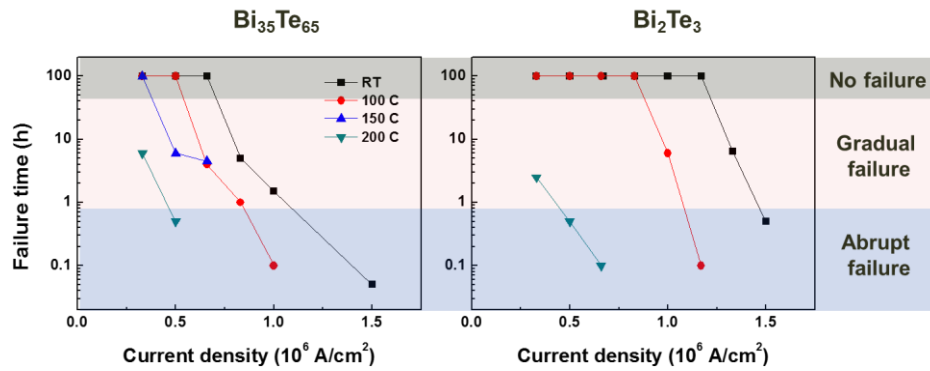


**Figure 6.9** The failure time according to current density and temperature in the  $\text{Bi}_{35}\text{Te}_{65}$  and  $\text{Bi}_2\text{Te}_3$ . Failure time is displayed in the log-scale.

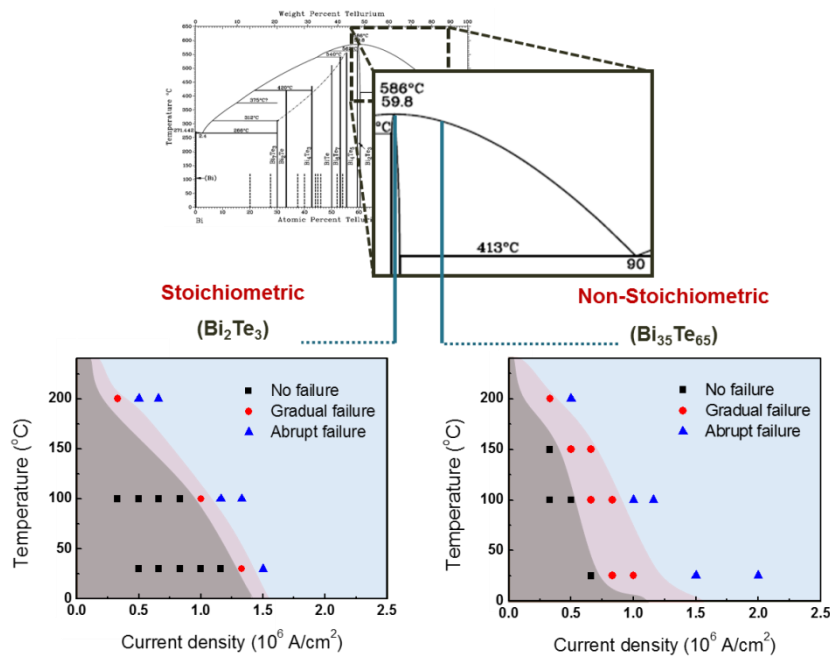


**Figure 6.10** Expanded phase diagram of Bi and Te with atomic percent of Te ranged from 60 to 90 at. %, and mechanism map of stoichiometric Bi<sub>2</sub>Te<sub>3</sub> (Te : 60 at. %) and non-stoichiometric Bi<sub>35</sub>Te<sub>65</sub> (Te : 65 at. %).

## **CHAPTER 7**

### **Conclusions**

#### **7.1. Summary of results**

This study investigated the degradation behavior that was induced by electric currents in phase-change materials by using a simple line-shaped structure, instead of PcRAM cells. The atomic displacement from a low current of approximately  $10^6$  A/cm<sup>2</sup> is negligible compared to that from a high current because the driving force for migration at low currents is insufficient to generate a massive flux of atoms. Although no catastrophic failure is induced by electric currents in crystalline phase-change materials, various phenomena that have not been reported were observed in crystalline Ge-Sb-Te compounds.

We chose Ge-Sb-Te compounds, which are commonly used materials for phase change memory, and applied electric currents on these materials to investigate the effect of electric current on crystalline phase-change materials. The resistivity and morphology of crystalline Ge<sub>2</sub>Sb<sub>2</sub>Te<sub>5</sub> were changed by electric currents and time with three different behaviors. At a high current density, greater than approximately 1 MA/cm<sup>2</sup>, the resistivity rapidly increased within a minute after the formation of micro-

scaled agglomerated voids. This catastrophic failure is electromigration in a molten state that is caused by severe Joule heating. In this case, the compositional de-mixing of constituent elements and voids originated from the free volume of  $\text{Ge}_2\text{Sb}_2\text{Te}_5$  after current stressing. At a low current density, less than approximately  $1 \text{ MA/cm}^2$ , no resistivity or morphological changes were observed with the exception of a decrease in the initial resistance. This decrease in resistivity originated from the ordering of the initial vacancies in  $\text{Ge}_2\text{Sb}_2\text{Te}_5$ . Interestingly, a gradual increase in the resistivity over 10-20 hours was observed under intermediate current density conditions of approximately  $1 \text{ MA/cm}^2$ . The failure morphology revealed that numerous nanometer-sized voids formed throughout the entire area. We can denote these phenomena according to current density as “abrupt failure”, “no failure”, and “gradual failure”, respectively.

A gradual degradation in resistivity was only observed under DC bias, while resistivity and morphological changes were not observed under AC bias. Because the only difference between DC and AC bias is the directionality of the electric current, gradual failure is related to the bias dependence during current stressing, which is electromigration. The local composition near nano-scale voids exhibited a Ge-deficient and Sb-excess composition, while the total composition was maintained at the initial state. The local non-stoichiometry of these void areas is distinct evidence of localized melting. Based on the pseudo-binary phase diagram of  $\text{Sb}_2\text{Te}_3$  and  $\text{GeTe}$ , the Sb-excess liquid phase and Ge-excess solid phase were separated during solidification, which produced Ge-deficient and Sb-excess compositions at the void areas. The origin of these voids was electromigration in the crystalline state. Although electromigration in crystalline phases is not sufficient to induce a catastrophic de-mixing of elements, this process can induce an amorphous phase at the grain boundary

or surface. This amorphous phase can act as defect points and generate localized melting, which is called defect-induced melting. Void generation is a prominent factor in this gradual increase in resistivity. These results indicate that devices can fail because of atomic migration in the crystalline phase and in liquid states. Although catastrophic failure is not induced by electric currents in the crystalline states of phase-change materials, the degradation of crystalline phases is cumulative in the non-active regions of PcRAM devices, which can be a fatal reliability problem even at intermediate currents.

A decrease in resistivity in crystalline  $\text{Ge}_2\text{Sb}_2\text{Te}_5$  at low currents is called the metal-insulator transition. From the theoretical literature, the origin of this phenomenon is known to be the rearrangement of vacancies. We first demonstrated a resistivity change in the cubic phase of  $\text{Ge}_2\text{Sb}_2\text{Te}_5$  by using an electric current of approximately  $1 \text{ MA/cm}^2$ . The final resistivity is determined by the current density regardless of the initial resistivity. The material property of  $\text{Ge}_2\text{Sb}_2\text{Te}_5$  changed from an insulator to a metal under a current density of  $1 \text{ MA/cm}^2$ , which was analyzed from the slope change of the resistivity versus temperature. The time-dependent behavior of the resistivity shows that the change only occurred during the early current stressing phase, while a continuous change was observed over long periods under isothermal annealing. The major difference between electrical and thermal stress is the microstructure. The current stressed  $\text{Ge}_2\text{Sb}_2\text{Te}_5$ , which had a current density of  $1 \text{ MA/cm}^2$ , had a small grain size of approximately 20 nm and maintained a cubic phase, similar to unstressed  $\text{Ge}_2\text{Sb}_2\text{Te}_5$ . The temperature stressed  $\text{Ge}_2\text{Sb}_2\text{Te}_5$ , however, had a grain size that was greater than 100 nm and transformed to a hexagonal phase. The origin of the difference between electrical and thermal stress is the migration energy. The rearrangement of vacancies is a thermodynamically spontaneous process. The

role of electric currents is a kinetic factor that accelerates vacancy rearrangement. Phase transitions, however, require more energy to generate a new phase compared to vacancy rearrangements because phase transitions are accompanied by a global change in atoms. Therefore, the minimum resistivity of cubic phases can be achieved kinetically quickly by applying a current density without a phase transition.  $\text{GeSb}_4\text{Te}_7$  shows the same behavior as  $\text{Ge}_2\text{Sb}_2\text{Te}_5$ , while  $\text{GeSb}_4\text{Te}_7$  is much more sensitive to electric currents compared to  $\text{Ge}_2\text{Sb}_2\text{Te}_5$ .  $\text{GeSb}_4\text{Te}_7$  and  $\text{Ge}_2\text{Sb}_2\text{Te}_5$  have different intrinsic vacancy fractions, specifically, 14.7 % and 10 %, respectively. Therefore, current-induced resistivity changes are determined by the intrinsic vacancy of materials.

The failure mode depends on the electric current and temperature, so a mechanism map can be suggested. The mechanism maps of  $\text{Bi}_2\text{Te}_3$  and  $\text{Bi}_{35}\text{Te}_{65}$  show that the “no failure” area in  $\text{Bi}_2\text{Te}_3$  is far wider than that in  $\text{Bi}_{35}\text{Te}_{65}$ . This result indicates that  $\text{Bi}_2\text{Te}_3$  is more stable for current-induced failure than  $\text{Bi}_{35}\text{Te}_{65}$ . In conclusion, the non-stoichiometry of materials seriously reduces the reliability of devices and should be considered for device failure. This result suggests that small composition changes of only 5 at.% from stoichiometry can greatly impede the reliability of devices and that matching an accurate composition is important. Moreover, this result suggests guidelines for designing devices that consider the non-stoichiometry of chalcogenide materials by using mechanism map.

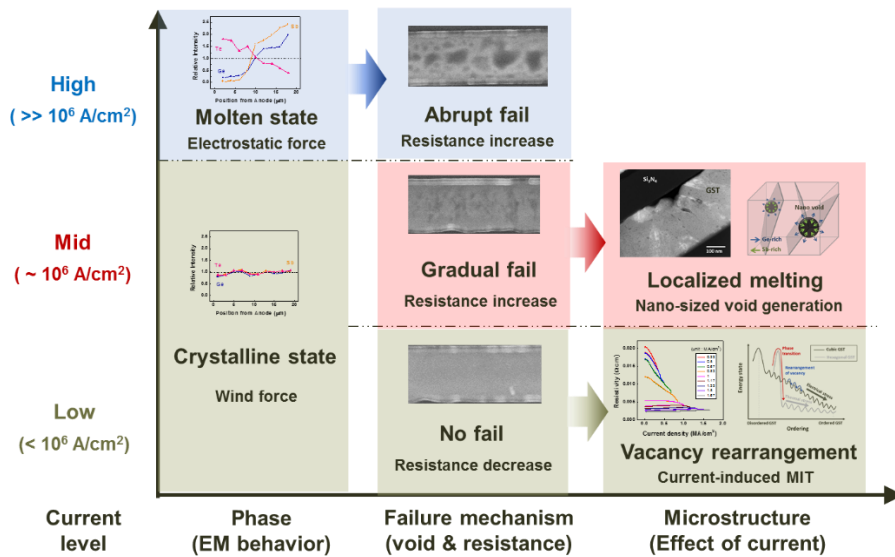


**Figure 7.1** Summary of behavior in phase change materials according to current density.

## **7.2. Future works and suggested research**

In this study, the slope of the TCR, which is obtained from the relationship between resistivity and temperature, was used to distinguish metallic and insulating behavior. A positive TCR relationship implies metallic behavior, while a negative TCR relationship implies insulating behavior. However, the behavior of resistivity near zero Kelvin is a more powerful method for confirming electrical characteristics compared to TCR measurements. The conductivity of insulators vanishes as the temperature approaches zero Kelvin, while metals maintain finite conductivity. The conductivity of current-stressed  $\text{Ge}_2\text{Sb}_2\text{Te}_5$  will be analyzed near zero Kelvin to confirm the transition to metal under electrical stress. In addition, we are scheduled to study the dependence of the dimensions on the current-induced metal transition. An electric current generates a current path, so not all materials can be affected by electric currents. In this case, current-induced transitions can be determined from the dimensions of the materials.

A sample structure with a line shape was used for a model study in this study. By using a line structure, we could clearly identify the various degradation mechanisms and structural changes in phase-change materials depending on the current density. However, the factors that influence a material's structure and environment are mixed in actual devices. Device level studies will be considered to identify suitable application. For example, crystalline  $\text{Ge}_2\text{Sb}_2\text{Te}_5$  had a fixed resistivity value depending on the applied current density in our work. When the current density reached the corresponding resistivity, the resistivity followed the universal curve of  $\text{Ge}_2\text{Sb}_2\text{Te}_5$ , which can be applicable for a crystalline-based device because the resistivity was controlled by an electric current.



A mechanism map for various materials will help guide device operation. Based on the failure mode, gradual increases in resistance in the constituent materials and catastrophic failure with melting are critical reliability problems. The “no failure” mode is the only safe condition for operating devices. We believe that this work provides new insight into the electrical reliability of the crystalline phase of chalcogenides and offers design rules and guidelines for chalcogenide-based devices.

## Reference

- 1 Bedeschi, F., Resta, C., Khouri, O., Buda, E., Costa, L., Ferraro, M., Pellizzer, F., Ottogalli, F., Pirovano, A., Tosi, M., Bez, R., Gastaldi, R., and Casagrande, G., *IEEE Symposium on VLSI Circuits, Digest of Technical Papers*. CIRCUITS SYMP. edn 442-445 (2004).
- 2 Pirovano, A., Lacaita, A. L., Benvenuti, A., Pellizzer, F., and Bez, R. *IEEE Transactions on Electron Devices* **51**(3), 452-459 (2004).
- 3 Lai, S. *Technical Digest - International Electron Devices Meeting*, 255-258 (2003).
- 4 Wuttig, M., and Yamada, N., *Nature Materials* **6**(11), 824-832 (2007).
- 5 Ielmini, D., Lacaita, A. L., Pirovano, A., Pellizzer, F., and Bez, R., *IEEE Electron Device Letters* **25**(7), 507-509 (2004).
- 6 Cho, W. Y., Cho, B. H., Choi, B. G., Oh, H. R., Kang, S., Kim, K. S., Kim, K. H., Kim, D. E., Kwak, C. K., Byun, H. G., Hwang, Y., Ahn, S., Koh, G. H., Jeong, G., Jeong, H., and Kim, K., *IEEE Journal of Solid-State Circuits* **40**(1), 293-298 (2005).
- 7 Kim, K., and Ahn, S. J., *IEEE International Reliability Physics Symposium Proceedings*. 157-162 (2005).

- 8 Yoon, S. M., Choi, K. J., Lee, N. Y., Lee, S. Y., Park, Y. S., and Yu, B. G., *Applied Surface Science* **254**(1), 316-320 (2007).
- 9 Park, J. B., Park, G. S., Baik, H. S., Lee, J. H., Jeong, H., and Kim, K., *Journal of the Electrochemical Society* **154**(3), H139-H141 (2007).
- 10 Nam, S. W., Kim, C., Kwon, M. H., Lee, H. S., Wi, J. S., Lee, D., Lee, T. Y., Khang, Y., and Kim, K. B., *Applied Physics Letters* **92**(11), 111913 (2008).
- 11 Kang, D., Lee, D., Kim, H. M., Nam, S. W., Kwon, M. H., and Kim, K. B., *Applied Physics Letters* **95**(1), 011904 (2009).
- 12 Nam, S. W., Lee, D., Kwon, M. H., Kang, D., Kim, C., Lee, T. Y., Heo, S., Park, Y. W., Lim, K., Lee, H. S., Wi, J. S., Yi, K. W., Khang, Y., and Kim, K. B., *Electrochemical and Solid-State Letters* **12**(4), H155-H159 (2009).
- 13 Yang, T. Y., Park, I. M., Kim, B. J., and Joo, Y. C., *Applied Physics Letters* **95**(3), 032104 (2009).
- 14 Chen, C. F., Schrott, A., Lee, M. H., Raoux, S., Shin, Y. H., Breitwisch, M., Baumann, F. H., Lai, E. K., Shaw, T. M., Flaitz, P., Cheek, R., Joseph, E. A., Chen, S. H., Rajendran, B., Lung, H. L., and Lam, C., *IEEE International Memory Workshop*, 5090589 (2009)
- 15 Huntington, H. B., and Grone, A. R. *Journal of Physics and Chemistry of Solids* **20**(1), 76-87 (1961).

- 16 Nam, S. W., Chung, H. S., Lo, Y. C., Qi, L., Li, J., Lu, Y., Johnson, A. T. C., Jung, Y., Nukala, P., and Agarwal, R., *Science* **336**(6088), 1561-1566 (2012).
- 17 Cheong, B. K., Lee, S., Jeong, J. H., Park, S., Hang, S., Wu, Z., and Ahn, D. H., *Physica Status Solidi (B) Basic Research* **249**(10), 1985-1991 (2012).
- 18 Yamada, N., and Matsunaga, T. *Journal of Applied Physics* **88**(12), 7020-7028 (2000).
- 19 Ovshinsky, S. R., *Physical Review Letters* **21**(20), 1450-1453 (1968).
- 20 Abrikosov, N. K., and DANILOVA, D. *IZV AKAD NAUK SSSR NEORGAN MATERIALY* **1**(2), 204-207 (1965).
- 21 Bordas, S., Clavaguer-Mora, M. T., Legendre, B., and Hancheng, C., *Thermochimica Acta* **107**(C), 239-265 (1986).
- 22 Yamada, N., Ohno, E., Nishiuchi, K., Akahira, N., and Takao, M., *Journal of Applied Physics* **69**(5), 2849-2856 (1991).
- 23 Yamada, N., Nishiuchi, K., Sanai, S., Nagata, K., Takao, M., and Akahira, N., *National technical report* **35**(2), 12-19 (1989).
- 24 Kuypers, S., van Tendeloo, G., van Landuyt, J., and Amelinckx, S., *Journal of Solid State Chemistry* **76**(1), 102-108 (1988).
- 25 Karpinsky, O. G., Shelimova, L. E., Kretova, M. A., and Fleurial, J. P., *Journal of Alloys and Compounds* **268**(1), 112-117 (1998).

- 26 Shelimova, L. E., Karpinskii, O. G., Konstantinov, P. P., Kretova, M. A., Avilov, E. S., and Zemskov, V. S., *Inorganic Materials* **37**(4), 342-348 (2001).
- 27 Friedrich, I., Weidenhof, V., Njoroge, W., Franz, P., and Wuttig, M., *Journal of Applied Physics* **87**(9), 4130-4134 (2000).
- 28 WeŁnic, W., Pamungkas, A., Detemple, R., Steimer, C., Blügel, S., and Wuttig, M., *Nature Materials* **5**(1), 56-62 (2006).
- 29 Wuttig, M., Lüsebrink, D., Wamwangi, D., WeŁnic, W., Gilleen, M., and Dronskowski, R., *Nature Materials* **6**(2), 122-128 (2007).
- 30 Zhou, J., Sun, Z., Pan, Y., Song, Z., and Ahuja, R., *Europhysics Letters* **95**(2), 27002 (2011).
- 31 Petrov, I. I., and Imamov, R. M., *Ussr* **13**(3), 339 (1968).
- 32 Sun, Z., Zhou, J., and Ahuja, R., *Physical Review Letters* **96**(5), 055507 (2006).
- 33 Kooi, B. J., and De Hosson, J. T. M., *Journal of Applied Physics* **92**(7), 3584-3590 (2002).
- 34 Kolobov, A. V., Fons, P., Frenkel, A. I., Ankudinov, A. L., Tominaga, J., and Uruga, T., *Nature Materials* **3**(10), 703-708 (2004).
- 35 Kolobov, A. V., Haines, J., Pradel, A., Ribes, M., Fons, P., Tominaga, J., Katayama, Y., Hammouda, T., and Uruga, T., *Physical Review Letters* **97**(3),

- 035701 (2006).
- 36 Fons, P., Kolobov, A. V., Tominaga, J., and Katayama, Y., *Nuclear Instruments and Methods in Physics Research, Section B: Beam Interactions with Materials and Atoms* **238**(1), 160-162 (2005).
  - 37 Kolobov, A. V., Haines, J., Pradel, A., Ribes, M., Fons, P., Tominaga, J., Steimer, C., Aquilanti, G., and Pascarelli, S., *Applied Physics Letters* **91**(2), 021911 (2007).
  - 38 Lyeo, H. K., Cahill, D. G., Lee, B. S., Abelson, J. R., Kwon, M. H., Kim, K. B., Bishop, S. G., and Cheong, B. G., *Applied Physics Letters* **89**(15), 151904 (2006).
  - 39 Siegrist, T., Jost, P., Volker, H., Woda, M., Merkelbach, P., Schlockermann, C., and Wuttig, M., *Nature Materials* **10**(3), 202-208 (2011).
  - 40 Mott, N. *Proceedings of the Royal Society of London A: Mathematical, Physical and Engineering Sciences*. 1-24 (1982).
  - 41 Anderson, P. W. *Physical review* **109**(5), 1492 (1958).
  - 42 Lee, P. A., and Ramakrishnan, T. V., *Reviews of Modern Physics* **57**(2), 287-337 (1985).
  - 43 Belitz, D., and Kirkpatrick, T. R., *Reviews of Modern Physics* **66**(2), 261-380 (1994).

- 44 Denteneer, P. J. H., Scalettar, R. T., and Trivedi, N., *Physical Review Letters* **87**(14), 146401 (2001).
- 45 Siegrist, T., Merkelbach, P., and Wuttig, M., *Annual Review of Condensed Matter Physics* **3**(1), 215-237 (2012).
- 46 Lee, B. S., Abelson, J. R., Bishop, S. G., Kang, D. H., Cheong, B. K., and Kim, K. B., *Journal of Applied Physics* **97**(9), 093509 (2005).
- 47 Kato, T., and Tanaka, K., *Japanese Journal of Applied Physics, Part 1: Regular Papers and Short Notes and Review Papers* **44**(10), 7340-7344 (2005).
- 48 Zhang, W., Thiess, A., Zalden, P., Zeller, R., Dederichs, P. H., Rat, J. Y., Wuttig, M., Blugel, S., and Mazzarello, R., *Nature Materials* **11**(11), 952-956 (2012).
- 49 Shportko, K., Kremers, S., Woda, M., Lencer, D., Rovertson, J., and Wuttig, M., *Nature Materials* **7**(8), 653-658 (2008).
- 50 Jost, P., Volker, H., Poitz, A., Poltorak, C., Zalden, P., Schäfer, T., Lange, F. R. L., Schmidt, R. M., Holländer, B., Wirtsohn, M. R., and Wuttig, M. *Advanced Functional Materials* **25**(40), 6399-6406 (2015).
- 51 Fiks, V., *Soviet Physics-Solid State* **1**(1), 14-28 (1959).
- 52 Pearson, R. G., *Inorganic Chemistry* **27**(4), 734-740 (1988).

- 53 Nix, W. D., and Arzt, E., *Metallurgical transactions. A, Physical metallurgy and materials science* **23A**(7), 2007-2013 (1992).
- 54 Smigelskas, A., and Kirkendall, E. *Trans. Aime* **171**, 130-142 (1947).
- 55 Ragone, D. V., *Thermodynamics of materials*. Wiley (1995).
- 56 Yang, T.-Y., Cho, J.-Y., Park, Y.-J., and Joo, Y.-C. *Current Applied Physics* **13**(7), 1426-1432 (2013).
- 57 Lloyd, J. R., Polcari, M. R., and MacKenzie, G. A., *Applied Physics Letters* **36**(6), 428-430 (1980).
- 58 Yoon, S. M., Lee, S. Y., Jung, S. W., Park, Y. S., and Yu, B. G., *Solid-State Electronics* **53**(5), 557-561 (2009).
- 59 Nardone, M., Simon, M., Karpov, I. V., and Karpov, V. G. *Journal of Applied Physics* **112**(7), 071101 (2012).
- 60 Reynolds, J. A., and Hough, J. M., *Proceedings of the Physical Society. Section B* **70**(8), 769-775 (1957).
- 61 Ivanov, D. S., and Zhigilei, L. V., *Physical Review Letters* **98**(19), 195701 (2007).
- 62 Mei, Q. S., and Lu, K., *Progress in Materials Science* **52**(8), 1175-1262 (2007).
- 63 Dash, J., *Reviews of Modern Physics* **71**(5), 1737 (1999).



- 64 Fecht, H., and Johnson, W., *Nature* **334**(6177), 50-51 (1988).
- 65 Kauzmann, W., *Chemical Reviews* **43**(2), 219-256 (1948).
- 66 Yang, T. Y., Cho, J. Y., Park, Y. J., and Joo, Y. C., *Acta Materialia* **60**(5), 2021-2030 (2012).
- 67 Lencer, D., Salanga, M., and Wuttig, M., *Advanced Materials* **23**(18), 2030-2058 (2011).
- 68 Park, Y. J., Yang, T. Y., Cho, J. Y., Lee, S. Y., and Joo, Y. C. *Applied Physics Letters* **103**(7), 073503 (2013).
- 69 Nukala, P., Agarwal, R., Qian, X., Jang, M. H., Dhara, S., Kumar, K., Johnson, A. T. C., Li, J., and Agarwal, R., *Nano Letters* **14**(4), 2201-2209 (2014).
- 70 Sun, Z., Kyrsta, S., Music, D., Ahuja, R., and Schneider, J. M., *Solid State Communications* **143**(4), 240-244 (2007).
- 71 Gaspard, J. P., Pellegatti, A., Marinelli, F., and Bichara, C., *Philosophical Magazine B: Physics of Condensed Matter; Statistical Mechanics, Electronic, Optical and Magnetic Properties* **77**(3), 727-744 (1998).
- 72 Goldsmid, H., and Douglas, R., *British Journal of Applied Physics* **5**(11), 386 (1954).
- 73 Venkatasubramanian, R., Siivola, E., Colpitts, T., and O'quinn, B., *Nature* **413**(6856), 597-602 (2001).

## 요약(국문초록)

상변화 메모리(PcRAM)는 높은 온도 및 전류밀도라는 가혹한 동작 조건에 의해 재료 내부에 공동(void) 형성과 같은 심각한 신뢰성 문제가 존재한다. 전류밀도에 상변화 물질에 미치는 영향에 대해 지금까지 많은 연구가 진행되어 왔지만 대부분의 파손기구에 관한 연구는 용융상에 한정되어 있다. 용융상 내의 원자의 확산은 결정상에 비해 매우 빠르게 이루어 지기 때문에 재료의 파손은 용융상에서 주도적으로 발생하고 결정상은 상대적으로 전류에 안정한 상으로 지금까지 알려져 왔다. 본 연구에서는 결정상 상변화 물질에서 발생하는 전류에 의한 전도도의 증가 또는 감소 현상을 최초로 발견하였고 선형 형태의 간단한 구조의 모사실험을 통해 실제 소자에서 발생할 수 있는 다양한 외적 요인을 배제시켰다.

결정상  $\text{Ge}_2\text{Sb}_2\text{Te}_5$  물질에 전류를 인가할 시 전류밀도에 따라 크게 3 가지의 다른 현상이 발생한다. 이때의 기준은 재료의 저항 변화 양상과 공동의 형태를 들 수 있다. 결정상  $\text{Ge}_2\text{Sb}_2\text{Te}_5$  물질에 약  $1 \sim 1.5 \text{ MA/cm}^2$ 의 전류 인가시 저항은 수십 시간동안 지속적으로 증가하고 내부에 나노 사이즈의 공동을 형성시키는 데, 이러한 현상은 기존에 보고된 용융상에서 발생하는 파손기구와는 확연히 다른 양상이다. 결정상에서 발생하는 열화현상은 전류에 의한 원자이동 (electro-migration)에 의한 것으로, 교류 전류 하에서는 본 현상이 발생하지 않는 것을 통해 확인이 가능하다. 원자이동에 의해 발생한 결함에서 국소적인 용융이 발생하게 되는데 이러한 용융상이 공동으로 형성된다. 이러한 현상을 결함 유도 용융 (defect-induced melting)이라고 한다. 지속적인 저항의 증가는 내부에 발생하는 나노 공동에 의해 발생한다.

1 MA/cm<sup>2</sup> 이하의 전류밀도 인가시 발생하는 저항의 감소는 재료 내부의 고유 공공(intrinsic vacancy)의 재배열에 기인 한다. 전류와 온도 모두 결정상 Ge<sub>2</sub>Sb<sub>2</sub>Te<sub>5</sub>의 물질 특성을 절연체에서 금속성으로 변화시키는 데 이를 금속-절연체 전이(metal-insulator transition)라고 한다. 하지만 전류를 인가할 경우 금속성을 띄지만 면심 입방 구조를 유지하는 Ge<sub>2</sub>Sb<sub>2</sub>Te<sub>5</sub>를 최초로 얻을 수 있었으며, 이는 육방 밀집 구조로의 상변화를 수반하는 열에 의한 전이와는 매우 다른 현상이다. 전류에 의한 저항 감소는 가장 높은 전류밀도 (peak current density)에 의존하고 초기의 저항이나 온도와는 무관하게 결정된다. 또한 전류에 의한 본 변화는 고유 공공 농도가 다른 GeSb<sub>4</sub>Te<sub>7</sub>와 Ge<sub>2</sub>Sb<sub>2</sub>Te<sub>5</sub>에서 다르게 발생하는 데, 이를 통해 본 현상이 고유 공공에 의존하여 발생함을 확인할 수 있다.

본 연구는 소자가 작아질수록 결정상에 흐르는 전류가 높아질 경우 발생 가능한 새로운 형태의 문제를 시사한다. 상변화 메모리에서 상변화가 발생하는 부분은 하부 전극과 맞닿은 일부의 영역에 한정된다. 따라서 상변화가 발생하지 않는 영역에서는 용융에 의한 회복이 없기 때문에 전류에 의한 영향이 계속해서 누적된다. 결정상에서의 저항의 변화는 SET 상태의 신뢰성과 매우 밀접한 관계를 가지고 있으며 다중 레벨 셀 (multi level cell)로 변화하는 현재 추세에 따라 더욱 중요해질 것으로 생각된다.

본 연구는 결정상 상변화 물질에서 발생하는 전기적인 불안정성에 관한 기준을 처음으로 규명함으로써 높은 신뢰성을 위한 상변화 메모리 소자의 설계 규칙 (design rule) 및 새로운 형태의 소자로의 응용 가능성을 제시하였다.

**표제어:** 상변화 메모리, 일렉트로마이그레이션, 결정상 칼코지나이드, 파손기구 분류, 전류 유도 금속-절연체 전이

학 번: 2010-20602